TECHNISCHE UNIVERSITÄT WIEN
Vienna University of Technology

DIPLOMARBEIT

Reservoir Theory and its Application on Peripheral Arteries

Ausgeführt am
Institut für Analysis und Scientific Computing
der Technischen Universität Wien

unter der Anleitung von
Ao. Univ.Prof. Dipl.-Ing. Dr.techn. Felix Breitenecker
und
Univ. Lektor Dipl.-Ing. Dr.techn. Bernhard Hametner

durch
Michael Ebner, BSc
Freistädter Straße 80
4040 Linz, Österreich

Wien, 21. Oktober 2014 Michael Ebner

TECHNISCHE
UNIVERSITÄT
WIEN
Vienna University of Technology

DIPLOMA THESIS

Reservoir Theory and its Application on Peripheral Arteries

written at the
Institute of Analysis and Scientific Computing
at the Vienna University of Technology

supervised by
Ao. Univ.Prof. Dipl.-Ing. Dr.techn. Felix Breitenecker
and
Univ. Lektor Dipl.-Ing. Dr.techn. Bernhard Hametner

by
Michael Ebner, BSc
Freistädter Straße 80
4040 Linz, Austria

Vienna, October 21, 2014 Michael Ebner

Danksagung

Mit dem Verfassen der Diplomarbeit befindet man sich in der sehr komfortablen Situation die (meisten) großen Hürden des Studiums bereits genommen zu haben. Jede einzelne von ihnen war jedoch notwendig um nun auf eine Zeit mit vielen wertvollen und lehrreichen Erfahrungen zurückblicken zu können. Viel mehr noch: Das Studium der Technischen Mathematik und die Zeit, die ich damit verbinde, haben mich geformt und zu meiner Persönlichkeitsentwicklung in einer Art und Weise beigetragen wie ich es davor nicht für möglich gehalten hätte. Insofern freue ich mich mit dem Schreiben dieser Zeilen tiefste Wertschätzung der letzten Jahre ausdrücken zu können.

Weiters möchte ich mich bei Prof. Felix Breitenecker und den Mitarbeitern des AIT Austrian Institute of Technology bedanken, dass ich unter ihrer Leitung meine Diplomarbeit auf dem spannenden Gebiet der Modellierung des Herz-Kreislauf-Systems schreiben durfte. Insbesondere gilt mein Dank Bernhard Hametner und Stephanie Parragh. Ohne sie hätte diese Arbeit nicht entstehen können. Hier möchte ich auch die vielen interessanten Unterredungen hervorheben, die solche Erlebnisse für mich erst zu etwas ganz Besonderem machen. Auch im Bezug auf den Schlusssprint dieser Arbeit sind sie es, denen ich zu tiefsten Dank verpflichtet bin. In diesem Zusammenhang möchte ich auch Cornelia Bartholner danken, die mir in dieser Phase tatkräftig zur Seite stand und mich bei dem einen oder anderen Fall und Beistrich unterstützte.

So sehr die universitäre und fachliche Weiterbildung ihren festen Platz in meinem Leben auch eingenommen hat, ist es besonders die Familie, die ich niemals missen möchte. Ihr seid es, die mir alles ermöglicht haben, auf die ich immer zählen kann und die mich immer anspornen neue Wege zu gehen. Dafür möchte ich Euch außerordentlich danken.

Auch möchte ich hier die Familie Bartholner erwähnen, die mich das gesamte Studium über begleitet und unterstützt hat. Für mich war das absolut keine Selbstverständlichkeit.

Nicht zuletzt sollen auch die vielen Persönlichkeiten und Weggefährten ihren Platz auf dieser Seite finden, die ich im Zuge der letzten Jahre kennen und schätzen gelernt habe. Von Judo und Linz, bis Wien über Alicante nach Lübeck und wieder zurück habt ihr alle mein Leben mitgeprägt und zu einem fantastischen Traum gemacht. Vielen Dank Euch allen.

Zusammenfassung

Herz-Kreislauf-Erkrankungen stellen in der heutigen Zeit die häufigste Todesursache weltweit dar. Methoden, die eine verbesserte Früherkennung, Diagnose und Behandlung ermöglichen, sind demnach von globaler Bedeutung. Mithilfe von mathematischen Modellen können wesentliche Einblicke in die komplexen Vorgänge innerhalb des Herz-Kreislauf-Systems gewonnen werden. Von besonderem Interesse ist hierbei ein verbessertes Verständnis für die zeitlichen Änderungen von Druck und Fluss, da diese Rückschlüsse auf den Zustand der arteriellen Gefäße ermöglichen. Die mathematische Beschreibung des Zusammenspiels dieser beiden Größen wird jedoch empfindlich durch verschiedenste Ausbreitungsphänomene von Wellen innerhalb des Arterienbaumes erschwert. Die sogenannte „Reservoir-Theorie“ setzt hier an und modelliert die tatsächliche Druckkurve als eine Summe bestehend aus *Reservoir*- und *Exzess*-Druck. Ersterer ist hauptsächlich durch die Elastizität der großen Arterien bestimmt, während zweiterer die Wellenphänomene abbilden soll. Auf Basis dieser Methode konnten bereits bemerkenswerte Resultate im Bereich der aufsteigenden Aorta erzielt werden. Gestützt auf die zwei Beobachtungen, dass zum Einen der Druckabfall an verschiedensten Orten im Arterienbaum sehr ähnlich und zum Anderen der berechnete Exzess-Druck proportional zum aortalen Fluss ist, glaubt man das Konzept auf herzfernere Orte übertragen zu können. Um diese Erweiterung zu rechtfertigen, wurden jedoch obige *Beobachtungen* zu zwei wesentlichen *Annahmen*.

Für die Anwendung der Reservoir-Theorie auf peripheren Arterien waren insgesamt 110 Druck- und Flusskurvenpaare, gemessen an der Arteria brachialis und carotis, verfügbar. Zuerst wurde das Reservoir-Konzept mathematisch hergeleitet und theoretisch untersucht. Insbesondere wurden zwei – für die Praxis wichtige – Methoden betrachtet: Methode 1 setzt die Flusskenntnis an der entsprechenden Arterie voraus während Methode 2 auf obigen beiden Annahmen beruht und die Flusskenntnis folglich nicht erforderlich ist. Insgesamt kamen drei unterschiedliche Algorithmen zur Anwendung, wobei zwei verschiedene Berechnungsansätze für die zweite Methode untersucht wurden. Vor der Aufspaltung des Druckes in Reservoir- und Exzess-Komponente wurden die Datensätze aufbereitet und deren Auswirkungen untersucht. Weiters wurde die Sensitivität der Algorithmen auf ihre jeweiligen Eingabeparameter, wie etwa

der geschätzten Systolendauer, ausgewertet, auf dessen Basis in weiterer Konsequenz die Parametrisierung der Algorithmen erfolgte. Im Anschluss wurden die Brachialis- und Carotis-Druckkurven gemäß des Reservoir-Konzeptes separiert, die resultierenden Reservoir-Drücke verglichen und systematische Unterschiede zwischen den Implementierungen diskutiert. Zu guter Letzt wurden alle berechneten Reservoir-Kurven und einige aus ihnen abgeleitete Parameter untersucht, wobei ein Hauptaugenmerk auf klinisch relevante Indikatoren, wie etwa Pulsamplitude und Fläche des Drucks über diastolischem Blutdruck, lag.

Die numerischen Experimente zeigten ähnliche Ergebnisse bei beiden Algorithmen der Methode 2. Im Gegensatz dazu wurden deutliche Differenzen beim Vergleich beider Methoden untereinander im Hinblick auf Kurvenform und zugehöriger Parameter festgestellt. Beim Großteil der Resultate lieferte die erste Methode systematisch höhere Pulsamplituden und geringere Zeitkonstanten, die damit auf einen steileren Druckabfall in der Diastole hindeuten. Des Weiteren wurde auch eine merkliche Sensitivität bezogen auf die geschätzte Systolendauer bei sämtlichen Implementierungen beobachtet. Darüber hinaus wiesen die Reservoir-Kurven Unterschiede je Arterie auf. Generell besitzten die Reservoir-Kurven der Brachialis kleinere Pulsamplituden und Flächen bei sämtlichen Implementierungen während die Pulsamplituden bei den Brachialis-Messwerten geringfügig höher waren. Speziell waren die Pulsamplituden im Mittel um 4 mmHg und die Flächen um 2 mmHg s bei der Brachialis kleiner gemäß Methode 2. Die dazu entsprechenden gemessenen Brachialis-Druckkurven hingegen hatten nach der Datenaufbereitung eine um etwa 4 mmHg höhere Pulsamplitude und eine um ca. 5 mmHg s kleinere Fläche verglichen mit der Carotis. Dennoch konnte bewiesen werden, dass die zweite wesentliche Annahme der Reservoir-Theorie des zum Exzess-Druck proportionalen Aortaflusses, im Falle ihrer Gültigkeit, mathematisch genauer charakterisiert werden kann.

Insgesamt deuten die Ergebnisse darauf hin, dass die Voraussetzungen für die Anwendung der Reservoir-Theorie an der Arteria brachialis und carotis nicht erfüllt sind. Demnach sollte die durchgeführte Separation des Druckes eher als eine entsprechend eines Lumped Parameter Modells interpretiert werden. Ferner bestehen aufgrund der Sensitivität gegenüber der geschätzten Systolendauer Zweifel im Hinblick auf eine zuverlässige Bestimmung medizinisch relevanter Parameter.

Abstract

In modern times cardiovascular diseases (CVDs) constitute the major cause of death worldwide. Thus, improvements in diagnosis, treatment and prevention of CVDs could mean a further significant enhancement in global health care. In this context cardiovascular modelling plays a key role in order to gain valuable information on the human circulatory system. Especially a profound understanding of the pressure and flow waveforms of blood are of high interest since they reflect the physical state of a patient's arterial system. However, the mathematical models have to deal with considerably complex phenomena related to the wave propagation within the arterial tree. A very recent modelling approach meant to address this issue properly is called the *Reservoir Theory*. Several results have testified a promising ansatz of regarding the actual pressure waveform as an instantaneous sum consisting of an arterial compliance-related *reservoir* and a wave-associated *excess* pressure at the aortic root. Due to various experiments, it is believed that the same concept might suit for more distal locations too. Nonetheless, two assumptions are crucial to justify this *extended* reservoir concept: A similar pressure waveform decay at different arterial locations during diastole and a corresponding excess pressure proportional to the flow at the aortic root.

In total 110 pairs of pressure and flow curves measured at the brachial and carotid artery were available in order to apply the Reservoir Theory on this data. Firstly, the reservoir concept was mathematically derived and theoretically investigated. In particular, two distinct – and practically important – methods were regarded: Method 1 is based on the knowledge of flow at the respective artery and method 2 relies on the *extended* reservoir concept which does not require the flow. Three different algorithms were used whereby two distinct computational approaches were considered for the latter method. Prior to the pressure separation, necessary data preprocessing was performed and its effects analysed. Moreover, the sensitivity of all algorithms to input parameters such as estimated notch time was pointed out. Based on these findings the respective algorithms got parametrized and, in further consequence, both the brachial and carotid pressure waveforms got separated. Their resulting reservoir curves were compared and systematic differences among all implementations discussed. Lastly, all computed reservoir waveforms

and their deviated parameters were examined whereby a particular focus was put on clinically relevant indicators such as pulse pressure and area of pressure above diastolic blood pressure.

The numerical results showed similar results of both algorithms associated with method 2. In contrast, remarkable differences with respect to both the reservoir pressures and their deviated parameters were witnessed as opposed to the first method. In the majority of cases, method 1 generated systematically higher pulse pressures and lower time constants indicating a steeper pressure decay in diastole. Furthermore, a notable sensitivity on the estimated notch time was observed among all implementations. Apart from that, the obtained reservoir curves differed for brachial and carotid data. In general, brachial reservoir curves exhibited lower figures in pulse pressure and area of pressure above diastolic blood pressure among both methods whereas total pulse pressure was slightly higher for brachial readings. Particularly, and with respect to method 2, the differences in pulse pressure and area of pressure above diastolic blood pressure between the corresponding brachial and carotid reservoir curves were, on average, about $-4\,\mathrm{mmHg}$ and $-2\,\mathrm{mmHg\,s}$ respectively. In contrast, the provided measured pressure waveforms exhibited mean figures of approximately $4\,\mathrm{mmHg}$ and $-5\,\mathrm{mmHg\,s}$ for the respective differences after data preprocessing. Nevertheless, the second main assumption for the extended Reservoir Theory was, in case of its validity, mathematically refined.

Overall, the findings suggest that the brachial and carotid reservoir curves do not meet the necessary assumptions to justify the application of the extended Reservoir Theory at these arterial locations. In particular, the assumed similarity of arterial reservoir curves is questionable. Thus, the pressure separation at the respective artery might rather be considered as a separation according to a local lumped parameter model. Moreover, the observed sensitivity to the estimated notch time of all algorithms causes doubts in terms of the reliable prediction of clinically relevant parameters.

Contents

List of Figures

List of Tables

Chapter 1

Introduction

Since the beginning of mortality and morbidity recordings a steady rise of life expectancy has been witnessed globally. According to the World Health Organization (WHO) a person who was born in 1955 was likely to live 48 years and in 1995 already 65 years [35]. By 2025 it is expected that no country worldwide will exhibit a life expectancy of less than 50 years. Moreover, the WHO states an average life expectancy of 70 years of the global population born in 2012, having its peak in Japan with 84 years.

Modern medicine and its ability of curing and preventing diseases has been an essential driver for this trend. The number one cause of death worldwide is still rooted in cardiovascular diseases (CVDs). With reference to [20] CVDs are responsible for approximately 47 % of all deaths in Europe and for about 40 % in the European Union. In Austria the national statistical office Statistik Austria recorded that 42.7 % of the deaths in 2012 were caused by CVDs, followed by cancer achieving a proportion of 25.5 % [4]. Therefore, improvements in diagnosis, treatment and prevention of CVDs could mean a further significant enhancement in global health care.

Against this background many approaches have been developed to model the cardiovascular system so as to describe the underlying phenomena of hemodynamics and, hence, gain valuable information complementing those provided by medical doctors. In this context pressure and flow waveforms of blood in combination with their deduced parameters are of main interest since they are capable to describe the physical state of a patient's arterial system. For example systolic blood pressure, pulse pressure and arterial compliance[1] were revealed as major predictors of cardiovascular morbidity and mortality in recent years [5, 11, 33].

However, in order to obtain reliable information one has to deal with numerous and considerably complex phenomena related to the propa-

[1] The pulse pressure represents the difference between the systolic and diastolic blood pressure whereas the arterial compliance constitutes an indicator for the elasticity of the main arteries.

gation of pressure and flow waveforms within the cardiovascular system. One approach meant to address this issue properly is called the *Reservoir Theory*. Promoters believe that this fairly new concept might contribute a deeper insight to the challenging and very important subject of wave travel in arteries. Initially the Reservoir Theory was developed to examine pressure and flow waveforms originating in the ascending aorta [31]. Nonetheless, since generally pressure and flow waveforms cannot be obtained easily in the aortic root its inherent concept was subsequently extended to arbitrary points within the arterial tree under some assumptions [1]. These assumptions are crucial for the applicability of the Reservoir Theory and therefore are currently subject of further investigation.

1.1 Reservoir Theory: The Main Principles and Assumptions

For many years scientists have puzzled over the different waveforms between pressure and flow at the aortic root which have never been explained satisfactorily [31]. Despite various kinds of models this issue is still persistent which, in turn, propels scientists to new modelling approaches. According to [7] two observed phenomena were the basis for introducing a new concept – the *Reservoir Theory*:

(i) The elasticity of arteries induces a cushioning and recoiling effect which smooths the pulsatile pressure and flow of every cardiac ejection. As a consequence an almost steady perfusion at tissue level is achieved.

(ii) Travelling waves get reflected at different sites within the vascular tree. Hence, the measured pressure and flow waves are a result of superimposed forward- and backward-travelling waves which depend strongly on the site and characteristics of the arterial location.

Indeed, these observations are believed to contribute to the pressure and flow waveforms at any site along the arterial tree. Taking into account these aspects a reasonable ansatz for a further investigation is to separate them from the measured pressure waveform. The main idea of the Reservoir Theory is now to divide the measured pressure waveform p into a time-dependent *reservoir* pressure p_{res} and the remaining time- and location-dependent *excess* pressure p_{ex}. Consequently, p is considered as an instantaneous sum of the compliance-related reservoir pressure and the excess pressure depending on local conditions which formally reads

$$p = p_{\text{res}} + p_{\text{ex}}.$$

This approach was firstly published in [31] in 2003 and was applied to pressure and flow waveforms measured at the ascending aorta which yielded remarkable results in terms of potentially solving some long-lasting problems in this field.

In a subsequent publication [1] this concept was evolved further such that the Reservoir Theory was meant to not only be able to model waveforms at the aortic root, but also to predict corresponding pressure waveforms at any arbitrary location in arteries when the flow rate into the arterial system q_{in} is not known. This was concluded from two empirical observations [1, §2.2]:

(A1) The pressure waveform decay measured at different locations in the arterial system is very similar during diastole.

(A2) The excess pressure at any aortic location is approximately proportional to the flow in the aortic root.

Therefore, on locations where these *assumptions* are true, the respective separation in reservoir and excess pressure can be performed by the mere knowledge of the pressure waveform p at this arterial site without knowing the aortic flow. In other words it is believed to overcome the lack of information by simply assuming (A2)

$$q_{\text{in}} \sim p_{\text{ex}} = p - p_{\text{res}},$$

whereby the reservoir pressure is supposed to be computed reliably due to (A1).

Hence, *if* these assumptions are true, the description of many phenomena within the cardiovascular system would be tremendously simplified since in practice it is difficult to acquire both waveforms of arterial flow and pressure simultaneously.

However, for conducting this thesis 110 pairs of measured pressure and flow velocity waveforms at both the brachial and carotid artery are available. This data was thankfully provided by Prof. Alun D. Hughes[2] and acquired in the course of the Hypertension Associated Cardiovascular Disease ASCOT[3] substudy at the St. Mary's Hospital center, London, UK.

1.2 Thesis Objectives

The opportunity of holding numerous pressure and flow velocity waveforms at both the brachial and carotid artery enables manifold possibil-

[2]Prof. Alun D. Hughes, International Centre for Circulatory Health, NHLI, Imperial College London, St Mary's Hospital, London W2 1LA, United Kingdom.

[3]Abbreviation for "Anglo-Scandinavian Cardiac Outcome Trial".

ities related to the application of the Reservoir Theory. In respect of this thesis the objectives were related to the application of two different approaches of the Reservoir Theory:

Method 1: Separate the measured pressure waveform at each artery by using the flow velocity.

Method 2: Separate the measured pressure waveform at each artery by *assuming* (A1) and (A2).

Thus, the second method does not use the arterial flow rate for the pressure separation but assumes to know the waveform at the aortic root by (A2) instead. In combination with (A1), this is sufficient to perform the pressure separation at the respective artery. In further consequence one has to expect differences in their corresponding pressure separations which give rise to the three objectives of this thesis:

Objective 1: Compare the results of method 1 and 2 based on physiologically meaningful parameters. Quantify the reservoir pressures in terms of clinically relevant parameters such as the pulse pressure and the area of pressure above diastolic blood pressure.

Objective 2: Investigate the sensitivity of the implemented algorithms on input parameters such as the estimated notch time[4].

Objective 3: Examine the validity of (A1) by comparing the reservoir pressure decays at both arterial locations.

1.3 Thesis Outline

The thesis is structured in five chapters. In the **current chapter** the general motivation for introducing a new model concept for describing the cardiovascular system was given. It was pointed out that the Reservoir Theory suggests to separate two phenomena from the actual pressure waveform at the ascending aorta: The elasticity of the main arteries and wave travelling phenomena. In further consequence, based on empirical observations, the Reservoir Theory is believed to be applicable at any arterial location by *assuming* those findings.

In the **second chapter**, necessary basics of hemodynamics and important models for describing the the cardiovascular system are provided

[4]The notch time indicates the end of systole when the aortic valve shuts and the fillings of both ventricles start anew.

so as to build up the Reservoir Theory on them. In particular, the classic two- and three-element Windkessel Models are presented.

The **third chapter** is dedicated to the concept of the Reservoir Theory and its mathematical description. Two kinds of modelling approaches are illustrated: Firstly, the separation of pressure based on the *knowledge* of the aortic flow into the arterial system is described. And secondly, the ansatz of dividing the pressure by the *assumed knowledge* of the aortic flow is pointed out. In further consequence, relying on the *assumed* observations (A1) and (A2), the extended Reservoir Theory is presented which is supposed to be applicable at any arterial location. Available data sets of pressure and flow velocity waveforms of the brachial and carotid are discussed. The necessity of performing some data preprocessing prior to the application of the Reservoir Theory is pointed out and the methods used are documented. Additionally, two methods for estimating the systolic time duration used in this thesis are described. Lastly, three different implementation approaches of the Reservoir Theory are presented. One relies on the classic approach incorporating the flow rate, and the others implement the extended concept meant to perform the pressure separation in case that the flow is not available. Since they base on different input parameters possible model interpretations are presented and a possible conversion formula of important peripheral parameters is deviated.

The **fourth chapter** is dedicated to the comparison of the numerical results and their discussion. Beside the documentation of the impact of data preprocessing on the altered waveforms the sensitivity of the respective algorithms on their parametrization is investigated as well before performing the Reservoir Theory. In the following the pressure separations acquired by all implementation methods are examined and interpreted. An extension of (A2) was formulated under which both concepts theoretically should yield identical results at any arterial location. The complete output parameters of all algorithms are checked against each other at both the brachial and carotid artery. Systematic differences in the corresponding pressure separation are pointed out by means of several indicators. Furthermore, clinically relevant parameters are deviated from the the respective reservoir curves and compared for both arterial locations. Finally, the assumption (A1) is investigated based on the brachial and carotid reservoir waveforms.

In the **last chapter**, a conclusion of all findings is given. Further improvements are suggested and other possible applications of the Reservoir Theory are stated.

Chapter 2

Pressure and Flow Waves in Arteries

In this chapter necessary basics of hemodynamics and important models for describing the cardiovascular system are provided in order to build up the Reservoir Theory on them in chapter 3.

2.1 Cardiovascular Physiology

Beside many other tasks the main function of the cardiovascular system[1] is to transport sufficient oxygen and nutrients to all parts of the body whilst simultaneously being responsible for the removal of waste products. The driving force of this procedure is the heart by providing cyclic heart beats to pump the blood periodically into the vascular system. A general overview of the circulatory system is given by fig. 2.1.

Oxygenated blood, gathered in the left atrium, is forwarded to the left ventricle, where the contraction of the heart pumps blood with high pressure into the *systemic arteries* starting at the aorta. Then the blood is conducted to the arterioles and capillaries where the *microcirculation* is happening. Oxygen is transferred to the tissues and carbon dioxide is passed to the blood. The capillaries merge into *venules* where the deoxygenated blood enters the *systemic veins* bringing the blood back to the heart by reaching the right atrium. The blood is ejected into the *pulmonary circulatory system* by the right ventricle in which oxygen-depleted blood gets reoxygenated in the lungs and finally returns to the left atrium where the cycle starts again. Since blood never leaves this network of blood vessels, it is referred to as a *closed* cardiovascular system.

The pressures occurring in both the pulmonary and systemic system exhibit remarkable differences as can be observed in fig. 2.2. Pressures within the aorta and systemic arteries fluctuate considerably in time be-

[1] Also called circulatory system.

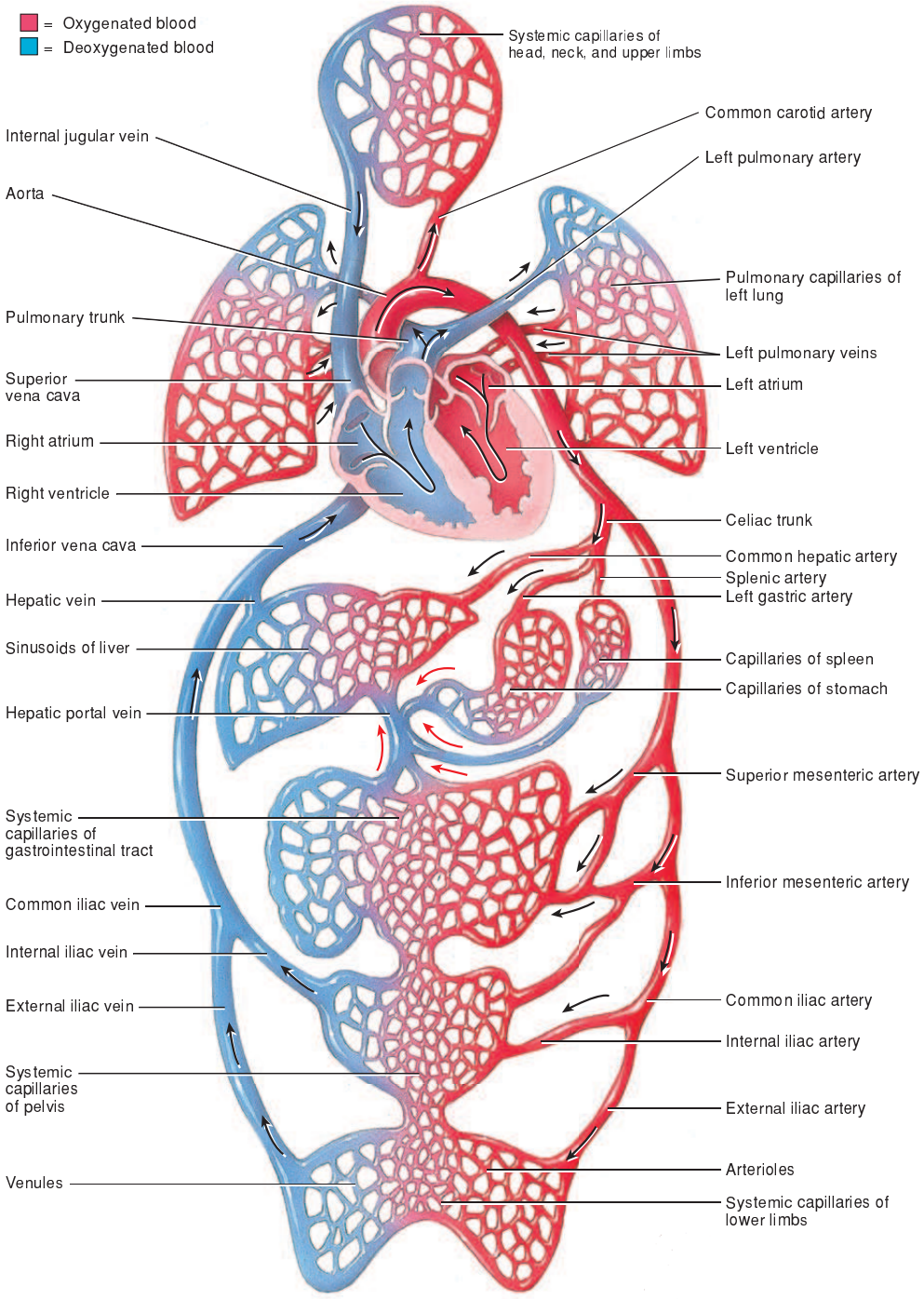

Figure 2.1: The cardiovascular system
Source: [29, Fig. 21.17]

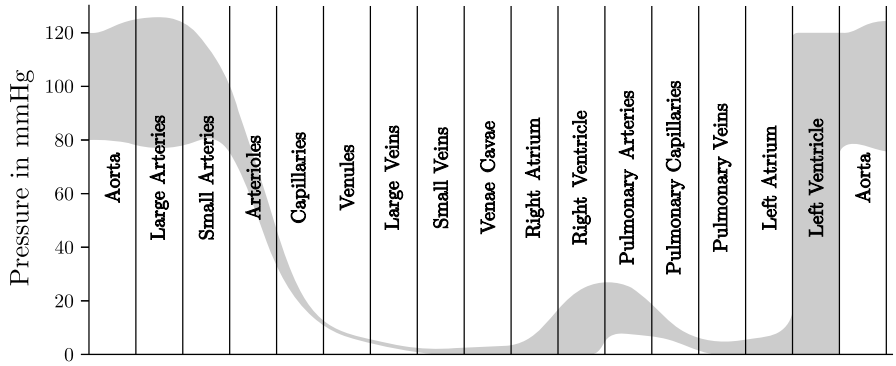

Figure 2.2: Pressure distribution in the human cardiovascular system
Source: Modified from [24, Fig. 2.2] which originally stems from [22]

tween approximately 80 mmHg and 120 mmHg with a gradual decrease towards capillaries whilst the pressures in the venous system remain insubstantial at around 10 mmHg. The pressures in the right ventricle and the pulmonary arteries are slightly higher, oscillating at about 30 mmHg. In contrast, the pressure in the left ventricle is highly volatile ranging from 0 mmHg to 120 mmHg.

However, regarding the blood volume, vessels located at the systemic veins contain about 54 %, whilst systemic arteries and pulmonary circulation comprise approximately 20 % and 14 % respectively. The rest is stored in capillaries [24].

2.1.1 The Cardiac Cycle

After this overall outline of the circulatory system a more detailed description is given so as to get a better understanding of the corresponding aortic pressure waveform.

One cardiac cycle is divided into several stages. Each stage can be addressed separately by two important terms, namely the *systole* and *diastole*. Referring to the electrocardiogram (ECG) signal in fig. 2.3 the former starts with the the ventricular contraction, indicated by the QRS-complex, and the latter with the ventricular relaxation, initiated by the T-wave, respectively. The sequence of events for a single heart beat of the left heart is now as follows [8, § 4.2.2], whereby the numbers indicate the stage associated with fig. 2.3:

1. **Atrial filling** (mid to late diastole): The two atrioventricular (AV) valves of the right and left atrium are open and both the pulmonary and aortic valves are closed. In fig. 2.1 this situation is depicted. Therefore blood enters the left and right atrium but cannot get

out of the ventricles. In the end of this stage an electrical stimulus activates both atria forwarding blood to the ventricles.

2. **Ventricular contraction**, stage I (early systole): After stimulation the ventricles contract which gives rise to a higher ventricular pressure forcing the AV valves to snap shut. The corresponding sound is known as the *first heart sound* and can be detected by a stethoscope. Given that blood is incompressible, the ventricular blood volume remains unchanged causing a steady rise in ventricular pressure. When the increasing ventricular pressure exceeds aortic pressure the aortic valve snaps open yielding to an ejection of the blood.

3. **Ventricular contraction**, stage II (mid to late systole): Aortic pressure increases, achieving a peak and then drops gradually. As soon as aortic pressure is undershot the aortic valve snaps shut leading to the *second heart sound* indicating the end of systole.

4. **Ventricular relaxation** (early diastole): Due to the ongoing ventricular relaxation the decreasing ventricular pressures fall below atrial pressures which, subsequently, opens the AV valves and the ventricular fillings start anew, introducing again the first stage in this periodic process.

As described above the heart is the driving force to pump the blood into the arterial system leading to pressure waveforms varying in time and location depending on the conditions along the vascular tree. The related pressure differences at different sites cause a flow and vice versa. For the very beginning of the arterial tree, at the aortic root, both the flow and pressure patterns are illustrated in fig. 2.4. The flow is given in l/s and its curve is scaled such that pressure and flow have comparable heights in systole. At an early stage of systole pressure and flow are closely aligned until, at some point, this characteristic diminishes. The ongoing deviation can be partly explained due to existence of *travelling waves* which arrive at a later stage and partly due to the *elastic compliance* of the aorta which acts as storage of blood. The presence of those two phenomena constitutes the basic idea of the new approach called *Reservoir Theory*. However, before discussing the phenomena of wave reflection in the vascular bed and the elasticity of larger arteries in more detail, their direct impact on locally distinct waveforms is described in the following subsection.

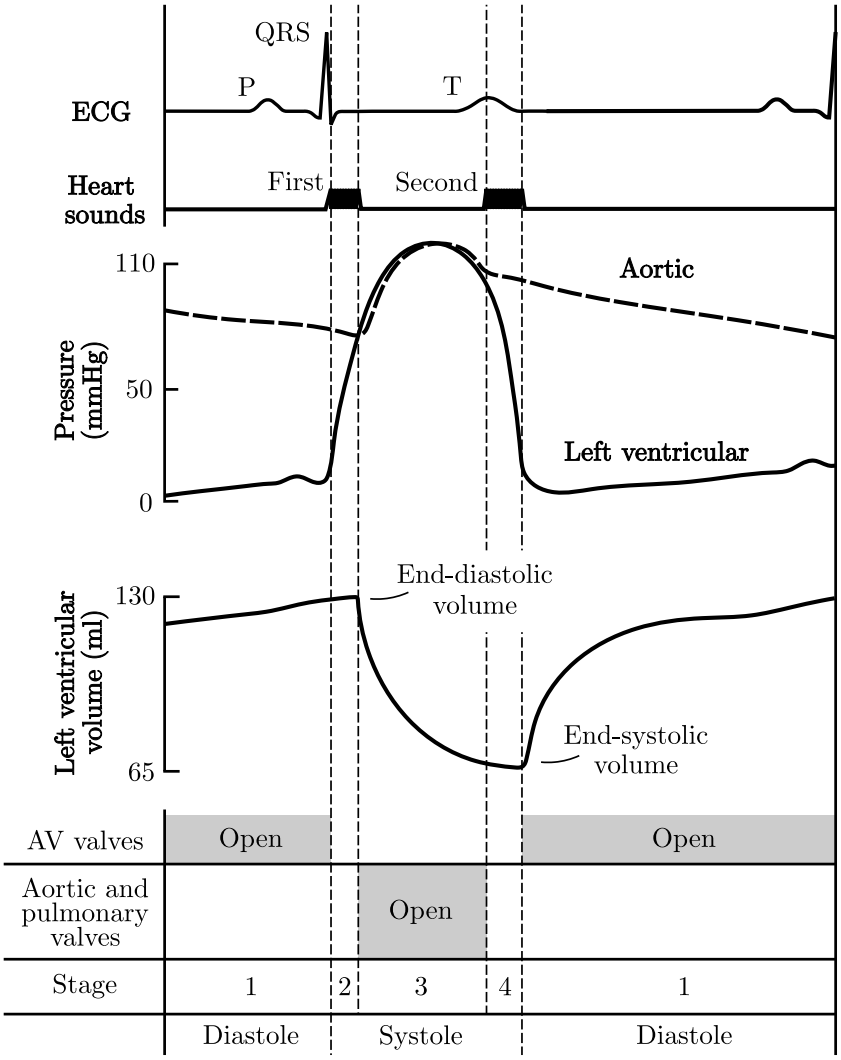

Figure 2.3: Cardiac cycle of the left heart
Source: Modified from [8, Fig. 4.9] which was modified from [30]

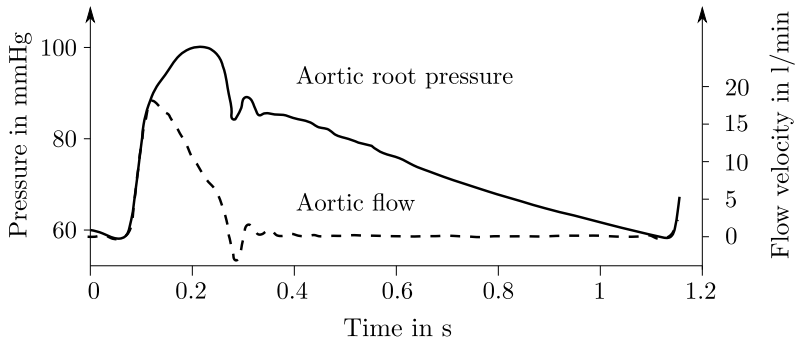

Figure 2.4: Aligned pressure and flow waves in the aortic root
Source: Modified from [31, Fig. 1]

2.1.2 Different Waveforms at Different Locations

As already observed in fig. 2.2 pressures vary remarkably within the arterial tree. The periodic cardiac contraction and relaxation combined with local characteristics of the circulatory system lead to time- and location-dependent pressure and flow distributions throughout the arterial circulation. Schematic pressure waveforms along the arterial tree including their mean levels are depicted in fig. 2.5. It indicates the highly volatile pressure waveform in the left ventricle depending on the stage of the cardiac cycle. Furthermore, the pressure waveforms tend to exhibit higher amplitudes with steeper changes the more distal located they are from the heart whilst simultaneously exhibiting a decreasing mean pressure. Moreover, at the end of systole a notch is visible at the ascending aorta which is known as the *dicrotic notch* and indicates the closure of the aortic valve. Along the arterial tree this dicrotic notch becomes less evident until it diminishes completely which is as well observable in the upper panel of fig. 2.6. Referring to the bottom panel similar results hold for the flow velocity but, as opposed to the changes in pressure, the velocities tend to decrease along the arterial tree. It is important to notice that flow and velocity waves are related to each other by the corresponding cross-sectional area A of the respective arterial location, i.e.

$$u = \frac{q}{A}. \tag{2.1}$$

This relationship is a deduction of the mass conservation law for incompressible fluids. Hence, the flow velocity u may be understood as the *cross-sectional average* velocity determined by the volume flow rate q through an artery of cross-sectional area A. For further considerations one has to keep in mind that the waveforms of both the pressure and flow vary along the cardiovascular system whose causes are rooted in local circumstances which are hard to predict and therefore constitute severe difficulties in modelling the arterial system.

2.2 Cardiovascular Modelling

In this section several definitions and concepts helping to characterize the cardiovascular system are provided in order to describe widely used model approaches.

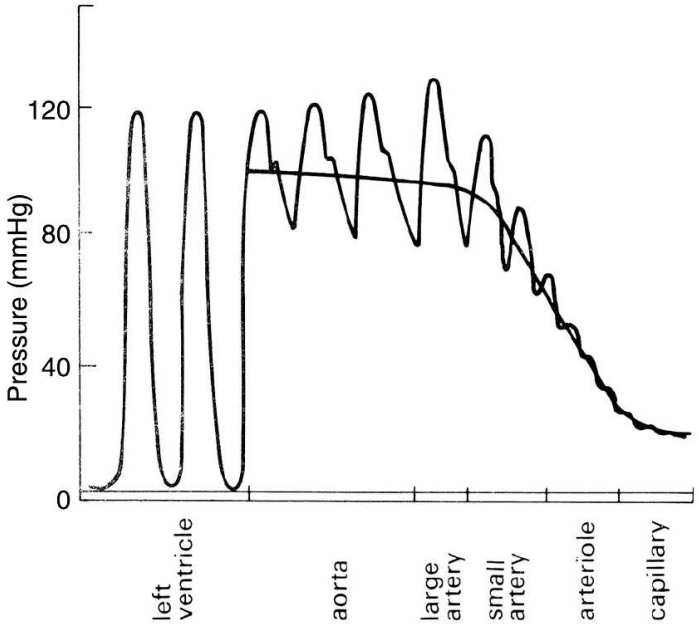

Figure 2.5: Pressure distribution in the arterial circulation
Source: [6, Fig. 12.12]

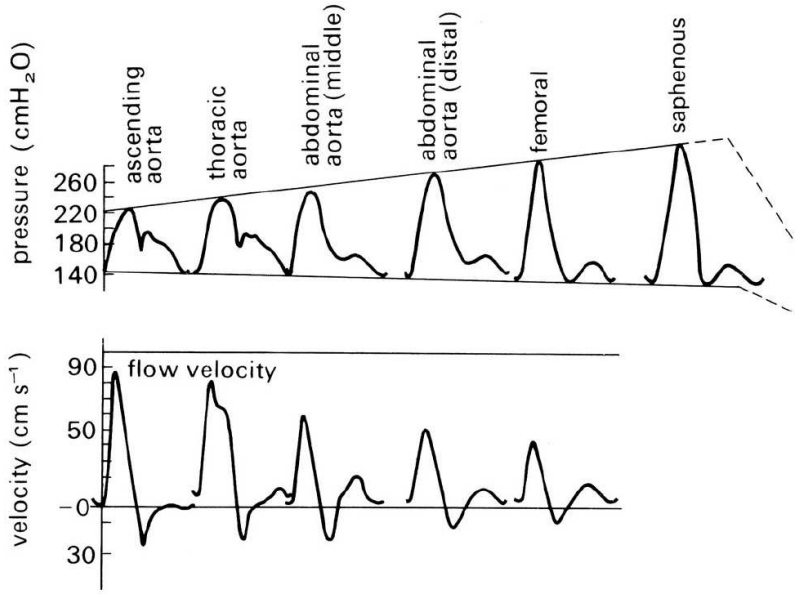

Figure 2.6: Pressure and flow velocities at different sites in dog arteries
Source: [6, Fig. 12.19] which is based on [21]

2.2.1 Resistance

In the context of describing the circulatory system several types of resistances are used. Generally, a *resistance* R quantifies the ratio between the pressure drop Δp and flow rate q through a vessel, i.e.

$$R := \frac{\Delta p}{q}.$$

The unit of resistance is given by $\mathrm{mmHg\,s/m^3}$. In the simple case of a single uniform vessel Poiseuille's law predicts the flow

$$q = \frac{\pi}{8\,\eta}\frac{r^4\,\Delta p}{\ell}$$

and hence the resistance R to be

$$R = \frac{\Delta p}{q} = \frac{8\,\eta}{\pi}\frac{\ell}{r^4}$$

where η denotes the blood's viscosity, r the radius and ℓ the length of the vessel. It is evident that general vessels do not obey these characteristics but Poiseuille's law is widely used as a convenient approximation though.

The total vascular resistance[2] is referred to as the total resistance of all arteries, arterioles, capillaries, venules and veins which is mainly determined by the small arteries and arterioles [34, §6]. Therefore it is often called (total) *peripheral resistance*. In a first approximation this becomes clear by considering the vessels' diameters and applying Poiseuille's law to the diameters given in table 2.1 which identifies the small vessels as the major contributors to the resistance. Nevertheless, even though capillaries possess small diameters they remain insubstantial in comparison [34, §6].

Other important resistances, which are in fact *impedances* since they are defined in the complex plane, are the *input* and the *characteristic* impedances. Impedances are given by the ratio between pressure and flow rate for oscillatory signals and consequently are stated in the same unit as resistances. These sinusoidal signals can be derived by the application of Fourier Analysis. The input impedance describes the net impedance of all vessels downstream the point of definition. For example the *aortic* input impedance defines the total impedance of all vessels downstream the ascending aorta including all peripheral arteries. In contrast, the characteristic impedance describes the pressure flow ratio during the absence of reflections. It will be important later on in section 2.2.4.

[2] Also called systemic vascular resistance.

Vessel	**Average diameter** (mm)	**Wall thickness** (mm)	**Average length** (cm)	**Ratio of wall thickness to radius**
Aorta	25.000	2.000	40.00	0.16
Medium arteries	4.000	0.800	15.000	0.40
Arterioles	0.300	0.020	0.200	0.75
Capillaries	0.008	0.001	0.075	0.25
Venules	0.020	0.002	0.200	0.20
Medium veins	5.000	0.500	15.000	0.20
Large veins	15.000	0.800	20.000	0.10
Venae cavae	30.000	1.500	40.000	0.10

Table 2.1: Approximate physical characteristics of different components of the vascular system
Source: [16, Table 9.1] which is based on [12, Section 2]

2.2.2 Compliance

The *compliance* refers to the elasticity of arteries. By definition it quantifies the pressure-volume relation by

$$C := \frac{dV}{dp}$$

where V denotes the Volume and p the pressure at the specific point of interest[3]. Its unit is stated in $m^3/mmHg$. The elastic compliance of the systemic arteries is largely determined by the proximal 10 % of the aorta, which furthermore constitutes the most compliant part of the aorta [21]. Thus the total *arterial* compliance, as an important example, obtained by addition of all vessel compliances in the arterial system is mainly given by the elasticity of the large (or conduit) arteries [33]. Studies have revealed the clinical relevance of compliance as it gives a "quantitative measure of mechanical and structural properties" [34, p. 45] of organs, which alter throughout the lifetime and with diseases [13, 14].

2.2.3 Wave Velocity, Wave Travel and Wave Reflections

Basically, every heart beat causes pressure and flow waves to run downwards the arterial tree with a certain speed which is called *wave speed* or *pulse wave velocity*. A good overview of this situation is given by fig. 2.7 where several blood pressure waveforms are depicted for different sites located downstream a dog's aorta. By comparing two curves, e.g. those

[3]The *elastance* E, in contrast, is defined as the inverse of the compliance, i.e. $E = 1/C$.

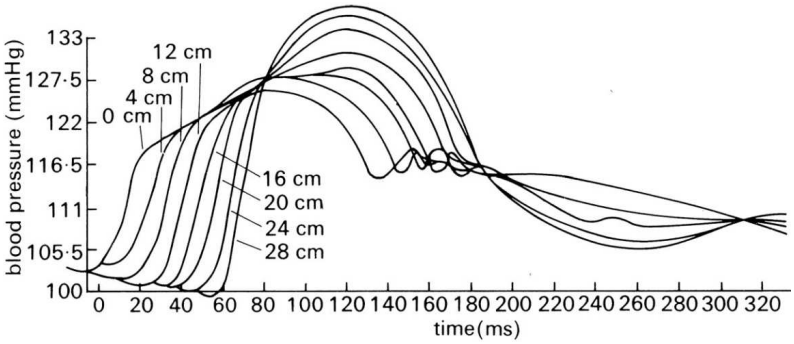

Figure 2.7: Blood pressures in systemic arteries of a dog
Source: [6, Fig. 12.14] which originally stems from [23]

Figure 2.8: Transverse elastic wave
Source: Modified from [8, Fig. 4.17]

belonging to the points $x = 0\,\text{cm}$ and $x = 12\,\text{cm}$, a time-lag can be observed which corresponds to the actual time it takes the pressure *wave* to reach its new location. It has to be mentioned that the actual pulse wave velocity superimposes the velocity of blood. Whilst the flow velocity itself decreases along the arterial tree (as seen in the lower panel of fig. 2.6) the wave speed (responsible for the time-lag between the curves) increases instead. This is a consequence of stiffening and the decrease of radius which can formally be described by means of the *Moens-Korteweg equation*

$$c = \sqrt{\frac{E\,d}{\varrho\,D}} \tag{2.2}$$

where E denotes the Young's modulus[4], d the wall thickness of the vessel, D the internal diameter of the vessel and ϱ the blood viscosity. In table 2.1 the ratio $d/(2\,D)$ is stated which explains the increase in wave speed towards the small arteries. Consequently, since pulse waves are way faster then the blood flow velocity in most locations the latter is usually neglected [34].

Moreover, these waves travel as *transverse elastic waves*. In order to explain that an elastic tube filled with blood is regarded whereby the blood is, on average, at rest for the sake of simplicity [8, §4.3.4]. Existing

[4]It is also known as tensile or elastic modulus and measures the stiffness of an elastic material. Generally holds: The higher the value the stiffer the material.

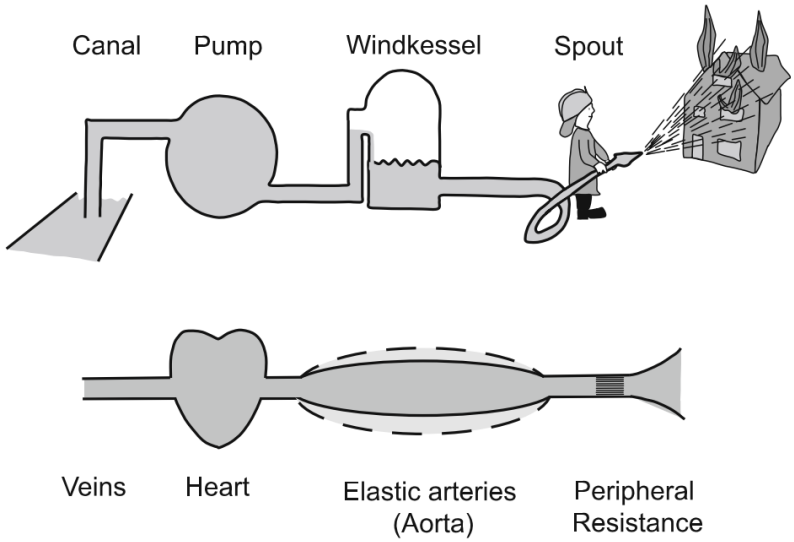

Figure 2.9: The concept of the Windkessel
Source: [33, Fig. 1]

pressure differences within the tube at a given time lead to a specific distension distribution, c.f. fig. 2.8. Given that at some point the wall is locally distended the corresponding pressure difference to some point next to it causes the fluid (i.e. the blood) particles to move. Two mechanisms involved are the blood inertia and the elasticity of the wall which act against this particle displacement. Due to this movement the pressure drops at point 1 and increases at point 2. Hence the wave moves to the right as a *distension* wave. It is important to notice that fluid particles are not moving along the tube in the assumed case of dealing with no net flow. They give rise to the fluid displacement until they move backward to its original location. Therefore they rather "execute back-and-forth oscillatory motions" [8, p. 188]. However, generally the wave speed can be estimated by means of the Moens-Korteweg equation (2.2).

Furthermore, travelling waves not only propagate throughout the arterial system but also get *reflected* whenever an impedance mismatch occurs, e.g. at bifurcations. Hence, measured waves at any location are a result of superimposed forward- and backward travelling waves.

2.2.4 The Windkessel Model

One of the earliest models used to describe the cardiovascular system are called *Windkessel Models*. To date there exist several variations but the first representative was the two-element Windkessel introduced by Frank in 1899 [9]. The idea behind was to take into account the already known blood storage effect of arteries in combination with peripheral resistance.

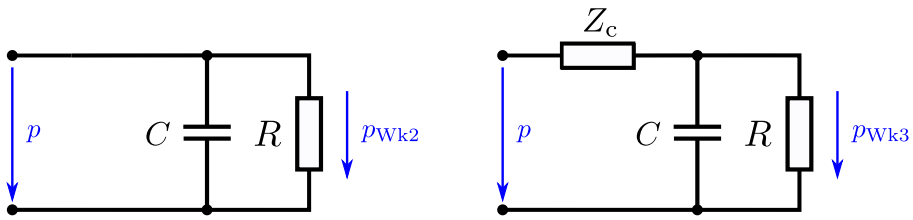

(a) Two-element Windkessel (b) Three-element Windkessel

Figure 2.10: Windkessel models in electrical analogy

The concept can simply be presented with fig. 2.9. The elastic aorta acts as air chamber in order to provide an almost steady flow throughout the whole cardiac cycle for a sufficient perfusion on tissue level. In electrical analogy it can be illustrated with fig. 2.10a whereby R denotes the (total) peripheral resistance and C the (total) arterial compliance. Therefore the compliance is regarded as *electrical capacitance* and the peripheral resistance as *electrical resistance*. Such analogies are widely used but one has to bear in mind that they sometimes could cause some misunderstandings. For example an electrical capacitor needs an in- and outlet and the *currents* involved are necessarily equal at both sides. In contrast, a fluid compliance chamber (e.g. the ascending aorta) many times only has one inlet and the corresponding *flow rates* in and out of them do not have to be the same [8, Box 4.4].

The Windkessel model can also be regarded as a so-called *lumped parameter model*. Since the arterial system, with pressure and flow at its entrance, is described by two parameters only – without caring about exact local phenomena – this term is also justified. In particular these parameters convey a special physiological meaning, namely the arterial compliance and arterial resistance. However, wave travel phenomena which happen inside the arterial tree, such as wave reflections, cannot be described with this type of model [33].

In a two-element Windkessel model the pressure decay during diastole can be stated as

$$p_{\mathrm{Wk2}}(t) = p_{\mathrm{es}}\, e^{-t/(R\,C)} \tag{2.3}$$

where p_{es} denotes the end-systolic aortic pressure and $t \geq 0$ indicates the time within diastole. As a result the two-element Windkessel model predicts an exponential decay with characteristic time constant $R\,C$ and, when either R or C is known, the missing parameter can be found after fitting the Windkessel pressure p_{Wk2} to the measured pressure p by adjusting the time constant $R\,C$. Generally, with (2.3) it is possible

to approximate the diastolic pressure behaviour quite well but the two-element Windkessel generally poorly predicts systolic pressure.

An improvement of the two-element Windkessel model can be achieved by simply adding the characteristic impedance Z_c as shown in fig. 2.10b. The crucial point is that, now by extending the model with an impedance, also characteristics for higher frequencies of the arterial system are considered. This particular shortcoming of the two-element Windkessel model becomes obvious by regarding the impedance of the in parallel connected arterial compliance and peripheral resistance in the frequency domain. With the angular frequency $\omega := 2\,\pi\,f$ for a frequency f the impedance X_c of the compliance reads

$$X_c = \frac{1}{\mathrm{i}\,\omega\,C}.$$

Thus the parallel circuit of R and C yield an input impedance

$$\begin{aligned} Z_{\mathrm{Wk2}}(\omega) &:= \frac{R\,X_c}{R + X_c} = \frac{R}{R/X_c + 1} = \frac{R}{1 + \mathrm{i}\,\omega\,R\,C} \\ &= \frac{R}{1 + (\omega\,R\,C)^2}\,(1 - \mathrm{i}\,\omega\,R\,C) \end{aligned}$$

of the two-element Windkessel in the complex plane. Equivalently written in polar form this means

$$Z_{\mathrm{Wk2}}(\omega) = \frac{R}{\sqrt{1 + (\omega\,R\,C)^2}}\,e^{-\mathrm{i}\,\arctan(\omega\,R\,C)}.$$

Consequently, the magnitude becomes negligibly small for high frequencies and the phase $\phi = -\arctan(\omega\,R\,C) \to -90°$. Therefore the input impedance of a two-element Windkessel constitutes a "short circuit" for high frequencies.

In contrast, by adding the (real valued) characteristic impedance Z_c, one obtains an input impedance

$$Z_{\mathrm{Wk3}}(\omega) := Z_c + Z_{\mathrm{Wk2}}(\omega).$$

and hence

$$\lim_{\omega\to\infty} Z_{\mathrm{Wk3}}(\omega) = Z_c. \tag{2.4}$$

As a consequence, for high frequencies only the characteristic impedance contributes to aortic input impedance. Indeed, the input impedance in humans for high frequencies is measured to be non-zero and stated in literature as the characteristic impedance [34, Appendix 3]. Given that at

high frequencies wave reflections cancel, the characteristic impedance can be regarded as the input impedance when no reflections exist at all. "Thus the higher the frequency the closer you 'look' into the arterial system. The three-element Windkessel indeed contains these three elements." [33, p. 138] meaning the three elements depicted in fig. 2.10b.

Chapter 3

Reservoir Theory

The cardiovascular system can be described with several time and frequency domain models. However, no matter what kind of approach is chosen its purpose is the same: To understand the phenomena yielding the actual (measured) flow and pressure waveforms. One plain fact is that central flow and pressure waveforms exhibit differences which are difficult to describe satisfactorily. In fig. 3.1 a typical pair of aortic pressure and flow waveforms is illustrated[1]. It can be witnessed that whilst the pressure decreases steadily during diastole the flow already has diminished. Moreover, the waveforms in general exhibit different characteristics even when the flow is substantially greater than zero which corresponds to the ejection time of the heart in systole.

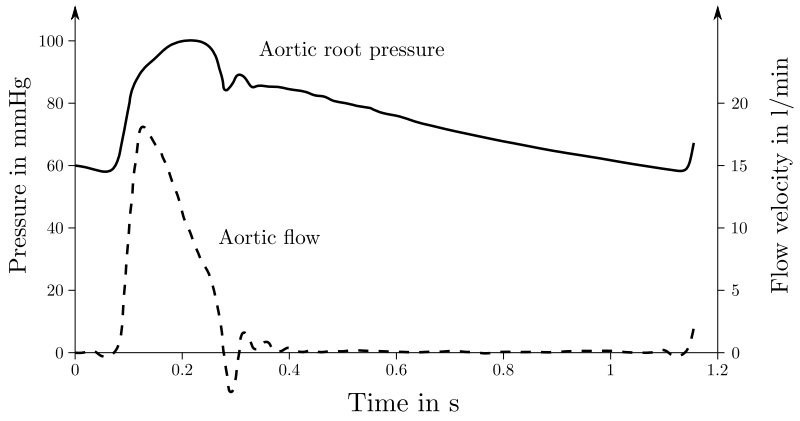

Figure 3.1: Pressure and flow waveforms in aortic root
Source: Modified from [31, Fig. 1]

Indeed, commonly accepted and widely used one-dimensional wave-only theories necessarily lead to "standing waves" as a result of self-cancelling forward and backward travelling waves in the arterial tree during diastole which are difficult to explain in terms of physical or physiological mechanisms, cf. [7, 32]. To date science is still unsure about its

[1]The picture for the aligned waveforms was already shown in fig. 2.4.

interpretation as, for example, Mynard et al. state that "a complete wave-based explanation of self-cancelling diastolic expansion (pressure-decreasing) waves has not yet been advanced" in [19]. Therefore ideas coming up with new approaches beyond the classic theories have a place. One of them is the *Reservoir Theory* whose idea arose in the early 2000's and on which it will be emphasized in this chapter.

But before starting with the modelling, some remarks on the notation shall be given so as to provide a collection of all necessary and important variables.

3.1 Notation

Variable	Description	Unit
p	(Measured) arterial pressure	mmHg
q	(Measured) arterial flow	m^3/s
P_∞	Asymptotic pressure	mmHg
R	Resistance	$\mathrm{mmHg\,s}/\mathrm{m}^3$
C	Compliance	$\mathrm{m}^3/\mathrm{mmHg}$
T_s	Time duration of systole	s
T_d	Time duration of diastole	s
T_b	Total time duration of one cardiac cycle or beat, i.e. $T_\mathrm{b} = T_\mathrm{s} + T_\mathrm{d}$	s

Table 3.1: Reservoir Theory – Important notation

Variables which will be used throughout this chapter are summarized in table 3.1. Their meaning and corresponding unit are also given. Generally capital letters indicate constants and small letters time (and distance) dependent variables. It shall be emphasized that hereafter the beginning of *systole* is defined for each pressure curve separately corresponding to the upslope of the waveform. E.g., referring to fig. 2.3, the start of systole for the left ventricular pressure is defined with the beginning of stage 2 and for the aortic pressure with the initiation of stage 3. Thus for further considerations the time shifts of the curves are virtually set to zero. Since the travel time is not of special interest this procedure implies considerable simplifications in further data handling. Obviously, a generic definition of the start of systole for a pressure waveform is necessary. On this particular issue will be focussed on in section 3.3. For the moment it is presumed $t = 0$ indicates the start of systole. Additionally,

T_s denotes the time *duration* of the systole and T_b the time duration of one cardiac beat.

3.2 Modelling

Knowing that both the aortic cushioning effect and the superposition of travelling waves originating in the left ventricle contribute to the measured waveforms [7], one may attempt to separate these phenomena in a proper way. The *Reservoir Theory*, firstly published in [31], picks up this idea and presumes the separation of the pressure waveform in a time-dependent *reservoir pressure* $p_\mathrm{res}(t)$ and the remaining local *excess pressure* $p_\mathrm{ex}(x,t)$ depending on time and distance along the arteries. Hence, for the pressure p it holds that, according to this assumption,

$$p(x,t) = p_\mathrm{res}(t) + p_\mathrm{ex}(x,t) \tag{3.1}$$

with x indicating the location at the arterial tree. Thus, a 1D-model is assumed implicitly. The reservoir pressure p_res is defined as the solution of the mass conservation law and therefore represents the solution of a two-element Windkessel model. Nonetheless, a spatially uniform reservoir pressure curve at every site of the arterial tree would implicitly suggest an infinite wave speed which could only be obtained in rigid arteries with reference to (2.2). Since the Windkessel effect is based on the arterial compliance an infinite wave speed would contradict the Windkessel model.

Therefore, due to the fact that the ascending aorta is the main driver of cushioning and recoiling [21], the reservoir pressure might be regarded as

$$p_\mathrm{res}(x,t) = p_\mathrm{res}(t - \theta(x)), \tag{3.2}$$

where $\theta(x) \geq 0$ is considered as the time it takes for the travelling wave to get from the ascending aorta to the vessel at site x [26]. Consequently, the reservoir pressure waveform at different sites is assumed to be delayed in time but without altering its waveform. A more exact procedure will be illustrated in the subsequent sections.

3.2.1 Reservoir Pressure when Aortic Flow is known

This section introduces the original idea of the Reservoir Theory and is mainly based on explanations found in [26] and extended by information

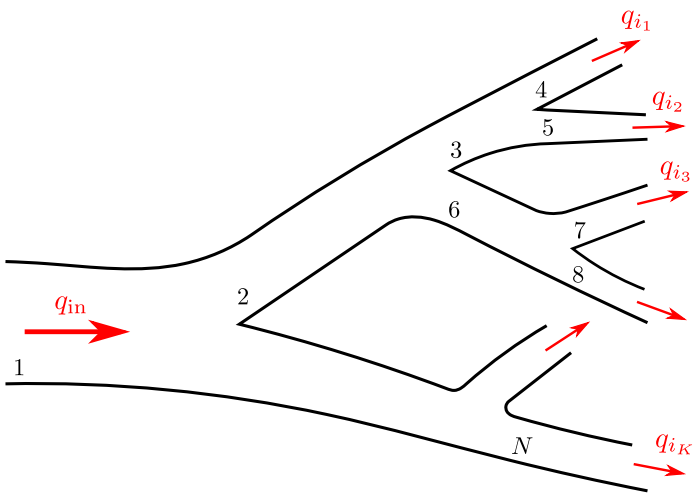

Figure 3.2: Modelling of the arterial tree

provided by the homepage of Kim H. Parker[2].

Firstly, one can assume the arterial tree as being composed of N vessels with $K \ll N$ terminal vessels, where each vessel splits into two daughter vessels. The terminal vessels indicate the border to the microcirculation. This situation is schematically depicted in fig. 3.2. At vessel 1 (aorta) the ventricular outflow q_{in} enters the arterial system. The mass conservation law describes the total change of volume by

$$\frac{dV}{dt}(t) = q_{\text{in}}(t) - q_{\text{out}}(t) \tag{3.3}$$

whereby q_{out} represents the flow out of the system into the microcirculation. According to fig. 3.2 the total volume is split up into N vessels with volume V_n, $n \in \{1, \ldots, N\}$, which means

$$V = \sum_{n=1}^{N} V_n. \tag{3.4}$$

Apart from that, the flow into the microcirculation q_{out} is composed of the sum of the flows through the K terminal vessels with indices $\{i_1, i_2, \ldots, i_K\} \subseteq \{1, 2, \ldots, N\}$. Stating the pressure of each vessel n with length L_n as an instantaneous average pressure

$$p_n(t) = \frac{1}{L_n} \int_0^{L_n} p(x,t)\, dx \quad \text{for all} \quad n = 1, 2, \ldots, N,$$

[2]Department of Bioengineering, Imperial College London, U.K. His homepage: `http://www.bg.ic.ac.uk/research/k.parker/res_press_web/rp_index.html`. Retrieved: October 17, 2014.

the flow through the k^{th} terminal vessel with resistance R_{i_k} can be described by

$$q_{i_k}(t) = \frac{p_{i_k}(t) - P_\infty}{R_{i_k}},$$

whereby P_∞ represents the pressure at which the flow through the microcirculation ceases. Based on the objective of using computable parameters which, additionally, can as well be acquired by clinical measurements, the asymptotic pressure P_∞ is assumed to be uniform throughout the body [26]. Therefore it holds

$$q_{\text{out}}(t) = \sum_{k=1}^{K} q_{i_k}(t) = \sum_{k=1}^{K} \frac{p_{i_k}(t) - P_\infty}{R_{i_k}}. \tag{3.5}$$

Inserting (3.4) and (3.5) into (3.3) leads to

$$\sum_{n=1}^{N} \frac{dV_n}{dt}(t) = q_{\text{in}}(t) - \sum_{k=1}^{K} q_{i_k}(t) = q_{\text{in}}(t) - \sum_{k=1}^{K} \frac{p_{i_k}(t) - P_\infty}{R_{i_k}}.$$

Taking into account the arterial compliances $C_n := \frac{dV_n}{dp_n}$ and assuming them to be constant one infers

$$q_{\text{in}}(t) = \sum_{n=1}^{N} C_n \frac{dp_n}{dt}(t) + \sum_{k=1}^{K} \frac{p_{i_k}(t) - P_\infty}{R_{i_k}}. \tag{3.6}$$

However, finally an equation for computing the *reservoir* pressure p_{res} is aimed. At the first step, p_{res} is regarded to be uniform throughout the arterial system, but delayed by the time θ_n it takes the waveform from the root to vessel n according to (3.2). Thus, one obtains

$$p_{\text{res},n}(t) = p_{\text{res}}(t - \theta_n) \tag{3.7}$$

as the (instantaneous average) reservoir pressure at vessel n. By assuming that the mass conservation law (3.6) is also valid for the reservoir pressures, one infers

$$q_{\text{in}}(t) = \sum_{n=1}^{N} C_n \frac{dp_{\text{res}}}{dt}(t - \theta_n) + \sum_{k=1}^{K} \frac{p_{\text{res}}(t - \theta_{i_k}) - P_\infty}{R_{i_k}} \tag{3.8}$$

which constitutes a time-delay differential equation with constant coefficients for the reservoir pressure[3]. Nevertheless, a fully specified equation necessarily requires the knowledge of all vessel compliances C_n, $n =$

[3] In [26] it is stated that ODE-theory guarantees existence and uniqueness of (3.8) according to [10, 27].

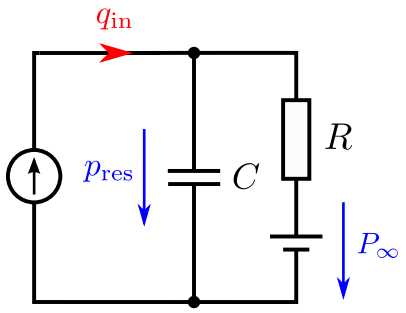

Figure 3.3: Electric analogy of reservoir pressure ODE (3.12)

$1, \ldots, N$ and of all terminal vessel resistances R_{i_k}, $k = 1, \ldots, K$ which are clinically unavailable. Therefore, by applying the Taylor series it holds that

$$p_{\text{res}}(t - \theta_n) = p_{\text{res}}(t) - \theta_n \frac{dp_{\text{res}}}{dt}(t) + \mathcal{O}(\theta_n^2).$$

By simply neglecting the terms $\mathcal{O}(\theta_n)$ with reference to [26] it holds that[4]

$$p_{\text{res}}(t) \approx p_{\text{res}}(t - \theta_n) \tag{3.9}$$

and consequently (3.8) simplifies to

$$q_{\text{in}}(t) = \frac{dp_{\text{res}}}{dt}(t) \sum_{n=1}^{N} C_n + (p_{\text{res}}(t) - P_\infty) \sum_{k=1}^{K} \frac{1}{R_{i_k}}. \tag{3.10}$$

Defining

$$R := \Big(\sum_{k=1}^{K} \frac{1}{R_{i_k}} \Big)^{-1} \quad \text{and} \quad C := \sum_{n=1}^{N} C_n \tag{3.11}$$

as the *resistance* and *net compliance of the arterial system* respectively, finally yields the linear inhomogeneous ordinary differential equation

$$q_{\text{in}}(t) = C \frac{dp_{\text{res}}}{dt}(t) + \frac{p_{\text{res}}(t) - P_\infty}{R}. \tag{3.12}$$

In electric analogy this equation is illustrated with fig. 3.3 containing a source of flow rate q_{in}. An equivalent form of (3.12) can be written as

$$\frac{d(p_{\text{res}} - P_\infty)}{dt}(t) = \frac{p_{\text{res}}(t) - P_\infty}{RC} - \frac{q_{\text{in}}(t)}{C} \tag{3.13}$$

[4]It is assumed that θ_n is small compared to the beat duration T_{b} [26].

whose solution reads

$$p_{\text{res}}(t) = \frac{e^{-t/(RC)}}{C} \int_0^t q_{\text{in}}(s)\, e^{s/(RC)}\, ds + \big(p_{\text{res}}(0) - P_\infty\big)\, e^{-t/(RC)} + P_\infty \tag{3.14}$$

with $0 \leq t \leq T_{\text{b}}$ and $p_{\text{res}}(0) = p(0)$ being the initial pressure at the system inlet at the beginning of systole.

In order to gain the solution p_{res} in (3.14) one has to determine three degrees of freedom R, C and P_∞. One ansatz in order to achieve this goal is to align the reservoir pressure waveform p_{res} to the measured pressure curve p during diastole. This is motivated by two reasons: Firstly, in diastole the pressure waveform is assumed to be caused mainly due to the recoiling of the ascending aorta representing the reservoir effect. And secondly, which has a pleasant impact to the computation, during this stage the flow q_{in} out of the left ventricle is approximately zero since the aortic valve is shut. In fact, this supports the assumption that p_{ex} is assumed to be minimal in this phase because the wave activity is expected to diminish at the aortic root shortly after the valve closure. Thus by neglecting the flow rate during diastole the solution of (3.13) is given by

$$p_{\text{res}}(T_{\text{s}} + t) = \big(p_{\text{res}}(T_{\text{s}}) - P_\infty\big)\, e^{-t/(RC)} + P_\infty \tag{3.15}$$

for $0 \leq t \leq T_{\text{d}}$ and therefore representing an exponential decay. Based on the assumption that the excess pressure is minimal during diastole the difference

$$\|p_{\text{res}} - p\|$$

may be minimized with a proper norm on an appropriate interval of time during diastole. A possible norm and choice of interval will be introduced in section 3.4 which is dedicated to the implementation of this *classic* approach. However, when the reservoir pressure p_{res} is determined, the excess pressure p_{ex} can simply be computed by subtracting p_{res} from p according to (3.1).

3.2.2 Reservoir Pressure when Aortic Flow is not known

As can be witnessed from (3.14) the knowledge of the aortic flow q_{in} is essential so as to be able to compute the reservoir pressure. In general this is a very stringent demand since the flow out of the left ventricle cannot be obtained easily. Furthermore it is quite difficult to measure

pressure and flow simultaneously and small time discrepancies may cause considerably different results. Hence, in practice, another approach is preferable. Here one of the main advantages of the separation (3.1) comes into play: In [31] the similarity of the excess pressure curve p_{ex} and the aortic flow q_{in} was pointed out. Indeed, this observation constitutes one of the most important implications of the Reservoir Theory since it suggests the application of Ohm's law in hydraulic analogy. For the next step, this aspect is used as an assumption rather than an observation, i.e. it is assumed that

$$q_{\mathrm{in}} = \zeta\, p_{\mathrm{ex}} = \zeta\,(p - p_{\mathrm{res}}) \tag{3.16}$$

where ζ denotes a proportionality factor with unit $\mathrm{m}^3/(\mathrm{mmHg\,s})$. The following procedure was firstly published in [1]: Substituting the rate constants

$$a := \frac{\zeta}{C} \quad \text{and} \quad b := \frac{1}{R\,C} \tag{3.17}$$

of the arterial system with units $1/\mathrm{s}$, (3.12) becomes

$$\frac{dp_{\mathrm{res}}}{dt}(t) + b\,\big(p_{\mathrm{res}}(t) - P_\infty\big) = \frac{q_{\mathrm{in}}(t)}{C} = a\,\big(p(t) - p_{\mathrm{res}}(t)\big) \tag{3.18}$$

and equivalent transformation yields

$$\frac{d(p_{\mathrm{res}} - P_\infty)}{dt} + (a+b)\,(p_{\mathrm{res}} - P_\infty) = a\,(p - P_\infty). \tag{3.19}$$

The solution of (3.19) becomes

$$\begin{aligned} p_{\mathrm{res}}(t) = e^{-(a+b)\,t} \int_0^t a\,\big(p(s) - P_\infty\big)\, e^{(a+b)\,s}\, ds \\ + \big(p_{\mathrm{res}}(0) - P_\infty\big)\, e^{-(a+b)\,t} + P_\infty. \end{aligned}$$

or, in equivalent notation after elementary transformation,

$$\begin{aligned} p_{\mathrm{res}}(t) = e^{-(a+b)\,t}\Bigg(p_{\mathrm{res}}(0) - \frac{b}{a+b}\,P_\infty \\ + a\int_0^t p(s)\, e^{(a+b)\,s}\, ds\Bigg) + \frac{b}{a+b}\,P_\infty. \end{aligned} \tag{3.20}$$

By assuming the ventricular flow rate q_{in} to be zero during diastole the corresponding exponential decay behaviour (3.15) in the new variables corresponds to

$$p_{\mathrm{res}}(T_{\mathrm{s}} + t) = \big(p_{\mathrm{res}}(T_{\mathrm{s}}) - P_\infty\big)\, e^{-b\,t} + P_\infty \tag{3.21}$$

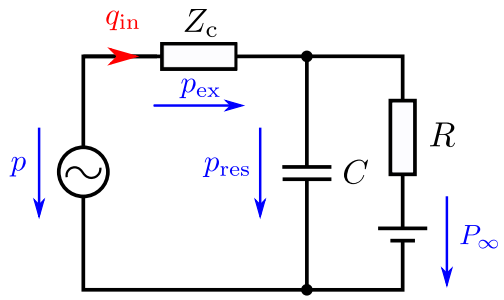

Figure 3.4: Electric analogy of reservoir pressure ODE (3.18)

for $0 \leq t \leq T_{\text{d}}$.

In electric analogy the ODE (3.18) can be illustrated with fig. 3.4 containing a source which provides the pressure p. Hence, according to this analogy and the ansatz (3.16), the proportionality factor ζ represents the inverse of the characteristic impedance Z_{c}, i.e.

$$\zeta = \frac{1}{Z_{\text{c}}}. \tag{3.22}$$

Therefore, the underlying model basically represents a three-element Windkessel model.

In summary again three degrees of freedom, namely the asymptotic pressure P_∞ and the rate constants a and b, need to be estimated by means of an optimization routine. But as opposed to (3.14), where the knowledge of the aortic inflow q_{in} is essential, here the aortic pressure p is the only independent variable. Finally, when the reservoir pressure p_{res} is determined, the subsequent pressure separation can again easily be obtained due to (3.1).

3.2.3 Reservoir Theory at Arbitrary Locations

So far the Reservoir Theory for the pressure separation of the measured pressure waveform in the *aortic root* was described where the flow q_{in} into the arterial system is known or, as in the preceding section, *assumed* to be known by (3.16). Hence, as introduced in [31] and described in the previous sections 3.2.1 and 3.2.2, the Reservoir Theory was originally meant the resolve the differences of pressure and flow waveforms in the ascending aorta, cf. fig. 3.1. However, when applied to simultaneously measured pressure and flow curves of dogs along the aorta two observations were found [1, §2.2]:

(A1) The pressure waveform decay measured at different locations in the arterial system is very similar during diastole.

(A2) The excess pressure at any aortic location is approximately proportional to the flow in the aortic root.

It is hoped that when both of these observations are true the Reservoir Theory can be extended to any arterial location in the arterial system where these *assumptions* are true. Hence, by *assuming* (A1) and (A2), the reservoir pressure can be determined from any pressure waveform p regardless its spot of measurement with the procedure documented in section 3.2.2.

In this thesis this *extended* Reservoir Theory will be applied particularly to the arterial locations of brachial and carotid artery where measured data sets are available. Since beside pressure waveforms as well flow velocities are provided, two different computation methods may be performed:

1. Use the *extended* Reservoir Theory so as to compute the reservoir pressure p_{res} determined by only the measured pressure waveform of both the brachial and carotid artery. Hence by assuming the assumptions (A1) and (A2) the concept of section 3.2.2 is applied.

2. In addition to the measured pressure, use the flow velocities and apply the *classic* theory as described in section 3.2.1 in order to acquire the reservoir pressure p_{res}. Two interpretations may be possible:

   a) The measured data sets at the brachial and carotid artery are considered as an approximation to the aortic root waveforms and therefore the application of the Reservoir Theory may be justified.

   b) The flow and pressure signals are regarded as involved parameters of a lumped parameter model like illustrated in fig. 3.4. But importantly, in this case the relating parameters do not describe the (simplified) situation at the aortic root. Indeed, referring to fig. 3.4, p then denotes the pressure and q_{in} the flow at the brachial or carotid artery respectively. Hence, in fact, one does not apply the Reservoir Theory in the narrow sense but rather use a classic three-element Windkessel model.

Obviously some of the stated assumptions would require further justifications. At this point it is referred to chapter 4 where all these results will be opposed to each other and discussed explicitly. But prior to that the following section is devoted to the measured data sets.

3.3 Data, Data Preprocessing and Estimation of Notch Time

The final aim is to apply the Reservoir Theory on peripheral arteries as just described in section 3.2.3. In total a bundle of 110 pressure and velocity curves non-invasively measured at both the brachial and carotid artery are available for this purpose. Since this data cannot be used straight forward some data preprocessing is necessary. For example it is recalled that all pressure curves are assumed to begin with the systolic part. Moreover an estimation of the systolic time duration is essential so as to apply the Reservoir Theory. This section shall mainly be understood as prestage in order to apply the corresponding Reservoir Theory algorithms which will be subject of the subsequent section 3.4.

3.3.1 Measured Data

In total 110 pairs of pressure and flow curves measured at the brachial and carotid artery were available in order to apply the Reservoir Theory on them. This data was thankfully provided by Prof. Alun D. Hughes[5] and acquired in the course of the Hypertension Associated Cardiovascular Disease ASCOT[6] substudy at the St. Mary's Hospital center, London, UK. The used measurement procedure corresponds to those in [17] or [36].

In fig. 3.5 a generic set of the provided waveforms is shown where p^{b} denotes the pressure at brachial and p^{c} the pressure at the carotid artery. The same notation is used for the velocities u^{b} and u^{c}. Referring to these waveforms it is important to notice that

(i) the brachial and carotid curves are shifted due to wave propagation phenomena.

(ii) the end of the curves generally do not match their beginning.

(iii) the depicted beat time of the brachial curve is usually different compared to the carotid counterpart. In contrast the pressure and velocity signals related to the same location exhibit the same length.

(iv) even though it was intended to adjust the carotid curve to the same brachial mean pressures they are usually distinct.

(v) the dicrotic notch becomes less evident for the brachial pressure.

[5] Prof. Alun D. Hughes, International Centre for Circulatory Health, NHLI, Imperial College London, St Mary's Hospital, London W2 1LA, United Kingdom.

[6] Abbreviation for "Anglo-Scandinavian Cardiac Outcome Trial".

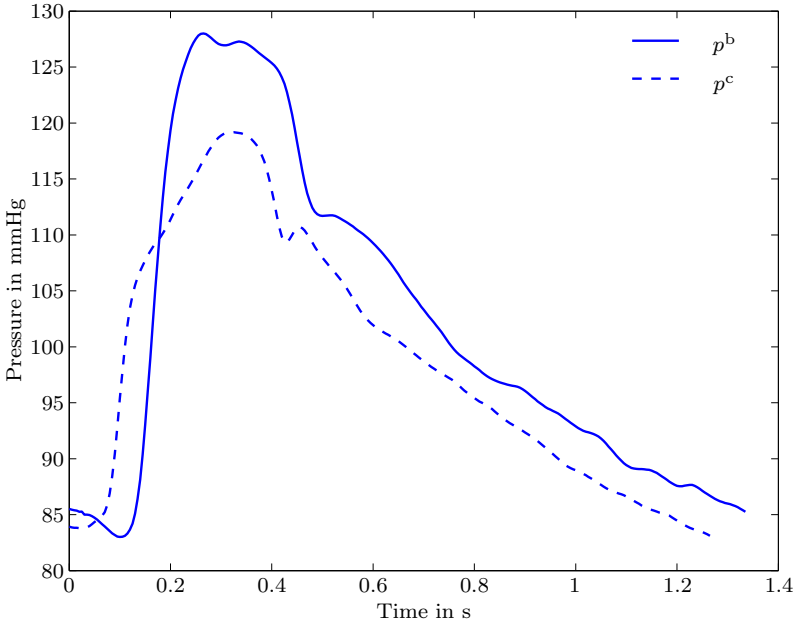

(a) Pressure waveforms

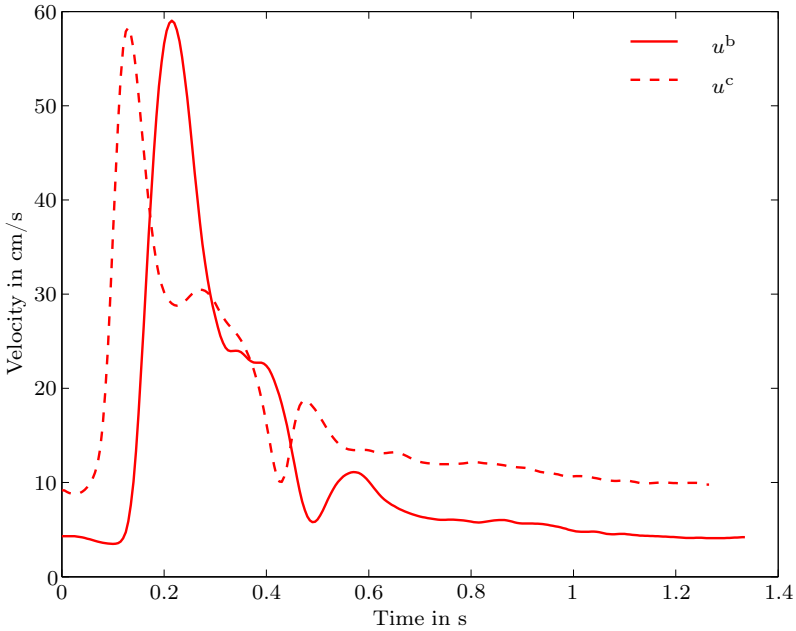

(b) Velocity waveforms

Figure 3.5: Non-invasively, simultaneously measured waveforms at brachial and carotid artery

(vi) the diastolic brachial flow velocity is smaller than the carotid one but generally both curves are greater than 0 during diastole.

Taking into account these observations one has to perform some data preprocessing in order to apply the Reservoir Theory algorithms appropriately and compare its results adequately. Referring to (i), each curve must be shifted such that every single curve begins with systolic stage. In order to resolve (ii) each curve needs to be smoothly extended. Obviously this must be regarded equally for the velocity waveforms. The beat duration of both the pressure curves cannot be matched but the carotid curve can be scaled so as to dispose of curves with equal mean pressures which addresses (iii) and (iv). Provided that the knowledge of the systolic time duration T_s is essential in order to apply the Reservoir Theory, one has to estimate it reliably. Since, referring to (v), the dicrotic notch may diminish for some curves another stable and generic technique needs to be applied. The last observation (vi) is not of particular interest in terms of data preprocessing but it will be important for the discussion of the numerical results.

Therefore some data preprocessing needs to be done in order to dispose of meaningful signals and a method for estimating the notch time T_s is indispensable. The impact on the results of the chosen procedures of data preprocessing will then be examined in chapter 4.

Before going on it has to be emphasized on the fact that the measured waveforms of course are not continuous since the signals are gained with a sampling rate of $f = 200\,\mathrm{Hz}$ meaning a time step of

$$\Delta t := \frac{1}{f} = 0.005\,\mathrm{s}.$$

Against this background

$$\mathcal{T} := \{t_i \,:\, i = 0, \ldots, N\} \quad \text{with} \quad t_i = i\,\Delta t$$

is defined as the discrete set of all sampled points of time and

$$\mathcal{T}_\alpha^\beta := \{t_i \in \mathcal{T} \,:\, t_\alpha \leq t_i \leq t_\beta\}$$

denotes the range between t_α and t_β with $t_\alpha,\, t_\beta \in \mathcal{T}$. Hence all methods applied need to deal with discrete functions of pressure p^b, p^c and velocity u^b, u^c at the brachial and carotid artery respectively. Operations, like differential operations, are implemented as discrete ones. However, for the theoretical investigation it is taken advantage of the fact that the measured waveforms can be extended on the whole interval $[0,\, T_\mathrm{b}]$ such that they may be regarded as sufficiently smooth. The corresponding smooth extensions of pressure and flow signals will be denoted with the same letter. Nevertheless, it has to be kept in mind that these waveforms basically are discrete.

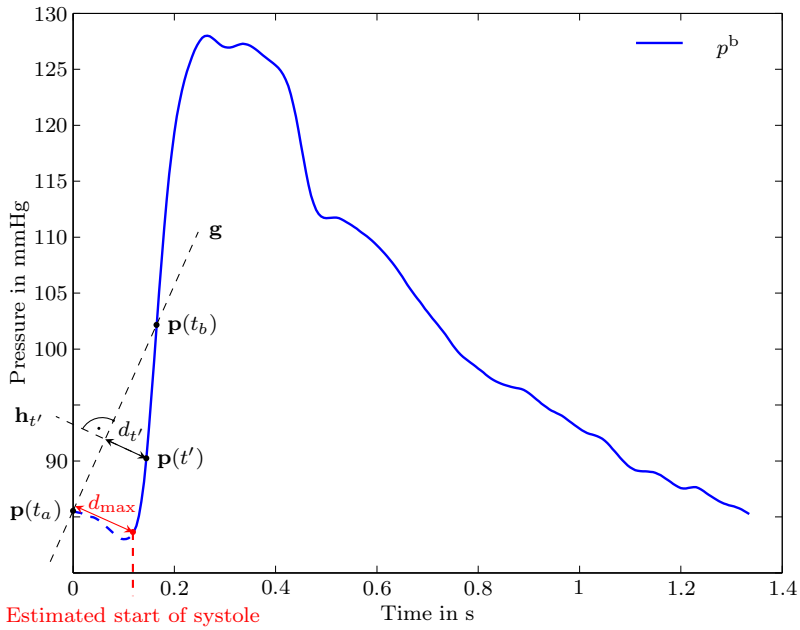

Figure 3.6: Estimated start of systole

3.3.2 Data Preprocessing

The data preprocessing is done in several steps and addresses the stated observations (i) to (iv):

(DP1) Estimate the start of systole in the pressure curves. Its time will be chosen for the flow curve too.

(DP2) Make signals periodical by appending the waveforms appropriately.

(DP3) Scale carotid pressure such that brachial and carotid pressures have the same mean pressure.

(DP4) Align the carotid to the brachial curves so that they virtually "start at the same time".

(DP1): Estimation of start of systole

In fig. 3.6 the procedure is depicted schematically for a brachial pressure waveform p^{b}. In the following it will be denoted by p since the same procedure is applied for the carotid curve too. With the notation

$$\mathbf{p}(t) := \begin{pmatrix} t \\ p(t) \end{pmatrix}$$

two points $\mathbf{p}(t_a)$ and $\mathbf{p}(t_b)$, $t_a < t_b$, are chosen through which a straight line $\mathbf{g}$ is put. Therefore it holds

$$\mathbf{g} = \left\{ \begin{pmatrix} t_a \\ p(t_a) \end{pmatrix} + c \begin{pmatrix} t_b - t_a \\ p(t_b) - p(t_a) \end{pmatrix} \,:\, c \in \mathbb{R} \right\}$$

or, in a more compact form,

$$\mathbf{g} = \left\{ \mathbf{p}(t_a) + c \left(\mathbf{p}(t_b) - \mathbf{p}(t_a) \right) \,:\, c \in \mathbb{R} \right\}.$$

In the algorithm the parameters are set to

$$t_a := 0 \quad \text{and} \quad t_b := \underset{t_i \in \mathcal{T}}{\operatorname{argmax}} \left(\frac{dp}{dt}(t_i) \right).$$

In a next step a finite amount of straight lines $\mathbf{h}_t$ perpendicular to $\mathbf{g}$ for $t \in \mathcal{T}_a^b$ are introduced with

$$\mathbf{h}_t := \left\{ \begin{pmatrix} t \\ p(t) \end{pmatrix} + d \begin{pmatrix} -\big(p(t_b) - p(t_a)\big) \\ t_b - t_a \end{pmatrix} \,:\, d > 0 \right\}. \tag{3.23}$$

The intersection of $\mathbf{g}$ and $\mathbf{h}_t$ is denoted by

$$\mathbf{x}_t := \mathbf{g} \cap \mathbf{h}_t \tag{3.24}$$

which is distinct from the empty set if and only if c_t, $d_t > 0$ exist such that

$$\begin{pmatrix} t_a \\ p(t_a) \end{pmatrix} + c_t \begin{pmatrix} t_b - t_a \\ p(t_b) - p(t_a) \end{pmatrix} = \begin{pmatrix} t \\ p(t) \end{pmatrix} + d_t \begin{pmatrix} -\big(p(t_b) - p(t_a)\big) \\ t_b - t_a \end{pmatrix}.$$

Equivalent transformation yields the linear equation

$$\begin{pmatrix} t_a - t_b & p(t_a) - p(t_b) \\ p(t_a) - p(t_b) & t_b - t_a \end{pmatrix} \begin{pmatrix} c_t \\ d_t \end{pmatrix} = \begin{pmatrix} t_a - t \\ p(t_a) - p(t) \end{pmatrix}$$

with a regular matrix which consequently infers the solution

$$\begin{pmatrix} c_t \\ d_t \end{pmatrix} = \frac{1}{\det} \begin{pmatrix} t_b - t_a & p(t_b) - p(t_a) \\ p(t_b) - p(t_a) & t_a - t_b \end{pmatrix} \begin{pmatrix} t_a - t \\ p(t_a) - p(t) \end{pmatrix}$$

whereby det denotes the determinant

$$\det = -(t_b - t_a)^2 - \big(p(t_b) - p(t_a)\big)^2 < 0.$$

Reformulating leads to

$$\begin{pmatrix} c_t \\ d_t \end{pmatrix} = \frac{1}{|\det|} \begin{pmatrix} t_b - t_a & p(t_b) - p(t_a) \\ p(t_b) - p(t_a) & t_a - t_b \end{pmatrix} \begin{pmatrix} t - t_a \\ p(t) - p(t_a) \end{pmatrix} \tag{3.25}$$

which uniquely determines $\mathbf{x}_t$ for all $t \in \mathcal{T}$ in the case $d_t > 0$, i.e. when

$$\begin{aligned} d_t > 0 &\Leftrightarrow \big(p(t_b) - p(t_a)\big)(t - t_a) + \big(p(t) - p(t_a)\big)(t_a - t_b) > 0 \\ &\Leftrightarrow \big(p(t_b) - p(t_a)\big)(t - t_a) > \big(p(t) - p(t_a)\big)(t_b - t_a) \\ &\Leftrightarrow \frac{p(t_b) - p(t_a)}{t_b - t_a} > \frac{p(t) - p(t_a)}{t - t_a}. \end{aligned}$$

The estimated start of systole is now defined as:

$$\text{Find } t_\star \in \mathcal{T}_a^b \;:\; \|\mathbf{x}_{t_\star} - \mathbf{p}(t_\star)\|_2 = \max_{t \in \mathcal{T}_a^b} \|\mathbf{x}_t - \mathbf{p}(t)\|_2 \,. \tag{3.26}$$

Bearing in mind (3.23) and (3.24) one obtains

$$\mathbf{x}_t - \mathbf{p}(t) = \mathbf{p}(t) + d_t \begin{pmatrix} -\big(p(t_b) - p(t_a)\big) \\ t_b - t_a \end{pmatrix} - \mathbf{p}(t) = d_t \begin{pmatrix} p(t_a) - p(t_b) \\ t_b - t_a \end{pmatrix}.$$

As a result (3.26) is equivalent to:

$$\text{Find } t_\star \in \mathcal{T}_a^b \;:\; d_{t_\star} = \max_{t_i \in \mathcal{T}_a^b} d_{t_i}. \tag{3.27}$$

Assuming $d : t \to d(t)$ to be the smooth extension of d_t on $t_a \le t \le t_b$, the optimization (3.27) requires for the derivations of d due to (3.25)

$$\begin{aligned} \dot{d}(t) \sim p(t_b) - p(t_a) - (t_b - t_a)\,\dot{p}(t) = 0 \quad &\Leftrightarrow \quad \dot{p}(t) = \frac{p(t_b) - p(t_a)}{t_b - t_a} \\ \ddot{d}(t) \sim -(t_b - t_a)\,\ddot{p}(t) < 0 \quad &\Leftrightarrow \quad \ddot{p}(t) > 0 \end{aligned}$$

for $t_a \le t \le t_b$. In other words: The tangent of the continuous pressure at the defined start of systole would be parallel to $\mathbf{g}$ and the waveform itself convex.

In order to find $t_\star \in \mathcal{T}_a^b$ only the factor

$$\big(p(t_b) - p(t_a)\big)\,t_i - (t_b - t_a)\,p(t_i) + (t_b - t_a)\,p(t_a) - \big(p(t_b) - p(t_a)\big)\,t_a$$

of the second row of (3.25) needs to be evaluated for all $t_i \in \mathcal{T}_a^b$ so as to find the maximum of d_t since it equals d_t up to the constant factor det. The corresponding $t_\star \in \mathcal{T}_a^b$ is then set as the start of the pressure curve. In fig. 3.6 the part $p(\mathcal{T}_0^\star)$ is illustrated as a dashed and $p(\mathcal{T} \setminus \mathcal{T}_0^\star)$ as a solid line. This procedure is done separately for the brachial and carotid pressure waveform.

(DP2): Periodization and Filtering

Figured out an estimate for the start of systole $t_\star$ the signal values $p(\mathcal{T}_0^\star)$ need to be shifted to the end of the curve so as not to lose any information.

Since the measured signal waveforms are not expected to be periodical themselves a proper method has to be applied. Two cases can occur: The waveforms either depict "more than a heart cycle or less"[7]. In the first case it is possible to find a pressure level at the end of the curve close to a point before the estimated start of systole in the former part of the curve. In the second case this cannot be achieved. Thus three approaches are implemented in order to obtain a periodic curve. The method of choice is "top-down": Preferring the upper and going downwards if it is not applicable.

(P1) Determine the greatest time $t_{\text{Cut}} \in \mathcal{T}_0^\star$ such that $p(t_{\text{Cut}}) \approx p(t_N)$. Hence it is sought to attach the waveform at the end in a natural and smooth way. Append $p(\mathcal{T}_{\text{Cut}}^\star)$ at the end of the curve $p(t_N)$.

(P2) Find the smallest time t_{Cut} in the later stage of diastole such that $p(t_{\text{Cut}}) \approx p(t_0)$. Therefore the duration of one beat is not prolonged artificially. Append the part of curve $p(\mathcal{T}_0^\star)$ to $p(t_{\text{Cut}})$.

(P3) Simply move $p(\mathcal{T}_0^\star)$ to the end of curve.

For all these approaches the transitions need to be smoothed, in particular in (P3) where no natural appending is possible. In the figs. 3.7 to 3.9 all three approaches are illustrated on curves of the respective type. In the upper panel of each figure the appending procedure is shown whereas in the lower the filtering is depicted.

The favoured approach (P1) in terms of obtaining seamless signals is illustrated in fig. 3.7. In fig. 3.7a the red dash-dotted curve represents the part $p(\mathcal{T}_{\text{Cut}}^\star)$ of $p(\mathcal{T}_0^\star)$ which fits best to the end of the curve $p(\mathcal{T})$. The dotted line indicates the pressure level $p(t_N)$ which was used as the pressure level within $p(\mathcal{T}_0^\star)$ for the enhancement. In a next step the transition of these two parts got filtered which is illustrated in the bottom panel. For this purpose the MATLAB-function `smooth` was used with a span of 5 points. Since `smooth` implements a moving average method the

[7] Of course, this formulation is an oversimplistic description but it helps to address the issue directly. On the one hand the discrepancy between the start and the end of each curve may be a consequence of the averaging procedure of several pressure curves. On the other, pressure and flow curves by no means need to be periodical due to physiological aspects of breathing etc.

entries $\{p_1, p_2, \ldots, p_M\}$ are filtered according to

$$\begin{aligned}
\overline{p}_1 &= p_1 \\
\overline{p}_2 &= \frac{1}{3}(p_1 + p_2 + p_3) \\
\overline{p}_3 &= \frac{1}{5}\sum_{i=1}^{5} p_i \\
&\vdots \\
\overline{p}_j &= \frac{1}{5}\sum_{i=j-2}^{j+2} p_i \\
&\vdots \\
\overline{p}_{M-1} &= \frac{1}{3}(p_{M-2} + p_{M-1} + p_M) \\
\overline{p}_M &= p_M.
\end{aligned}$$

This smoothing operation was applied to 5 points before until, at maximum, the 14^{th} point after the attached point[8] such that it is guaranteed that at least the last 3 points of the patched curve remain untouched in order to get a smooth and periodic waveform with view to the beginning of the curve. In total, this smoothing procedure is applied three times. As a result, by prolonging the part $p(\mathcal{T}_\star^N)$ with $p(\mathcal{T}_{\text{Cut}}^\star)$ and the subsequent smoothing procedure, the periodic and smooth curve $\tilde{p}$ is obtained.

Applying (P2) to a measured curve where (P1) was not possible yields fig. 3.8. This happens when the end of the measured pressure with value $p(t_N)$ falls below the values in $p(\mathcal{T}_0^\star)$. In this case a carotid pressure waveform is depicted. The pressure $p(t_{\text{Cut}})$ at the later stage of the measured curve with a magnitude close to $p(t_0)$ is marked with the dotted line. Then the signal $p(\mathcal{T}_0^\star)$ is appended at t_{Cut} (red dash-dotted line) and subsequently filtered (green thick solid line) in order to get $\tilde{p}$. The used procedure and the choice of its parameters is the same as in (P1).

If both procedures (P1) and (P2) are not applicable (P3) is performed which is illustrated in fig. 3.9. It seems that no full cardiac cycle is sampled. Assuming that the beat duration is still correct the values $p(\mathcal{T}_0^\star)$ are simply added at the end of the curve and afterwards the transition zone gets smoothed. Because of generally substantial discrepancies of the pressure magnitudes `smooth` is applied with a span of 11 to a range beginning with 20 points before and, at maximum, 24 points after the

[8] Hence, in total a maximum sum of 20 points is filtered including the first attached point.

first appended pressure value. Like before, at least the last 3 points of the added signal remain unfiltered.

In total (P1) was applied 69, (P2) 16 and (P3) 135 times yielding the overall sum of all 220 measured pressure curves of both sites. Determined by the pressure waveform the same procedure was then used for the associated flow velocity so as to have the same duration of time T_b for both signals.

Due to the preceding steps all curves are periodic and "smooth"[9]. Furthermore an initial guess for the beginning of systole is given. Assuming that the systole begins at the minimum pressure both pressure and flow curves are shifted (after the filtering) such that the pressure curves begin with their minimum. The minimum of the pressure curves was then set to the diastolic blood pressure (DBP) provided by the measured brachial data.

(DP3): Scaling of the Carotid Pressure

Given that both the carotid and brachial pressure curves now are periodic and begin with their minimum which furthermore corresponds to the the brachial DBP, the scaling can be performed easily. For this purpose

$$p^\mathrm{b}_\mathrm{mean} := \frac{1}{T^\mathrm{b}_\mathrm{b}} \int_0^{T^\mathrm{b}_\mathrm{b}} \left(p^\mathrm{b}(t) - \mathrm{DBP}\right) dt \tag{3.28}$$

and

$$p^\mathrm{c}_\mathrm{mean} := \frac{1}{T^\mathrm{c}_\mathrm{b}} \int_0^{T^\mathrm{c}_\mathrm{b}} \left(p^\mathrm{c}(t) - \mathrm{DBP}\right) dt \tag{3.29}$$

are computed, whereby T^b_b and T^c_b denote the beat duration of the brachial and carotid pressure waveform respectively. By defining

$$\lambda := \frac{p^\mathrm{b}_\mathrm{mean}}{p^\mathrm{c}_\mathrm{mean}}$$

the scaled carotid pressure waveform

$$\bar{\bar{p}}^\mathrm{c} := \lambda \left(p^\mathrm{c} - \mathrm{DBP}\right) + \mathrm{DBP}$$

exhibits the same mean blood pressure as the brachial curve. In fig. 3.10 the results of the MATLAB-implementation of step (DP3) is illustrated whereby on the y-axis the pressure above diastole $p - \mathrm{DBP}$ is plotted. For solving the integrals the function `trapz` is used. The value p^c denotes the carotid pressure after (DP2) and $\bar{\bar{p}}^\mathrm{c}$ its scaling according to the lines above. Thus the area under the graphs divided by their respective beat duration correspond to each other indicating equal mean pressures.

[9] In a sense that they do not provide implausible jumps. Still they are discrete.

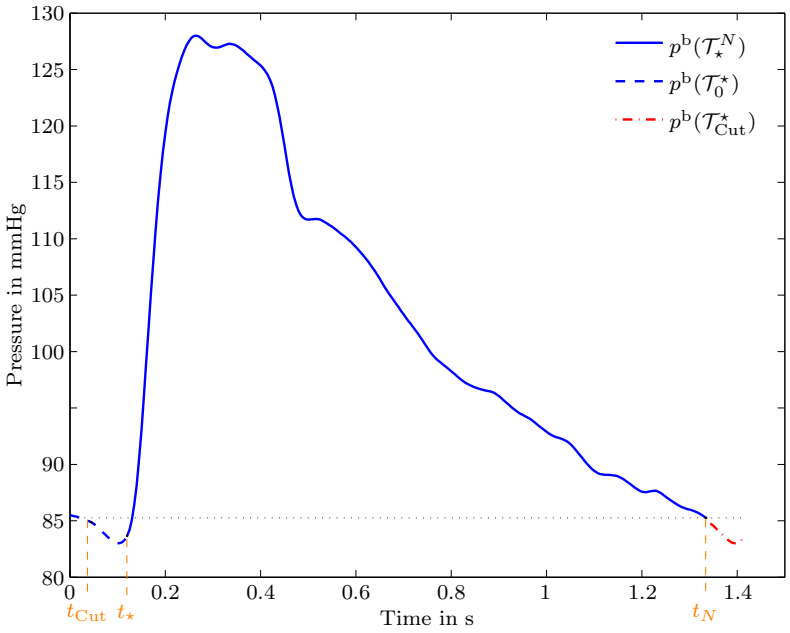

(a) Signal appending

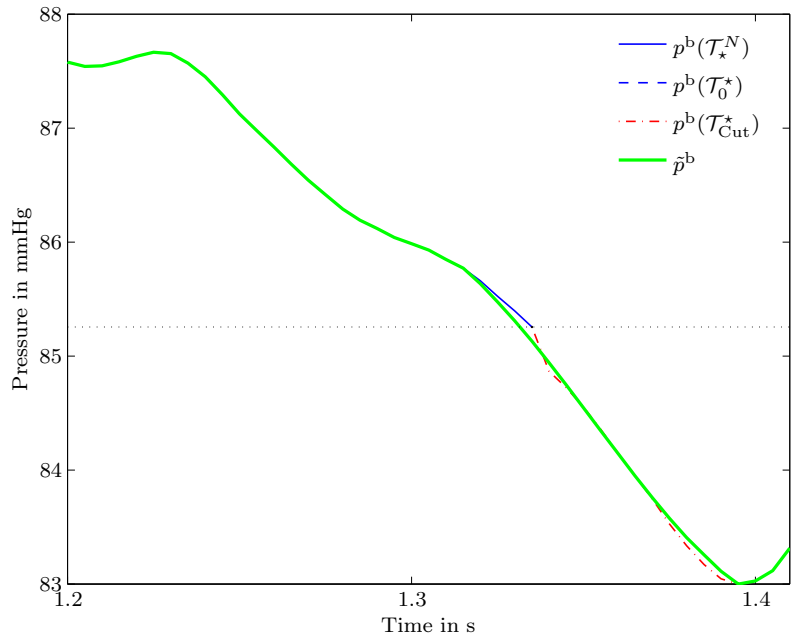

(b) Signal filtering

Figure 3.7: (P1)-Periodization and filtering of measured pressure waveform

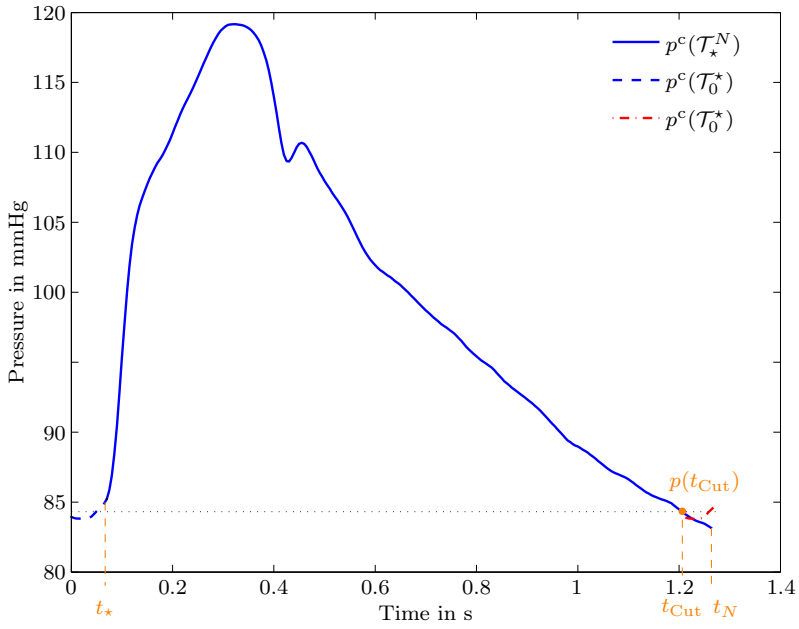

(a) Signal appending

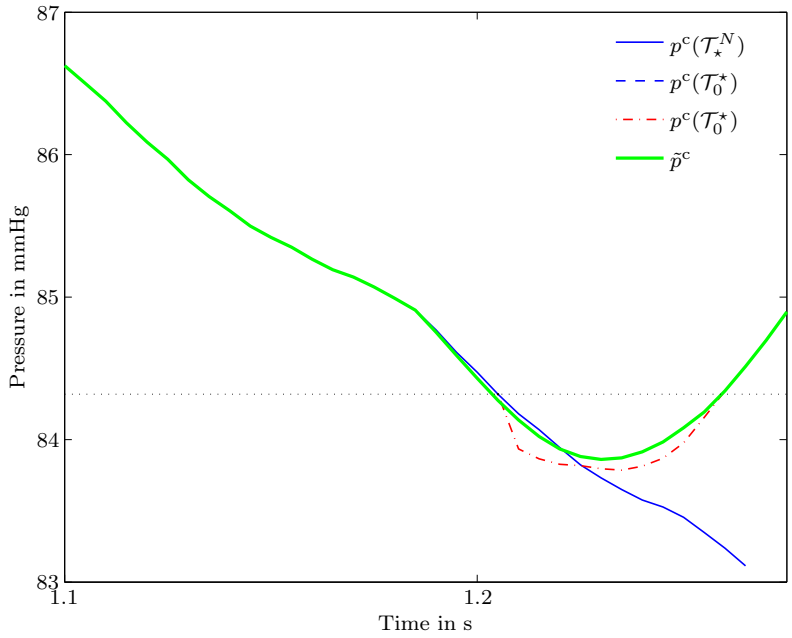

(b) Signal filtering

Figure 3.8: (P2)-Periodization and filtering of measured pressure waveform

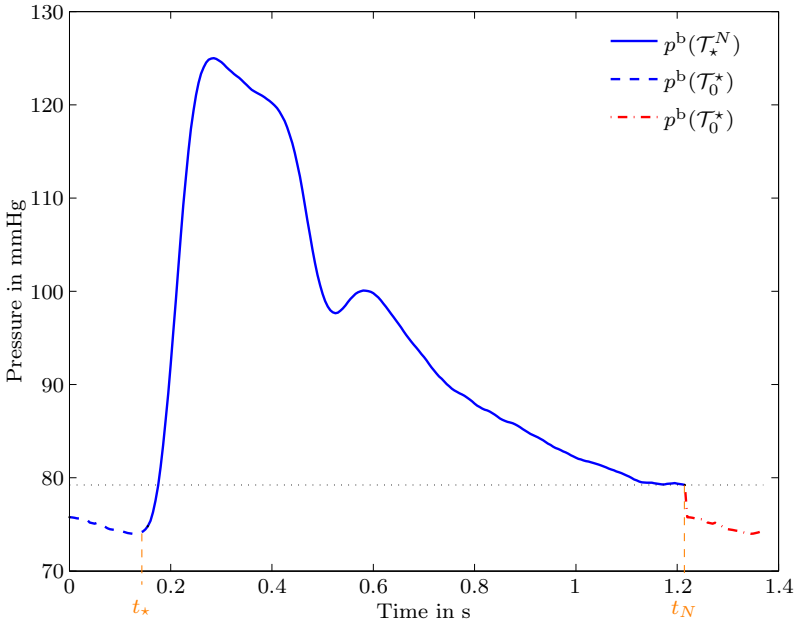

(a) Signal appending

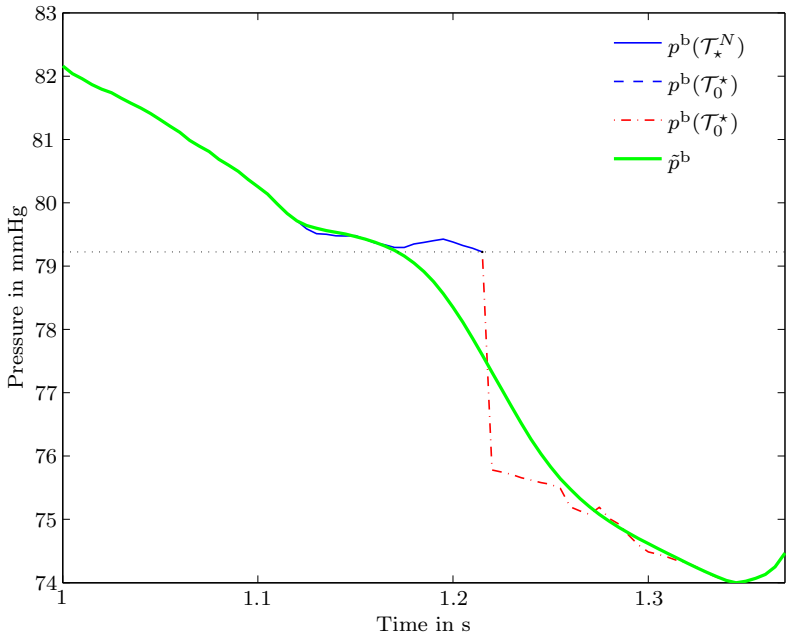

(b) Signal filtering

Figure 3.9: (P3)-Periodization and filtering of measured pressure waveform

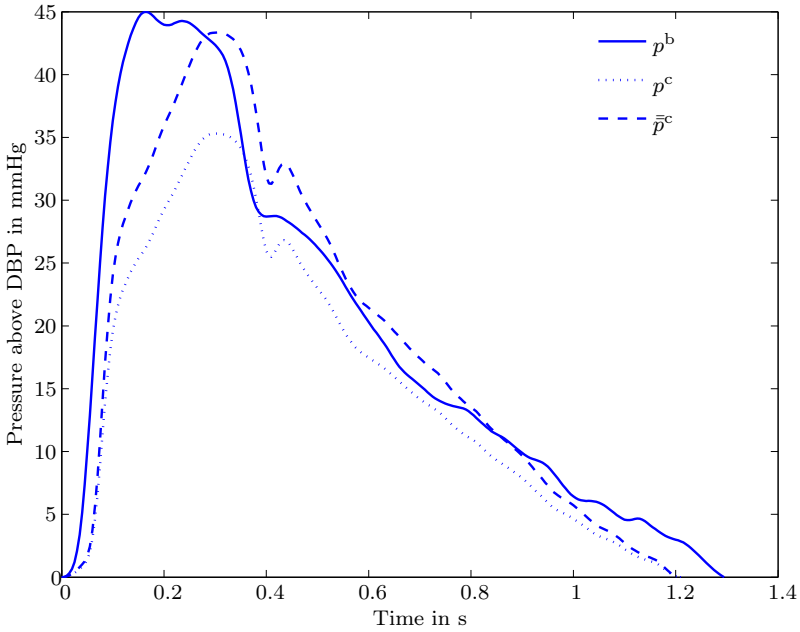

Figure 3.10: Pressure waveforms after carotid pressure scaling

(DP4): Alignment of Brachial and Carotid Curve

The measured curves of pressure and flow velocity of the same site exhibit the same beat duration T_{b}, but generally the measured beat time of the carotid pressure does not match the brachial one. This is likewise true for the flow rates as flow and pressure waveforms related to the same site were recorded simultaneously, cf. fig. 3.5. This characteristic is still preserved after the steps (DP1) to (DP3). Both input pressure curves of (DP4) start with their minimum pressure which was set to the DBP. As can be witnessed from fig. 3.10 the pressure upslopes generally are not aligned to each other. Whereas the brachial pressure is not altered the carotid curve is shifted during (DP4) such that the initial carotid pressure slope matches the brachial one closely. The outcome is exemplarily illustrated for one data set in fig. 3.11. The variables without an arrow represent the curves after (DP3) and the carotid ones with arrow denote the data after alignment. Overall, fig. 3.11 represents the final data after data preprocessing which are used for the Reservoir Theory algorithms.

3.3.3 Estimation of Notch Time

Provided that the data processing is already done for all measured waveforms the time $t = 0$ indicates the beginning of systole of each signal. Hence the interval $[0, T_{\mathrm{s}}]$ denotes the systole and $(T_{\mathrm{s}}, T_{\mathrm{b}}]$ the diastole.

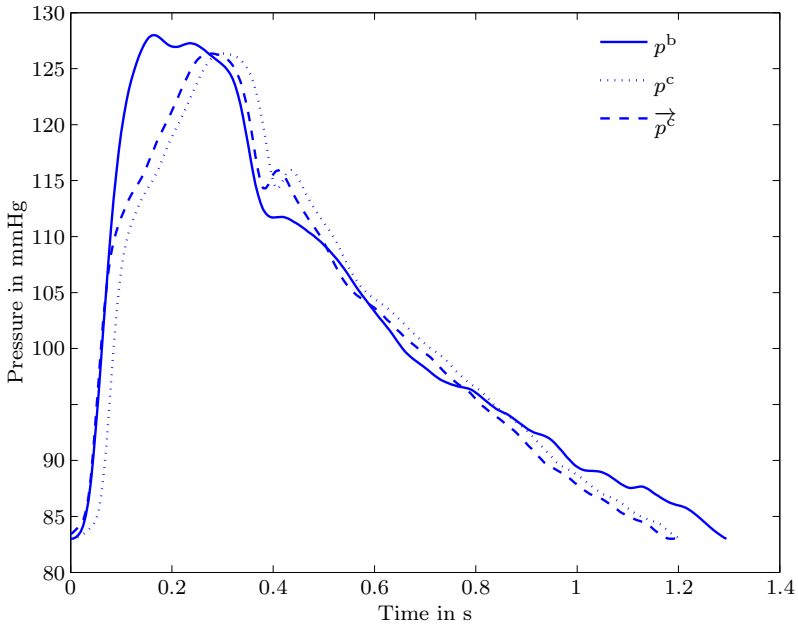

(a) Pressure waveforms

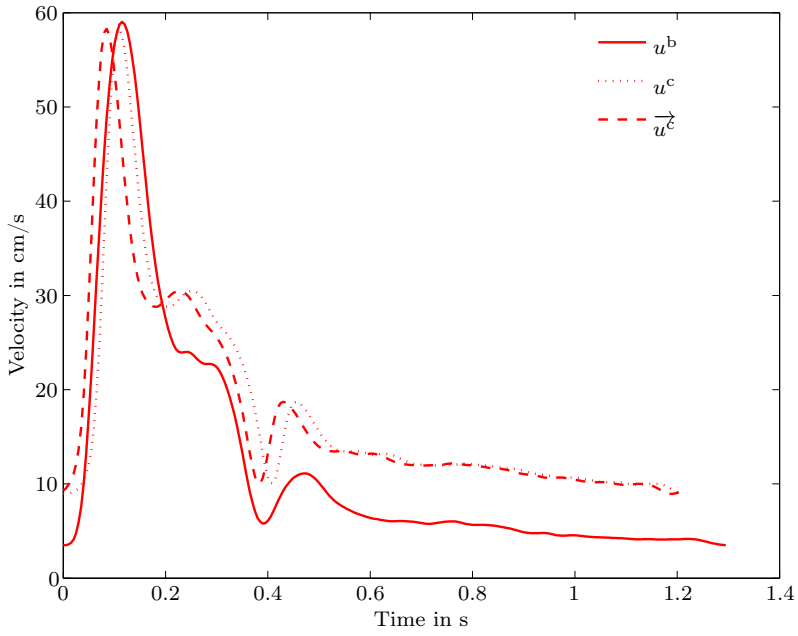

(b) Velocity waveforms

Figure 3.11: Final waveforms after data preprocessing

From a practical point of view it is important to be able to estimate the start of diastole from the pressure waveform. In this thesis two methods are used in order to fulfil this task.

Maximum Curvature

One idea to estimate the notch time of the measured pressure waveforms is to define

$$T_{\mathrm{s,A}} := \operatorname{argmax}\left(\frac{d^2p}{dt^2}(t')\right) \tag{3.30}$$

with p being the pressure at any arterial location and t' within a range around an initial guess of T_{s}.

Hence the time $T_{\mathrm{s,A}}$ corresponds to the pressure with *maximum curvature*. The exact time $T_{\mathrm{s,A}}$ can only be acquired when p is sufficiently smooth. Since p is a discrete signal the differentiation has to be implemented as a discrete operation. Therefore in reality only an approximation $t_{\mathrm{s,A}}$ of the systolic time duration $T_{\mathrm{s,A}}$ can be found.

Minimum Derivation

Another approach to estimate duration of systole of the measured pressure waveforms is to define

$$T_{\mathrm{s,B}} := \operatorname*{argmin}_{0\le t'\le T_{\mathrm{b}}}\left(\frac{dp}{dt}(t')\right). \tag{3.31}$$

Again, in practice only an approximation $t_{\mathrm{s,B}} \approx T_{\mathrm{s,B}}$ of the systolic time duration is possible.

Both possibilities are depicted in fig. 3.12 for a measured brachial pressure waveform. As can be witnessed in this figure, it holds $T_{\mathrm{s,B}} < T_{\mathrm{s,A}}$ for all data sets with reference to section 4.3.1.

3.4 Implementation of the Reservoir Theory

In this section the focus is put on how the Reservoir Theory is implemented in MATLAB in the course of this thesis. Generally the theory described in section 3.2 can be implemented through several approaches. One ansatz is to translate the formulas more or less directly by using optimization routines provided by MATLAB to obtain the missing parameters. Another possibility is to acquire some of the parameters of interest by virtue of introducing other equations in order to reduce the

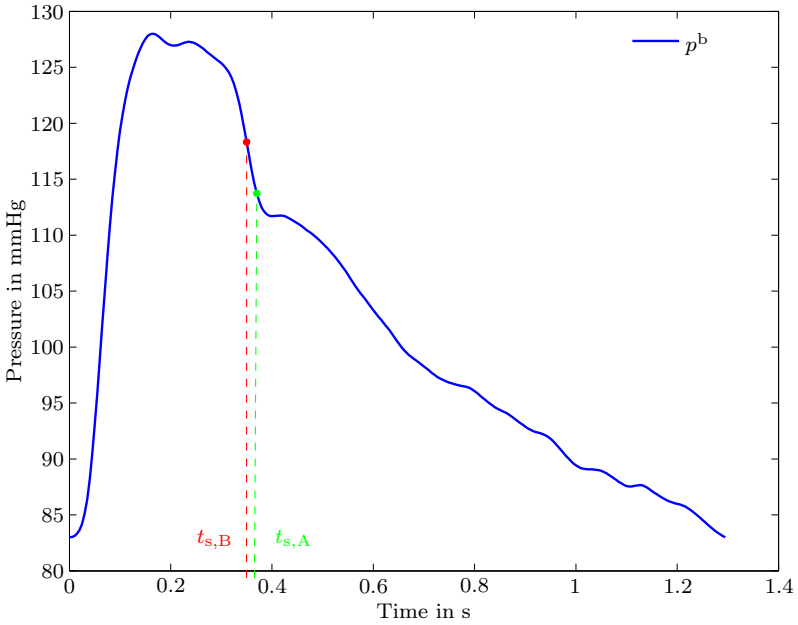

Figure 3.12: Brachial pressure waveform with proposed notch times

application of optimization routines to a minimum. The algorithm of Prof. Kim H. Parker[10] is based on such an approach and thankfully was provided for doing some further analysis.

3.4.1 Reservoir Pressure by using Flow Velocity

The main statements and a general overview are already introduced in section 3.2.1. But instead of disposing of flow rates the measured data corresponds to flow velocity waveforms which, moreover, characterize the flow at the brachial or carotid artery and not at the ascending aorta. One the one hand, as stated in section 3.2.3, one could regard this data as approximation to the aortic root waveforms. On the other, it is possible to assume them of being part of a three-element Windkessel model for the brachial or carotid artery respectively, as illustrated in fig. 3.3 where the inlet flow q_{in} is replaced by q representing the flow rate at the respective artery. In the following the latter approach will be considered for further explanations. Thus the resistance R and the capacitance C represent the peripheral resistance and compliance of the respective site. Since peripheral flow waveforms differ from those at the ascending aorta, cf. fig. 2.6, it is subject of further investigation whether

[10]Prof. Kim H. Parker is a member of the working group of the Department of Bioengineering, Imperial College London, U.K.

the obtained reservoir pressure is similar.

For the implementation some facts have to be taken into account: The conservation law (3.3) is still valid and the subsequent steps in section 3.2.1 too. Bearing in mind the different meanings of the involved parameters the solution of the ODE (3.13) reads

$$p_{\text{res}}(t) = \frac{e^{-t/(R\,C)}}{C} \int_0^t q(s)\, e^{s/(R\,C)}\, ds + \big(p_{\text{res}}(0) - P_\infty\big)\, e^{-t/(R\,C)} + P_\infty.$$

Using the relationship (2.1) as

$$q = A\,u$$

with u the flow velocity at either the brachial or carotid artery and A denoting their respective cross-sectional area it follows

$$p_{\text{res}}(t) = \frac{e^{-t/(R\,C)}}{C} \int_0^t A(s)\, u(s)\, e^{s/(R\,C)}\, ds + \big(p_{\text{res}}(0) - P_\infty\big)\, e^{-t/(R\,C)} + P_\infty.$$

With the sloppy assumption of having a time-independent cross-sectional area A one infers

$$p_{\text{res}}(t) = \frac{e^{-t/(R\,C)}}{C/A} \int_0^t u(s)\, e^{s/(R\,C)}\, ds + \big(p_{\text{res}}(0) - P_\infty\big)\, e^{-t/(R\,C)} + P_\infty.$$

Defining the resistance and compliance with respect to the area A

$$\mathcal{R} := A\,R \qquad \text{and} \qquad \mathcal{C} := \frac{C}{A} \tag{3.32}$$

with the units mmHg s/m and m/mmHg respectively, the time constant τ is preserved since

$$\tau = R\,C = A\,R\,\frac{C}{A} = \mathcal{R}\,\mathcal{C}. \tag{3.33}$$

Consequently

$$p_{\text{res}}(t) = \frac{e^{-t/(\mathcal{R}\,\mathcal{C})}}{\mathcal{C}} \int_0^t u(s)\, e^{s/(\mathcal{R}\,\mathcal{C})}\, ds + \big(p_{\text{res}}(0) - P_\infty\big)\, e^{-t/(\mathcal{R}\,\mathcal{C})} + P_\infty. \tag{3.34}$$

Looking at the formulas (3.14) and (3.34) reveals that the structure of these equations is identical and independent from the use of either the flow velocity or flow rate. Solely the peripheral parameters of resistance and net compliance are scaled by the (as constant assumed) cross-sectional area A.

However, since the flow cannot be assumed to be zero during diastole, cf. fig. 3.11b, formula (3.34) does not simplify like it happened before in (3.15). Nonetheless, the graphs of the measured flow data suggest that the flow in later stage of diastole remains almost constant. To investigate the impact of an steady flow in later diastole on the reservoir pressure (3.34), u is assumed to be constant for $t \geq T_{\underline{v}}$ with $T_{\underline{v}} \geq T_{\mathrm{s}}$. Thus, for the moment, it is assumed that

$$u(t) = u_{\underline{v}} \quad \text{for } t \geq T_{\underline{v}} \geq T_{\mathrm{s}}.$$

Hence (3.34) reads for $t \geq T_{\underline{v}} \geq T_{\mathrm{s}}$

$$\begin{aligned} p_{\mathrm{res}}(t) &= \frac{e^{-t/(\mathcal{R}\,\mathcal{C})}}{\mathcal{C}} \left(\int_0^{T_{\underline{v}}} u(s)\, e^{s/(\mathcal{R}\,\mathcal{C})}\, ds + u_{\underline{v}} \int_{T_{\underline{v}}}^{t} e^{s/(\mathcal{R}\,\mathcal{C})}\, ds \right) \\ &\quad + \big(p_{\mathrm{res}}(0) - P_\infty\big)\, e^{-t/(\mathcal{R}\,\mathcal{C})} + P_\infty \\ &= \left(p_{\mathrm{res}}(0) - P_\infty + \frac{1}{\mathcal{C}} \int_0^{T_{\underline{v}}} u(s)\, e^{s/(\mathcal{R}\,\mathcal{C})}\, ds \right) e^{-t/(\mathcal{R}\,\mathcal{C})} \\ &\quad + \mathcal{R}\, u_{\underline{v}}\, e^{-t/(\mathcal{R}\,\mathcal{C})} \left(e^{t/(\mathcal{R}\,\mathcal{C})} - e^{T_{\underline{v}}/(\mathcal{R}\,\mathcal{C})} \right) + P_\infty \end{aligned}$$

and subsequently

$$\begin{aligned} p_{\mathrm{res}}(t) = e^{-t/(\mathcal{R}\,\mathcal{C})} \Bigg(& p_{\mathrm{res}}(0) - P_\infty + \frac{1}{\mathcal{C}} \int_0^{T_{\underline{v}}} u(s)\, e^{s/(\mathcal{R}\,\mathcal{C})}\, ds \\ & - \mathcal{R}\, u_{\underline{v}}\, e^{T_{\underline{v}}/(\mathcal{R}\,\mathcal{C})} \Bigg) + \mathcal{R}\, u_{\underline{v}} + P_\infty. \end{aligned} \tag{3.35}$$

Since the terms in the bracket are constant for all $t \geq T_{\underline{v}} \geq T_{\mathrm{s}}$ an exponential decay with time constant $\mathcal{R}\,\mathcal{C} = R\,C$ is observable too which states a similar behaviour compared to (3.15) for this particular stage. Moreover, one could assume the waves to be minimal when the flow is almost steady and therefore this period of time in later diastole could constitute an appropriate phase for fitting the reservoir pressure to the measured one. Indeed, in literature the last two-thirds of diastole are frequently used for this purpose [1, 3, 31]. With the least squared error defined by the ℓ^2-Norm

$$\|p_{\mathrm{res}} - p\|_{\mathcal{T}_\alpha^\beta} := \sqrt{\sum_{i=\alpha}^{\beta} |p_{\mathrm{res}}(t_i) - p(t_i)|^2}$$

for $t_\alpha < t_\beta$ and $t_\alpha, t_\beta \in \mathcal{T}$ the reservoir pressure (3.34) is fitted to the measured pressure by minimizing the error

$$\|p_{\text{res}} - p\|_{\mathcal{T}_{\text{s}}^N}$$

during diastole[11]. Thus with the minimization

$$\text{find parameters } \mathcal{R}, \mathcal{C} \text{ and } P_\infty \,:\, \|p_{\text{res}} - p\|_{\mathcal{T}_{\text{s}}^N} \to \min,$$

which shall be denoted by

$$\min_{\mathcal{R},\mathcal{C},P_\infty} \|p_{\text{res}} - p\|_{\mathcal{T}_{\text{s}}^N},$$

all missing parameters $\mathcal{R}$, $\mathcal{C}$ and the asymptotic pressure P_∞ are estimated. Consequently the reservoir pressure p_{res} can be computed for all $t_i \in \mathcal{T}_0^N$ due to (3.34) and the pressure separation (3.1) of the measured pressure p can easily be obtained.

For the implementation the specific choice of the estimated notch time and minimization interval during diastole is arbitrary but the particular choice of $t_{\text{s}} \approx T_{\text{s,B}}$ and performing the curve fitting over the *whole* diastole have some advantages which will become clear in section 4.3. The implemented procedure can be applied on both the brachial and carotid data whereby all computed parameters are denoted with a tilde-symbol. Its steps are summarized in the following

Algorithm 3.1 (Reservoir pressure by using flow velocity).
Input:

- *Measured brachial or carotid pressure waveform p*
- *Measured brachial or carotid flow velocity u*
- *Sampling frequency f*

Method:

(1) Compute beat duration T_{b} and corresponding time step Δt determined by the sampling frequency f and the number of sampled values. It holds $t_N = T_{\text{b}}$.

(2) Determine $t_s \approx T_{\text{s,B}}$ of (3.31) in the form

$$t_s := \underset{t' \in \mathcal{T}_0^N}{\operatorname{argmin}} \left(\frac{dp}{dt}(t') \right) \tag{3.36}$$

[11] In chapter 4 one particular focus is put on the specific choice of optimization interval in the course of the sensitivity analysis in section 4.3.

in the sense of discrete differentiation.

(3) Extract the peripheral net parameters $\widetilde{\mathcal{R}}$, $\widetilde{\mathcal{C}}$ *and the asymptotic pressure* $\widetilde{P}_\infty$ *by performing*

$$\min_{\widetilde{\mathcal{R}},\widetilde{\mathcal{C}},\widetilde{P}_\infty} \|\widetilde{p}_{\text{res}} - p\|_{\mathcal{T}_{\text{s}}^N} \tag{3.37}$$

in diastole and

$$\begin{aligned}\widetilde{p}_{\text{res}}(t) \approx \frac{e^{-t/(\widetilde{\mathcal{R}}\,\widetilde{\mathcal{C}})}}{\widetilde{\mathcal{C}}} \int_0^t u_{\text{in}}(s)\, e^{s/(\widetilde{\mathcal{R}}\,\widetilde{\mathcal{C}})}\, ds \\ + \left(\widetilde{p}_{\text{res}}(0) - \widetilde{P}_\infty\right) e^{-t/(\widetilde{\mathcal{R}}\,\widetilde{\mathcal{C}})} + \widetilde{P}_\infty.\end{aligned} \tag{3.38}$$

The integral in (3.38) *is implemented through the* MATLAB*-function* `trapz` *based on the trapezoidal rule which yields* $\widetilde{p}_{\text{res}}$. *For the minimization* (3.37) *the* MATLAB*-routine* `lsqnonlin` *based on a non-linear least square method is used with set optional bound*

$$0.7 \min_{\mathcal{T}_0^N}(p) \le \widetilde{P}_\infty \le \min_{\mathcal{T}_0^N}(p) \tag{3.39}$$

for the asymptotic pressure and initial values

$$\begin{aligned}\widetilde{\mathcal{R}}_0 &= 440\,\text{mmHg}\,\text{s/m}, \\ \widetilde{\mathcal{C}}_0 &= 0.001\,\text{m/mmHg}, \\ \widetilde{P}_{\infty,0} &= \min(p).\end{aligned}$$

Output:

- *Reservoir pressure* $\widetilde{p}_{\text{res}}$ *based on either brachial or carotid data*
- *Asymptotic pressure* $\widetilde{P}_\infty$ *based on either brachial or carotid data*
- *Peripheral brachial or carotid area resistance* $\widetilde{\mathcal{R}}$
- *Peripheral brachial or carotid area compliance* $\widetilde{\mathcal{C}}$

In the following the implementation of two different approaches to compute the reservoir pressure without knowing the aortic flow are described. It has to be emphasized again that (A1) and (A2) are the crucial assumptions for applying the *extended* Reservoir Theory to arbitrary locations at the arterial tree as mentioned in section 3.2.2.

3.4.2 Reservoir Pressure without Flow – Variant A

The first step to obtain the missing parameters is similar to the procedure in the prior section 3.4.1 by using (3.21) to minimize

$$\min_{b,\, p_{\mathrm{res}}(t_s),\, P_\infty} \|p_{\mathrm{res}} - p\|_{\mathcal{T}_s^N}$$

in order to determine P_∞ and the inverse time constant $b = 1/(RC)$. Thereafter, assuming that the reservoir pressure exhibits an exponential decay in diastole, an optimization for the rate constant a is performed such that p_{res} of (3.20) closely aligns p_{res} of (3.21) in $\mathcal{T}_{\mathrm{s}}^N$. Consequently the reservoir pressure is fully identified by (3.14) which finally determines the excess pressure via (3.1).

The implementation is described in the following algorithm. In order to distinguish more clearly the computed parameters are denoted with a hat-symbol.

Algorithm 3.2 (Reservoir pressure without using flow, A).
Input:

- *Measured brachial or carotid pressure waveform p*
- *Sampling frequency f*

Method:

(1) Compute beat duration T_{b} and corresponding time step Δt determined by the sampling frequency f and the number of sampled values. It holds $t_N = T_{\mathrm{b}}$.

(2) Determine $t_s \approx T_{\mathrm{s,B}}$ through (3.36).

(3) Fit reservoir pressure to the measured curve by minimizing

$$\min_{\widehat{b},\, \widehat{p}_{\mathrm{res,d}}(t_s),\, \widehat{P}_\infty} \|\widehat{p}_{\mathrm{res,d}} - p\|_{\mathcal{T}_s^N}\,, \tag{3.40}$$

in diastole where the reservoir pressure is assumed to be (3.21)*, i.e.*

$$\widehat{p}_{\mathrm{res,d}}(t_i) := \big(\widehat{p}_{\mathrm{res,d}}(t_s) - \widehat{P}_\infty\big)\, e^{-\widehat{b}\,(t_i - t_s)} + \widehat{P}_\infty \quad \textit{with } t_i \in \mathcal{T}_s^N.$$

The minimization is done by the MATLAB*-function* `lsqnonlin` *with condition* (3.39) *for asymptotic pressure $\widehat{P}_\infty$ and initial*

values

$$\widehat{b}_0 = 3 \cdot 1/\mathrm{s}, \qquad \widehat{p}_{\mathrm{res,d}}(t_s)_0 = p(t_s), \qquad \widehat{P}_{\infty,0} = \min(p).$$

Therefore the parameters $\widehat{b}$, $\widehat{p}_{\mathrm{res}}(t_s)$ *and* $\widehat{P}_\infty$ *are computed.*

(4) Apply `lsqnonlin` *so as to*

$$\text{find } \widehat{a} > 0 \,:\, \left|\widehat{p}_{\mathrm{res,s}}(t_s) - \widehat{p}_{\mathrm{res,d}}(t_s)\right| \to \min \tag{3.41}$$

with the initial value

$$\widehat{a}_0 = 15 \cdot 1/\mathrm{s}$$

and the reservoir pressure being (3.20)*, i.e.*

$$\widehat{p}_{\mathrm{res,s}}(t) = e^{-(\widehat{a}+\widehat{b})\,t}\left(\widehat{p}_{\mathrm{res}}(0) - \frac{\widehat{b}}{\widehat{a}+\widehat{b}}\,\widehat{P}_\infty + \widehat{a}\int_0^t p(s)\,e^{(\widehat{a}+\widehat{b})\,s}\,ds\right) + \frac{\widehat{b}}{\widehat{a}+\widehat{b}}\,\widehat{P}_\infty,$$

whereby the integral is implemented by means of the MATLAB*-function* `trapz`*.*

(5) The final reservoir pressure $\widehat{p}_{\mathrm{res}}$ *is then set*

$$\widehat{p}_{\mathrm{res}}(t_i) := \begin{cases} \widehat{p}_{\mathrm{res,d}}(t_i), & \text{if } t_i \in \mathcal{T}_s^N \\ \widehat{p}_{\mathrm{res,s}}(t_i) & \text{otherwise.} \end{cases}$$

Output:

- *Reservoir pressure* $\widehat{p}_{\mathrm{res}}$ *based on either brachial or carotid data*
- *Asymptotic pressure* $\widehat{P}_\infty$ *based on either brachial or carotid data*
- *Peripheral brachial or carotid rate constants* $\widehat{a}$, $\widehat{b}$

3.4.3 Reservoir Pressure without Flow – Variant B

The ansatz of implementing section 3.2.2 taken by Prof. Kim H. Parker is somewhat different.

With the assumption of having an exponential pressure decay in dias-

tole one can set

$$p_{\mathrm{d}}(t) := \alpha\, e^{-b\,t} + P_\infty \quad \text{for} \quad 0 \le t \le T_{\mathrm{d}} \tag{3.42}$$

where $t = 0$ represents the start of diastole which lasts $T_{\mathrm{d}} = T_{\mathrm{b}} - T_{\mathrm{s}}$. Just like in (3.21) the parameter $b = 1/(R\,C)$ denotes the inverse time constant and P_∞ the pressure at which flow into microcirculation ceases. Thus the positive valued variables $\alpha, b,\ P_\infty$ in (3.42) are wanted. It holds

$$E_0 := \frac{1}{T_{\mathrm{d}}} \int_0^{T_{\mathrm{d}}} p_{\mathrm{d}}(t)\, dt = -\frac{\alpha}{b\,T_{\mathrm{d}}}(e^{-b\,T_{\mathrm{d}}} - 1) + P_\infty \tag{3.43}$$

whereby $b, T_{\mathrm{d}} > 0$ and thus always $b\,T_{\mathrm{d}} > 0$. The functions pde_1 and pde_2 are defined as

$$\mathrm{pde}_k(t) := \big(p_{\mathrm{d}}(t) - E_0\big)\, e^{k\,\frac{t}{T_{\mathrm{d}}}} = \alpha \left(e^{t\left(\frac{k - b\,T_{\mathrm{d}}}{T_{\mathrm{d}}}\right)} + \frac{e^{-b\,T_{\mathrm{d}}} - 1}{b\,T_{\mathrm{d}}}\, e^{k\,\frac{t}{T_{\mathrm{d}}}} \right) \tag{3.44}$$

for $k \in \{1, 2\}$. The advantage is that pde_1 and pde_2 are independent of P_∞. Further equations aim to get a relationship of only *one* unknown which can be obtained more easily. For this sake the integrals

$$E_k := \int_0^{T_{\mathrm{d}}} \mathrm{pde}_k(t)\, dt \quad \text{with} \quad k \in \{1, 2\} \tag{3.45}$$

are defined with the solutions

$$E_k = \alpha\, T_{\mathrm{d}} \left(\frac{e^{k - b\,T_{\mathrm{d}}} - 1}{k - b\,T_{\mathrm{d}}} + (e^k - 1) \frac{e^{-b\,T_{\mathrm{d}}} - 1}{k\,b\,T_{\mathrm{d}}} \right) \tag{3.46}$$

for $b\,T_{\mathrm{d}} \neq k \in \{1, 2\}$. However, this does not imply any restriction since these points constitute a removable discontinuity. With l'Hôpital's rule it can be shown that

$$\lim_{b\,T_{\mathrm{d}} \to k} E_k = \alpha\, T_{\mathrm{d}} \left(1 + \frac{1}{k^2}\big(2 - e^k - e^{-k}\big) \right). \tag{3.47}$$

The crucial point now is that the quotient

$$Q := \frac{E_2}{E_1}$$

only depends on the single factor $y := b\,T_{\mathrm{d}} > 0$. With (3.46) and (3.47)

it holds that

$$Q(y) = \begin{cases} \dfrac{\frac{e^{2-y}-1}{2-y} + (e^2-1)\frac{e^{-y}-1}{2\,y}}{\frac{e^{1-y}-1}{1-y} + (e-1)\frac{e^{-y}-1}{y}}, & \text{if } y \neq 1, 2 \\ \dfrac{e-1+(e^2-1)(e^{-1}-1)/2}{3-e-e^{-1}}, & \text{if } y = 1 \\ \dfrac{1+(2-e^2-e^{-2})/4}{1-e^{-1}+(e-1)(e^{-2}-1)/2}, & \text{if } y = 2. \end{cases} \tag{3.48}$$

The implementation of this approach now reads as follows, whereby the computed results are denoted with a breve-symbol:

Algorithm 3.3 (Reservoir pressure without using flow, B).
Input:

- *Measured brachial or carotid pressure waveform p*
- *Sampling frequency f*

Method:

(1) Compute beat duration T_b and corresponding time step Δt determined by the sampling frequency f and the number of sampled values. It holds $t_N = T_\mathrm{b}$.

(2) Determine $t_s \approx T_\mathrm{s}$ through (3.36).

(3) Using the ansatz (3.42) *of assuming*

$$p_\mathrm{d}(t) = \alpha\, e^{-b\,t} + P_\infty \approx p(T_\mathrm{s} + t)$$

for $0 \leq t \leq T_\mathrm{d}$ in diastole, set

$$\breve{p}_\mathrm{d} := p(\mathcal{T}_s^N) \tag{3.49}$$

(4) Approximate the parameters (3.43) *to* (3.45) *by using* (3.49) *and solving the integrals with Simpson's rule[a] yielding results in the order $\breve{E}_0$, $\breve{\mathrm{pde}}_1$, $\breve{\mathrm{pde}}_2$, $\breve{E}_1$ and $\breve{E}_2$.*

(5) Determine

$$\breve{Q} := \frac{\breve{E}_2}{\breve{E}_1}.$$

(6) Compute the quotient Q analytically according to (3.48).

(7) Find $\breve{y} > 0$ such that

$$Q(\breve{y}) - \breve{Q} = 0. \tag{3.50}$$

Since $y = b\,T_\mathrm{d}$ the rate constant $\breve{b} = \breve{y}/T_\mathrm{d}$ is known.

(8) Determine $\breve{\alpha}$ and $\breve{P}_\infty$ consecutively through the analytical relationships (3.46) *with E_1 and* (3.43) *with E_0. Hence the reservoir pressure in diastole is given due to the assumption* (3.42)*, i.e.*

$$\breve{p}_{\mathrm{res,d}}(t_i) := \breve{\alpha}\, e^{-\breve{b}\, t_i} + \breve{P}_\infty \quad \textit{for} \quad t_i \in \mathcal{T}_s^N.$$

(9) For determination of the systolic part minimize

$$\min_{\breve{a}} \|\breve{p}_{\mathrm{res,s}} - \breve{p}_{\mathrm{res,d}}\|_{\mathcal{T}_s^N} \tag{3.51}$$

in diastole with initial value

$$\breve{a}_0 = \breve{b},$$

whereby the reservoir pressure is assumed to be (3.20)*, i.e.*

$$\breve{p}_{\mathrm{res,s}}(t) = e^{-(\breve{a}+\breve{b})\,t}\left(\breve{p}_{\mathrm{res}}(0) - \frac{\breve{b}}{\breve{a}+\breve{b}}\,\breve{P}_\infty + \breve{a}\int_0^t p(s)\, e^{(\breve{a}+\breve{b})\,s}\, ds\right) + \frac{\breve{b}}{\breve{a}+\breve{b}}\,\breve{P}_\infty,$$

in order to get the last missing parameter $\breve{a}$. The optimization is performed with the MATLAB*-function* `fminsearch` *based on a least square method. The integral is approximated with trapezoidal rule.*

(10) Find crossover point of $\breve{p}_{\mathrm{res,d}}$ *and* $\breve{p}_{\mathrm{res,s}}$ *in* $t_x \in \mathcal{T}_s^N$ *which is implemented by finding the first index* x *such that*

$$\big(\breve{p}_{\mathrm{res,s}}(t_x) - \breve{p}_{\mathrm{res,d}}(t_x)\big)\,\big(\breve{p}_{\mathrm{res,s}}(t_{x+1}) - \breve{p}_{\mathrm{res,d}}(t_{x+1})\big) \leq 0. \quad (3.52)$$

The reservoir pressure is then set

$$\breve{p}_{\mathrm{res}}(t_i) := \begin{cases} \breve{p}_{\mathrm{res,s}}(t_i), & \text{if } t_i \in \mathcal{T}_0^x \\ \breve{p}_{\mathrm{res,d}}(t_i), & \text{otherwise.} \end{cases}$$

Output:

- *Reservoir pressure* $\breve{p}_{\mathrm{res}}$ *based on either brachial or carotid data*
- *Asymptotic pressure* $\breve{P}_\infty$ *based on either brachial or carotid data*
- *Peripheral brachial or carotid rate constants* $\breve{a}$, $\breve{b}$

[a] If N is an odd number apply the composite Simpson's rule on $\mathcal{T}_0^{N-1}$ and the trapezoidal rule for the remaining part $\mathcal{T}_{N-1}^N$. The Simpson's rule applied on one part $[a,b] \subseteq \mathbb{R}$ reads

$$\mathcal{Q}_S f \approx \int_a^b f(t)\,dt \quad \text{with} \quad \mathcal{Q}_S f := \frac{b-a}{6}\left(f(a) + 4\,f\Big(\frac{a+b}{2}\Big) + f(b)\right)$$

and the trapezoidal rule

$$\mathcal{Q}_T f \approx \int_a^b f(t)\,dt \quad \text{with} \quad \mathcal{Q}_T f := \frac{b-a}{2}\big(f(a) + f(b)\big).$$

Discussion of Algorithm 3.3

Even though the algorithm 3.3 is stated as "reasonably robust" in [1] a closer analysis of the implementation shall be provided since several steps are crucial in order to compute the reservoir pressure $\breve{p}_{\mathrm{res}}$ successfully.

One key point is the computation of $\breve{y}$ in (3.50). In fig. 3.13 the function Q given by (3.48) is plotted. Although this function is defined for all $y \in \mathbb{R}$ only the part for $y > 0$ (solid line) is valid in order to constitute a reasonable zero of (3.50) since $y = b\,T_{\mathrm{b}}$ is necessarily positive. Therefore the computed values $\breve{Q}$ need to be in the range of

$$\big(\lim_{y\to\infty} Q(y),\, Q(0)\big) \approx (3.06,\, 3.55).$$

In any case, if $\breve{Q}$ has values out of this interval one may conclude that the

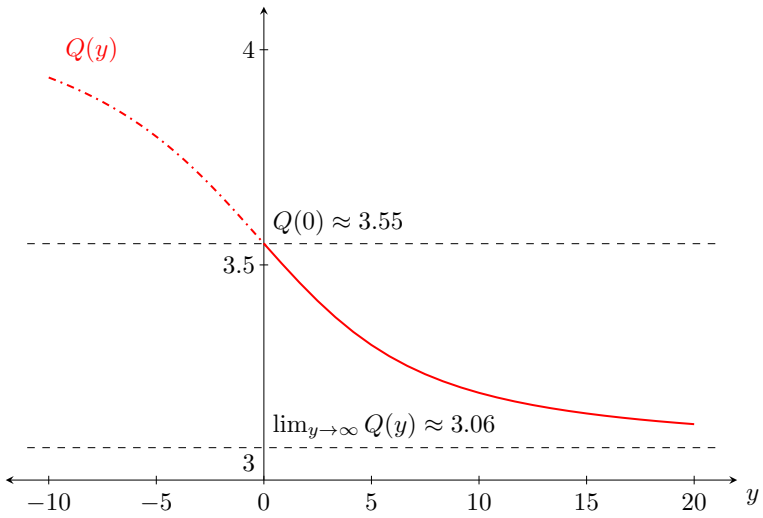

Figure 3.13: Algorithm 3.3 – Quotient Q

initial ansatz of an exponential decay (3.42) is not justified and therefore algorithm 3.3 not applicable. In particular, when $\breve{Q}$ is in the interval

$$\big(Q(0),\ \lim_{y\to-\infty} Q(y)\big) \approx (3.55,\ 4.19)$$

the algorithm would confer a negative $y = bT_\mathrm{d}$. Since $T_\mathrm{d} > 0$ this result would yield an implausible rate constant $b < 0$ and consequently the corresponding reservoir pressure need to be excluded from further considerations.

Furthermore, it has to be guaranteed that a crossover point exist and thus can be found by (3.52). The procedure of the respective steps of algorithm 3.3 is illustrated in fig. 3.14. The values of $\breve{p}_{\mathrm{res,d}}$ (red solid line) constitute an initial estimate in diastole of the reservoir pressure of the measured pressure waveform p^b (blue dash-dotted line). After having applied the optimization (3.51) in diastole in order to find the systolic part $\breve{p}_{\mathrm{res,s}}$ of the reservoir pressure (green dashed line) a reasonable conjunction of both waveforms is aimed. Defining it to be the first intersection point of the pressures $\breve{p}_{\mathrm{res,s}}$ and $\breve{p}_{\mathrm{res,d}}$ fulfils both an exponential pressure decay in diastole and an "optimal" reservoir waveform for the systole due to (3.51). The resulting patched pressure wave $\breve{p}_{\mathrm{res}}$ is then considered as the reservoir pressure of p^b. A positive side effect of this method is that the crossover point in t_x may be understood as the indicator for the notch time yielding a systolic duration greater than the initial estimate for T_s. Since the (calculated) notch time T_s may be too short from a physiological point of view the crossover time t_x might be more plausible. However, the estimated notch time results are going to be presented in section 4.3.1.

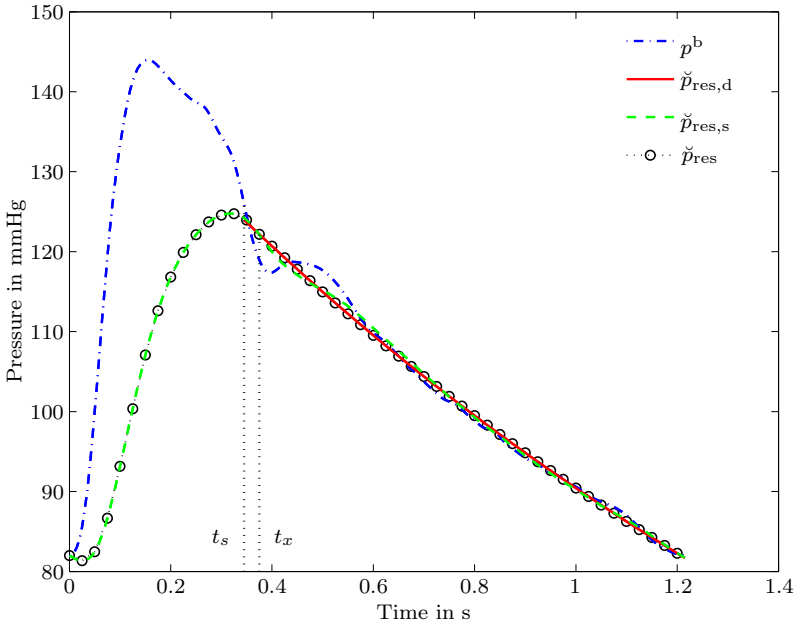

(a) Pressure waveforms

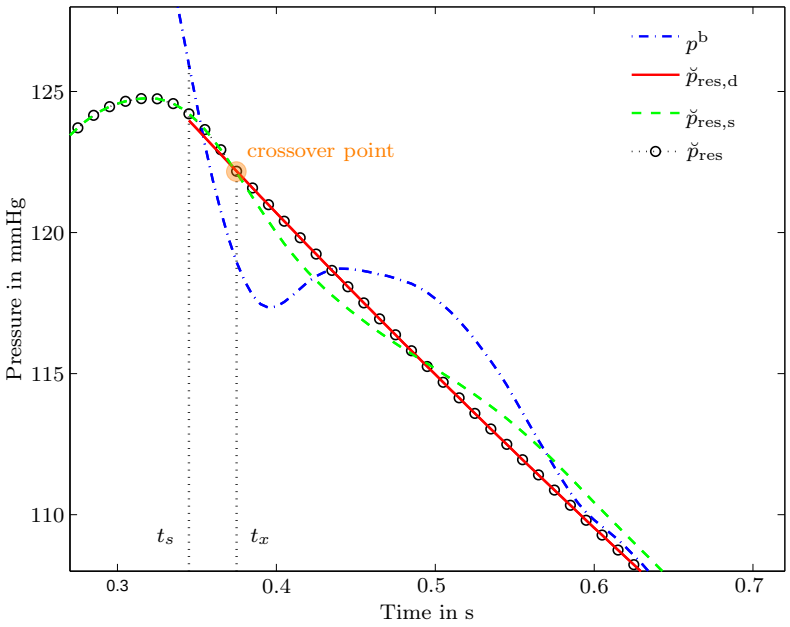

(b) Crossover point

Figure 3.14: Algorithm 3.3 – Crossover point

3.4.4 Conversion of Peripheral Parameters

Beside extracting information from the differently computed reservoir pressure waveforms $\widetilde{p}_{\mathrm{res}}$, $\widehat{p}_{\mathrm{res}}$ and $\breve{p}_{\mathrm{res}}$ and their comparisons at different sites one may seek to use the peripheral parameters provided by the algorithms 3.1 to 3.3 too. More precisely, in this section it is aimed to provide some relationships in order to compare the results of

- the net area parameters $\widetilde{\mathcal{R}}$ and $\widetilde{\mathcal{C}}$ from algorithm 3.1
- the rate constants $\widehat{a}$ and $\widehat{b}$ from algorithm 3.2
- the rate constants $\breve{a}$ and $\breve{b}$ from algorithm 3.3

so as to incorporate these findings in the final discussion too. Given that relationships between these parameters will be provided by theoretical investigation the accents will be omitted.

Firstly, a recapitulation is done: Due to the assumption (A2) and the subsequent definition

$$q_{\mathrm{in}} = \zeta\, p_{\mathrm{ex}}$$

in (3.16) the relationship (3.22) between the proportionality factor ζ and the (volumetric) characteristic impedance Z_{c}, i.e.

$$Z_{\mathrm{c}} = \frac{1}{\zeta},$$

was shown. Therefore it holds

$$Z_{\mathrm{c}} = \frac{p_{\mathrm{ex}}}{q_{\mathrm{in}}} \tag{3.53}$$

with the excess pressure $p_{\mathrm{ex}} = p - p_{\mathrm{res}}$ and the cardiac output q_{in}. On the other hand the rate constant a, defined in (3.17), becomes with (3.22)

$$a = \frac{\zeta}{C} = \frac{1}{Z_{\mathrm{c}}\, C}. \tag{3.54}$$

The rate constant

$$b = \frac{1}{R\, C} \tag{3.55}$$

is already fully specified. In other words: Provided that one already disposes of the flow into the arterial system q_{in} and the excess pressure p_{ex} the characteristic impedance Z_{c} can be computed by means of Ohm's law in hydraulic analogy (3.53). In further consequence the net parameters a

and b can easily be transformed to the resistance R and the compliance C.

In case of dealing with flow *velocities* instead of flow *rates*, switching to the area parameters

$$\mathcal{R} = A\,R \qquad \text{and} \qquad \mathcal{C} = \frac{C}{A},$$

as defined in section 3.4.1, seems to be more natural. The relationships (3.54) and (3.55) are then altered to

$$a = \frac{1}{Z_\mathrm{c}\,\mathcal{C}\,A} \qquad \text{and} \qquad b = \frac{1}{\mathcal{R}\,\mathcal{C}}$$

or, equivalently,

$$\mathcal{C} = \frac{1}{a\,A\,Z_\mathrm{c}} \qquad \text{and} \qquad \mathcal{R} = \frac{1}{b\,\mathcal{C}}. \tag{3.56}$$

With the mass conservation law holds for the flow rate

$$q_\mathrm{in} = A_\mathrm{in}\,u_\mathrm{in}$$

at the ascending aorta with cross-sectional area A_in. As a result the characteristic impedance in (3.53) becomes

$$Z_\mathrm{c} = \frac{p_\mathrm{ex}}{A_\mathrm{in}\,u_\mathrm{in}}.$$

Consequently, the net area compliance in (3.56) is given by

$$\mathcal{C} = \frac{A_\mathrm{in}}{a\,A}\frac{u_\mathrm{in}}{p_\mathrm{ex}}. \tag{3.57}$$

In reality the cross-sectional A_in varies substantially within one cardiac cycle since the ascending aorta is highly elastic. In contrast, the cross-sectional area A is assumed to be constant and represents a *mean* area. To get rid of this lack of knowledge one can simply assume $A_\mathrm{in} = A$ and approximate $u_\mathrm{in}/p_\mathrm{ex}$ by proceeding to the mean values of one cardiac cycle. With the mean operator

$$\langle v \rangle := \frac{1}{T_\mathrm{b}} \int_0^{T_\mathrm{b}} v(t)\,dt \quad \text{for all} \quad v \in L^1(0,\,T_\mathrm{b})$$

the parameters a, b and $\mathcal{R}, \mathcal{C}$ are (approximately) related to each other by

$$\mathcal{C} = \frac{1}{a}\frac{\langle u_\mathrm{in} \rangle}{\langle p_\mathrm{ex} \rangle} \qquad \text{and} \qquad \mathcal{R} = \frac{1}{b\,\mathcal{C}} \tag{3.58}$$

which finally constitute computable relationships.

Some remarks on the conversion of peripheral parameters

It has to be emphasized that the transformation given by (3.58) constitutes an (approximated) relation in case that

- $\mathcal{R}$ corresponds to the *area* resistance of the *arterial system*.
- $\mathcal{C}$ indicates the net *area* compliance of the *arterial system*.
- a and b denote the rate constants of the *arterial system*.

In fact, according to the assumption that the reservoir pressure is uniform throughout the arterial tree due to (3.7) and (3.9), the concept of the *extended* Reservoir implicitly suggests that the peripheral parameters and net rate constants refer to the whole arterial system regardless the arterial location of their associated reservoir pressure waveform. Therefore the output parameters of algorithms 3.2 and 3.3 may be understood as arterial system related parameters. In contrast, since algorithm 3.1 uses the flow of the respective location, the corresponding results refer rather to either the brachial or carotid artery instead. But by substituting $\langle u^{\mathrm{b}} \rangle$ or $\langle u^{\mathrm{c}} \rangle$ for $\langle u_{\mathrm{in}} \rangle$ at least an evaluation of (3.58) and a subsequent comparison of the obtained parameters is possible. Nonetheless, by applying (3.58), one has to bear in mind that this compares parameters designated to describe the whole arterial system ($\widehat{a}$, $\widehat{b}$ and $\breve{a}$, $\breve{b}$) with parameters computed by the local flow velocities which are generally distinct to the ventricular flow ($\widetilde{\mathcal{R}}$, $\widetilde{\mathcal{C}}$).

Chapter 4

Numerical Results and Discussion

In this chapter all the results provided by the implemented algorithms are summarized. Firstly, the effects of the data preprocessing as described in section 3.3.2 are examined.

4.1 Notation

In table 4.1 a summary of the already introduced variables and parameters necessary for this chapter is provided.

Beside the stated notation in table 4.1, several additional symbols are used:

- The superindices of "b" and "c" always indicate the particular location at either the brachial or the carotid artery of the respective variable. For example p^{b} corresponds to the measured pressure at the brachial and p^{c} to the carotid artery.

- The accent-symbols $\widetilde{\ }$, $\widehat{\ }$ and $\breve{\ }$ specify the origin of the *computed* variable and refer to the algorithms 3.1 to 3.3, respectively. E.g. $\widetilde{p}_{\mathrm{res}}$ denotes the computed reservoir pressure of algorithm 3.1. The algorithms themselves are defined in the sections 3.4.1 to 3.4.3.

4.2 Effects of Data Preprocessing

Several impacts rooted in the choice of periodization methods (P1) to (P3) are investigated in this section. In table 4.2 the statistic is provided of how many times each periodization method was applied on the measured data sets of totally 220 waveform pairs. Overall, for the majority of waveforms (P3) was used. Therefore it was not possible to find

Variable	Description	Unit	Def.
a, b	Rate constants	$1/\mathrm{s}$	(3.17)
C	Net compliance	$\mathrm{m}^3/\mathrm{mmHg}$	(3.11)
$\mathcal{C}$	Net area compliance	m/mmHg	(3.32)
p	Measured pressure	mmHg	
P_∞	Asymptotic pressure	mmHg	
p_{ex}	Theoretical excess pressure	mmHg	(3.1)
p_{res}	Theoretical reservoir pressure	mmHg	(3.1)
u	Measured flow velocity	m/s	
R	Peripheral resistance	$\mathrm{mmHg\,s}/\mathrm{m}^3$	(3.11)
$\mathcal{R}$	Peripheral area resistance	$\mathrm{mmHg\,s}/\mathrm{m}$	(3.32)
τ	Time constant	s	(3.33)
T_{b}	Total time duration of one heart beat cycle, i.e. $T_{\mathrm{b}} = T_{\mathrm{s}} + T_{\mathrm{d}}$	s	
T_{d}	Time duration of diastole	s	
T_{s}	Time duration of systole	s	
$T_{\mathrm{s,A}}$	Estimated time duration of systole based on maximum pressure curvature	s	(3.30)
$T_{\mathrm{s,B}}$	Estimated time duration of systole based on minimum pressure derivation	s	(3.31)

Table 4.1: Numerical Results and Discussion – Important notation

	Brachial Artery	Carotid Artery	Total
(P1)	42	27	69
(P2)	5	11	16
(P3)	63	72	135

Table 4.2: Data preprocessing applied to 220 waveform pairs

a smoother transition for most of the signals by using (P1) or (P2) respectively. On the other hand, due to the simple shift from one part of the beginning of the (P3)-curve to its end, no precarious shortening of the beat duration T_b needs to be tolerated. The first section is devoted to this issue.

4.2.1 Shortening of Beat Duration

Provided that the periodization methods (P1) and (P2) determine a pressure level at the former part of the waveform with a magnitude close to the end the subsequent "chopping" of the waveform necessarily leads to a shorter beat duration, cf. figs. 3.7 and 3.8. Hence, in case that "more than one heart beat"[1] is measured, a proper region-picking for further processing is sought by the methods (P1) and (P2). In contrast, if this is not possible (P3) is used by basically simply shifting the signal waveform which preserves the measured beat duration T_b.

Due to the different approaches of the periodization methods (P1) to (P3) different impacts on the duration time T_b are expected. To quantify these effects the mean change and its standard deviation are computed. In a general case of a sample $y_1, y_2, \ldots, y_M$ its mean reads

$$\mu_y := \frac{1}{M} \sum_{i=1}^{M} y_i$$

and its standard deviation

$$\sigma_y := \sqrt{\frac{1}{M-1} \sum_{i=1}^{M} (y_i - \mu_y)^2}.$$

Thus, the sample can be characterized by

$$\mu_y \pm \sigma_y, \tag{4.1}$$

[1] Again it is emphasized that this impression is a consequence of the applied averaging procedures as described in section 3.3.1. In reality exactly one (averaged) beat defined by consecutive ECG R waves is depicted.

in s	Brachial Artery	Carotid Artery	Both arteries
(P1)	-0.032 ± 0.018	-0.028 ± 0.015	-0.030 ± 0.000
(P2)	-0.096 ± 0.047	-0.076 ± 0.032	-0.083 ± 0.037
(P3)	0.000 ± 0.000	0.000 ± 0.000	0.000 ± 0.000
(P1)–(P3)	-0.016 ± 0.027	-0.015 ± 0.027	-0.015 ± 0.027

Table 4.3: Mean change and standard deviation of ΔT_b in s

in %	Brachial Artery	Carotid Artery	Both arteries
(P1)	-3.402 ± 1.914	-2.641 ± 1.265	-3.104 ± 0.000
(P2)	-8.818 ± 3.986	-7.072 ± 2.710	-7.618 ± 3.136
(P3)	0.000 ± 0.000	0.000 ± 0.000	0.000 ± 0.000
(P1)–(P3)	-1.700 ± 2.659	-1.356 ± 2.445	-1.528 ± 2.554

Table 4.4: Mean change and standard deviation of ΔT_b in %

meaning that in case of an assumed normal distribution about 68.27 % of the sample $y_1, y_2, \ldots, y_M$ is located in the interval $(\mu_y - \sigma_y, \mu_y + \sigma_y)$.

To examine the effect of the periodization methods the *absolute* and *relative* duration changes are going to be considered. Therefore, the absolute deviation of beat duration is defined as

$$\Delta T_{\mathrm{b},i} := T_\mathrm{b}(x_{\mathrm{final},i}) - T_\mathrm{b}(x_{\mathrm{raw},i}) \tag{4.2}$$

whereby $T_\mathrm{b}(x_{\mathrm{final},i})$ represents the beat duration of the respective data x related to curve i after the data preprocessing and $T_\mathrm{b}(x_{\mathrm{raw},i})$ prior to it[2]. Moreover the *relative* deviation for each curve reads

$$\frac{T_\mathrm{b}(x_{\mathrm{final},i}) - T_\mathrm{b}(x_{\mathrm{raw},i})}{T_\mathrm{b}(x_{\mathrm{raw},i})} = \frac{\Delta T_{\mathrm{b},i}}{T_\mathrm{b}(x_{\mathrm{raw},i})}. \tag{4.3}$$

The quantification (4.1) was evaluated for both the absolute and relative duration changes and is summarized in tables 4.3 and 4.4 whereby the respective sample size of each comparison is given in table 4.2. Obviously (P3) has no impact at all on the beat duration of any waveform whereby (P2) yields the greatest shortenings of about -0.1 s or -8 % on average depending on the regarded arteries. The most substantial deviation is observable when only considering (P2) for the 5 brachial data waveforms. However, bearing in mind the time step $\Delta t = 0.005$ s, after the whole periodization procedure and regarding all waveforms, on average approximately 3 nodes are dropped.

In fig. 4.1 the box plots related to table 4.3 are given whereby the bottom and top of the box illustrate the first and third quartiles and the band

[2]For the evaluation (4.2) the pressures p^b and p^c were used, but the velocities could have been used too.

inside the median of the sample of duration changes ΔT_b. Additionally, possible outliers are depicted with plus-symbols. Again it becomes visible that (P2) has the most considerable impact on the change of beat duration. Nonetheless, the affected group only contains in total 16 curves, cf. table 4.2.

4.2.2 Impact on Waveforms

It is important to examine the impact on the actual waveform due to chosen types of data preprocessing. In the tables 4.5 to 4.8 the corresponding changes for the brachial and carotid pressures and velocities are quantified in the form (4.1). The stated parameters are:

- Root mean squared error (RMSE)

$$\mathrm{RMSE}_i = \sqrt{\frac{1}{N}\sum_{j=1}^{N}\left(x_{\mathrm{final},i}(t_j) - x_{\mathrm{raw},i}(t_j)\right)^2}$$

  for each curve i with x being p^b, p^c, u^b or u^c. The index "final" indicates the waveform after the whole data preprocessing procedure and "raw" after (DP2) such that their beat durations coincide but still are not altered in their waveform.

- Deviations in each curve i with respect to
  - the pulse pressure (in case of dealing with pressures)

$$\mathrm{PP}(p_i) := \max_{\mathcal{T}_0^N}(p_i) - \min_{\mathcal{T}_0^N}(p_i)$$

  - the pulse velocity (in case of dealing with flow velocities)

$$\mathrm{PV}(u_i) := \max_{\mathcal{T}_0^N}(u_i) - \min_{\mathcal{T}_0^N}(u_i).$$

  The differences are stated in absolute differences

$$\Delta\mathrm{PP}_i := \mathrm{PP}(p_{\mathrm{final},i}) - \mathrm{PP}(p_{\mathrm{raw},i})$$

  or

$$\Delta\mathrm{PV}_i := \mathrm{PV}(u_{\mathrm{final},i}) - \mathrm{PV}(u_{\mathrm{raw},i})$$

  and in the relative form

$$\frac{\Delta\mathrm{PP}_i}{\mathrm{PP}(p_{\mathrm{raw},i})} \quad \text{or} \quad \frac{\Delta\mathrm{PV}_i}{\mathrm{PV}(u_{\mathrm{raw},i})}$$

  respectively.

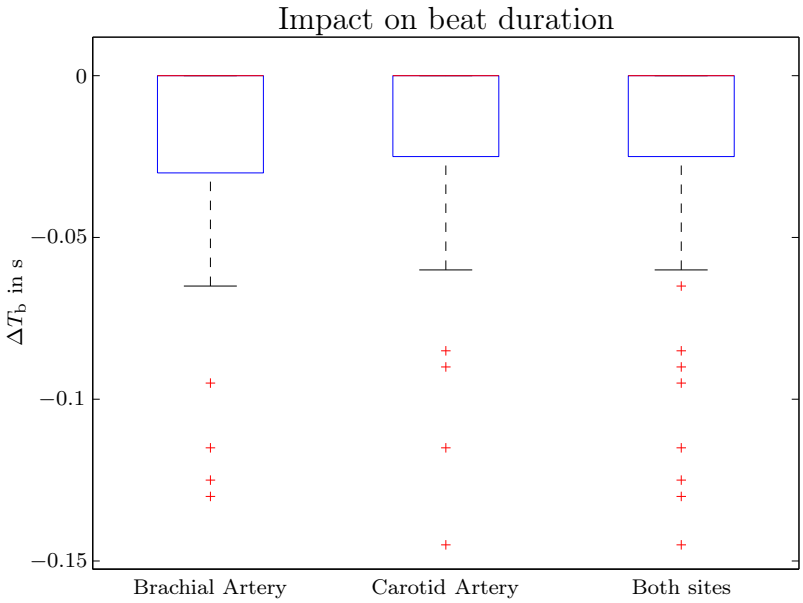

(a) Brachial and carotid artery

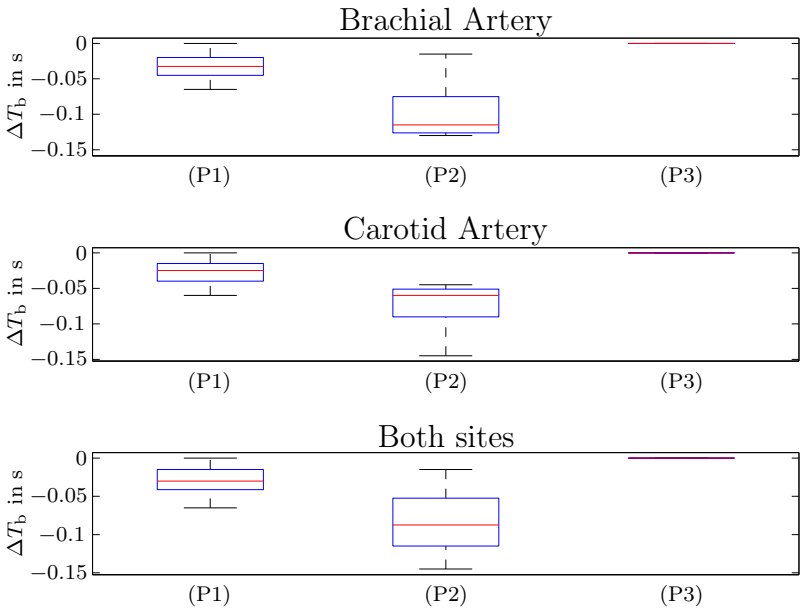

(b) Breakdown by periodization method

Figure 4.1: Data Preprocessing – Impact on beat duration T_b

p^{b}	**(P1)**	**(P2)**	**(P3)**
RMSE (mmHg)	0.029 ± 0.021	0.032 ± 0.011	0.212 ± 0.173
ΔPP (mmHg)	-0.018 ± 0.051	0.000 ± 0.000	-0.030 ± 0.096
ΔPP (%)	-0.027 ± 0.073	0.000 ± 0.000	-0.053 ± 0.166
$\mathbf{\Delta A_p}$ (mmHg s)	-0.016 ± 0.049	0.000 ± 0.002	-0.028 ± 0.088
$\mathbf{\Delta A_p}$ (%)	-0.065 ± 0.192	0.001 ± 0.010	-0.115 ± 0.348

Table 4.5: Impact on p^{b}-waveforms

p^{c}	**(P1)**	**(P2)**	**(P3)**
RMSE (mmHg)	0.025 ± 0.011	0.036 ± 0.022	0.212 ± 0.127
ΔPP (mmHg)	-0.075 ± 0.134	-0.031 ± 0.059	-0.112 ± 0.219
ΔPP (%)	-0.162 ± 0.272	-0.060 ± 0.106	-0.211 ± 0.381
$\mathbf{\Delta A_p}$ (mmHg s)	-0.076 ± 0.133	-0.033 ± 0.063	-0.111 ± 0.212
$\mathbf{\Delta A_p}$ (%)	-0.381 ± 0.652	-0.133 ± 0.242	-0.483 ± 0.877

Table 4.6: Impact on p^{c}-waveforms

u^{b}	**(P1)**	**(P2)**	**(P3)**
RMSE (cm/s)	0.000 ± 0.000	0.000 ± 0.000	0.001 ± 0.000
ΔPV (cm/s)	0.000 ± 0.000	0.000 ± 0.000	0.000 ± 0.000
ΔPV (%)	-0.015 ± 0.069	0.000 ± 0.000	-0.017 ± 0.068
$\mathbf{\Delta A_u}$ (cm/s^2)	0.000 ± 0.000	0.000 ± 0.000	0.000 ± 0.000
$\mathbf{\Delta A_u}$ (%)	0.013 ± 0.026	-0.014 ± 0.010	-0.009 ± 0.106

Table 4.7: Impact on u^{b}-waveforms

u^{c}	**(P1)**	**(P2)**	**(P3)**
RMSE (cm/s)	0.001 ± 0.001	0.001 ± 0.000	0.001 ± 0.001
ΔPV (cm/s)	-0.001 ± 0.002	-0.001 ± 0.001	-0.002 ± 0.002
ΔPV (%)	-0.334 ± 0.444	-0.128 ± 0.187	-0.381 ± 0.408
$\mathbf{\Delta A_u}$ (cm/s^2)	0.000 ± 0.000	0.000 ± 0.000	0.000 ± 0.000
$\mathbf{\Delta A_u}$ (%)	0.012 ± 0.015	0.005 ± 0.012	0.017 ± 0.062

Table 4.8: Impact on u^{c}-waveforms

- Deviations in each curve i with respect to the area[3]

$$\mathrm{A}_p(p_i) := \int_0^{T_\mathrm{b}} \left(p_i(s) - \min_{\mathcal{T}_0^N}(p_i)\right) ds$$

or

$$\mathrm{A}_u(u_i) := \int_0^{T_\mathrm{b}} u_i(s)\, ds$$

which are as well given in absolute and relative quantities as described above.

Referring to the results in tables 4.5 and 4.6 of the pressure waveforms p^b and p^c, the pulse pressure PP became slightly smaller, having its peak at (P3). The same applies to the change in area. Bearing in mind that (P3) incorporates the most substantial smoothing-procedure among the periodization methods these results confirm this fact. With a view to the relative proportions and the root mean squared error the deviations due to data preprocessing may be considered as insubstantial.

With respect to the tables 4.7 and 4.8 only little impact on the flow velocities can be attested. Nevertheless, in this case the areas are generally increasing albeit the relative augmentations are less remarkable compared to their pressure counterparts.

4.2.3 Effects of Data Preprocessing: Summary

Overall, and according to the stated quantities, the impact on the actual waveform due to data preprocessing may be neglected. In contrast, the impact on the beat duration yielding a shortening of, on average, $-1.53\,\%$ could influence the results. However, since these changes indicate a mean shortening of $-0.02\,\mathrm{s}$ within the big sample of 220 curves these results are regarded as acceptable for further investigations.

4.3 Notch Time and Sensitivity Analysis

In section 3.3.3 two different concepts for estimating the notch time by only regarding the pressure curve were described. However, no method can be attested as "better than the other" a-priori which, of course, always depends on the context of application and the used algorithms.

[3] In MATLAB the integral got implemented through `trapz`.

Moreover, whereas the reservoir pressure $\breve{p}_{\mathrm{res}}$ obtained by algorithm 3.3 is only affected by this choice[4], the reservoir pressures $\widetilde{p}_{\mathrm{res}}$ and $\widehat{p}_{\mathrm{res}}$ of the other algorithms 3.1 and 3.2 additionally depend on the minimization interval for performing the minimization routines (3.37) and (3.40). I.e. in algorithm 3.1 the corresponding minimization reads

$$\min_{\widetilde{\mathcal{R}},\widetilde{C},\widetilde{P}_\infty} \|\widetilde{p}_{\mathrm{res}} - p\|_{\mathcal{T}_n^N} \tag{4.4}$$

and for algorithm 3.2

$$\min_{\widehat{b},\widehat{p}_{\mathrm{res,d}}(t_s),\widehat{P}_\infty} \|\widehat{p}_{\mathrm{res,d}} - p\|_{\mathcal{T}_n^N}\,, \tag{4.5}$$

whereby $\mathcal{T}_n^N \subseteq \mathcal{T}_s^N$ denotes the interval in diastole for the optimization. Relating to the choice of the particular optimization interval $\mathcal{T}_n^N$ one disposes over a variety of options in order to obtain the parameters necessary to compute the reservoir pressure.

Against this background the sensitivity of the algorithms on these two estimated notch times and the intervals for minimization is investigated whereby the initial values for the start of optimization routines remain untouched. The principal aim of this section is to conclude which parameter configuration should be preferred for the final evaluation.

To begin with, the general relationship between the two estimated notch times is investigated in section 4.3.1. Based on that, the sensitivity of the reservoir pressures obtained by the algorithms 3.1 and 3.2 on the minimization intervals is pointed out in section 4.3.2. Subsequently, in section 4.3.3, the sensitivity analysis is devoted to the impact of the particular choice of notch time which eventually will conclude the final configuration for the algorithms:

- The estimated notch time is set $t_s := t_{\mathrm{s,B}} \approx T_{\mathrm{s,B}}$
- The minimizations for the algorithms 3.1 and 3.2 are performed over the whole diastole.

4.3.1 Notch Time

In fig. 4.2 the results for the computed notch times $T_{\mathrm{s,A}}$ of (3.30) and $T_{\mathrm{s,B}}$ of (3.31) are shown. The former estimation of notch time represents the time of pressure with maximum curvature and the latter the time of pressure with minimum first derivation. As can be observed in

[4]In fact, one could change the interval for the optimization in (3.51) too. However, since algorithm 3.3 is provided by Kim H. Parker only the notch time is varied which can be assigned as optional input parameter to the algorithm.

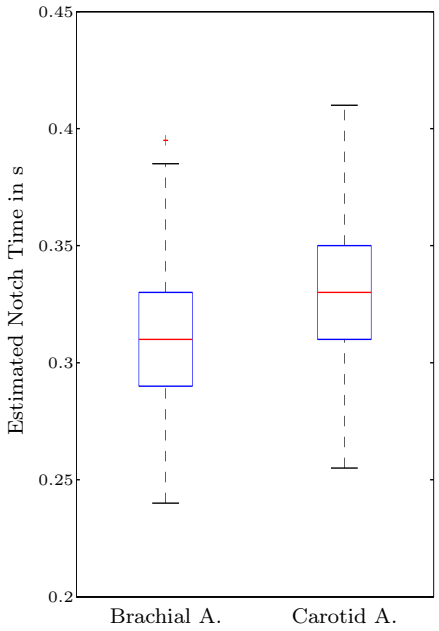

(a) Notch Time $T_{\mathrm{s,B}}$ (Min. Der.)

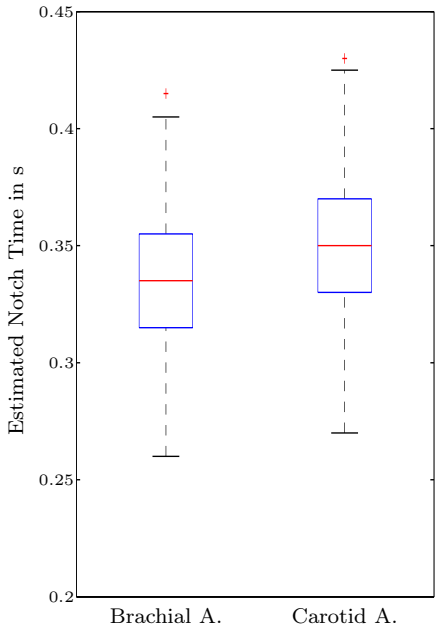

(b) Notch Time $T_{\mathrm{s,A}}$ (Max. Curv.)

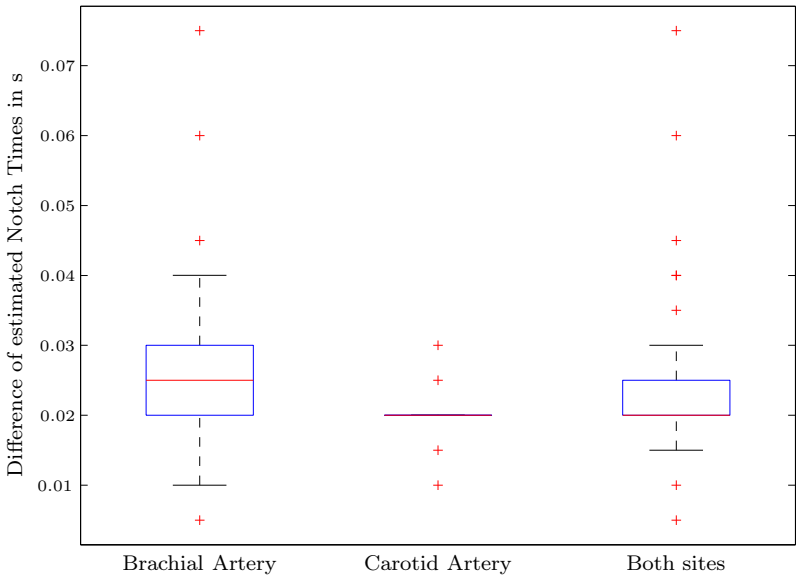

(c) Difference $t_{\mathrm{s,A}} - t_{\mathrm{s,B}}$

Figure 4.2: Comparison of estimated Notch Times

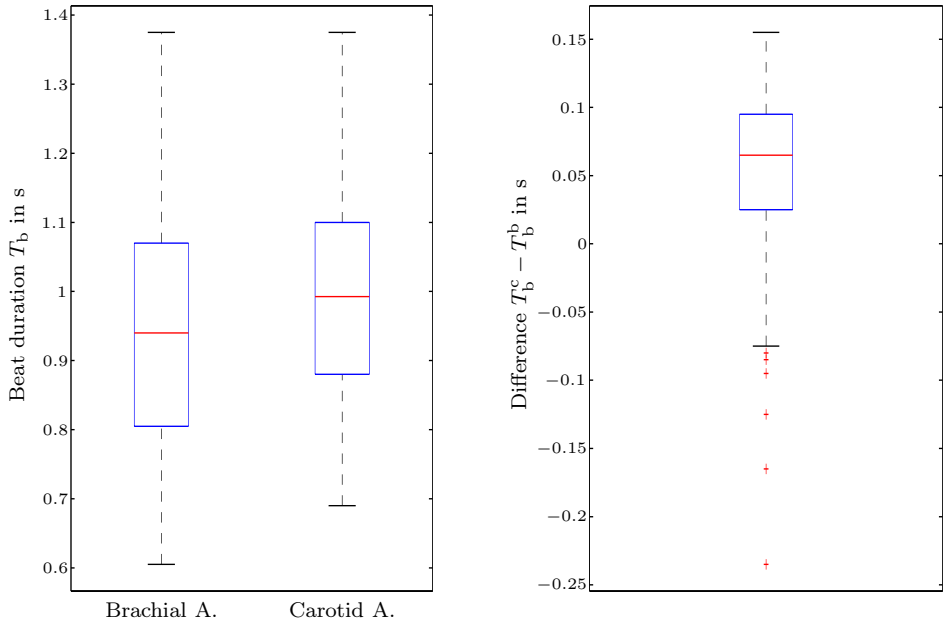

(a) Beat durations related to arteries (b) Difference of beat duration

Figure 4.3: Notch Time – Impact of beat duration

figs. 4.2a and 4.2b, the estimated notch times for the brachial curves are generally smaller compared to the carotid ones. Beside changes in pressure waveforms at different locations within the arterial tree due to travelling waves, cf. figs. 2.5 and 2.6, also the generally positive difference $T_\mathrm{b}^\mathrm{c} - T_\mathrm{b}^\mathrm{b}$ between the brachial and carotid beat duration of each data set, cf. fig. 4.3, might be a reason. Since the beat duration of the measured carotid waveform is longer, it is likely that the respective estimated notch time occurs later. Moreover, fig. 4.2c reveals that the maximum curvature-related notch time $T_{\mathrm{s,A}}$ is always greater than the minimum derivation-associated $T_{\mathrm{s,B}}$. In particular, for the carotid artery the difference between the two computed notch times equals the constant value of 0.02 s in the majority of cases.

4.3.2 Sensitivity on Minimization Interval

In this section it shall be investigated how the reservoir pressures $\widetilde{p}_\mathrm{res}$ and $\widehat{p}_\mathrm{res}$ of the algorithms 3.1 and 3.2 depend on the choice of the minimization interval $\mathcal{T}_n^N$ for performing (4.4) and (4.5) during diastole. Moreover, $\mathcal{T}_n^N$ depends on the particular selection of notch time since the estimated duration of diastole reads $T_\mathrm{d} = T_\mathrm{b} - T_\mathrm{s}$ where T_s either represents $T_{\mathrm{s,A}}$ or $T_{\mathrm{s,B}}$.

In this thesis it is restricted to the possibilities that $\mathcal{T}_n^N$ either corresponds to the whole diastole or only to the last two-thirds of it. The latter is very common in literature since little wave activity is expected in this particular stage and therefore could constitute an appropriate interval for fitting the reservoir pressure to the measured one [1, 3, 31]. However, it is of great importance that the *overall* reservoir curve exhibits a meaningful waveform. For example, it is not excluded a-priori due to findings of analytical investigations that the final results of the algorithms cannot constitute erratic waveforms in a neighbourhood of T_s or that they are based on negative parameters – like mentioned in the discussion of algorithm 3.3 in section 3.4.3 – which would contradict the Reservoir Model. Hence, a trade-off between an aligned pressure decay at later diastole and an overall reasonable waveform has to be found. As a consequence the sensitivity of the reservoir pressures gained by the algorithms 3.1 to 3.3 on the choice of the estimated notch time and the minimization interval is examined. Finally, a parameter setting is sought which fits best for the majority of measured data sets.

In order to compare these results the respective modi need to be addressed appropriately. Hence, the starting time t_n for the minimization interval $\mathcal{T}_n^N$ shall either indicate the estimated notch times $t_{\mathrm{s,A}} \approx T_{\mathrm{s,A}}$ and $t_{\mathrm{s,B}} \approx T_{\mathrm{s,B}}$ or be related to the time

$$T_{1/3\mathrm{D}} := T_\mathrm{s} + \frac{1}{3}T_\mathrm{d} = T_\mathrm{s} + \frac{1}{3}(T_\mathrm{b} - T_\mathrm{s})$$

which indicates start of the last two-thirds of diastole. In summary, with $t_{1/3\mathrm{D}} \in \mathcal{T}_s^N$ as the approximation of $T_{1/3\mathrm{D}}$, the minimization routines stated in (4.4) and (4.5) are restricted to the following parameter set-up:

(1) Estimated notch time:
   - $t_s = t_{\mathrm{s,A}} \approx T_{\mathrm{s,A}}$ or
   - $t_s = t_{\mathrm{s,B}} \approx T_{\mathrm{s,B}}$

(2) Minimization interval $\mathcal{T}_n^N$:
   - Minimization over the whole diastole: $t_n = t_s \in \{t_{\mathrm{s,A}}, t_{\mathrm{s,B}}\}$ determined by the choice of (1) or
   - Minimization over the last two-thirds of diastole: $t_n = t_{1/3\mathrm{D}}$ whereby

$$t_{1/3\mathrm{D}} \approx T_{\mathrm{s,A}} + \frac{1}{3}(T_\mathrm{b} - T_{\mathrm{s,A}})$$

   or

$$t_{1/3\mathrm{D}} \approx T_{\mathrm{s,B}} + \frac{1}{3}(T_\mathrm{b} - T_{\mathrm{s,B}})$$

respectively, depending on the chosen notch time in (1).

The subsequent table 4.9 illustrates the used notation for the reservoir pressures corresponding to the chosen parameter configuration of the respective algorithms:

		Minimization Interval	
		Two-third Diastole $\mathcal{T}^N_{1/3\mathrm{D}}$	**Diastole $\mathcal{T}^N_{\mathrm{s}}$**
Notch Time	$\boldsymbol{t}_{\mathrm{s,A}}$	$p_{\mathrm{res}(t_{\mathrm{s,A}},\mathcal{T}^N_{1/3\mathrm{D}})}$	$p_{\mathrm{res}(t_{\mathrm{s,A}},\mathcal{T}^N_{\mathrm{s}})}$
	$\boldsymbol{t}_{\mathrm{s,B}}$	$p_{\mathrm{res}(t_{\mathrm{s,B}},\mathcal{T}^N_{1/3\mathrm{D}})}$	$p_{\mathrm{res}(t_{\mathrm{s,B}},\mathcal{T}^N_{\mathrm{s}})}$

Table 4.9: Notation of reservoir pressures relating to parameter set-up

Sensitivity on Minimization Intervals with Notch Time $t_{\mathrm{s,A}}$

Firstly the impact of the minimization interval on the results is shown by regarding $t_s = t_{\mathrm{s,A}}$. Therefore the reservoir pressures located in the first row of table 4.9 are compared for the algorithms 3.1 and 3.2 whose results are denoted with $\widetilde{p}_{\mathrm{res}}$ and $\widehat{p}_{\mathrm{res}}$.

The deviations in the corresponding pressure waveforms by using the whole diastole for the optimizations (4.4) and (4.5) instead of only the last two-thirds of it are stated in table 4.10. The notation $p_{\mathrm{res}(t_{\mathrm{s,A}},\mathcal{T}^N_{1/3\mathrm{D}})} \mapsto p_{\mathrm{res}(t_{\mathrm{s,A}},\mathcal{T}^N_{\mathrm{s}})}$ shall indicate that the deviation from $p_{\mathrm{res}(t_{\mathrm{s,A}},\mathcal{T}^N_{1/3\mathrm{D}})}$ to $p_{\mathrm{res}(t_{\mathrm{s,A}},\mathcal{T}^N_{\mathrm{s}})}$ is investigated with $p_{\mathrm{res}(t_{\mathrm{s,A}},\mathcal{T}^N_{1/3\mathrm{D}})}$ being the reference. Referring to all the indicators RMSE, the relative ΔPP and $\Delta \mathrm{A}_p$ it can be witnessed that for both the computed reservoir pressures $\widetilde{p}_{\mathrm{res}}$ and $\widehat{p}_{\mathrm{res}}$ the sensitivity on the chosen interval is considerably high. These indicate that the waveforms experience substantial changes due to the change of the minimization interval. Even though the absolute differences of PP and area remain – on average – almost zero the remarkably high figure in their standard deviations point out that the positive changes cancel the negative ones. When comparing $\widehat{p}_{\mathrm{res}}$ with $\widetilde{p}_{\mathrm{res}}$ similar features can be witnessed but

	$\widetilde{\boldsymbol{p}}_{\mathrm{res}(\boldsymbol{t}_{\mathrm{s,A}},\boldsymbol{\mathcal{T}}^{\boldsymbol{N}}_{\boldsymbol{1/3\mathrm{D}}})} \mapsto \widetilde{\boldsymbol{p}}_{\mathrm{res}(\boldsymbol{t}_{\mathrm{s,A}},\boldsymbol{\mathcal{T}}^{\boldsymbol{N}}_{\mathrm{s}})}$	$\widehat{\boldsymbol{p}}_{\mathrm{res}(\boldsymbol{t}_{\mathrm{s,A}},\boldsymbol{\mathcal{T}}^{\boldsymbol{N}}_{\boldsymbol{1/3\mathrm{D}}})} \mapsto \widehat{\boldsymbol{p}}_{\mathrm{res}(\boldsymbol{t}_{\mathrm{s,A}},\boldsymbol{\mathcal{T}}^{\boldsymbol{N}}_{\mathrm{s}})}$
RMSE (mmHg)	5.618 ± 4.902	5.619 ± 5.661
ΔPP (mmHg)	0.294 ± 15.003	-2.521 ± 12.649
ΔPP (%)	13.851 ± 42.091	-0.909 ± 26.037
$\Delta \mathbf{A}_{\boldsymbol{p}}$ (mmHg s)	0.642 ± 4.424	-0.695 ± 4.159
$\Delta \mathbf{A}_{\boldsymbol{p}}$ (%)	9.350 ± 30.738	-1.709 ± 20.233

Table 4.10: Sensitivity on minimization interval with notch time $t_{\mathrm{s,A}}$

the influence of the optimization interval on particular reservoir pressure waveforms $\widetilde{p}_{\text{res}}$ by algorithm 3.1 seems to be more considerable by regarding the relative area and PP deviations. Since the deviations in PP and area are comparable for both pressure waveforms they indicate a similar phenomenon: The respective deviations cancel on average over the whole sample. In the following, a closer investigation is done separately for $\widetilde{p}_{\text{res}}$ and $\widehat{p}_{\text{res}}$.

In fig. 4.4 the histogram for the changes in PP and two plots for indicating exemplarily a positive and negative deviation for the transition $\widetilde{p}_{\text{res}(t_{\text{s,A}},\mathcal{T}^N_{1/3\text{D}})} \mapsto \widetilde{p}_{\text{res}(t_{\text{s,A}},\mathcal{T}^N_{\text{s}})}$ are illustrated. The histogram shows the distribution of the PP changes for all 220 pressure waveforms. Bearing in mind a typical[5] PP of about 40 mmHg numerous curves alter more than a half of this figure. On average these deviations of the whole sample of all pressure curves almost cancel but the standard deviation of approximately 15 mmHg manifests this remarkable influence of the minimization interval. Taking into account that the RMSE constitutes a ratio for the absolute difference of the considered reservoir pressures the notable figure of the RMSE in table 4.10 becomes obvious. In fig. 4.4b the direct impact of the chosen minimization interval is illustrated yielding a positive change in PP of about 30 mmHg. The reservoir pressure $\widetilde{p}_{\text{res}(t_{\text{s,A}},\mathcal{T}^N_{1/3\text{D}})}$ is computed through minimizing the difference to the measured pressure waveform p over the last two-thirds of diastole whose beginning is indicated with $t_{1/3\text{D}}$. Since the used optimization method `lsqnonlin` of the MATLAB-implementation might only give *local* solutions the corresponding pressure waveform can be explained[6]. Using the whole diastole with its estimated beginning at $t_{\text{s,A}}$ for the curve fitting the more reasonable reservoir pressure waveform $\widetilde{p}_{\text{res}(t_{\text{s,A}},\mathcal{T}^N_{t_{\text{s}}})}$ is achieved. In fig. 4.4c a pressure curve with negative change in PP can be observed. Here the minimization-routine `lsqnonlin` detects a plausible solution in terms of getting an aligned pressure waveform during $\mathcal{T}^N_{1/3\text{D}}$. Nonetheless, compared to the reservoir pressure associated with the fitting over the whole diastole $\mathcal{T}^N_{\text{s,A}}$, it hits a magnitude in PP which may well be unreasonably high.

In fig. 4.5 the respective results of the reservoir pressure $\widehat{p}_{\text{res}}$ are depicted. With respect to the histogram similar assertions as stated above can be said about the PP deviations of this parameter setting. But, as op-

[5] It is assumed a systolic and a diastolic pressure of 120 mmHg and 80 mmHg respectively.

[6] In this concrete case, the optimization algorithm of MATLAB terminated since the change in the residual was smaller than the specified tolerance of 1×10^{-6}. This problem remains persistent for other common optimization methods implemented in MATLAB such as `fminsearch`.

	$\widetilde{\boldsymbol{p}}_{\mathrm{res}(\boldsymbol{t}_{\mathrm{s,B}},\boldsymbol{\mathcal{T}}^{\boldsymbol{N}}_{\boldsymbol{1/3D}})} \mapsto \widetilde{\boldsymbol{p}}_{\mathrm{res}(\boldsymbol{t}_{\mathrm{s,B}},\boldsymbol{\mathcal{T}}^{\boldsymbol{N}}_{\mathrm{s}})}$	$\widehat{\boldsymbol{p}}_{\mathrm{res}(\boldsymbol{t}_{\mathrm{s,B}},\boldsymbol{\mathcal{T}}^{\boldsymbol{N}}_{\boldsymbol{1/3D}})} \mapsto \widehat{\boldsymbol{p}}_{\mathrm{res}(\boldsymbol{t}_{\mathrm{s,B}},\boldsymbol{\mathcal{T}}^{\boldsymbol{N}}_{\mathrm{s}})}$
RMSE (mmHg)	5.350 ± 4.841	6.877 ± 7.943
ΔPP (mmHg)	-0.093 ± 14.676	-5.862 ± 16.593
ΔPP (%)	11.311 ± 41.659	-4.886 ± 30.190
$\boldsymbol{\Delta A_p}$ (mmHg s)	0.486 ± 4.267	-1.623 ± 5.223
$\boldsymbol{\Delta A_p}$ (%)	7.168 ± 29.684	-4.657 ± 24.423

Table 4.11: Sensitivity on minimization interval with notch time $t_{\mathrm{s,B}}$

posed to $\widetilde{p}_{\mathrm{res}}$ and with reference to the RMSE in table 4.10, the impact of the optimization interval on particular reservoir pressure waveforms $\widehat{p}_{\mathrm{res}}$ obtained by algorithm 3.2 is less considerable. In fig. 4.5b the respective curve with a positive PP change of about 40 mmHg is shown. Both reservoir pressures exhibit a good approximation to the measured pressure waveform in diastole but as opposed to $\widehat{p}_{\mathrm{res}(t_{t_{\mathrm{s,A}}},\mathcal{T}^N_{1/3\mathrm{D}})}$ the reservoir pressure $\widehat{p}_{\mathrm{res}(t_{t_{\mathrm{s,A}}},\mathcal{T}^N_{\mathrm{s}})}$ fails during systole. The responsible computational step in algorithm 3.2 for yielding such a flawed reservoir pressure is identified with the optimization (3.41). Hence, only a small discrepancy between $\widehat{p}_{\mathrm{res}(t_{t_{\mathrm{s,A}}},\mathcal{T}^N_{t_{\mathrm{s,A}}})}$ and $\widehat{p}_{\mathrm{res}(t_{t_{\mathrm{s,A}}},\mathcal{T}^N_{1/3\mathrm{D}})}$ in $t_{\mathrm{s,A}}$ leads to a tremendously different waveform in systole. This sensitivity will be important too in the sensitivity analysis associated with the notch time in section 4.3.3. Considering fig. 4.5c for discussing the impact of the minimization interval on a particular waveform with deviation of about -30 mmHg it can be observed that both reservoir pressures exhibit a smooth waveform within the whole cardiac cycle. Nevertheless, their discrepancy in PP due to the choice of the fitting interval is remarkable.

In conclusion, the computed reservoir pressure curves $\widetilde{p}_{\mathrm{res}}$ and $\widehat{p}_{\mathrm{res}}$ reveals that the algorithms 3.2 and 3.3 are remarkably sensitive on the minimization interval associated with the notch time $t_{\mathrm{s,A}}$. Due to the fact that the minimization routine `lsqnonlin` can only detect local minima and that measured pressure waveforms may vary substantially within the first third compared to the last two-thirds of diastole, a minimization over the whole diastole $\mathcal{T}^N_{t_{\mathrm{s,A}}}$ seems to be preferable. However, the sensitivity of the systolic part of reservoir pressure $\widehat{p}_{\mathrm{res}}$, cf. fig. 4.5b, needs to be investigated separately.

Sensitivity on Minimization Intervals with Notch Time $t_{\mathrm{s,B}}$

In this section the sensitivity of the reservoir pressure waveforms on the minimization interval is discussed by using the estimated notch time $t_{\mathrm{s,B}} \approx T_{\mathrm{s,B}}$ rather than $t_{\mathrm{s,A}} \approx T_{\mathrm{s,A}}$.

By comparing table 4.11 with table 4.10 similar results of all ratios can be observed for the deviations of the reservoir pressure $\widetilde{p}_{\mathrm{res}}$. Also

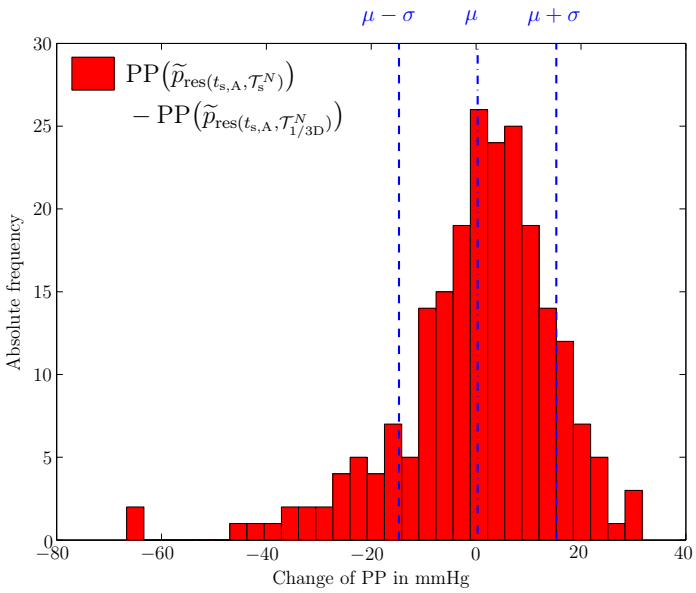

(a) Change of PP of all pressure curves

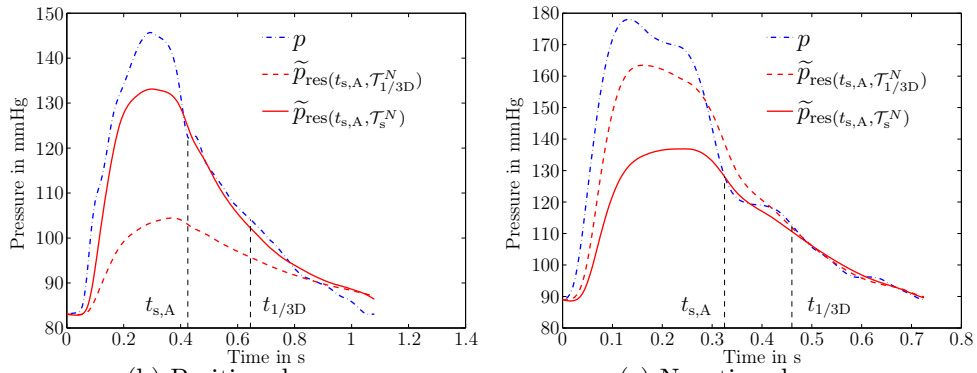

(b) Positive change

(c) Negative change

Figure 4.4: $\widetilde{p}_{\mathrm{res}}$-sensitivity on minimization interval with notch time $t_{\mathrm{s,A}}$

the figs. 4.4 and 4.6 depict similar characteristics: The last two-thirds of diastole may yield a reservoir pressure waveform which does not fit the whole diastolic behaviour (fig. 4.6b) and its corresponding reservoir PP might be too high (fig. 4.6c).

The situation for the pressures $\widehat{p}_{\mathrm{res}}$ obtained by algorithm 3.2 is somewhat different. All figures of $\widehat{p}_{\mathrm{res}}$ in table 4.11 are higher compared to those in table 4.10 which indicate an even more severe impact on average. However, the PP distribution does not differ substantially among them according to the histograms fig. 4.7a and fig. 4.5a. Fig. 4.7b does not contribute any new insight since it suggests as well that the last two-thirds of diastole might not be sufficient for a proper curve fitting. In contrast, fig. 4.7c indicates another possible phenomenon: Since algo-

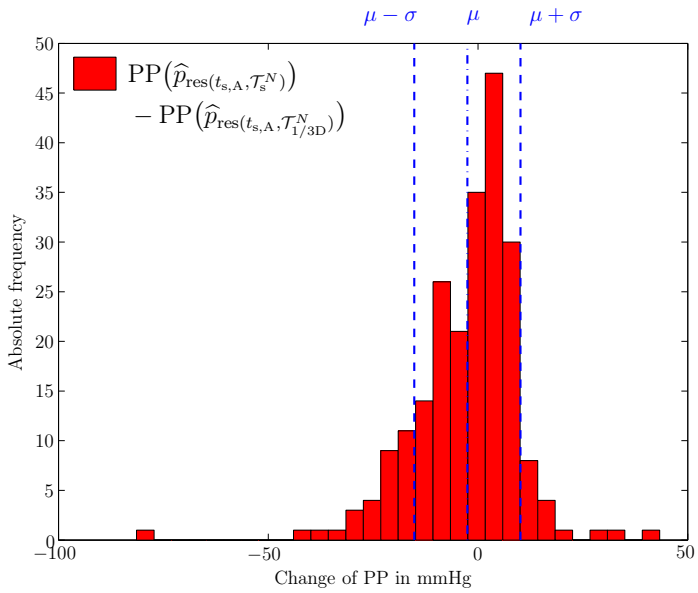

(a) Change of PP of all pressure curves

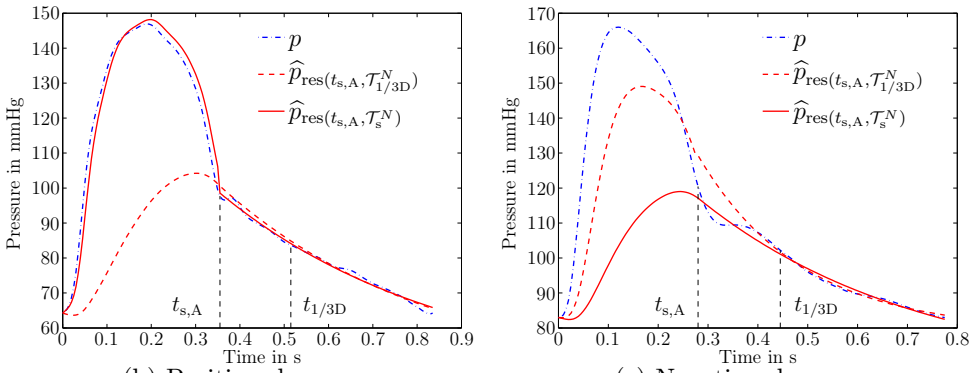

(b) Positive change

(c) Negative change

Figure 4.5: $\widehat{p}_{\mathrm{res}}$-sensitivity on minimization interval with notch time $t_{\mathrm{s,A}}$

rithm 3.2 returns a reservoir pressure obtained by sticking two pressure waveforms together, one related to systole and the other to diastole, the transition at the connection point t_{s} can be discontinuous. Therefore, in case of getting "inappropriate" pressures $\widehat{p}_{\mathrm{res}}(t_{\mathrm{s}})$ the corresponding reservoir pressure waveform may provide discontinuities (fig. 4.7c) or simply exhibit a "non-smooth" graph (fig. 4.5b).

Overall, by taking into account all the stated points above, it seems to be preferable to use the whole diastole $\mathcal{T}_{\mathrm{s}}^N$ for the algorithms 3.1 and 3.2 so as to compute the respective reservoir pressures. However, many pressure waveforms obtained by those algorithms depend considerably on the minimization interval. In order to get plausible waveforms which can be compared reasonably to each other further investigations need to be

done. In this context, the next step is meant to analyse the sensitivity of the computed reservoir pressure waveforms on the chosen type of notch time.

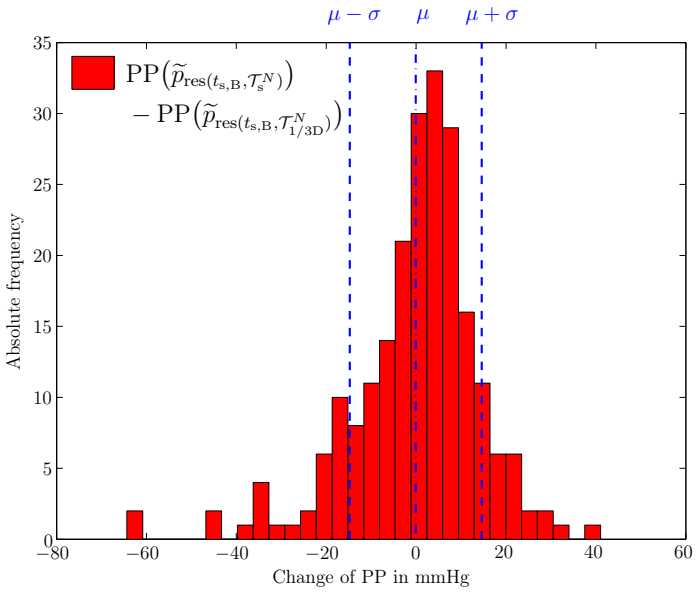

(a) Change of PP of all pressure curves

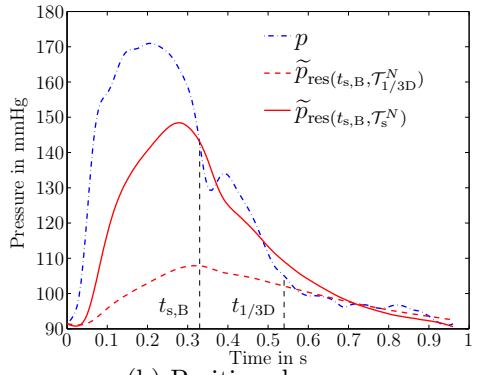

(b) Positive change

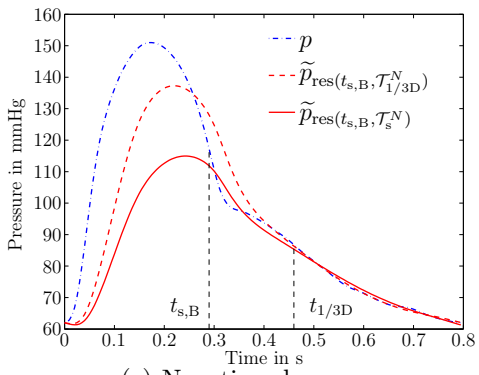

(c) Negative change

Figure 4.6: $\widetilde{p}_{\mathrm{res}}$-sensitivity on minimization interval with notch time $t_{\mathrm{s,B}}$

4.3.3 Sensitivity on Notch Time

In the preceding sections of the sensitivity analysis the differences between the two notch time estimations and the sensitivity of the computed pressure waveforms $\widetilde{p}_{\mathrm{res}}$ and $\widehat{p}_{\mathrm{res}}$ on the chosen type of minimization interval related to both notch times were pointed out. It was inferred that the obtained reservoir pressures seem to be more reasonable when using the whole diastole $\mathcal{T}_{\mathrm{s}}^N$ for fitting the reservoir to the measured pressure

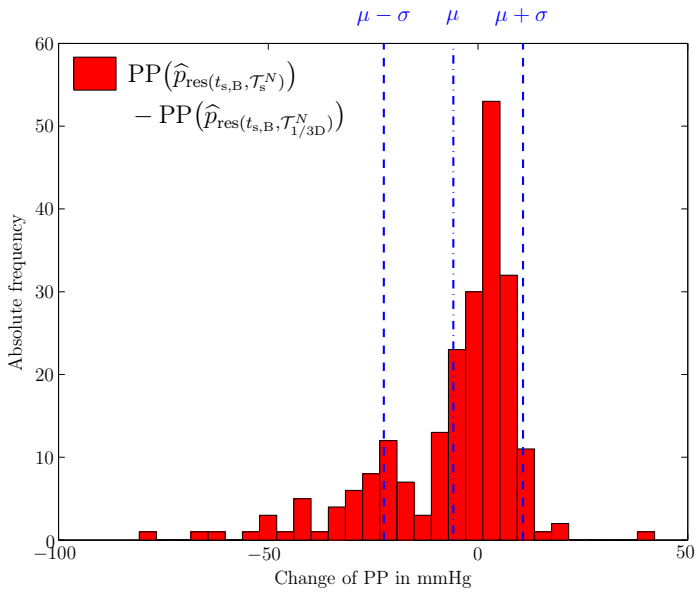

(a) Change of PP of all pressure curves

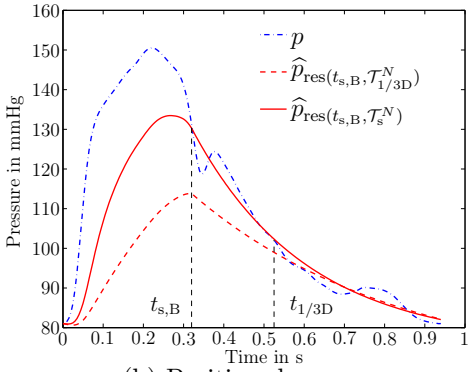

(b) Positive change

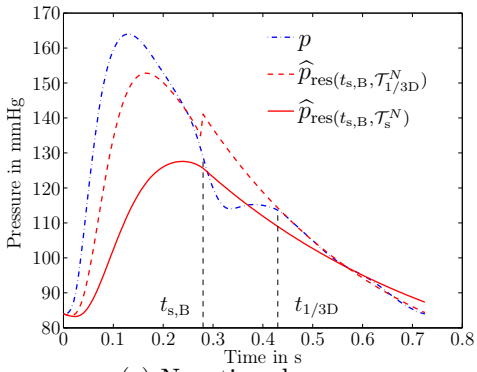

(c) Negative change

Figure 4.7: $\widehat{p}_{\mathrm{res}}$-sensitivity on minimization interval with notch time $t_{\mathrm{s,B}}$

curves. Nonetheless, to obtain plausible pressure waveforms in order compare their results and characteristics appropriately their dependency on the notch time has to be pointed out. In fact, even though the median of differences $t_{\mathrm{s,A}} - t_{\mathrm{s,B}}$ of all waveforms only exhibits 0.02 s, cf. fig. 4.2c, this deviation has considerable effects on some of the reservoir pressure waveforms. Partly this has already been observed in section 4.3.2. However, in this section the main focus is put on that issue.

The results of the algorithms 3.1 to 3.3 in this section are generated by using the following parameter set-up:

- All algorithms are executed for the estimated notch time $t_{\mathrm{s,A}} \approx T_{\mathrm{s,A}}$ of (3.30) and for $t_{\mathrm{s,B}} \approx T_{\mathrm{s,B}}$ of (3.31).

	$\widetilde{\boldsymbol{p}}_{\mathrm{res}(\boldsymbol{t}_{\mathrm{s,A}})} \mapsto \widetilde{\boldsymbol{p}}_{\mathrm{res}(\boldsymbol{t}_{\mathrm{s,B}})}$	$\widehat{\boldsymbol{p}}_{\mathrm{res}(\boldsymbol{t}_{\mathrm{s,A}})} \mapsto \widehat{\boldsymbol{p}}_{\mathrm{res}(\boldsymbol{t}_{\mathrm{s,B}})}$	$\breve{\boldsymbol{p}}_{\mathrm{res}(\boldsymbol{t}_{\mathrm{s,A}})} \mapsto \breve{\boldsymbol{p}}_{\mathrm{res}(\boldsymbol{t}_{\mathrm{s,B}})}$
RMSE (mmHg)	1.418 ± 2.485	1.776 ± 3.659	0.960 ± 2.369
ΔPP (mmHg)	0.636 ± 5.249	-1.068 ± 7.253	0.152 ± 4.709
ΔPP (%)	2.636 ± 16.686	-1.005 ± 12.568	1.210 ± 7.257
$\boldsymbol{\Delta A_p}$ (mmHg s)	0.158 ± 2.016	-0.267 ± 1.873	0.070 ± 0.967
$\boldsymbol{\Delta A_p}$ (%)	1.598 ± 14.235	-0.906 ± 8.904	0.692 ± 5.016

Table 4.12: Deviation due to sensitivity on notch time

- The optimization routines (3.37) and (3.40) of the algorithms 3.1 and 3.2, are performed over the whole Diastole $\mathcal{T}_s^N$. Therefore the corresponding optimization is done for all sampled points starting at either $t_s = t_{\mathrm{s,B}} \approx T_{\mathrm{s,B}}$ or $t_s = t_{\mathrm{s,A}} \approx T_{\mathrm{s,A}}$ respectively.

Thus, for every single pressure waveform p two different reservoir pressures $p_{\mathrm{res}(t_{\mathrm{s,A}})}$ and $p_{\mathrm{res}(t_{\mathrm{s,B}})}$ are computed. The former denotes the reservoir pressure based on the notch time $T_{\mathrm{s,A}}$ and the latter based on $T_{\mathrm{s,B}}$. As usual, the accent-symbols indicate the result of the respective implementation method.

In table 4.12 the RMSE, the differences in PP and in area are shown by regarding the transition from $p_{\mathrm{res}(t_{\mathrm{s,A}})}$ to $p_{\mathrm{res}(t_{\mathrm{s,B}})}$. Again, the RMSE indicates that many waveforms experience alterations in their waveform, albeit they appear less substantial compared to those related to the sensitivity analysis with respect to the minimization interval. In contrast to that, the mean of the other absolute ratios equals almost zero and the corresponding standard deviations are less considerable too. Therefore, the sensitivity on the notch time seems less striking compared with the minimization interval. However, the relative changes are still remarkable. For a closer investigation each implementation is discussed separately whereby the findings are similar to those already mentioned in the previous section 4.3.2.

Algorithm 3.1: Reservoir pressure based on the flow velocity

Basically, referring to fig. 4.8a and table 4.12, the mean deviation in PP remains approximately zero for the reservoir pressures $\widetilde{p}_{\mathrm{res}}$. Nonetheless, there are several curves which suffer severe deviations in their pulse pressure by simply using $T_{\mathrm{s,B}}$ instead of $T_{\mathrm{s,A}}$ in the algorithm. These effects can happen in both directions yielding PP changes in the range from approximately -20 mmHg to 30 mmHg. The figs. 4.8b and 4.8c illustrate affected curves[7]. In either case the usage of $T_{\mathrm{s,B}}$ leads to an improvement of the pressure waveform since the corresponding curve matches closely

[7] Again, the reservoir pressure $\widetilde{p}_{\mathrm{res}(t_{\mathrm{s,A}})}$ does not align closely to the measured pressure curve suggesting a non proper outcome of the optimization. However, the

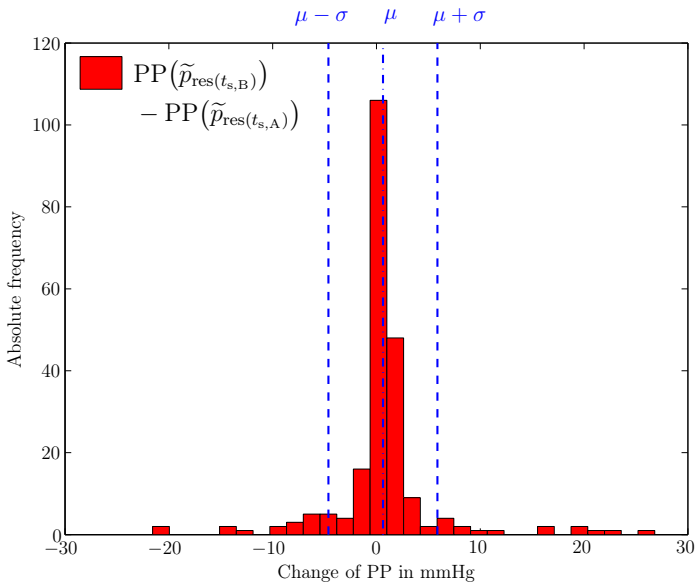

(a) Change of PP of all pressure curves

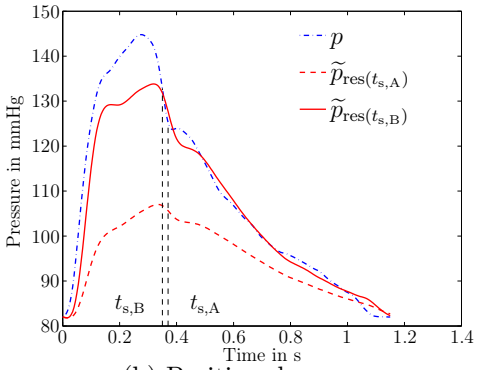

(b) Positive change

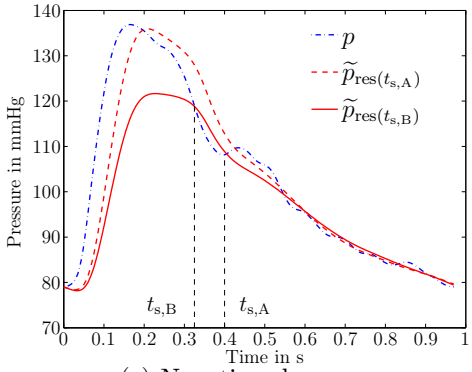

(c) Negative change

Figure 4.8: Sensitivity of $\widetilde{p}_{\mathrm{res}}$ on notch time

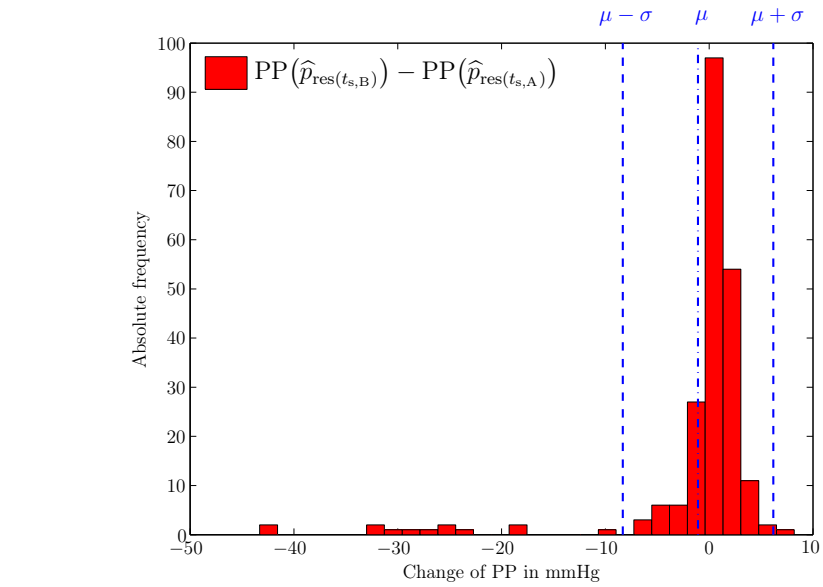

(a) Change of PP of all pressure curves

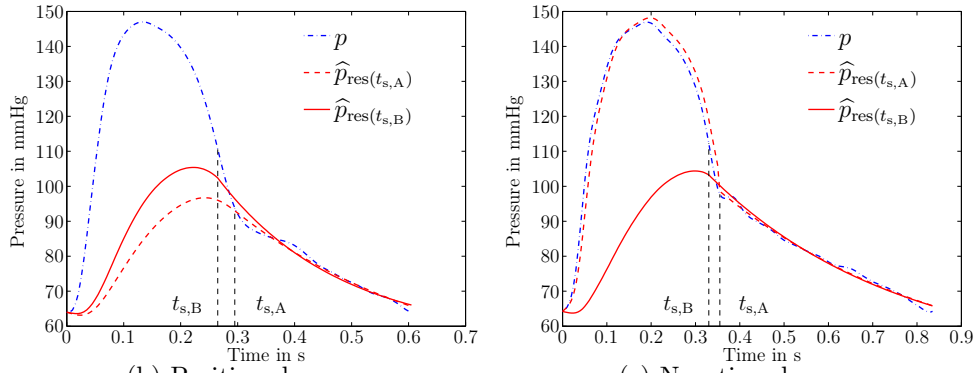

(b) Positive change

(c) Negative change

Figure 4.9: Sensitivity of $\widehat{p}_{\mathrm{res}}$ on notch time

the measured pressure waveform p in diastole and does not exhibit unreasonable pressure values throughout the whole cardiac cycle. However, the contrary may as well be possible: A "good" curve may well alter into a less plausible one too, which might be tied to a curve fitting in diastole based on a local rather than a global minimum. Thus, indicators for identifying suitable curves are proposed in the later section 4.3.4.

Algorithm 3.2: Reservoir pressure without flow – Variant A

Whereas a different notch time implies both positive and negative deviations in PP for the pressures $\widetilde{p}_{\text{res}}$, the PP deviations for the reservoir pressures $\widehat{p}_{\text{res}}$ are characterized by mainly (substantial) negative changes which therefore document a non-wanted results: Some of the curves $\widehat{p}_{\text{res}(t_{\text{s,A}})}$ do not seem to constitute a plausible reservoir pressure but rather match the pressure waveform for the whole cardiac cycle, cf. figs. 4.5b and 4.9c. Within the Reservoir Theory this would imply an excess pressure of almost zero according to (3.1) which would contradict the model since it is believed that wave activity is considerably high during systole. Hence a drop in PP is preferable for many of the reservoir pressure waveforms corresponding to $T_{\text{s,A}}$. Consequently, the choice of using $T_{\text{s,B}}$ instead of $T_{\text{s,A}}$ yields plausible reservoir pressure waveforms since numerous pressure curves undergo considerable changes in the PP. In further consequence, these waveform deviations give rise to the still notable value of RMSE in table 4.12.

Algorithm 3.3: Reservoir pressure without flow – Variant B

Algorithm 3.3 constitutes the most stable implementation method. This becomes clear by observing the means and standard deviations of the PP and area deviations in table 4.12. However, the, apparently contradictory, high figures corresponding to the RMSE can be explained by the existence of two curves exhibiting tremendous changes in PP which result in the high RMSE, cf. fig. 4.10a. The reservoir pressures $\breve{p}_{\text{res}(t_{\text{s,A}})}$ and $\breve{p}_{\text{res}(t_{\text{s,B}})}$ constitute reasonable waveforms for the majority of curves. Nonetheless, as mentioned in section 3.4.3, it is not excluded a-priori that some waveforms are based on negative parameters. Indeed, some pressures $\breve{p}_{\text{res}}$ belong to this group of waveforms which do not correspond to physiological plausible parameters.

Conclusion

The reservoir pressures $\widehat{p}_{\text{res}}$ of algorithm 3.2 are most reasonable when using the notch time $t_{\text{s,B}} \approx T_{\text{s,B}}$. Considering the reservoir pressure $\widetilde{p}_{\text{res}}$ no substantial difference is observable by performing algorithm 3.1 with the notch time based on $T_{\text{s,A}}$ or on $T_{\text{s,B}}$. The same applies to the reservoir pressures $\breve{p}_{\text{res}}$ obtained by algorithm 3.3. Hence, the choice for the notch time to be $t_s := t_{\text{s,B}} \approx T_{\text{s,B}}$ finally accomplishes the configuration for all algorithms since the initial values have always remained unchanged.

algorithm terminated regularly since the change in residual was less than the specified tolerance of 1×10^{-6}.

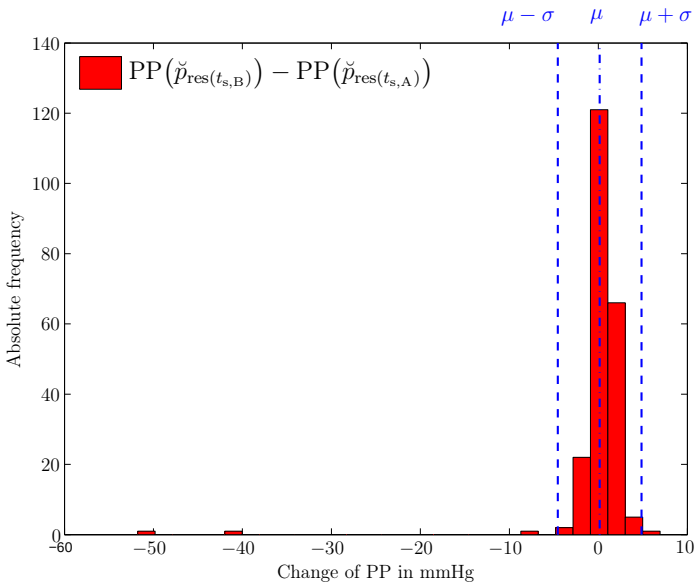

(a) Change of PP of all pressure curves

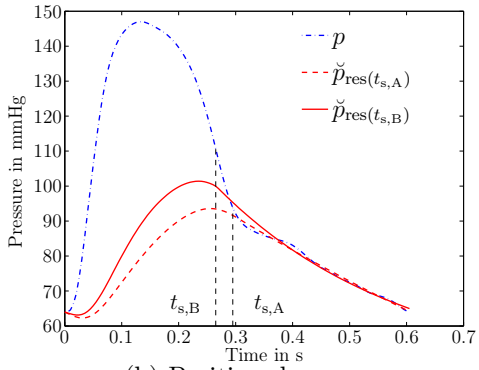

(b) Positive change

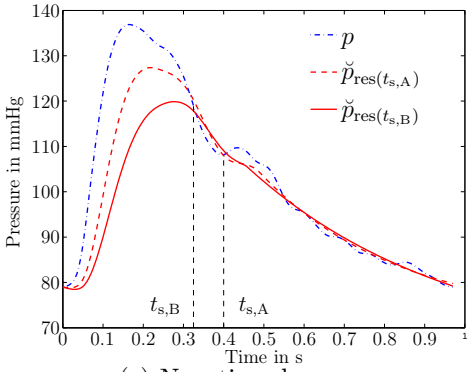

(c) Negative change

Figure 4.10: Sensitivity of $\breve{p}_{\mathrm{res}}$ on notch time

Therefore all algorithms are parametrized as originally documented in the algorithms 3.1 to 3.3.

4.3.4 Identification of Reasonable Reservoir Curves

Even though the algorithms 3.1 to 3.3 now provide a uniquely defined configuration which are supposed to be applicable for the majority of pressure curves it still may occur that some of the computed waveforms do not constitute physiological reasonable reservoir pressures which, in further consequence, shall not be considered for the final evaluation.

For the reservoir pressure $\breve{p}_{\mathrm{res}}$ this can be done straight-forward: One has to check only the sign of the parameters $\breve{a}$, $\breve{b}$ and $\breve{P}_{\infty}$. If any of those is negative the respective curve is excluded.

Regarding the reservoir pressure $\widehat{p}_{\mathrm{res}}$ the main problem constitutes the existence of curves like those in figs. 4.5b and 4.9c. Using a query for marking all curves which obey

$$\mathrm{A}_p\big(\widehat{p}_{\mathrm{res}}|_{\mathcal{T}_0^{\mathrm{s}}}\big) > \eta\, \mathrm{A}_p\big(p|_{\mathcal{T}_0^{\mathrm{s}}}\big)$$

with an appropriate $\eta > 0$ all such unreasonable waveforms can be detected.

Lastly, the reservoir pressures $\widetilde{p}_{\mathrm{res}}$ need to be classified which constitute the most vague identification. However, it is aimed to mark the reservoir curves which are based on local minima and therefore do not match the measured pressure waveform closely during diastole. For this purpose the optional output parameter `resnorm` of the MATLAB-function `lsqnonlin` is used which returns the squared euclidian norm of the residual. For example, by considering the minimization (3.37), i.e.

$$\min_{\widetilde{\mathcal{R}},\widetilde{\mathcal{C}},\widetilde{P}_{\infty}} \|\widetilde{p}_{\mathrm{res}} - p\|_{\mathcal{T}_{\mathrm{s}}^N},$$

it holds with $I := \big\{i \in \mathbb{N}_0 \,:\, t_i \in \mathcal{T}_{\mathrm{s}}^N\big\}$ that

$$\texttt{resnorm}(\widetilde{p}_{\mathrm{res}}) = \sum_{i\in I} \big|\widetilde{p}_{\mathrm{res}}(t_i) - p(t_i)\big|^2.$$

In case that the error with respect to the amount of fitting points $\#I$ is greater than a specified tolerance $\mathrm{tol} > 0$, i.e.,

$$\frac{\texttt{resnorm}(\widetilde{p}_{\mathrm{res}})}{\#I} > \mathrm{tol},$$

the respective reservoir pressure curve is regarded as unreasonable. Therefore the computed reservoir pressure does not match the measured pressure decay during diastole within a specified tolerance.

In summary, the final decision whether a computed reservoir curve is accepted for further investigations the following criteria are applied:

	Brachial A.	Carotid A.	Both sites
$\widetilde{\boldsymbol{p}}_{\mathrm{res}}$	98	90	81
$\widehat{\boldsymbol{p}}_{\mathrm{res}}$	110	110	110
$\breve{\boldsymbol{p}}_{\mathrm{res}}$	91	101	89
$\widetilde{\boldsymbol{p}}_{\mathrm{res}} \cap \widehat{\boldsymbol{p}}_{\mathrm{res}}$	98	90	81
$\widetilde{\boldsymbol{p}}_{\mathrm{res}} \cap \breve{\boldsymbol{p}}_{\mathrm{res}}$	84	83	67
$\widehat{\boldsymbol{p}}_{\mathrm{res}} \cap \breve{\boldsymbol{p}}_{\mathrm{res}}$	91	101	89
$\widetilde{\boldsymbol{p}}_{\mathrm{res}} \cap \widehat{\boldsymbol{p}}_{\mathrm{res}} \cap \breve{\boldsymbol{p}}_{\mathrm{res}}$	84	83	67

Table 4.13: Sample sizes of regarded reservoir pressures of totally 110 data sets

- $\widetilde{\boldsymbol{p}}_{\mathrm{res}}$ **:** The reservoir pressure $\widetilde{p}_{\mathrm{res}}$ is regarded as implausible, when

$$\frac{\texttt{resnorm}(\widetilde{p}_{\mathrm{res}})}{\#I} > \mathrm{tol} \quad \text{with} \quad \mathrm{tol} := 20\,\mathrm{mmHg}^2.$$

- $\widehat{\boldsymbol{p}}_{\mathrm{res}}$ **:** In case that

$$\mathrm{A}_p\big(\widehat{p}_{\mathrm{res}}|_{\mathcal{T}_0^{\mathrm{s}}}\big) > \eta\,\mathrm{A}_p\big(p|_{\mathcal{T}_0^{\mathrm{s}}}\big) \quad \text{with} \quad \eta := 0.85$$

  the corresponding reservoir pressure waveform is considered as unreasonable.

- $\breve{\boldsymbol{p}}_{\mathrm{res}}$ **:** When any of the parameters $\breve{a}$, $\breve{b}$ and $\breve{P}_\infty$ is negative the respective reservoir pressure is not taken into consideration for further investigations.

Sample Sizes of Considered Reservoir Curves

Applying the stated criteria above the resulting sample sizes for further investigations are denoted in table 4.13.

Therefore, by regarding only accepted reservoir pressures $\widetilde{p}_{\mathrm{res}}$ related to the brachial artery, the sample consists of 98 waveforms which means that 12 brachial reservoir waveforms are considered as flawed. Similarly, one disposes of in total 90 carotid reservoir waveforms. In case that comparisons between brachial and carotid pressure waveforms are aimed the intersection of reasonable waveforms yield a sample of 81 data sets.

As opposed to that, all reservoir pressures $\widehat{p}_{\mathrm{res}}$ are considered as plausible. Thus, no jumps and other discontinuities in the neighbourhood of $\widehat{p}_{\mathrm{res}}(t_{\mathrm{s}})$ exist with the chosen parametrization of algorithm 3.2.

In total 91 $\breve{p}_{\mathrm{res}}$-waveforms based on brachial data are accepted. Consequently, 19 brachial waveforms correspond to negative parameters and subsequently are excluded from further considerations. Moreover, 101

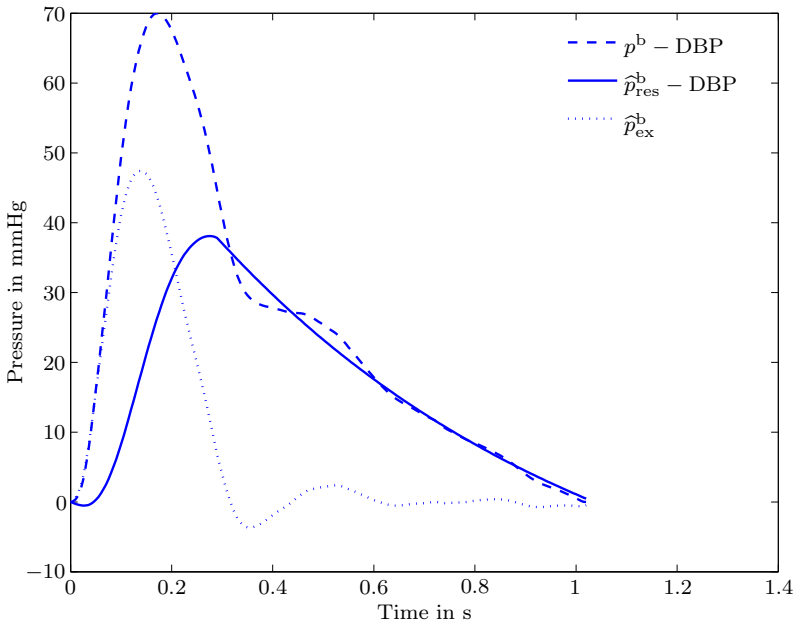

Figure 4.11: Pressure separation at brachial artery based on algorithm 3.2. The diastolic blood pressure DBP of this particular curve equals 76 mmHg

carotid reservoir curves are available yielding a sample size of totally 89 curves for comparisons between both sites.

The remaining rows of table 4.13 shall be understood such that for examinations with respect to various reservoir pressures the corresponding sample sizes are intersections of the involved pressure-related samples. For example, in case of considering all carotid reservoir pressures the corresponding sample consists of 83 waveforms.

4.4 Reservoir Theory applied on Peripheral Arteries

In this section the results of the Reservoir Theory applied on peripheral arteries are presented and discussed. Firstly, the pressure separation according to (3.1) is illustrated.

4.4.1 Pressure Separation

In fig. 4.11 both the reservoir pressure p_{res} and the excess pressure $p_{\mathrm{ex}} = p - p_{\mathrm{res}}$ is depicted for a brachial curve whereby the results are obtained

by application of the *extended* Reservoir Theory in the course of algorithm 3.2. Hence no flow velocity is considered and the assumptions (A1) and (A2) in combination with presuming spatially uniform reservoir pressures constitute the basis for performing the pressure separation at the artery. Basically this figure visualizes the main idea of the Reservoir Theory: The local pressure $p = p(x,t)$ is modelled as instantaneous sum of the time-dependent reservoir curve $p_{\text{res}} = p_{\text{res}}(t)$ and the time- and location dependent excess pressure $p_{\text{ex}} = p_{\text{ex}}(x,t) = p(x,t) - p_{\text{res}}(t)$. Thus, the reservoir pressure refers to the compliance related behaviour of the main arteries and the excess pressure is associated with the wave-related local phenomena. Nevertheless, an absolute separation of both main contributors to the actual (measured) pressure waveform seems virtually impossible. Indeed, since the reservoir pressure also drives the pressure, at least in diastole, the reservoir part needs to accommodate wave phenomena too.

However, by definition, the excess pressure is set to zero at the beginning of systole since wave phenomena are expected to be negligible at the end of diastole. Therefore the reservoir pressure corresponds to the magnitude of the measured pressure at this time. In fig. 4.11 the pressure above DBP is plotted on the ordinate axis which infers that both pressure components start at the zero level in this graph. It can be witnessed that the excess pressure is closely aligned to the measured pressure waveform during early systole whereas the reservoir pressure fits in late diastole. The underlying concept of the extended Reservoir Theory now implies that the excess pressure corresponds to the flow rate at the ascending aorta [1]. Since no simultaneously measured aortic pressure waveform is available this assumption (A2) cannot be verified. Nonetheless, (A1) and its assumed similar waveform decay of the measure pressure at different locations in the arterial system during diastole *can* be investigated. In total, 110 waveforms at both the brachial and carotid artery are available in order to fulfil this task. However, depending on the chosen algorithm not all of them are considered for this analysis.

4.4.2 Reservoir Pressure Waveforms

In the following two different sets of brachial and carotid curves and their corresponding reservoir pressures are discussed. A focus is put on the fact, that the majority of pressure sets do not exhibit the same beat duration, cf fig. 4.3.

In figs. 4.12 and 4.13 two pairs of measured pressure waveforms are depicted. For this discussion again algorithm 3.2 was used to generate the corresponding reservoir pressures. It is emphasized that for this par-

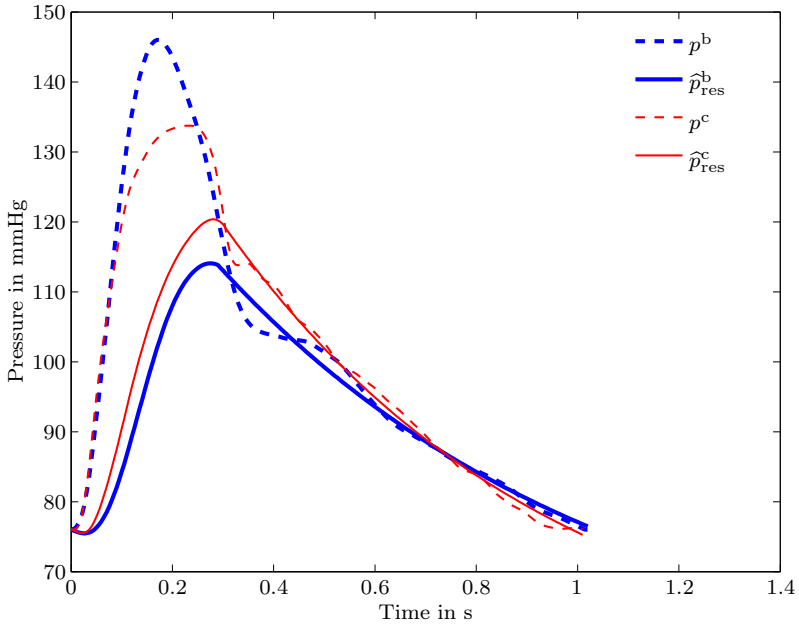

Figure 4.12: Reservoir pressure $\widehat{p}_{\mathrm{res}}$ at both arteries. Beat duration of measured brachial curve is slightly longer with $\Delta T_{\mathrm{b}} = 0.01\,\mathrm{s}$

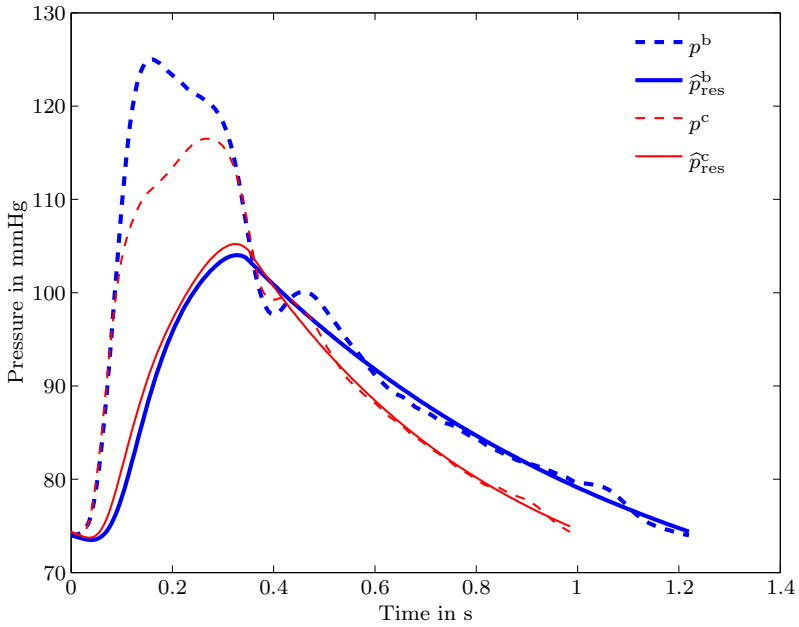

Figure 4.13: Reservoir pressure $\widehat{p}_{\mathrm{res}}$ at both arteries. Beat duration of measured brachial curve is considerably longer with $\Delta T_{\mathrm{b}} = 0.235\,\mathrm{s}$

ticular selection of waveforms the deviation of beat duration between the brachial and carotid waveform were the determining characteristic. Fig. 4.12 depicts the waveform with the shortest and fig. 4.13 with the greatest difference in the beat duration between brachial and carotid curve of all available data sets. It has already pointed out that the periodization methods have altered the beat duration of numerous curves. However, due to the fact that mostly (P3) was used, the influence of data preprocessing on the resulting beat duration as a whole has been considered as negligible, cf. section 4.2.1. Furthermore, the carotid pressure scaling during (DP3) inferred that both the brachial and carotid pressure waveforms exhibit the same mean pressure according to (3.28) and (3.29), which can also be observed in the figs. 4.12 and 4.13. Since these depicted waveforms constitute the most extreme representatives, cf. fig. 4.3b, they sketch a realistic situation of how the different beat durations can affect the reservoir pressure decay. Referring to fig. 4.12 it can be witnessed that even though the beat duration is almost identical, and therefore constitute an almost optimal example of a measured set, the reservoir pressures of the brachial and carotid artery may exhibit different waveforms. In other words: It cannot be taken for granted that brachial and carotid reservoir pressures are perfectly aligned to each other. In order to quantify whether measured pressure waveforms at the distinct locations of brachial and carotid artery have a "similar pressure decay" during diastole, the obtained parameters through the algorithms will be used. In this case, especially the time constant

$$\tau = R\,C = \mathcal{R}\,\mathcal{C} = \frac{1}{b} \tag{4.6}$$

is of major interest which can be evaluated by the (approximated) net area parameters $\mathcal{R}$, $\mathcal{C}$ and the rate constants a, b obtained by the algorithms. A particular focus is put on this issue in section 4.5.4.

In fig. 4.14 the results of all algorithms 3.1 to 3.3 applied to the curves in figs. 4.12 and 4.13 are illustrated. By comparing the results of $\widetilde{p}_{\mathrm{res}}$ in figs. 4.14a and 4.14b with $\widehat{p}_{\mathrm{res}}$ and $\breve{p}_{\mathrm{res}}$ in figs. 4.14c to 4.14f the discrepancies in their respective reservoir pressures become visible. However, the reservoir pressures $\widehat{p}_{\mathrm{res}}$ and $\breve{p}_{\mathrm{res}}$ seems to be quite comparable. Thus, both algorithms based on the same concept of the extended Reservoir Theory, produce similar results in this example whereas the one using the flow generates slightly distinct reservoir waveforms.

A direct comparison of the respective reservoir pressures is provided in fig. 4.15 for both the brachial and carotid artery associated with the pressure set with the difference of $\Delta T_{\mathrm{b}} = 0.01\,\mathrm{s}$ in their beat duration. Therefore, this closer examination reveals that $\widetilde{p}_{\mathrm{res}}$ is throughout higher than the others from the start of systole until the pressures begin to

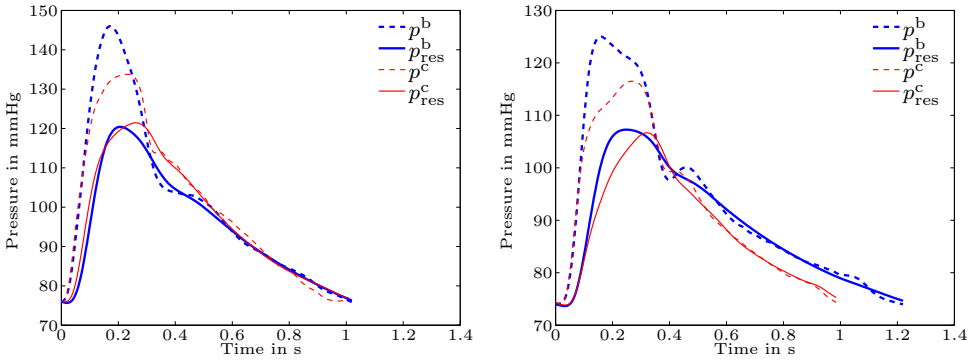

(a) $\widetilde{p}_{\mathrm{res}}$, $\Delta T_{\mathrm{b}} = 0.01\,\mathrm{s}$ (b) $\widetilde{p}_{\mathrm{res}}$, $\Delta T_{\mathrm{b}} = 0.235\,\mathrm{s}$

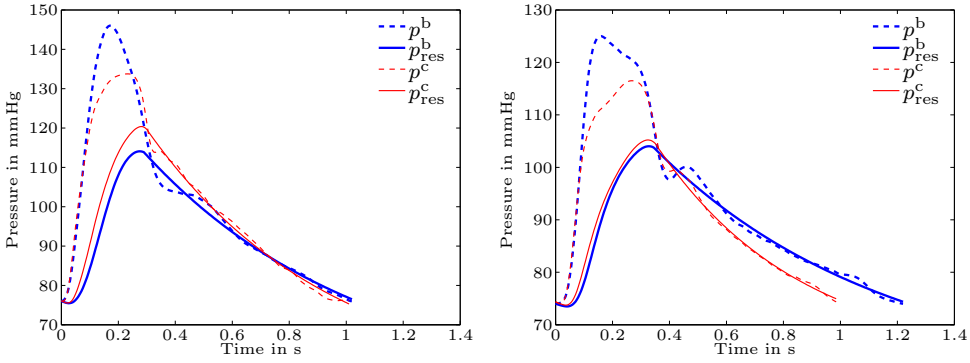

(c) $\widehat{p}_{\mathrm{res}}$, $\Delta T_{\mathrm{b}} = 0.01\,\mathrm{s}$ (d) $\widehat{p}_{\mathrm{res}}$, $\Delta T_{\mathrm{b}} = 0.235\,\mathrm{s}$

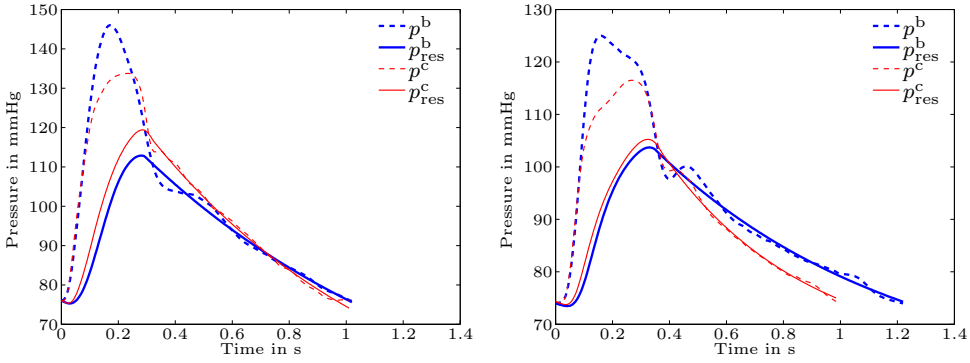

(e) $\breve{p}_{\mathrm{res}}$, $\Delta T_{\mathrm{b}} = 0.01\,\mathrm{s}$ (f) $\breve{p}_{\mathrm{res}}$, $\Delta T_{\mathrm{b}} = 0.235\,\mathrm{s}$

Figure 4.14: Comparison of reservoir pressures of all algorithms at both arteries for data sets with different deviations in their beat duration.

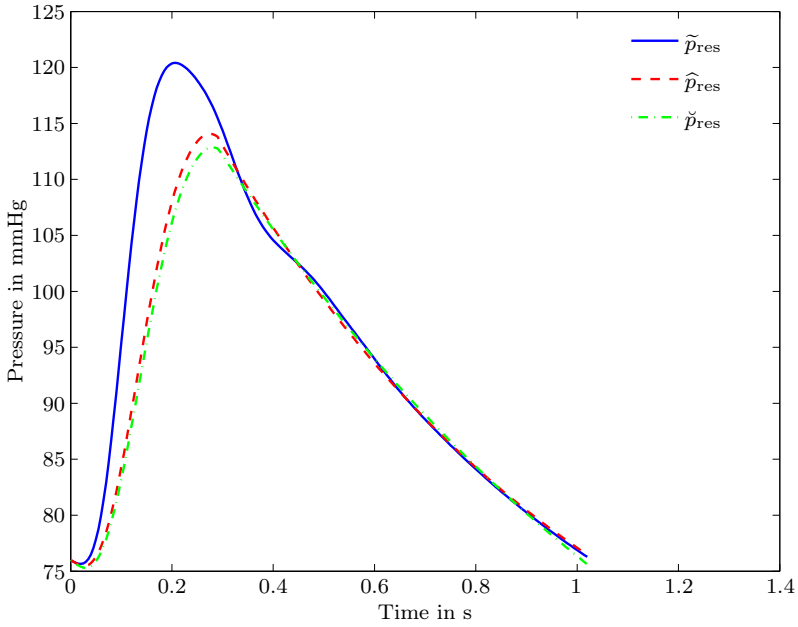

(a) Brachial Artery

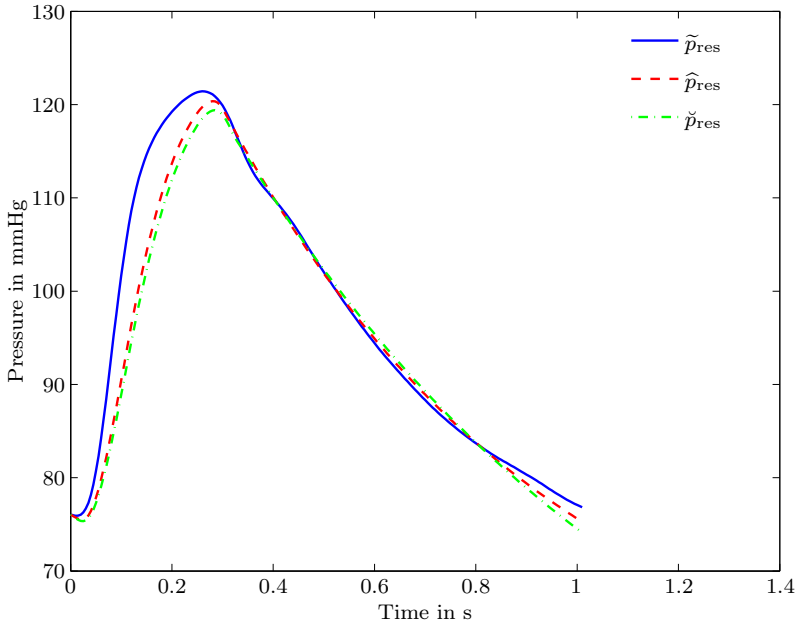

(b) Carotid Artery

Figure 4.15: Reservoir pressures of all algorithms at both arteries. Regarded set of measured pressure curves exhibits difference $\Delta T_{\mathrm{b}} = 0.01\,\mathrm{s}$

drop. At some point all waveforms merge together and provide a similar decreasing behaviour. Nonetheless, whilst the reservoir pressure $\widetilde{p}^{\mathrm{b}}_{\mathrm{res}}$ of the brachial curve suggests an exponential decay, the pressure $\widetilde{p}^{\mathrm{c}}_{\mathrm{res}}$ related to the carotid one slightly oscillates around the others. This issue is investigated in the following section.

4.4.3 Pressure Separation and Flow Velocity

In section 3.4.1 it was pointed out with (3.35) that in the case of a steady flow beyond a specific time the corresponding reservoir pressure also exhibits an exponential decay from this time point onwards. Fig. 4.16 illustrates the situation: By starting with the brachial curve in the upper panel it can be observed that the flow velocity diminishes within diastole and remains almost zero. Since it is common to regard the last two-thirds of diastole as the period of time when waves are believed to be minimal [1, 3, 31], its initial time is marked with $t_{1/3\mathrm{D}}$. As stated in the previous section 4.3.2, it does not constitute a proper start for the reservoir curve fitting to the measured pressure, but it possibly indicates the beginning when flow levels off. Indeed, the flow velocity (green dash-dotted line) not only remains almost steady but also corresponds to approximately zero during $\mathcal{T}^N_{1/3\mathrm{D}}$ with the magnitude of $(0.07 \pm 0.23)\,\mathrm{cm/s}$. As a consequence, (3.35) roughly simplifies to (3.15) indicating the same exponential behaviour compared to the pressures $\widehat{p}_{\mathrm{res}}$ and $\breve{p}_{\mathrm{res}}$ which *rely on* this equation during diastole. However, by comparing the excess pressure (red dotted line) with the flow velocity some discrepancies in their respective waveform are observable which remain persistent even when bearing in mind their different scales. For example, the minimum and maximum of the excess pressure are hit later than those of the flow velocity. Since the *extended* Reservoir Theory, and therefore the algorithms 3.2 and 3.3, assume a proportionality $u \sim p_{\mathrm{ex}}$ by (A2) the differences in systole of the respective reservoir pressures in fig. 4.15a can be explained[8]. More precisely, *if* the computed excess pressure is proportionally equal to the flow velocity, all algorithms should generate very similar results.

By recycling the stated arguments above and applying them to the carotid curve the situation depicted in fig. 4.16b can be described as follows: The flow within $\mathcal{T}^N_{1/3\mathrm{D}}$ is characterized by $(6.37 \pm 0.75)\,\mathrm{cm/s}$ indicating an approximately constant level as well. However, the standard deviation is about three times higher as opposed to the brachial one which consequently could cause the slight oscillations of $\widetilde{p}_{\mathrm{res}}$ in fig. 4.15b.

[8] In fact, in this case (A2) needs to be extended such that *flows in any arterial location with similar waveforms to the aortic flow* are approximately proportional to the excess pressure.

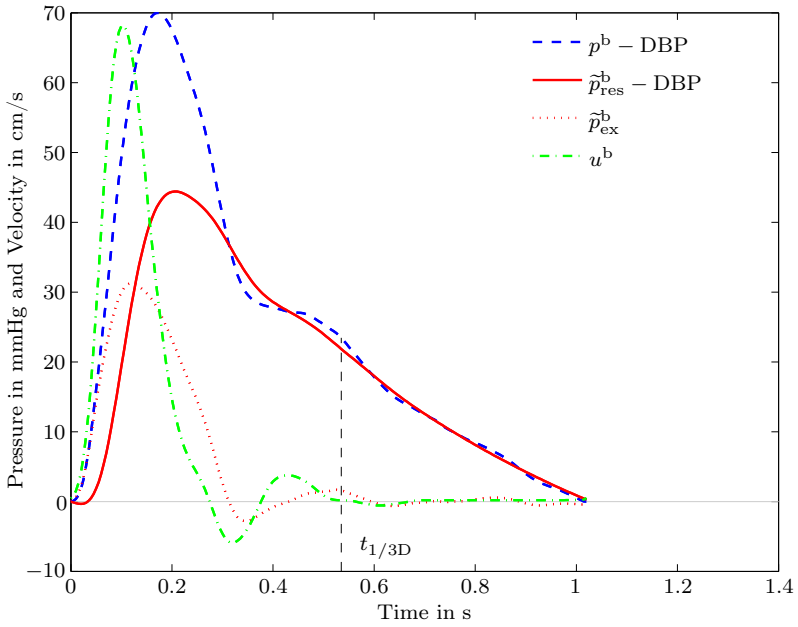

(a) Brachial Artery, DBP = 76 mmHg, $u|_{\mathcal{T}^N_{1/3\mathrm{D}}} = (0.07 \pm 0.23)\,\mathrm{cm/s}$

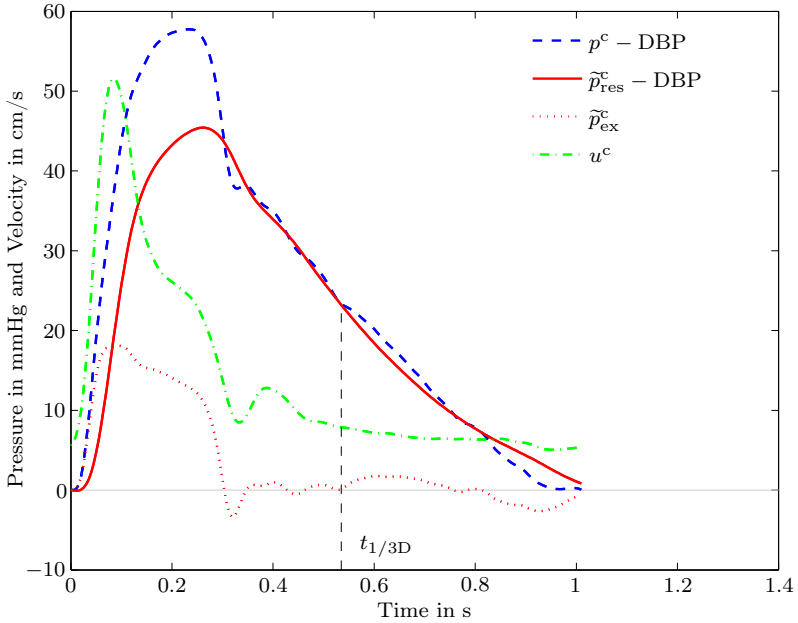

(b) Carotid Artery, DBP = 76 mmHg, $u|_{\mathcal{T}^N_{1/3\mathrm{D}}} = (6.37 \pm 0.75)\,\mathrm{cm/s}$

Figure 4.16: Flow velocity and reservoir pressure $\widetilde{p}_{\mathrm{res}}$ for both arteries. Regarded set of measured curves exhibits difference in beat duration of $\Delta T_{\mathrm{b}} = 0.01\,\mathrm{s}$

On the one hand, the velocity is always greater than zero and thus can never be scaled with a proportionality factor in order to obtain the excess pressure. On the other hand, their respective minima and maxima almost occur exactly at the same time. Consequently, by considering the velocity u as a sum of a waveform v shifted by a constant v_0, i.e.

$$u = v_0 + v \tag{4.7}$$

such that it holds $\mu_{u|_{\mathcal{T}^N_{1/3\mathrm{D}}}} = v_0$ for the mean of the flow velocity u over $\mathcal{T}^N_{1/3\mathrm{D}}$, the reservoir pressure (3.34) reads

$$\begin{aligned} p_{\mathrm{res}}(t) &= \frac{e^{-t/(\mathcal{R}\,\mathcal{C})}}{\mathcal{C}} \int_0^t \big(v_0 + v(s)\big)\, e^{s/(\mathcal{R}\,\mathcal{C})}\, ds \\ &\quad + \big(p_{\mathrm{res}}(0) - P_\infty\big)\, e^{-t/(\mathcal{R}\,\mathcal{C})} + P_\infty \\ &= v_0\, \mathcal{R}\, e^{-t/(\mathcal{R}\,\mathcal{C})}\Big(e^{t/(\mathcal{R}\,\mathcal{C})} - 1\Big) + \frac{e^{-t/(\mathcal{R}\,\mathcal{C})}}{\mathcal{C}} \int_0^t v(s)\, e^{s/(\mathcal{R}\,\mathcal{C})}\, ds \\ &\quad + \big(p_{\mathrm{res}}(0) - P_\infty\big)\, e^{-t/(\mathcal{R}\,\mathcal{C})} + P_\infty \end{aligned}$$

and subsequently

$$\begin{aligned} p_{\mathrm{res}}(t) = \frac{e^{-t/(\mathcal{R}\,\mathcal{C})}}{\mathcal{C}} &\int_0^t v(s)\, e^{s/(\mathcal{R}\,\mathcal{C})}\, ds \\ &+ \big(p_{\mathrm{res}}(0) - (v_0\,\mathcal{R} + P_\infty)\big)\, e^{-t/(\mathcal{R}\,\mathcal{C})} + (v_0\,\mathcal{R} + P_\infty). \end{aligned} \tag{4.8}$$

Hence, the right-hand sides of (3.34) and (4.8) correspond to each other by setting $v_0\,\mathcal{R} + P_\infty$ as the new (mathematical) asymptotic pressure in (4.8). Moreover, since (3.34) can be transformed to (3.14) by using the original net parameters of R and C and simply "do all steps backwards" in section 3.2.1, the *new* assumption of having

$$p_{\mathrm{ex}} \sim v \tag{4.9}$$

infers the theoretical solution of the reservoir pressure of the *extended* Reservoir Theory to be

$$\begin{aligned} p_{\mathrm{res}}(t) = e^{-(a+b)\,t}\Bigg(p_{\mathrm{res}}(0) - \frac{b}{a+b}\,(v_0\,\mathcal{R} + P_\infty) \\ + a \int_0^t p(s)\, e^{(a+b)\,s}\, ds\Bigg) + \frac{b}{a+b}\,(v_0\,\mathcal{R} + P_\infty). \end{aligned} \tag{4.10}$$

This equation is structurally identical to (3.20) and only differs in the definition of the asymptotic pressure. Therefore, one concludes the following: The theoretical solutions of the two different reservoir pressures sought by the three different algorithms during systole are, in case of (4.9), quite similar[9]. In other words, if it holds that $p_{\text{ex}} \sim v$ the asymptotic pressure $\widetilde{P}_\infty$ obtained by algorithm 3.1 might be regarded as the (mathematical) asymptotic pressures gained by the algorithms 3.2 or 3.3 reduced by $v_0\,\widetilde{\mathcal{R}}$, i.e. $\widetilde{P}_\infty \approx \widehat{P}_\infty - v_0\widetilde{\mathcal{R}}$ or $\widetilde{P}_\infty \approx \breve{P}_\infty - v_0\widetilde{\mathcal{R}}$ respectively. As a consequence the better alignment of all reservoir pressures during systole compared to the brachial counterpart as shown in the figs. 4.15a and 4.15b could be explained.

Based on this observation the assumption (A2) might be refined for the *extended* Reservoir Theory in the following way:

($\widetilde{\text{A2}}$) *The flow at the regarded arterial location is, up to a constant offset, approximately proportional to* the excess pressure at *the same site, which itself* is approximately proportional to the flow in the aortic root.

At the first glance this might not seem like an improvement, but it states that *if* the excess pressure is approximately proportional to the aortic flow[10] u_{in}, i.e.

$$p_{\text{ex}} = c_1\, u_{\text{in}}$$

with $c_1 \in \mathbb{R}$, *and* the flow u at the respective artery is, up to a constant offset, proportional to the excess pressure p_{ex}, i.e.

$$p_{\text{ex}} = c_2\, u + c_0$$

with $c_0,\ c_2 \in \mathbb{R}$, both (4.7) and (4.9) are fulfilled after parameter substitution and (A2) holds as well. More precisely, the procedure of computing the excess pressure remains the same as before[11] but ($\widetilde{\text{A2}}$) helps to characterize the situation in which the *extended* concept is applicable at this particular arterial location. Moreover, *if* ($\widetilde{\text{A2}}$) is fulfilled, both methods, and therefore all algorithms, should theoretically yield the same reservoir pressure at the respective arterial location[12]. Apart from that, ($\widetilde{\text{A2}}$)

[9] It is remembered, that algorithm 3.2 only describes the systolic part of the reservoir pressure through (3.20). During diastole an exponential pressure decay is assumed.

[10] In this context the flow is considered as the flow *velocity* u. Nonetheless, the same arguments are applicable in case of regarding the flow *rate* q.

[11] That means: Assume $q_{\text{in}} \sim p_{\text{ex}}$ and compute the reservoir pressure due to (A1).

[12] In case of using the mathematical solution of p_{res} for the extended Reservoir Theory implementations. Since an exponential decay is assumed the results might only be "similar".

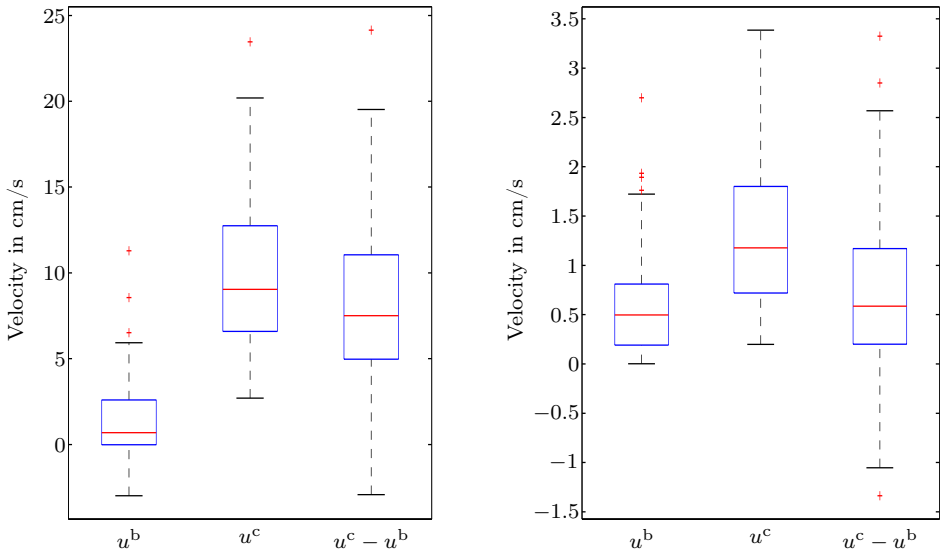

(a) Mean $\mu_{u|_{\mathcal{T}^N_{1/3\mathrm{D}}}}$ of flow velocities

(b) Standard deviation $\sigma_{u|_{\mathcal{T}^N_{1/3\mathrm{D}}}}$ of flow velocities

Figure 4.17: Mean and standard deviation of flow velocities in the last two-thirds of diastole broken down for samples of 110 brachial and carotid flow velocity-curves

		Brachial Artery	**Carotid Artery**	**Diff. (C-B)**
$\boldsymbol{\mu_{u}}_{\boldsymbol{\mathcal{T}^N_{1/3\mathrm{D}}}}$	(cm/s)	1.51 ± 2.31	9.87 ± 4.30	8.36 ± 5.00
$\boldsymbol{\sigma_{u}}_{\boldsymbol{\mathcal{T}^N_{1/3\mathrm{D}}}}$	(cm/s)	0.58 ± 0.49	1.28 ± 0.72	0.71 ± 0.83

Table 4.14: Mean $\mu_{u|_{\mathcal{T}^N_{1/3\mathrm{D}}}}$ and standard deviation $\sigma_{u|_{\mathcal{T}^N_{1/3\mathrm{D}}}}$ in the last two-thirds of diastole of all 110 brachial and carotid flow velocities

is a real generalization of (A2) since (A2) is based on the assumption $u = u_{\mathrm{in}} \sim p_{\mathrm{ex}}$ and therefore would be applicable as well by setting $c_0 = 0$ in $(\widetilde{\mathrm{A2}})$. However, since the flow at the aortic root is not available, $(\widetilde{\mathrm{A2}})$ cannot be verified for the respective data sets. Nonetheless, the flow velocities shall be investigated more detailed in order to discuss their impact on $\widetilde{p}_{\mathrm{res}}$.

With respect to distribution of the mean flow rates $\mu_{u|_{\mathcal{T}^N_{1/3\mathrm{D}}}}$ during the last two-thirds of diastole $\mathcal{T}^N_{1/3\mathrm{D}}$ in fig. 4.17a, it can be witnessed that the carotid flow velocity is generally higher compared to those at the brachial artery. In fact, the mean of the carotid flow velocities during this phase corresponds to almost 10 cm/s which is more than 5 times higher than the brachial ones, cf. table 4.14. The last column of table 4.14 states the

mean and standard deviation of the difference $\mu_{u^c}|_{\mathcal{T}^N_{1/3D}} - \mu_{u^b}|_{\mathcal{T}^N_{1/3D}}$ of each pair of velocity curves whose distribution is also depicted in the third box plot of fig. 4.17a. Referring to fig. 4.17b, it can be witnessed that brachial velocities remain quite stable and fluctuate less around their mean as opposed to the carotid counterparts.

Thus, the ansatz of regarding the data sets of pressure and flow as an approximation to those of the ascending aorta can, at most, be justified for brachial curves. This is simply concluded from the fact that the flow at the ascending aorta is approximately zero during diastole since the aortic valve is shut.

Interpretation of the reservoir concept based on the flow velocity

By taking into account all the stated findings above, the *classic* Reservoir Theory, i.e. the concept based on the flow velocity, can be interpreted in various ways.

Regarding the brachial artery the following interpretations, depending on the actual flow waveforms, might be possible:

- The brachial flow is approximately proportional to the flow at the ascending aorta: The Reservoir Theory applied at the brachial artery might be regarded as the *classic* concept and theoretically yields the same reservoir pressure results as the approach based on (A1) and (A2). (Apparently, in case that the brachial flow is only up to a constant offset proportional to the flow at the aortic root the same can be stated due to $(\widetilde{\text{A2}})$.)

- The brachial flows are not proportional to those at the ascending aorta: The pressure separation according to Reservoir Theory might rather be considered as one according to a local lumped parameter model.

With respect to the carotid curves, it holds similarly:

- The carotid flow is, up to a constant offset, approximately proportional to that at the ascending aorta: The classic reservoir concept is according to $(\widetilde{\text{A2}})$ comparable to the *extended* concept which is based on (A1) and (A2). Therefore both methods should theoretically generate similar results[13].

[13] To illustrate the situation, an exemplary carotid curve is regarded: With the figures $\widetilde{P}_\infty = 58.80\,\text{mmHg}$, $\widetilde{\mathcal{R}} = 167.80\,\text{mmHg}\,\text{s/m}$ of algorithm 3.1 and

- The carotid flow is not, up to a constant offset, approximately proportional to that at the ascending aorta: Like in the brachial case it holds that the pressure separation according to Reservoir Theory might rather be considered as one according to a local lumped parameter model.

Therefore, the interpretation of the *classic* Reservoir Theory markedly depends on the actual flow waveform. In general, it might be assumed that the respective flows are not "similar" to the ventricular flow. Hence, the classic concept at both arterial locations might commonly be regarded as a local lumped parameter model as illustrated in fig. 2.10b where in addition to the pressure p as well the flow q (or u) into the system through the characteristic impedance Z_c is already given.

Overall and bearing in mind the stated points above, it can be said that the application of the Reservoir Theory with flow depends crucially on the relation between pressure and flow curves. In fact, already slight inaccuracies, in the sense that the pressure and flow measurements are not perfectly matched to each other, might yield substantially different reservoir waveforms. From this point of view, the application of the extended Reservoir Theory might be more advantageous. However, a closer comparison of the two different concepts based on the results of the three algorithms 3.1 to 3.3 is done within the following sections.

4.4.4 Peripheral Reservoir Pressure Results: Overview

In this section an overview of the peripheral reservoir pressures of all algorithms is given for both the brachial and carotid data. It shall be understood as a rough comparison of all parameters associated with the the respective reservoir pressure waveforms. A more detailed investigation is then provided for both locations consecutively in the subsequent sections 4.4.5 and 4.4.6.

The tables 4.15 and 4.16 show all computed parameters of both Reservoir Theory approaches implemented by the three algorithms 3.1 to 3.3 for both arterial locations. Therefore the last two columns of each table correspond to the results of the extended Reservoir Theory which does

$v = (9.42 \pm 0.61)\,\mathrm{cm/s}$ it holds that

$$\widetilde{P}_\infty + v_0\,\widetilde{\mathcal{R}} = 58.80\,\mathrm{mmHg} + 15.81\,\mathrm{mmHg} = 74.61\,\mathrm{mmHg}$$

might be an approximation for the computed asymptotic pressures of the algorithms 3.2 or 3.3. However, the respective asymptotic pressures read $\widehat{P}_\infty = 62.97\,\mathrm{mmHg}$ and $\breve{P}_\infty = 62.48\,\mathrm{mmHg}$ in this case. Still it holds $\widetilde{P}_\infty < \widehat{P}_\infty$ and $\widetilde{P}_\infty < \breve{P}_\infty$ notably.

Brachial Artery	$\widetilde{\boldsymbol{p}}_{\text{res}}$	$\widehat{\boldsymbol{p}}_{\text{res}}$	$\breve{\boldsymbol{p}}_{\text{res}}$
PP (mmHg)	40.89 ± 7.86	36.87 ± 7.27	36.49 ± 7.27
$\mathbf{A}_{\boldsymbol{p}}$ (mmHg s)	17.90 ± 4.12	16.41 ± 3.95	16.31 ± 3.93
$\boldsymbol{\tau}$ (s)	0.47 ± 0.15	0.58 ± 0.17	0.66 ± 0.30
$\boldsymbol{P}_{\boldsymbol{\infty}}$ (mmHg)	63.77 ± 9.27	63.89 ± 8.65	59.48 ± 15.32
$\boldsymbol{a}$ (1/s)	——	8.44 ± 3.91	8.17 ± 3.48
$\boldsymbol{b}$ (1/s)	——	1.91 ± 0.63	1.78 ± 0.65
$\boldsymbol{\mathcal{R}}$ (mmHg s/m)	423.94 ± 193.45	416.79 ± 222.89	465.91 ± 280.60
$\boldsymbol{\mathcal{C}}$ (m/mmHg)	$(1.27 \pm 0.52) \times 10^{-3}$	$(1.70 \pm 0.84) \times 10^{-3}$	$(1.73 \pm 0.86) \times 10^{-3}$

Table 4.15: Brachial Artery – Parameters of all reservoir pressures based on the sample of 84 curves

Carotid Artery	$\widetilde{\boldsymbol{p}}_{\text{res}}$	$\widehat{\boldsymbol{p}}_{\text{res}}$	$\breve{\boldsymbol{p}}_{\text{res}}$
PP (mmHg)	42.17 ± 8.97	41.48 ± 8.74	40.81 ± 8.52
$\mathbf{A}_{\boldsymbol{p}}$ (mmHg s)	19.51 ± 4.98	18.71 ± 4.68	18.50 ± 4.54
$\boldsymbol{\tau}$ (s)	0.22 ± 0.07	0.48 ± 0.15	0.54 ± 0.22
$\boldsymbol{P}_{\boldsymbol{\infty}}$ (mmHg)	60.52 ± 8.27	67.48 ± 9.62	64.84 ± 12.84
$\boldsymbol{a}$ (1/s)	——	11.72 ± 2.81	11.16 ± 2.91
$\boldsymbol{b}$ (1/s)	——	2.27 ± 0.75	2.17 ± 0.91
$\boldsymbol{\mathcal{R}}$ (mmHg s/m)	224.19 ± 82.37	180.27 ± 77.08	195.30 ± 95.07
$\boldsymbol{\mathcal{C}}$ (m/mmHg)	$(1.04 \pm 0.40) \times 10^{-3}$	$(3.07 \pm 1.40) \times 10^{-3}$	$(3.11 \pm 1.40) \times 10^{-3}$

Table 4.16: Carotid Artery – Parameters of all reservoir pressures based on the sample of 83 curves

not use the flow velocities. In contrast, the first columns are related to classic theory at both arteries incorporating the respective arterial flows[14]. All results are stated in terms of means and standard deviations whereby the sample sizes for the comparisons consisted of 84 brachial and 83 carotid curves respectively, cf. table 4.13. In addition to the direct output parameters of the algorithms as well the pulse pressure PP and the area A_p of to the respective reservoir pressure above DBP were computed. Moreover, the time constants τ, as stated in (4.6), were determined by using either the net area parameters $\widetilde{\mathcal{R}}$, $\widetilde{\mathcal{C}}$ or the rate constants $\widehat{b}$, $\breve{b}$, depending on the type of algorithm. Furthermore, $\widehat{\mathcal{R}}$, $\breve{\mathcal{R}}$, $\widehat{\mathcal{C}}$, $\breve{\mathcal{C}}$ were approximated by means of (3.58) since they are not direct output results of the algorithms 3.2 and 3.3. As a consequence the figures of the first four rows indicate the values which can be inferred by all algorithms directly, whereas the remaining four are either not available for all algorithms or are obtained by further assumptions.

Referring to the brachial data, it can be observed that all parameters are of the same order of magnitude. In fact, table 4.15 suggests very similar results of algorithm 3.2 and 3.3. In particular, the pulse pressure PP and the area A_p related to $\widehat{p}_{\text{res}}$ and $\breve{p}_{\text{res}}$ are very close to each other for both the mean and the standard deviation whereas those related to $\widetilde{p}_{\text{res}}$ have, on average, higher figures. The rate constants of algorithms 3.2 and 3.3 exhibit similar values as well.

With reference to table 4.16, which is related to the carotid reservoir waveforms, it can be stated that the mean PP and A_p agree closely among all algorithms whereas the mean time constant of $\widetilde{p}_{\text{res}}$ differs considerably from the others'. The mean asymptotic pressures vary throughout all algorithms whereas the rate constants of the algorithms 3.2 and 3.3 agree quite well.

Nonetheless, it has to be stated that at both arterial locations, especially with respect to the asymptotic pressures, many results of the two algorithms 3.1 and 3.2 might be affected by the particular choice of P_∞ to be within the range $0.7 \min_{\mathcal{T}_0^N}(p) \leq P_\infty \leq \min_{\mathcal{T}_0^N}(p)$. In fact numerous computed asymptotic pressures of $\widetilde{P}_\infty$ and $\widehat{P}_\infty$ are situated close to the lower bound indicating that the algorithm might seek to decrease further the respective pressures.

In table 4.17 the amount of asymptotic pressures located within an absolute distance of 1 mmHg to the lower bound of $0.7 \min_{\mathcal{T}_0^N}(p)$ are shown, whereby only the samples according to table 4.13 have been considered. E.g., 37 out of 98 pressures $\widetilde{P}_\infty$ might be affected based on the brachial sample of $\widetilde{p}_{\text{res}}$- and 42 based on the brachial and carotid sample

[14]The different model approaches are described in section 3.2 and summarized in section 3.2.3.

P_∞	**Brachial A.**	**Carotid A.**	**Both sites**
$\widetilde{\boldsymbol{p}}_{\mathrm{res}}$	37	39	49
$\widehat{\boldsymbol{p}}_{\mathrm{res}}$	42	19	46
$\breve{\boldsymbol{p}}_{\mathrm{res}}$	0	0	0
$\widetilde{\boldsymbol{p}}_{\mathrm{res}} \cap \widehat{\boldsymbol{p}}_{\mathrm{res}}$	42	42	50
$\widetilde{\boldsymbol{p}}_{\mathrm{res}} \cap \breve{\boldsymbol{p}}_{\mathrm{res}}$	23	33	35
$\widehat{\boldsymbol{p}}_{\mathrm{res}} \cap \breve{\boldsymbol{p}}_{\mathrm{res}}$	23	10	25
$\widetilde{\boldsymbol{p}}_{\mathrm{res}} \cap \widehat{\boldsymbol{p}}_{\mathrm{res}} \cap \breve{\boldsymbol{p}}_{\mathrm{res}}$	28	35	36

Table 4.17: Amount of possibly affected waveforms within regarded curves, cf. table 4.13

of $\widetilde{p}_{\mathrm{res}} \cap \widehat{p}_{\mathrm{res}}$-curves since either algorithm 3.1 or 3.2 generated a result of the asymptotic pressure close to the lower border. In further consequence, other parameters computed within the same minimization step are likely to have compensated this possibly restriction in order to get an aligned reservoir waveform to the measured one during diastole. In case of algorithm 3.1 that are $\widetilde{\mathcal{R}}, \widetilde{\mathcal{C}}$ according to (3.37). With respect to algorithm 3.2 it is $\widehat{b} = 1/\widehat{\tau}$, cf. (3.40). Therefore, this has to be kept in mind during all considerations associated with the results of the algorithms 3.1 and 3.2.

However, for a closer examination of all algorithms and their parameters a different form of representation is needed. Hence, scatter and Bland-Altman plots are provided for both locations in the following sections so as to compare every method and its associated results more profoundly. The plots with respect to the brachial data are shown in figs. 4.18 to 4.24 and those related to the carotid one are given in figs. 4.25 to 4.31. For each plot, the maximal available amount of samples according to table 4.13 was considered. Every scatter plot contains, in addition to the actual data, its fitted regression line. Moreover, the correlation coefficient r of the respective variables is stated above each scatter plot. In the Bland-Altman plots the mean μ (green solid lines) and $\mu \pm 1.96\,\sigma$ (green dashed-lines) with standard deviation σ of the differences are displayed which indicate the 95 % limits of agreement in case of an assumed normal distribution.

4.4.5 Brachial Reservoir Pressure

Referring to fig. 4.18 it can be observed that $\widetilde{\mathrm{PP}}$ is systematically higher than $\widehat{\mathrm{PP}}$ and $\breve{\mathrm{PP}}$ with a bias of about $\mu = 4\,\mathrm{mmHg}$. Furthermore, the fluctuations indicated by the 95 % limits of agreement are very similar too, cf. figs. 4.18b and 4.18d. Nevertheless, both scatter plots exhibit a high correlation coefficient. With respect to lowest panel it can be

witnessed that the correspondence of $\widehat{\mathrm{PP}}$ and $\breve{\mathrm{P}}\mathrm{P}$ is even better with a correlation coefficient of 0.99. Moreover their mean difference and standard deviation are approximately zero indicating a pretty good alignment. The very same applies by regarding the areas of the reservoir pressures A_p in fig. 4.19. The most striking difference in this figure of areas compared to the one of the pulse pressures is the possible outlier in fig. 4.19e. Nonetheless, since both algorithms state a similar value the results fit as well for this particular curve. Referring to fig. 4.19f the differences are very small anyway.

By considering the time constants in fig. 4.20 one can observe that the results scatter more drastically compared to PP and A_p, especially when $\widetilde{\tau}$ is involved which is also indicated by the low correlation coefficients of 0.55 and 0.41 respectively. However, whilst the values in fig. 4.20b suggest a random scattering around a negative bias, fig. 4.20d indicates that the lower the figures of τ are the better the alignment seems to be. Again, the output parameters of algorithms 3.2 and 3.3 are better in agreement even though some single values of $\breve{\tau}$ are approximately twice as high as the corresponding $\widehat{\tau}$. The clustering of the majority of points around the mean in fig. 4.20f and the smaller σ confirms this superior alignment. Nonetheless, in this comparison the lower bound for $\widetilde{P}_\infty$ and $\widehat{P}_\infty$ could have affected the corresponding time constants $\widetilde{\tau}$ and $\widehat{\tau}$, cf. table 4.17. This "artificial" restriction might also be observable by comparing them to the values of $\breve{\tau}$ which exhibit values within a broader range, cf. figs. 4.20c and 4.20e. However, it is remarkable that $\widehat{\tau}$ and $\breve{\tau}$ still coincide quite well. Their mean difference is rather small ($\mu = -0.08\,\mathrm{s}$) and their correlation coefficient is still high. Generally, the alignment is better in lower figures. This indicates that, at least for lower time constants, the impact of the minimization bound on 23 out of 91 samples does not influence the results of $\widehat{\tau}$ substantially in the comparison of figs. 4.20e and 4.20f. This is still reasonable since curves with a flat pressure decay might not be described with a parameter setting of a low asymptotic pressure and a high time constant with algorithm 3.1 and 3.2. Instead, for such curves, a higher asymptotic pressure and a lower time constant is chosen in order to keep the error in the minimization small. The very same holds for the situation depicted in the upper panels which compare $\widetilde{\tau}$ and $\widehat{\tau}$. Here 23 out of 84 values might be affected.

The plots in fig. 4.21 illustrate the direct impact of the minimization bound: In total 42 of 98 excess pressures in figs. 4.21a and 4.21b are situated close to the lower bound yielding a mean difference of approximately zero. However, still a high standard deviation is stated, indicating considerable fluctuations for the other, not affected, values. With reference to figs. 4.21c and 4.21d it can be witnessed that the higher the values

of P_∞ are the better the asymptotic pressures $\widetilde{P}_\infty$ and $\breve{P}_\infty$ coincide. As already pointed out, this makes sense since excess pressures with higher values are not affected by the lower bound. In particular, in this setting 23 out of 84 values $\widetilde{P}_\infty$ are affected. By regarding the bottom figures of fig. 4.21 the high conformity of $\widehat{P}_\infty$ and $\breve{P}_\infty$ for higher values is also observable. The remarkably high standard deviation might be a consequence of the fact that in total 23 of 91 curves are influenced, but still they coincide quite well in general, which is also indicated by the still notable correlation coefficient $r = 0.75$. It also interesting to observe that in total 42 $\widehat{p}^{\,\mathrm{b}}_{\mathrm{res}}$-curves might be affected by the lower optimization bound but 19 of these curves are discarded since the corresponding $\breve{p}_{\mathrm{res}}$-waveforms are not considered as plausible. Consequently, 23 out of 91 $\widehat{P}_\infty$-values might be affected in this comparison. Hence, at least for the brachial curve, a lot of influenced $\widehat{P}_\infty$-curves are discarded anyway in the comparison in the bottom panels since any parameter related to $\breve{p}_{\mathrm{res}}$ is negative.

Fig. 4.22 indicate comparable results in terms of rate constants a and b of the respective algorithms 3.2 and 3.3. Rather small mean differences can be witnessed and also the possible outlier of a has similar values in both algorithms. In total similar results are shown for both algorithms in this respect.

The subsequent figs. 4.23 and 4.24 depict the comparisons for the peripheral net area parameters $\mathcal{R}$ and $\mathcal{C}$. Throughout all figures, the correlation coefficients are always greater than 0.8 which, in combination with the relatively small mean differences, indicate a quite good match for the majority of curves. A closer examination reveals that the alignment in both the resistances $\mathcal{R}$ and $\mathcal{C}$ is better in lower figures. Since the product $\mathcal{R}\mathcal{C}$ corresponds to the time constant this observation coincide with the already discussed situation depicted for the time constants in fig. 4.20. However, by bearing in mind that the peripheral parameters with respect to $\widehat{p}_{\mathrm{res}}$ and $\breve{p}_{\mathrm{res}}$ are computed by the approximated conversion formulas (3.58), it is remarkable that most of the computed values of $\widehat{\mathcal{R}}$ and $\widehat{\mathcal{C}}$ match closely their counterparts. This is especially true in fig. 4.24f where the mean difference exhibits a value of 1×10^{-5}. Moreover, the respective differences have values in the order of magnitude of 1×10^{-4} whereas the upper and middle panels have higher ones of about 1×10^{-3}.

Overall it can be said that the clinically important parameters of PP^{b} and $\mathrm{A}^{\mathrm{b}}_p$ obtained by the algorithms 3.2 and 3.3 are almost identical whereas algorithm 3.1 produces systematically higher results. With respect to the time constants associated with $\widehat{p}^{\,\mathrm{b}}_{\mathrm{res}}$ and $\breve{p}^{\mathrm{b}}_{\mathrm{res}}$, it has been witnessed that they are quite similar in general and in particular agree

even better for lower figures. In contrast, the time constants of the reservoir pressures $\vec{\widehat{p}}^{\,\mathrm{b}}_{\mathrm{res}}$ are systematically lower, indicating a steeper decay of the pressure-waveform. The systematic lower figure of $\widetilde{\tau}^{\mathrm{b}}$ compared to $\widehat{\tau}^{\mathrm{b}}$ and $\breve{\tau}^{\mathrm{b}}$ might be caused by the flow behaviour. Nevertheless, the figures indicate that the influence of the lower bound of the asymptotic pressures should not be neglected in this respect. On the contrary, in case of only regarding lower figures in fig. 4.20 for the comparison of all brachial time constants the systematic difference seems to be persistent. Regarding the brachial asymptotic pressures it has been observed that many pressures of $\widetilde{P}^{\mathrm{b}}_{\infty}$ and $\widehat{P}^{\mathrm{b}}_{\infty}$ have very likely been made to match for the same pressure waveform due to the lower bound. In fact 42 out of 98 curves might be affected in their direct comparison. Nonetheless, in case of only considering higher values of the respective asymptotic pressures it seems that all algorithms generate similar results regarding P^{b}_{∞}.

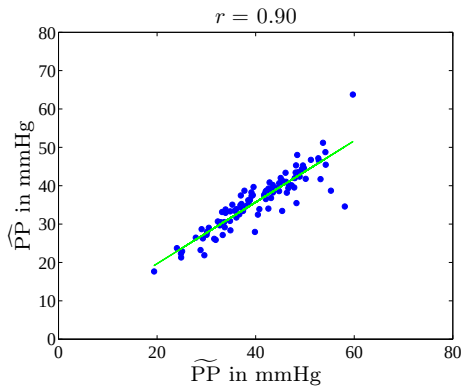

(a) Scatter plot: $\widetilde{\mathrm{PP}}$ vs. $\widehat{\mathrm{PP}}$

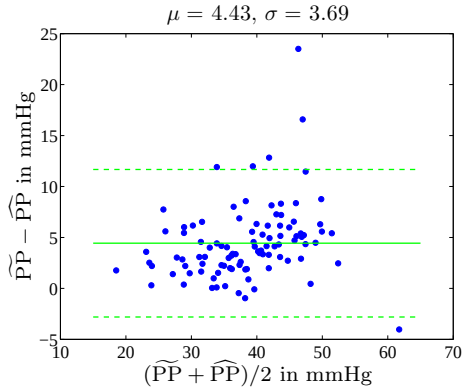

(b) Bland-Altman plot: $\widetilde{\mathrm{PP}}$ vs. $\widehat{\mathrm{PP}}$

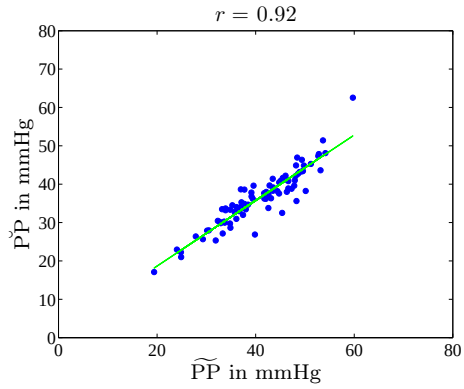

(c) Scatter plot: $\widetilde{\mathrm{PP}}$ vs. $\breve{\mathrm{P}}\mathrm{P}$

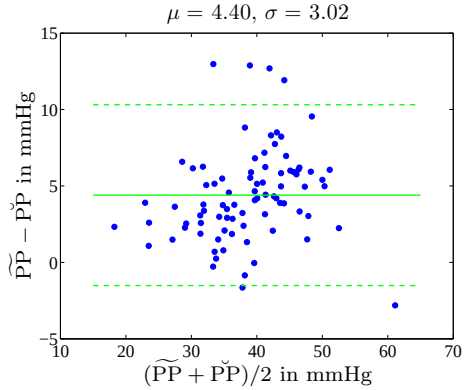

(d) Bland-Altman plot: $\widetilde{\mathrm{PP}}$ vs. $\breve{\mathrm{P}}\mathrm{P}$

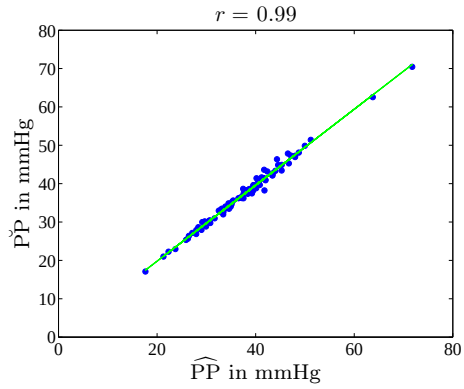

(e) Scatter plot: $\widehat{\mathrm{PP}}$ vs. $\breve{\mathrm{P}}\mathrm{P}$

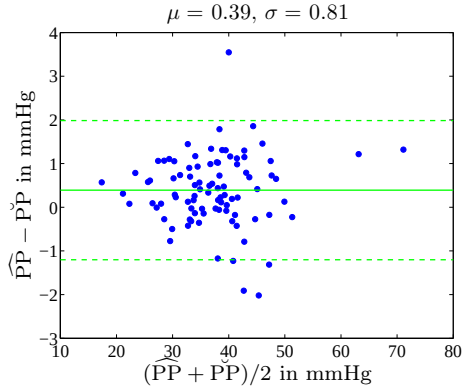

(f) Bland-Altman plot: $\widehat{\mathrm{PP}}$ vs. $\breve{\mathrm{P}}\mathrm{P}$

Figure 4.18: Brachial Artery: Direct comparison of reservoir pulse pressures PP

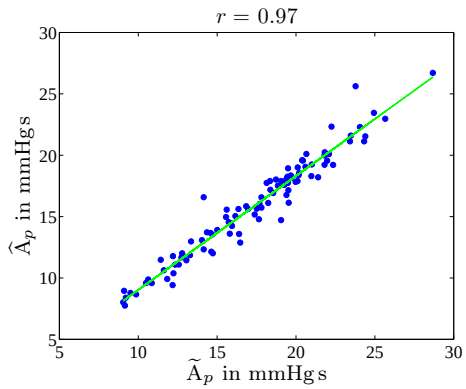

(a) Scatter plot: $\widetilde{\mathrm{A}}_p$ vs. $\widehat{\mathrm{A}}_p$

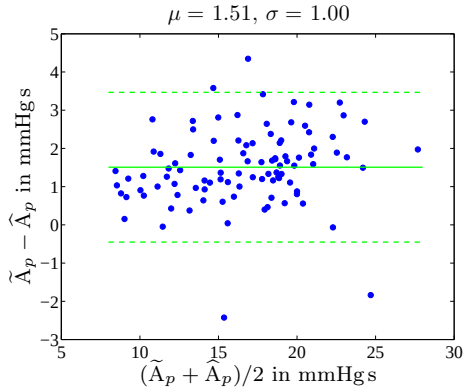

(b) Bland-Altman plot: $\widetilde{\mathrm{A}}_p$ vs. $\widehat{\mathrm{A}}_p$

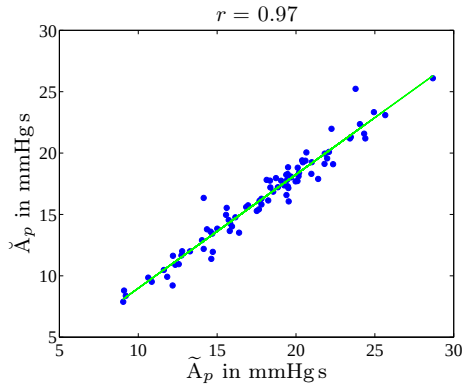

(c) Scatter plot: $\widetilde{\mathrm{A}}_p$ vs. $\breve{\mathrm{A}}_p$

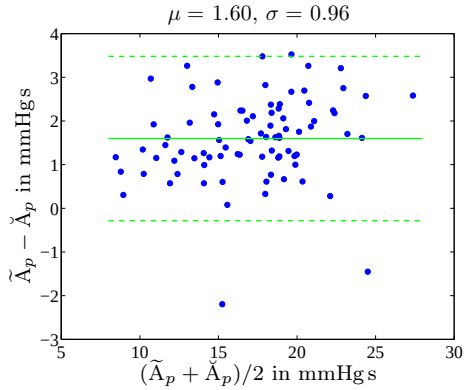

(d) Bland-Altman plot: $\widetilde{\mathrm{A}}_p$ vs. $\breve{\mathrm{A}}_p$

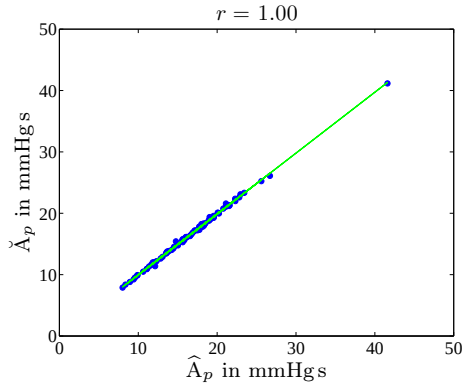

(e) Scatter plot: $\widehat{\mathrm{A}}_p$ vs. $\breve{\mathrm{A}}_p$

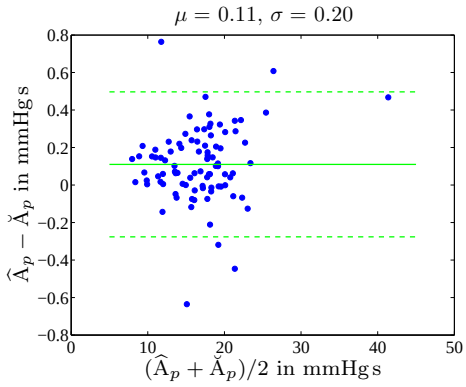

(f) Bland-Altman plot: $\widehat{\mathrm{A}}_p$ vs. $\breve{\mathrm{A}}_p$

Figure 4.19: Brachial Artery: Direct comparison of reservoir areas A_p

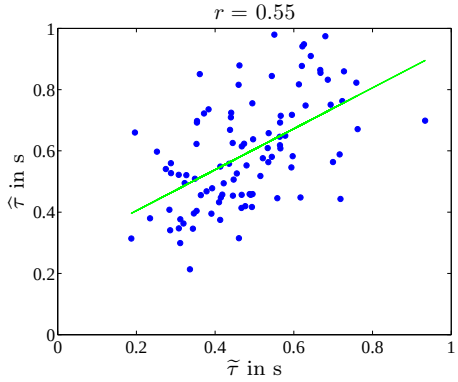

(a) Scatter plot: $\widetilde{\tau}$ vs. $\widehat{\tau}$

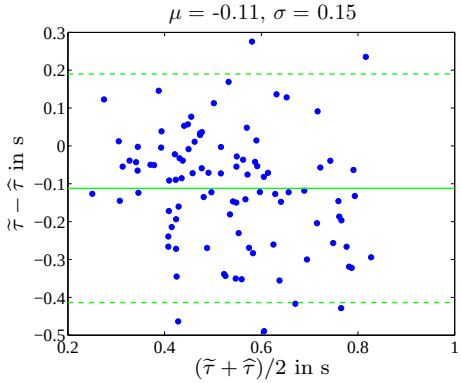

(b) Bland-Altman plot: $\widetilde{\tau}$ vs. $\widehat{\tau}$

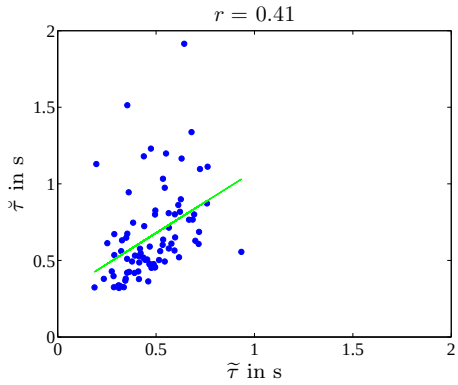

(c) Scatter plot: $\widetilde{\tau}$ vs. $\breve{\tau}$

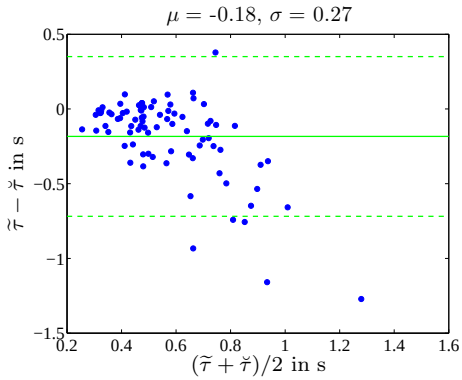

(d) Bland-Altman plot: $\widetilde{\tau}$ vs. $\breve{\tau}$

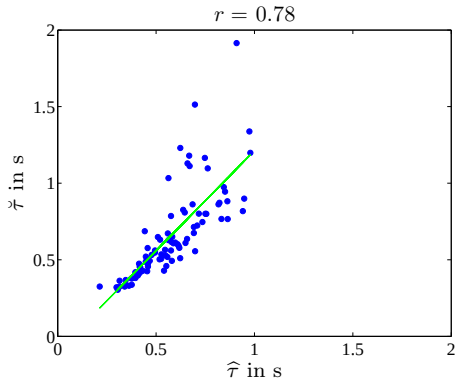

(e) Scatter plot: $\widehat{\tau}$ vs. $\breve{\tau}$

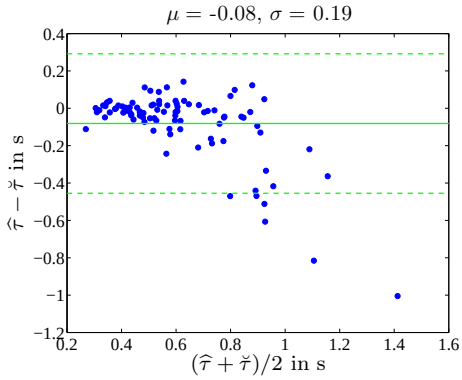

(f) Bland-Altman plot: $\widehat{\tau}$ vs. $\breve{\tau}$

Figure 4.20: Brachial Artery: Direct comparison of reservoir time constants τ

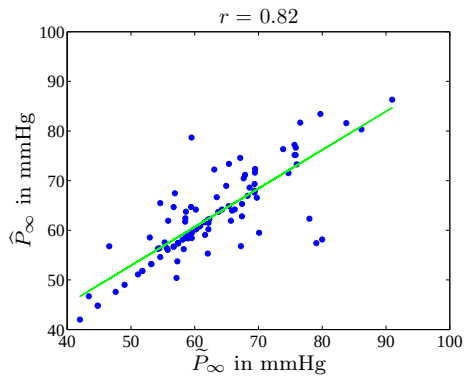

(a) Scatter plot: $\widetilde{P}_\infty$ vs. $\widehat{P}_\infty$

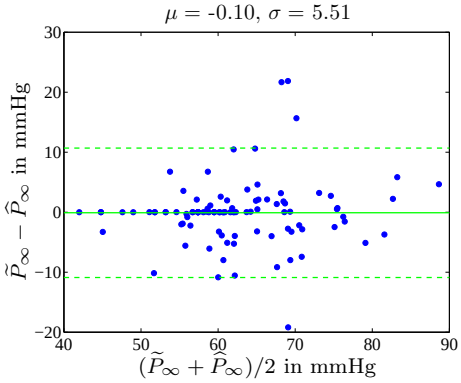

(b) Bland-Altman plot: $\widetilde{P}_\infty$ vs. $\widehat{P}_\infty$

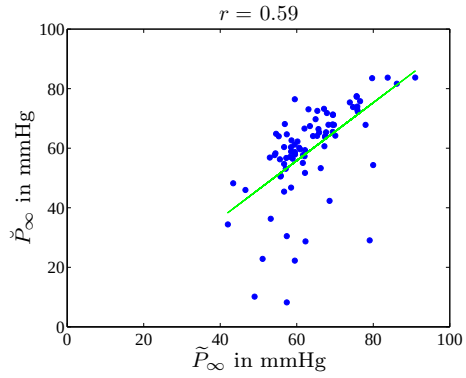

(c) Scatter plot: $\widetilde{P}_\infty$ vs. $\breve{P}_\infty$

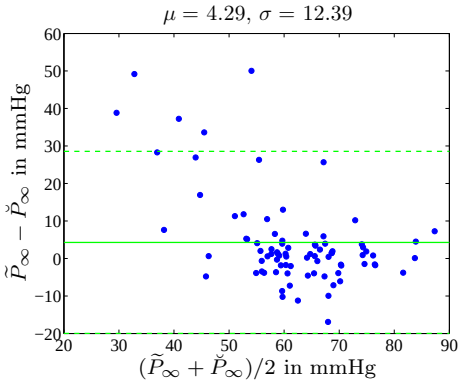

(d) Bland-Altman plot: $\widetilde{P}_\infty$ vs. $\breve{P}_\infty$

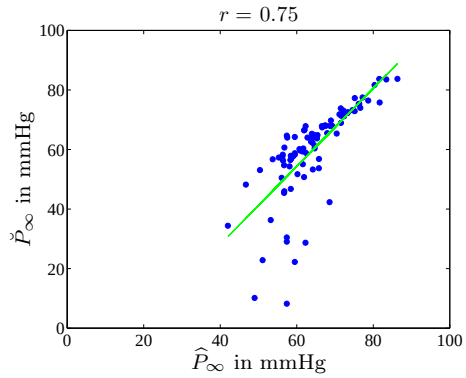

(e) Scatter plot: $\widehat{P}_\infty$ vs. $\breve{P}_\infty$

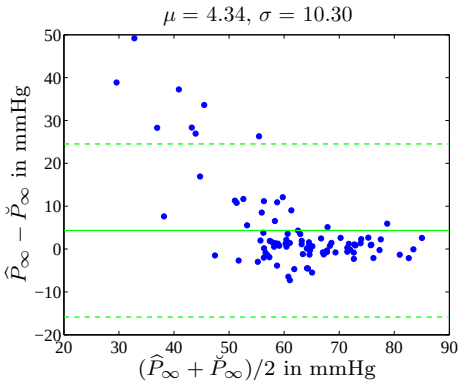

(f) Bland-Altman plot: $\widehat{P}_\infty$ vs. $\breve{P}_\infty$

Figure 4.21: Brachial Artery: Direct comparison of asymptotic pressures P_∞

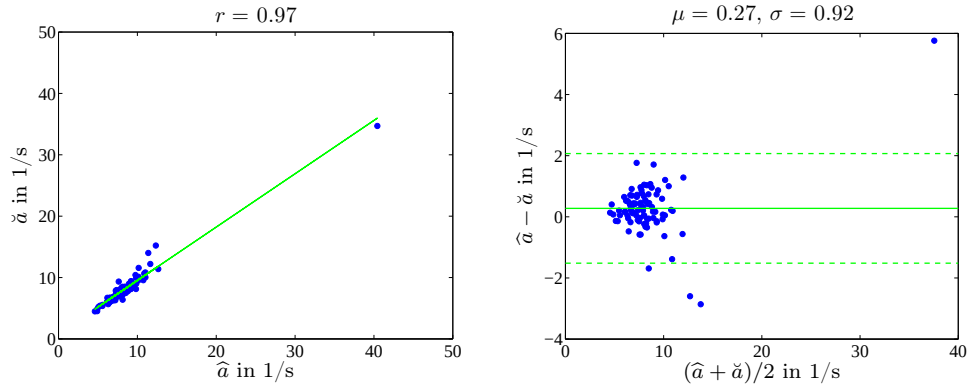

(a) Scatter plot: $\widehat{a}$ vs. $\breve{a}$

(b) Bland-Altman plot: $\widehat{a}$ vs. $\breve{a}$

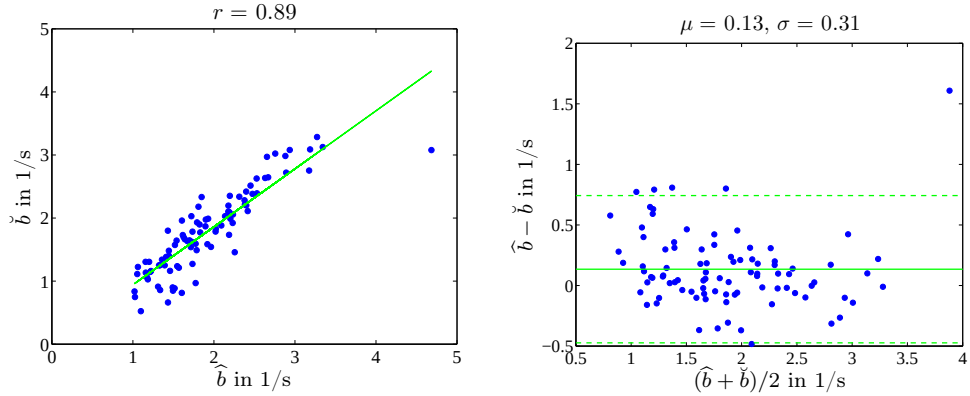

(c) Scatter plot: $\widehat{b}$ vs. $\breve{b}$

(d) Bland-Altman plot: $\widehat{b}$ vs. $\breve{b}$

Figure 4.22: Brachial Artery: Direct comparison of net parameters a, b

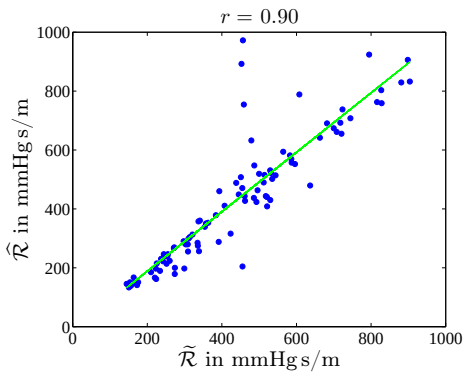

(a) Scatter plot: $\widetilde{\mathcal{R}}$ vs. $\widehat{\mathcal{R}}$

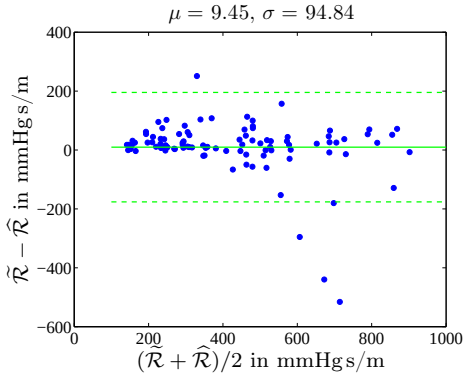

(b) Bland-Altman plot: $\widetilde{\mathcal{R}}$ vs. $\widehat{\mathcal{R}}$

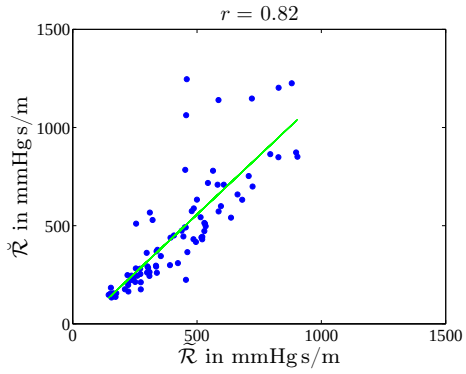

(c) Scatter plot: $\widetilde{\mathcal{R}}$ vs. $\check{\mathcal{R}}$

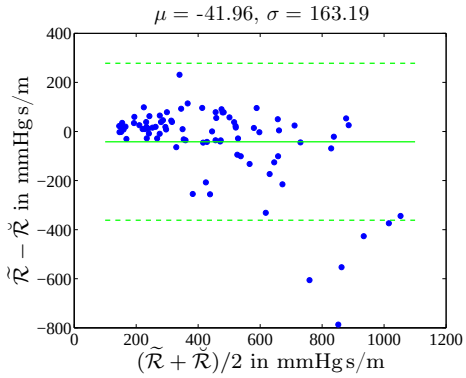

(d) Bland-Altman plot: $\widetilde{\mathcal{R}}$ vs. $\check{\mathcal{R}}$

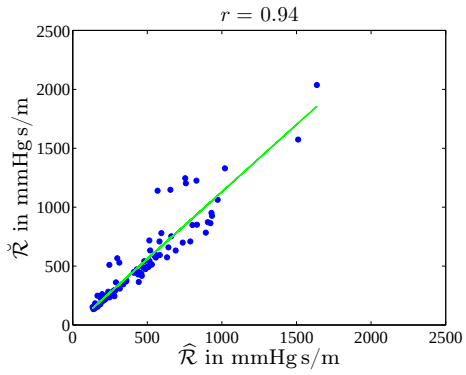

(e) Scatter plot: $\widehat{\mathcal{R}}$ vs. $\check{\mathcal{R}}$

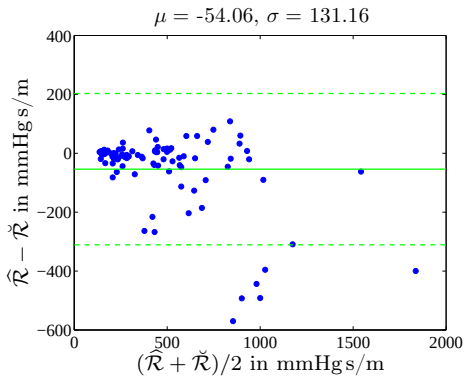

(f) Bland-Altman plot: $\widehat{\mathcal{R}}$ vs. $\check{\mathcal{R}}$

Figure 4.23: Brachial Artery: Direct comparison of peripheral area resistance $\mathcal{R}$

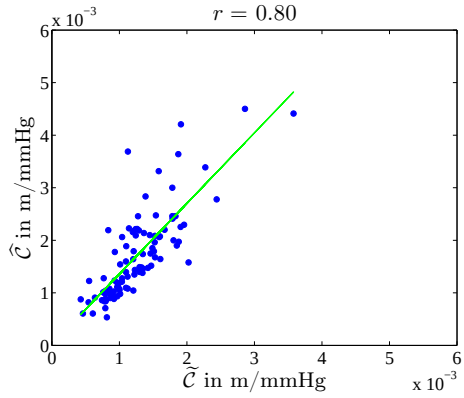

(a) Scatter plot: $\widetilde{\mathcal{C}}$ vs. $\widehat{\mathcal{C}}$

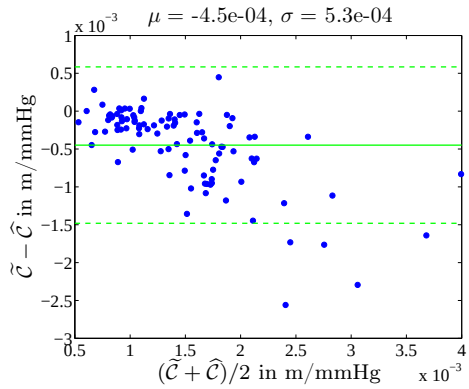

(b) Bland-Altman plot: $\widetilde{\mathcal{C}}$ vs. $\widehat{\mathcal{C}}$

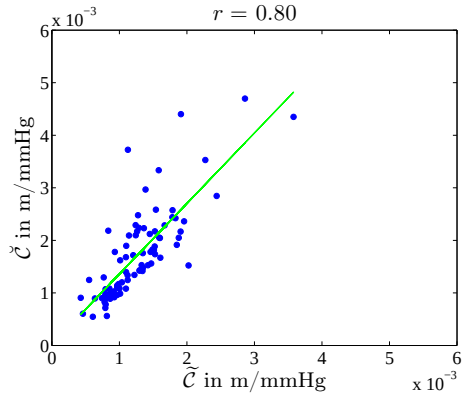

(c) Scatter plot: $\widetilde{\mathcal{C}}$ vs. $\check{\mathcal{C}}$

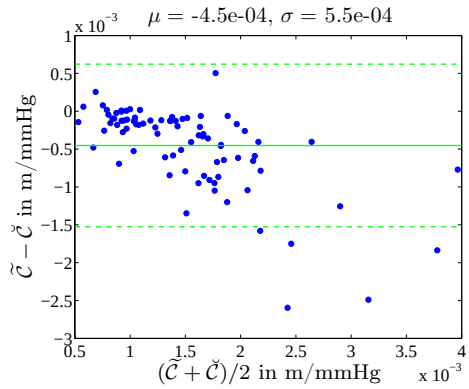

(d) Bland-Altman plot: $\widetilde{\mathcal{C}}$ vs. $\check{\mathcal{C}}$

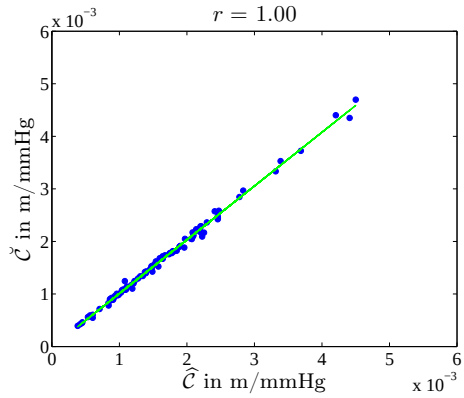

(e) Scatter plot: $\widehat{\mathcal{C}}$ vs. $\check{\mathcal{C}}$

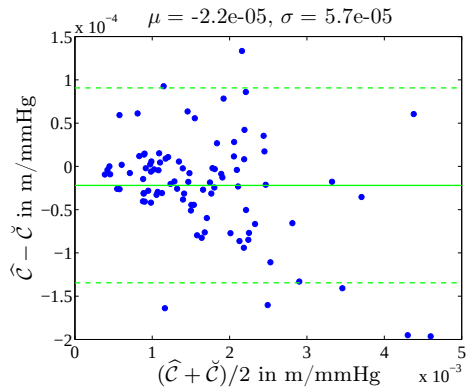

(f) Bland-Altman plot: $\widehat{\mathcal{C}}$ vs. $\check{\mathcal{C}}$

Figure 4.24: Brachial Artery: Direct comparison of net area compliance $\mathcal{C}$

4.4.6 Carotid Reservoir Pressure

In this section the results of all algorithms at the carotid artery are compared based on the figs. 4.25 to 4.31.

Regarding the pulse pressure PP the figures of algorithm 3.1 are slightly higher compared to those of the other algorithms but differ with a standard deviation of about $\sigma = 3\,\mathrm{mmHg}$, cf. figs. 4.25b and 4.25d. In contrast, by comparing algorithm 3.2 with algorithm 3.3, which both do not use the flow, a better agreement and a less standard deviation is observable. Moreover, the correlation coefficient equals almost 1, cf. fig. 4.25e. However, especially one curve is characterized by a striking PP among all algorithms and suggests that it does not belong to this cohort. In further consequence the high correlation coefficients at all comparisons are possibly overestimated. Nonetheless, by regarding the respective Bland-Altman plots the corresponding mean differences are quite small which indicate a good agreement of all algorithms for the majority of reservoir curves.

The just stated observations also apply to the area A_p by regarding fig. 4.26. I.e. those areas associated with $\widetilde{p}_{\mathrm{res}}$ are generally slightly higher and the remaining pressures $\widehat{p}_{\mathrm{res}}$, $\breve{p}_{\mathrm{res}}$ exhibit similar values. The possible outlier is as well observable. However, the areas $\widehat{\mathrm{A}}_p$ and $\breve{\mathrm{A}}_p$ agree even better compared to their respective pulse pressures.

As already suggested by table 4.16, the time constant $\widetilde{\tau}$ is for most of the reservoir curves smaller than $\widehat{\tau}$ and $\breve{\tau}$. With respect to figs. 4.27a and 4.27c it can be witnessed that $\widetilde{\tau}$ does not vary in the same range as those belonging to the extended Reservoir Theory algorithms. Furthermore, the correlation coefficients are rather small. As already observed for brachial curves, $\widetilde{\tau}$ is better in agreement with $\widehat{\tau}$ and $\breve{\tau}$ for lower figures, cf. figs. 4.27b and 4.27d. Since in total 39 out of 90 $\widetilde{P}^{\mathrm{c}}_{\infty}$-values are affected by the lower minimization bound this circumstance could have restricted the variability of $\widetilde{\tau}$. Therefore, this might have a quite considerable impact on the results. The same holds for 19 out of 110 $\widehat{P}_{\infty}$-values. Since, in relative numbers, $\widehat{p}_{\mathrm{res}}$-curves are not expected to be affected to the same extent as $\widetilde{p}_{\mathrm{res}}$-ones the higher variability of $\widehat{\tau}$ compared to $\widetilde{\tau}$ might be explained, cf. fig. 4.27a. With respect to the lower panels of fig. 4.27 it can be witnessed that $\widehat{\tau}$ and $\breve{\tau}$ agree well which is indicated by the small mean $\mu = -0.05\,\mathrm{s}$ and standard deviation $\sigma = 0.10\,\mathrm{s}$. Since only 10 of in total 101 regarded curves might be affected by the lower bound in the regarded comparison, this influence might be neglected. Therefore, a pretty good alignment of the algorithms 3.2 and 3.3 can be stated.

With a view to the asymptotic pressures in fig. 4.28 the observations are as follows: Firstly, it has to be recalled that 39 $\widetilde{P}_{\infty}$- and 19 $\widehat{P}_{\infty}$-

values of all their regarded curves are located close to the lower bound. Consequently, those which are associated to the same curve, are likely to correspond to each other. Several differences $\widetilde{P}_\infty - \widehat{P}_\infty$ are equal to zero and could be caused by this circumstance. Moreover, the values of $\widetilde{P}_\infty$ and $\widehat{P}_\infty$ are better in agreement with $\breve{P}_\infty$ for higher values. Again, it is likely that lower figures of $\widetilde{P}_\infty$ and $\widehat{P}_\infty$ were prevented by the threshold $0.7\ \min(p)$ of the respective curve. By bearing that in mind and therefore putting the focus on higher values instead, $\widehat{P}_\infty$ and $\breve{P}_\infty$ produce comparable results in general. In addition, the values of $\widetilde{P}_\infty$ are then identified as systematically lower compared to those of the implementations which do not rely on the flow. Since the velocities are generally greater than zero during later diastole, this is quite reasonable due to (4.10) and the subsequent explanations that the asymptotic pressures $\widetilde{P}_\infty$ are reduced by the (theoretical) offset $v_0\,\mathcal{R}$.

Referring to the results illustrated in fig. 4.29, it can be witnessed that the algorithms 3.2 and 3.3 generate very similar results in terms of the respective rate constants a and b. The high correlation coefficients and the small mean differences indicate a high correspondence of both associated algorithms. Since $b = 1/\tau$ the results of b basically have already been discussed.

The net area parameters show systematically higher resistances $\widetilde{\mathcal{R}}$ but lower compliances $\widetilde{\mathcal{C}}$ compared to those of the other ones. Figs. 4.31d and 4.31b suggest that $\widetilde{\mathcal{C}}$ is better in agreement with their counterparts in case of lower values. Again, the lower bound for $\widetilde{P}_\infty$ and $\widehat{P}_\infty$ might have affected these results. However, since $\widehat{\mathcal{C}}$ and $\breve{\mathcal{C}}$ are obtained by (3.58) – involving the excess pressure, the flow velocity and the rate constants – this behaviour might have several causes and could as well be artificial. Still, the high correlation coefficients among all comparisons shall be pointed out.

By taking into account the stated points above, it can be concluded that generally both algorithms 3.2 and 3.3 produce very similar results at the carotid artery as well. Therefore, the lower bound in the optimization routine in algorithm 3.2 does not seem to have a big influence on the sample of carotid reservoir curves $\widehat{p}^{\,\mathrm{c}}_{\mathrm{res}}$ in general. However, due to the higher quantity of possibly affected $\widetilde{P}^{\mathrm{c}}_\infty$ this cannot be stated for sure for algorithm 3.1 and the associated reservoir pressure $\widetilde{p}^{\,\mathrm{c}}_{\mathrm{res}}$, but the impact on the clinically important parameters PP and A_p is suggested to be minimal since they correlate quite well with those from the other algorithms. Compared to $\widehat{p}^{\,\mathrm{c}}_{\mathrm{res}}$ and $\breve{p}^{\,\mathrm{c}}_{\mathrm{res}}$ the pulse pressures $\widetilde{\mathrm{PP}}^{\mathrm{c}}$ and areas $\widetilde{\mathrm{A}}^{\mathrm{c}}_p$ are generally greater and the respective time constants $\widetilde{\tau}^{\mathrm{c}}$ smaller. However, $\widetilde{p}^{\,\mathrm{c}}_{\mathrm{res}}$ seems to be influenced more by the lower bound in the optimization routine than $\widehat{p}^{\,\mathrm{c}}_{\mathrm{res}}$ at the carotid artery.

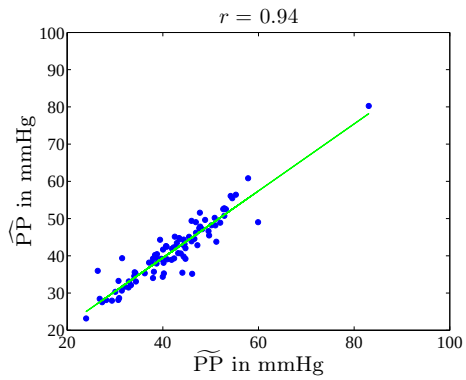

(a) Scatter plot: $\widehat{\widetilde{\mathrm{PP}}}$ vs. $\widehat{\mathrm{PP}}$

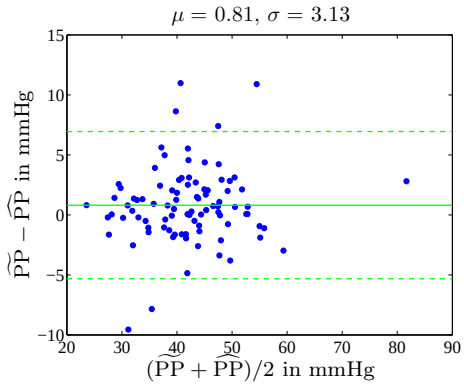

(b) Bland-Altman plot: $\widehat{\widetilde{\mathrm{PP}}}$ vs. $\widehat{\mathrm{PP}}$

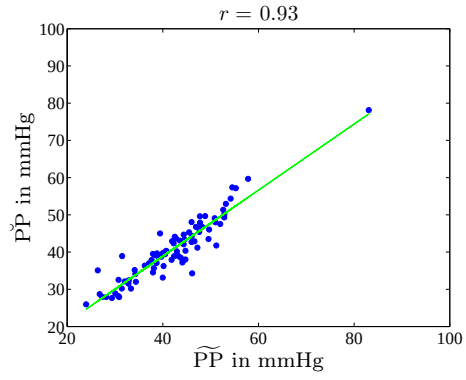

(c) Scatter plot: $\widehat{\widetilde{\mathrm{PP}}}$ vs. $\breve{\mathrm{PP}}$

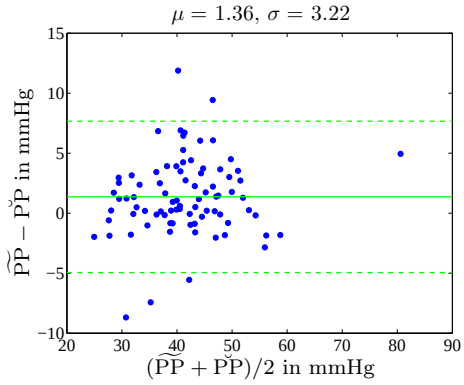

(d) Bland-Altman plot: $\widehat{\widetilde{\mathrm{PP}}}$ vs. $\breve{\mathrm{PP}}$

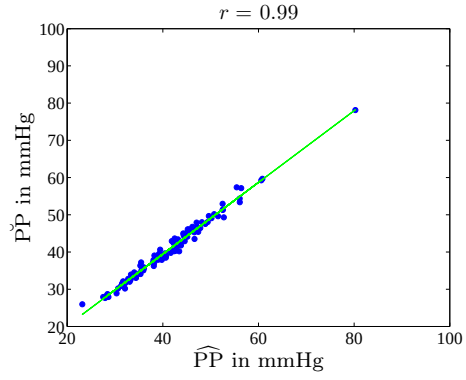

(e) Scatter plot: $\widehat{\mathrm{PP}}$ vs. $\breve{\mathrm{PP}}$

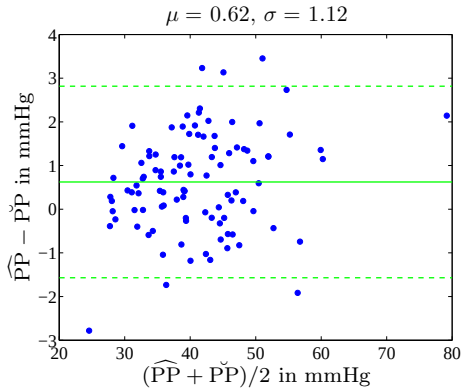

(f) Bland-Altman plot: $\widehat{\mathrm{PP}}$ vs. $\breve{\mathrm{PP}}$

Figure 4.25: Carotid Artery: Direct comparison of reservoir pulse pressures PP

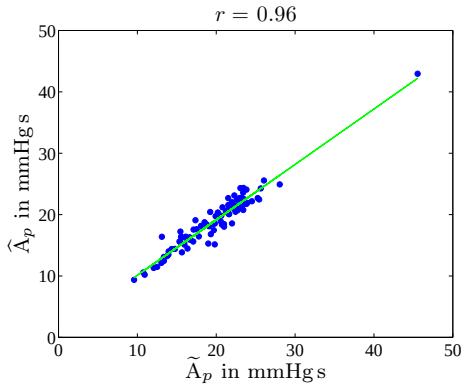

(a) Scatter plot: $\widetilde{\mathrm{A}}_p$ vs. $\widehat{\mathrm{A}}_p$

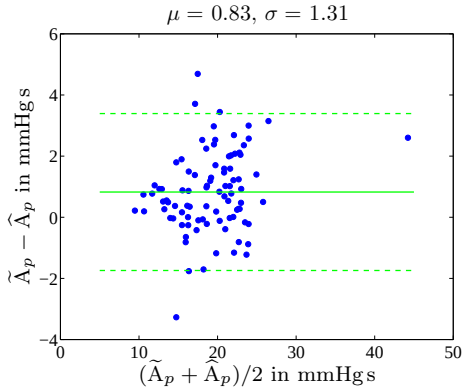

(b) Bland-Altman plot: $\widetilde{\mathrm{A}}_p$ vs. $\widehat{\mathrm{A}}_p$

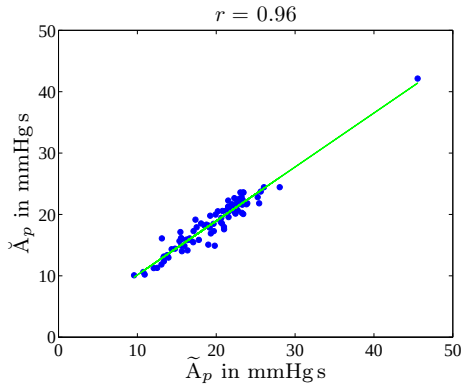

(c) Scatter plot: $\widetilde{\mathrm{A}}_p$ vs. $\breve{\mathrm{A}}_p$

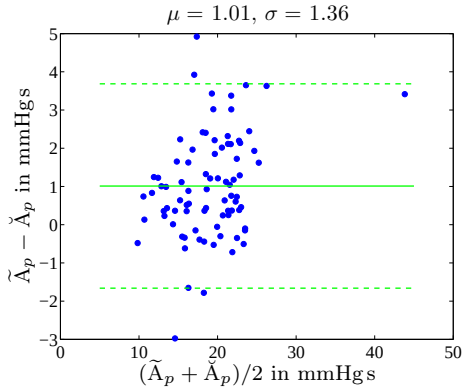

(d) Bland-Altman plot: $\widetilde{\mathrm{A}}_p$ vs. $\breve{\mathrm{A}}_p$

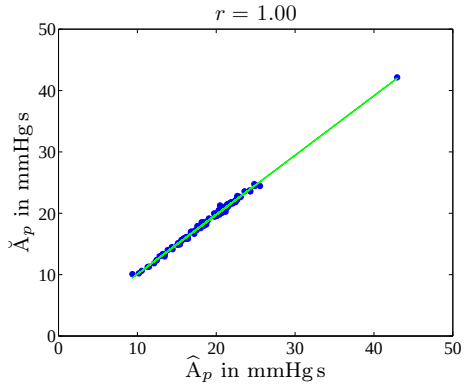

(e) Scatter plot: $\widehat{\mathrm{A}}_p$ vs. $\breve{\mathrm{A}}_p$

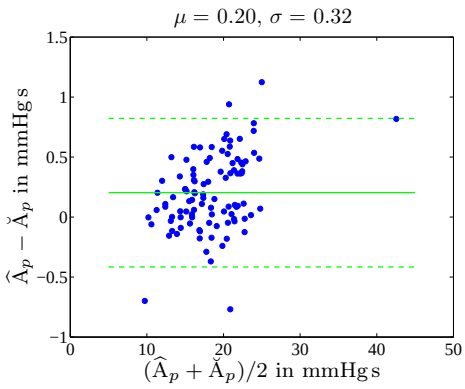

(f) Bland-Altman plot: $\widehat{\mathrm{A}}_p$ vs. $\breve{\mathrm{A}}_p$

Figure 4.26: Carotid Artery: Direct comparison of reservoir areas A_p

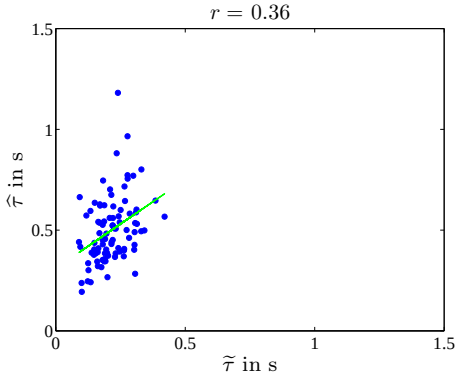

(a) Scatter plot: $\widetilde{\tau}$ vs. $\widehat{\tau}$

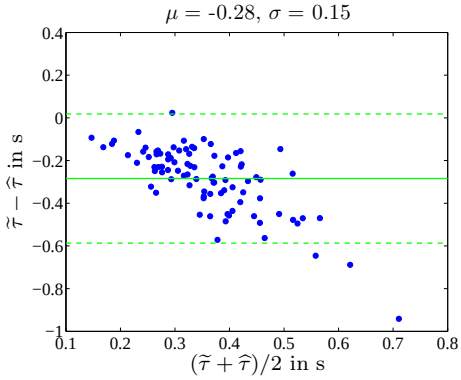

(b) Bland-Altman plot: $\widetilde{\tau}$ vs. $\widehat{\tau}$

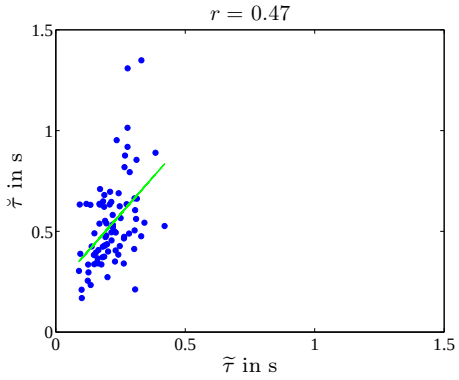

(c) Scatter plot: $\widetilde{\tau}$ vs. $\breve{\tau}$

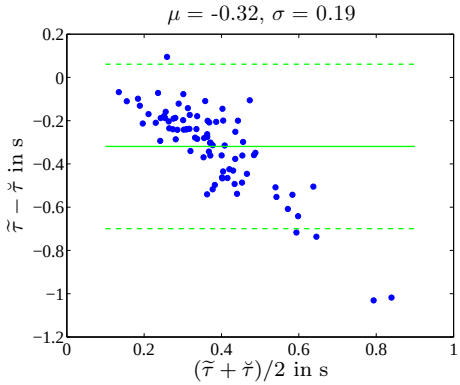

(d) Bland-Altman plot: $\widetilde{\tau}$ vs. $\breve{\tau}$

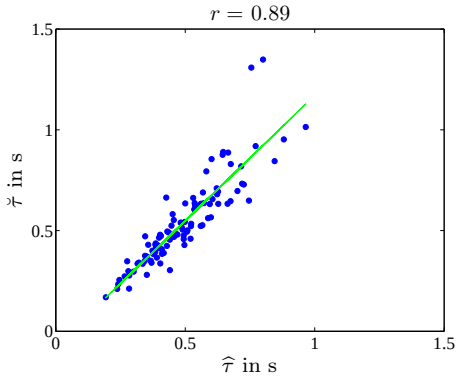

(e) Scatter plot: $\widehat{\tau}$ vs. $\breve{\tau}$

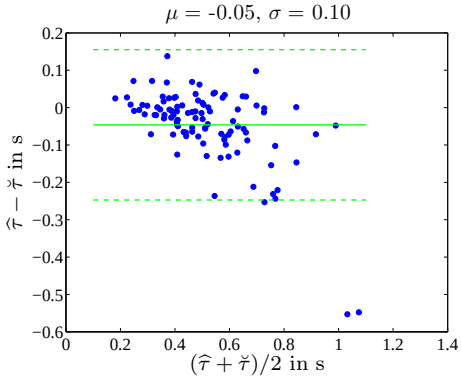

(f) Bland-Altman plot: $\widehat{\tau}$ vs. $\breve{\tau}$

Figure 4.27: Carotid Artery: Direct comparison of reservoir time constants τ

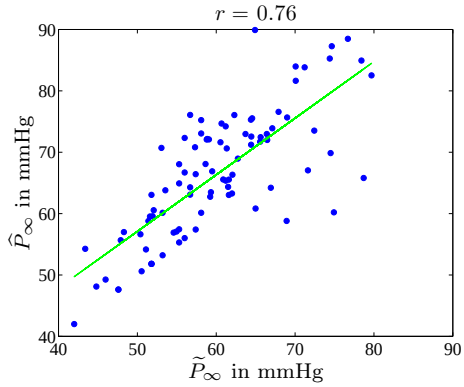

(a) Scatter plot: $\widetilde{P}_\infty$ vs. $\widehat{P}_\infty$

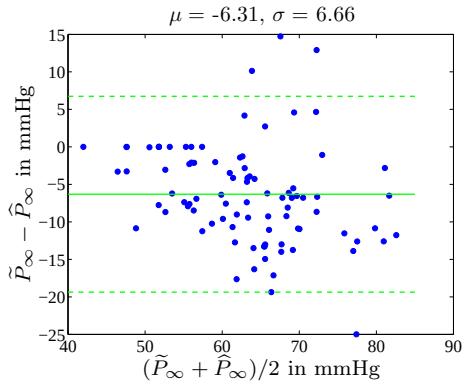

(b) Bland-Altman plot: $\widetilde{P}_\infty$ vs. $\widehat{P}_\infty$

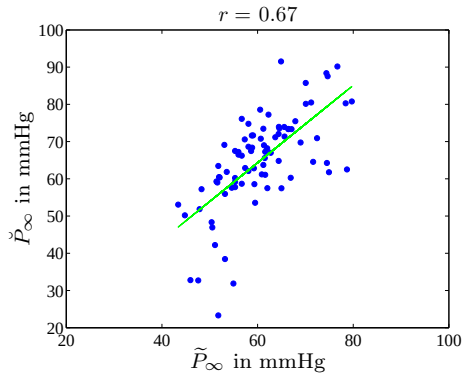

(c) Scatter plot: $\widetilde{P}_\infty$ vs. $\breve{P}_\infty$

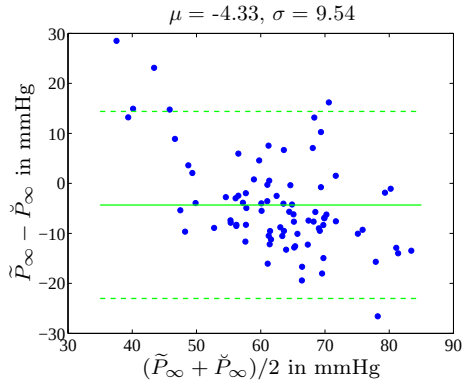

(d) Bland-Altman plot: $\widetilde{P}_\infty$ vs. $\breve{P}_\infty$

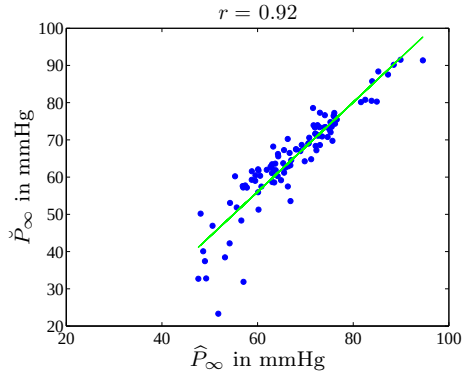

(e) Scatter plot: $\widehat{P}_\infty$ vs. $\breve{P}_\infty$

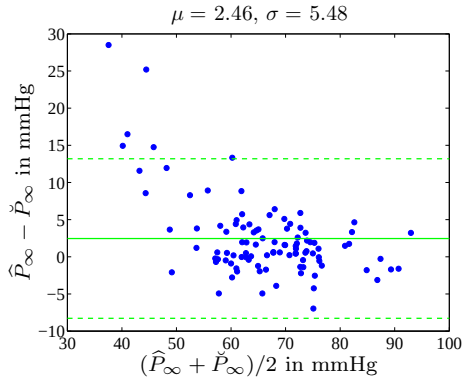

(f) Bland-Altman plot: $\widehat{P}_\infty$ vs. $\breve{P}_\infty$

Figure 4.28: Carotid Artery: Direct comparison of asymptotic pressures P_∞

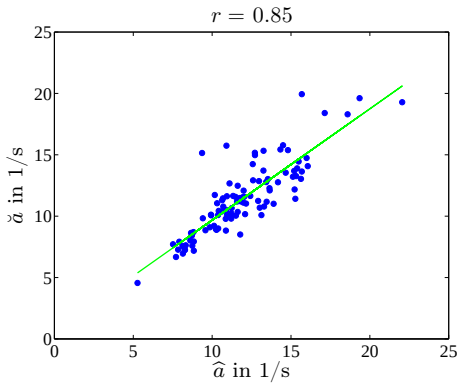

(a) Scatter plot: $\widehat{a}$ vs. $\breve{a}$

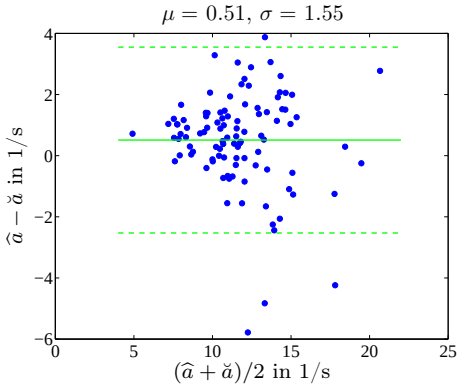

(b) Bland-Altman plot: $\widehat{a}$ vs. $\breve{a}$

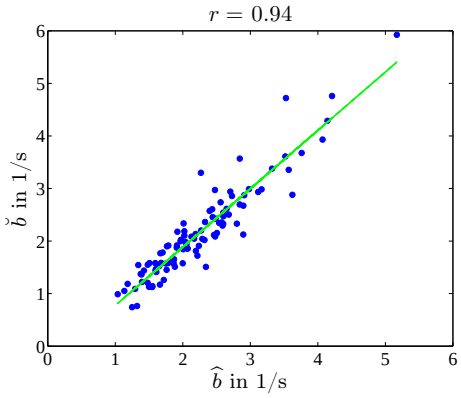

(c) Scatter plot: $\widehat{b}$ vs. $\breve{b}$

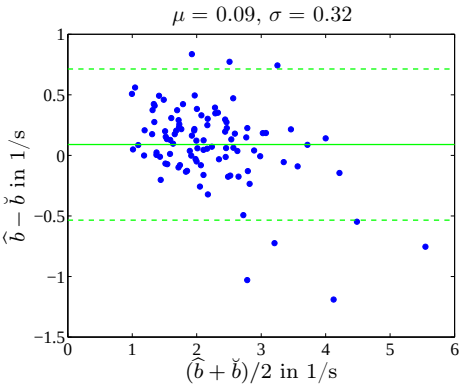

(d) Bland-Altman plot: $\widehat{b}$ vs. $\breve{b}$

Figure 4.29: Carotid Artery: Direct comparison of rate constants a, b

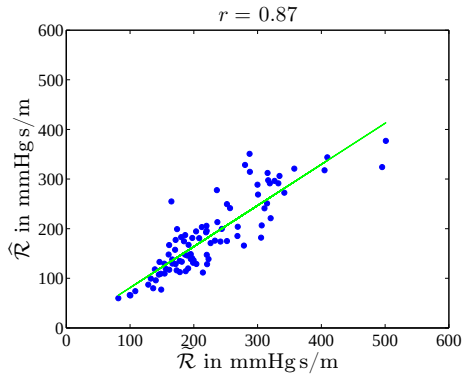

(a) Scatter plot: $\widetilde{\mathcal{R}}$ vs. $\widehat{\mathcal{R}}$

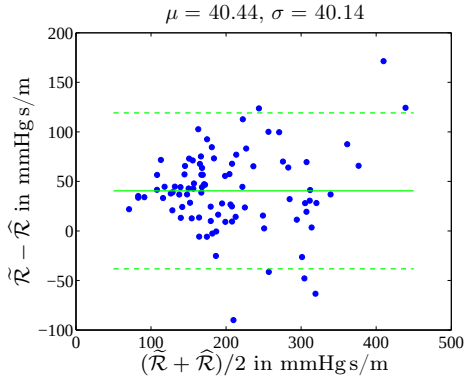

(b) Bland-Altman plot: $\widetilde{\mathcal{R}}$ vs. $\widehat{\mathcal{R}}$

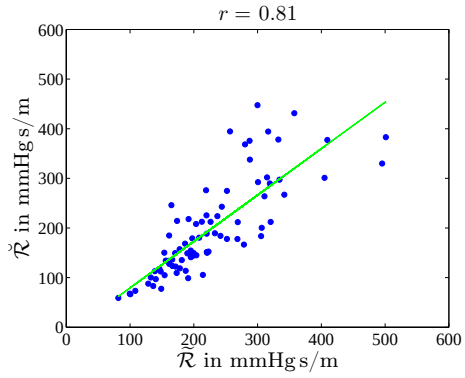

(c) Scatter plot: $\widetilde{\mathcal{R}}$ vs. $\breve{\mathcal{R}}$

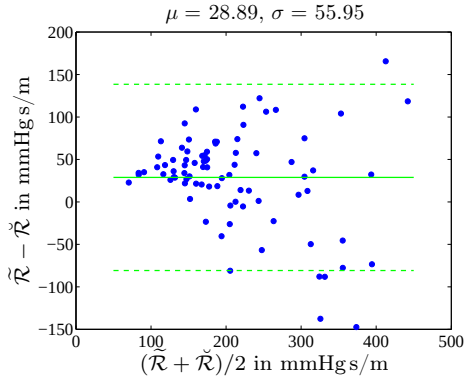

(d) Bland-Altman plot: $\widetilde{\mathcal{R}}$ vs. $\breve{\mathcal{R}}$

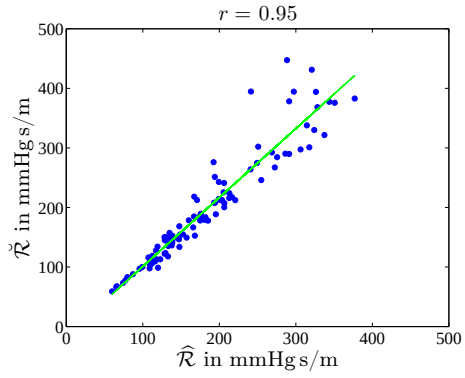

(e) Scatter plot: $\widehat{\mathcal{R}}$ vs. $\breve{\mathcal{R}}$

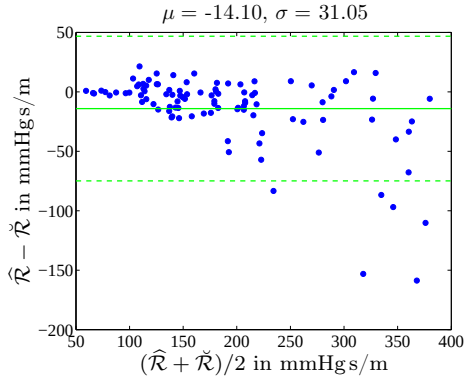

(f) Bland-Altman plot: $\widehat{\mathcal{R}}$ vs. $\breve{\mathcal{R}}$

Figure 4.30: Carotid Artery: Direct comparison of peripheral area resistance $\mathcal{R}$

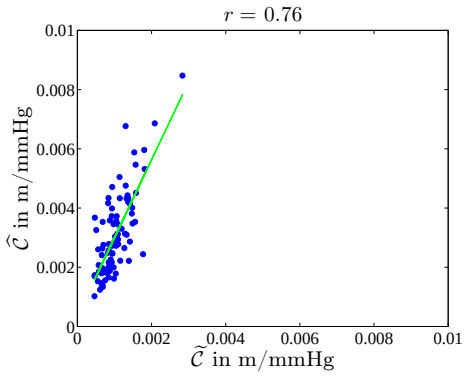

(a) Scatter plot: $\widetilde{\mathcal{C}}$ vs. $\widehat{\mathcal{C}}$

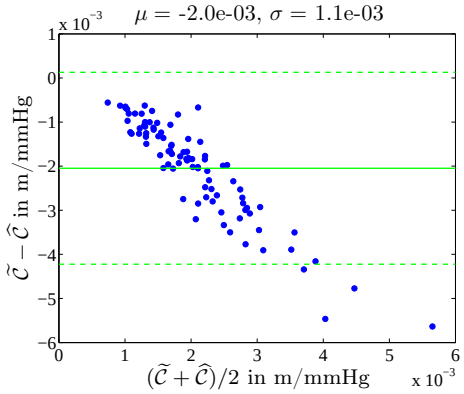

(b) Bland-Altman plot: $\widetilde{\mathcal{C}}$ vs. $\widehat{\mathcal{C}}$

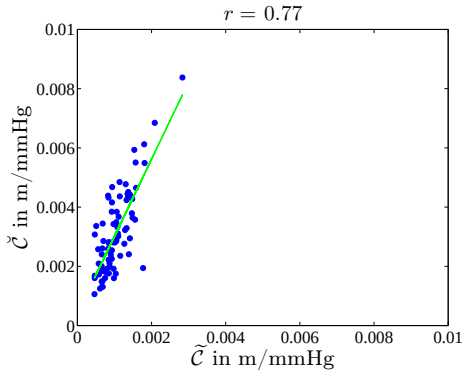

(c) Scatter plot: $\widetilde{\mathcal{C}}$ vs. $\check{\mathcal{C}}$

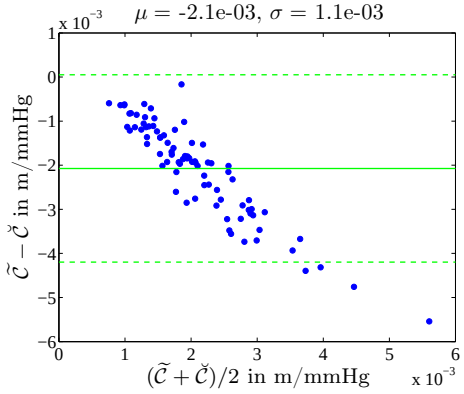

(d) Bland-Altman plot: $\widetilde{\mathcal{C}}$ vs. $\check{\mathcal{C}}$

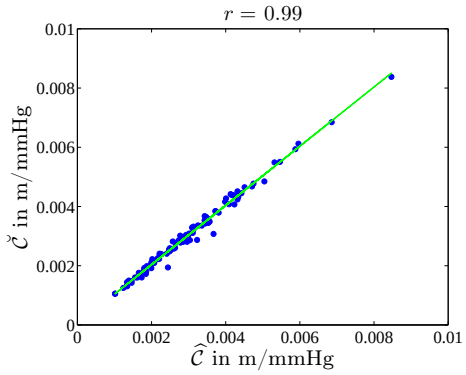

(e) Scatter plot: $\widehat{\mathcal{C}}$ vs. $\check{\mathcal{C}}$

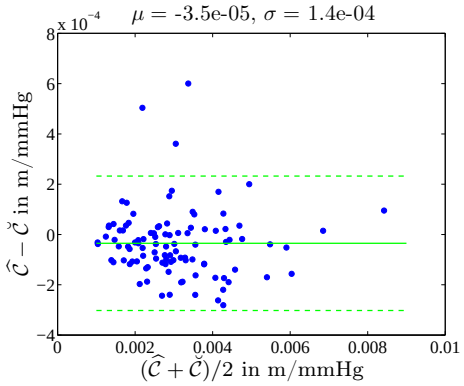

(f) Bland-Altman plot: $\widehat{\mathcal{C}}$ vs. $\check{\mathcal{C}}$

Figure 4.31: Carotid Artery: Direct comparison of net area compliance $\mathcal{C}$

4.5 Brachial vs. Carotid Reservoir Pressure

In the preceding section it was pointed out that both implementations of the extended Reservoir Theory which do not use the flow yield similar parameters. Furthermore it was observed that these results are generally different from those generated by the implementation of the classic approach which incorporates the arterial flow.

However, in this section the differences between the carotid and brachial reservoir pressures shall be investigated. A particular focus will be put on clinically relevant parameters of pulse pressure PP and area A_p of the reservoir pressure waveforms. Since one major objective of this thesis is to evaluate whether the pressure decays are similar at the arterial locations of brachial and carotid artery, the time constant τ will be investigated too. Moreover, to get a better insight of the influences of the lower threshold on the algorithms 3.1 and 3.2 the asymptotic pressure will as well be examined more closely. Before comparing these parameters between each arterial location individually, an overview of all parameters and methods shall be given and discussed.

4.5.1 Overviews of all Parameters and Methods

The results of each algorithm are going to be compared between the brachial and carotid artery. Therefore the maximal amount of curves which can be considered for both the brachial and carotid artery constitutes the sample for the respective algorithm. The resulting samples for the respective pressure separations are shown and characterized in tables 4.18 to 4.20. The corresponding results of each method, based on these samples, are illustrated in the tables 4.21 to 4.23

In the tables 4.18 to 4.20 the heart rate (HR), the diastolic blood pressure (DBP), the mean blood pressure (MBP), the systolic blood pressure (SBP), the pulse pressure (PP) and the area of pressure above DBP (A_p) of the measured pressure waveforms after data preprocessing associated with the respective sample are shown. Due to the steps during data preprocessing and the corresponding scaling the DBP and MBP have to be necessarily equal for the brachial and carotid curves. Moreover, since $PP = SBP - DBP$ the according differences match those of SBP.

In the tables 4.21 to 4.23 the results of the respective locations are illustrated, broken down by every single method. The figures in the first two columns illustrate the mean and standard deviation of all computed parameters for each arterial location separately. In the third column, the mean and standard deviation of all differences of the respective brachial and carotid curves are stated. Lastly, the fourth column denotes the correlation coefficient of these differences.

Sample for $\widetilde{p}_{\mathrm{res}}$	**Brachial A.**	**Carotid A.**	**Diff. (B-C)**	r
HR (1/min)	64.48 ± 10.76	60.91 ± 9.34	3.56 ± 4.36	0.92
DBP (mmHg)	78.80 ± 8.62	78.80 ± 8.62	0.00 ± 0.00	1.00
MBP (mmHg)	102.60 ± 9.40	102.60 ± 9.40	0.00 ± 0.00	1.00
SBP (mmHg)	139.27 ± 12.36	134.95 ± 13.55	4.32 ± 5.42	0.92
PP (mmHg)	60.47 ± 10.98	56.15 ± 11.53	4.32 ± 5.42	0.89
$\mathbf{A}_{\boldsymbol{p}}$ (mmHg s)	97.75 ± 16.33	102.99 ± 15.68	-5.24 ± 7.04	0.90

Table 4.18: Parameters of pressure curves regarded for $\widetilde{p}_{\mathrm{res}}$ (Sample size of 81 curves)

Sample for $\widehat{p}_{\mathrm{res}}$	**Brachial A.**	**Carotid A.**	**Diff. (B-C)**	r
HR (1/min)	65.48 ± 11.78	61.80 ± 9.79	3.68 ± 4.60	0.93
DBP (mmHg)	80.05 ± 8.53	80.05 ± 8.53	0.00 ± 0.00	1.00
MBP (mmHg)	104.30 ± 9.84	104.30 ± 9.84	0.00 ± 0.00	1.00
SBP (mmHg)	140.81 ± 13.67	136.84 ± 14.83	3.97 ± 5.41	0.93
PP (mmHg)	60.77 ± 12.23	56.80 ± 12.85	3.97 ± 5.41	0.91
$\mathbf{A}_{\boldsymbol{p}}$ (mmHg s)	98.32 ± 18.33	103.39 ± 16.79	-5.07 ± 7.09	0.92

Table 4.19: Parameters of pressure curves regarded for $\widehat{p}_{\mathrm{res}}$ (Sample size of all 110 curves)

Sample for $\breve{p}_{\mathrm{res}}$	**Brachial A.**	**Carotid A.**	**Diff. (B-C)**	r
HR (1/min)	62.97 ± 10.45	59.73 ± 8.56	3.24 ± 4.55	0.90
DBP (mmHg)	80.30 ± 8.49	80.30 ± 8.49	0.00 ± 0.00	1.00
MBP (mmHg)	104.36 ± 10.12	104.36 ± 10.12	0.00 ± 0.00	1.00
SBP (mmHg)	141.04 ± 14.20	137.47 ± 15.54	3.57 ± 5.36	0.94
PP (mmHg)	60.73 ± 12.27	57.17 ± 13.23	3.57 ± 5.36	0.91
$\mathbf{A}_{\boldsymbol{p}}$ (mmHg s)	101.71 ± 17.27	106.49 ± 15.62	-4.78 ± 7.58	0.90

Table 4.20: Parameters of pressure curves regarded for $\breve{p}_{\mathrm{res}}$ (Sample size of 89 curves)

$\widetilde{p}_{\mathrm{res}}$	**Brachial A.**	**Carotid A.**	**Diff. (B-C)**	r
$\widetilde{\mathbf{PP}}$ (mmHg)	40.62 ± 8.44	41.69 ± 7.87	-1.07 ± 6.12	0.72
$\widetilde{\mathbf{A}}_{\boldsymbol{p}}$ (mmHg s)	17.47 ± 4.32	19.20 ± 4.07	-1.74 ± 2.22	0.86
$\widetilde{\boldsymbol{\tau}}$ (s)	0.49 ± 0.14	0.22 ± 0.07	0.27 ± 0.16	-0.05
$\widetilde{\boldsymbol{P}}_{\boldsymbol{\infty}}$ (mmHg)	62.07 ± 9.17	59.40 ± 8.39	2.67 ± 7.17	0.67
$\widetilde{\boldsymbol{\mathcal{R}}}$ (mmHg s/m)	421.34 ± 191.06	220.79 ± 78.20	200.55 ± 208.24	-0.02
$\widetilde{\boldsymbol{\mathcal{C}}}$ (m/mmHg)	$(1.31 \pm 0.51) \times 10^{-3}$	$(1.05 \pm 0.40) \times 10^{-3}$	$(2.58 \pm 5.50) \times 10^{-4}$	0.30

Table 4.21: Parameters of reservoir pressures $\widetilde{p}_{\mathrm{res}}$ based on the sample of 81 curves

$\widehat{p}_{\mathrm{res}}$	**Brachial A.**	**Carotid A.**	**Diff. (B-C)**	r
$\widehat{\mathbf{PP}}$ (mmHg)	36.78 ± 8.11	41.53 ± 8.53	-4.76 ± 4.30	0.87
$\widehat{\mathbf{A}}_{\boldsymbol{p}}$ (mmHg s)	16.17 ± 4.75	18.54 ± 4.39	-2.36 ± 1.92	0.92
$\widehat{\boldsymbol{\tau}}$ (s)	0.59 ± 0.17	0.50 ± 0.16	0.09 ± 0.17	0.51
$\widehat{\boldsymbol{P}}_{\boldsymbol{\infty}}$ (mmHg)	62.85 ± 8.66	66.33 ± 10.23	-3.47 ± 6.99	0.74
$\widehat{\boldsymbol{a}}$ (1/s)	8.33 ± 3.55	11.94 ± 2.70	-3.61 ± 4.02	0.20
$\widehat{\boldsymbol{b}}$ (1/s)	1.86 ± 0.61	2.20 ± 0.74	-0.34 ± 0.68	0.51
$\widehat{\boldsymbol{\mathcal{R}}}$ (mmHg s/m)	478.72 ± 294.45	187.67 ± 74.88	291.05 ± 294.47	0.13
$\widehat{\boldsymbol{\mathcal{C}}}$ (m/mmHg)	$(1.61 \pm 0.85) \times 10^{-3}$	$(3.02 \pm 1.30) \times 10^{-3}$	$(-1.4 \pm 1.4) \times 10^{-3}$	0.26

Table 4.22: Parameters of reservoir pressures $\widehat{p}_{\mathrm{res}}$ based on the sample of 110 curves

$\breve{p}_{\mathrm{res}}$	**Brachial A.**	**Carotid A.**	**Diff. (B-C)**	r
$\breve{\mathbf{PP}}$ (mmHg)	37.07 ± 8.15	41.29 ± 8.59	-4.23 ± 4.86	0.83
$\breve{\mathbf{A}}_{\boldsymbol{p}}$ (mmHg s)	16.61 ± 4.76	18.79 ± 4.29	-2.18 ± 1.92	0.91
$\breve{\boldsymbol{\tau}}$ (s)	0.65 ± 0.29	0.54 ± 0.22	0.11 ± 0.32	0.24
$\breve{\boldsymbol{P}}_{\boldsymbol{\infty}}$ (mmHg)	60.32 ± 14.84	65.33 ± 12.95	-5.01 ± 15.13	0.41
$\breve{\boldsymbol{a}}$ (1/s)	8.19 ± 3.41	11.33 ± 2.78	-3.14 ± 4.12	0.12
$\breve{\boldsymbol{b}}$ (1/s)	1.80 ± 0.66	2.15 ± 0.91	-0.36 ± 0.95	0.29
$\breve{\boldsymbol{\mathcal{R}}}$ (mmHg s/m)	512.96 ± 356.72	201.61 ± 94.07	311.35 ± 358.77	0.11
$\breve{\boldsymbol{\mathcal{C}}}$ (m/mmHg)	$(1.65 \pm 0.89) \times 10^{-3}$	$(3.03 \pm 1.30) \times 10^{-3}$	$(-1.39 \pm 1.40) \times 10^{-3}$	0.23

Table 4.23: Parameters of reservoir pressures $\breve{p}_{\mathrm{res}}$ based on the sample of 89 curves

Referring to $\widetilde{p}_{\mathrm{res}}$ it can be witnessed that PP and A_p are comparable for both sites. Moreover, the high values of $r = 0.72$ and $r = 0.86$ indicate a notable linear correlation. Regarding the figures, the brachial reservoir pulse pressures $\widetilde{\mathrm{PP}}$ and areas $\widetilde{\mathrm{A}}_p$ are about one unit smaller than the carotid ones, cf. table 4.21. In contrast, the associated sample of measured pressure curves exhibits a brachial pulse pressure PP which is about 4 mmHg greater and the corresponding A_p is approximately 5 mmHg s lower as opposed to the carotid artery, cf. table 4.18. Hence, in direct comparison with the original data the difference in PP even changed the sign. In other words, whereas in the original pressure waveform the brachial PP is greater, for the reservoir holds the contrary. By considering the remaining parameters in table 4.21 the time constants and peripheral area resistances differ remarkably. In fact, the brachial resistance is on average almost twice as high compared to the carotid one. Furthermore, the brachial asymptotic pressure is generally bigger.

By considering the results of $\widehat{p}_{\mathrm{res}}$ and $\breve{p}_{\mathrm{res}}$ it can be stated that the brachial PP an A_p are, on average, about 4 mmHg and 2 mmHg s smaller in both cases and the corresponding correlation indices are all around 0.9. The time constant discrepancy has decreased compared to $\widetilde{p}_{\mathrm{res}}$. The regarded sample of pressure curves associated to $\widehat{p}_{\mathrm{res}}$ and $\breve{p}_{\mathrm{res}}$ exhibit similar figures, cf. tables 4.19 and 4.20. In short, the brachial readings provide about 4 mmHg higher pulse pressure and approximately 5 mmHg s lower areas compared to those at the carotid artery.

However, it has to be kept in mind that the possibly affected amount of asymptotic pressures are in the case of $\widetilde{P}_\infty$ 49 out of 81 and in the case of $\widehat{P}_\infty$ 46 out of 110 values, cf. table 4.17. Regarding $\widehat{p}_{\mathrm{res}}$ the preceding findings suggested that the results are barely influenced since the parameters of $\widehat{p}_{\mathrm{res}}$ and $\breve{p}_{\mathrm{res}}$ match closely each other which can be interpreted as that they verify each others' results. Unfortunately, this cannot be stated for $\widetilde{p}_{\mathrm{res}}$, but the observed results indicate systematic differences compared to $\widehat{p}_{\mathrm{res}}$ and $\breve{p}_{\mathrm{res}}$ regardless their existence. Nevertheless, the asymptotic pressure is examined first.

4.5.2 Asymptotic Pressure

Referring to fig. 4.32b it can be witnessed that the brachial asymptotic pressures $\widetilde{P}_{\infty}^{\mathrm{b}}$ are generally higher than the carotid ones. Moreover it can be stated that many, but not all, of the affected asymptotic pressures are located at the lower bound of 0.7 $\min(p)$ for the same data set of brachial and carotid curves. However, since in total 49 of 81 asymptotic pressures are affected no clear statement can be given about the direct comparison of both arteries associated with $\widetilde{P}_{\infty}$.

With respect to $\widehat{P}_{\infty}$ it holds similarly that many of the asymptotic pressures are located for the same pressure set at the lower minimization bound indicating that the algorithm most likely would have sought to decrease further the asymptotic pressure, cf. fig. 4.32d. Nonetheless, since a direct comparison to $\breve{P}_{\infty}$ is possible, the as systematically lower stated brachial values $\widehat{P}_{\infty}^{\mathrm{b}}$ are very likely to depict the real situation and outcome of $\widehat{p}_{\mathrm{res}}$.

With reference to fig. 4.32e it can be witnessed that the asymptotic pressures $\breve{P}_{\infty}$ vary remarkably for both the brachial and carotid artery within a broader range of values compared to the other ones $\widetilde{P}_{\infty}$, $\widehat{P}_{\infty}$. However, a clustering can be observed for higher values in both the scatter and Bland-Altman plot. This might also be the reason that the results of $\widehat{p}_{\mathrm{res}}$ and $\breve{p}_{\mathrm{res}}$ match closely each other since in the majority of cases a higher asymptotic pressure than 0.7 $\min_{\mathcal{T}_0^N} p$ might be plausible. In general, the brachial asymptotic pressure is lower than the carotid one whereas both do not correlate well – at least not linearly.

4.5.3 Clinically Relevant Parameters

For the direct comparison of the clinically relevant parameters PP and A_p only the algorithms 3.2 and 3.3 are considered. This is mainly based on the observation that the algorithm 3.3 seems to be the most stable one and its results are closely aligned to those of algorithm 3.2. Therefore the regarded sample sizes consisted of 110 $\widehat{p}_{\mathrm{res}}$- and 89 $\breve{p}_{\mathrm{res}}$-curves respectively.

The outcome is illustrated in figs. 4.33 and 4.34 whereby the left columns indicate the results associated with the reservoir pressure $\widehat{p}_{\mathrm{res}}$ and the right ones those related to $\breve{p}_{\mathrm{res}}$. Both methods testify the same observation: The PP and A_p are systematically lower for reservoir curves computed by brachial pressures. However, it has to be emphasized that the carotid pressure scaling during (DP3) has affected the pulse pressures and areas of the carotid waveforms. But, especially because of this step of data preprocessing it is believed that these comparisons in terms of PP and A_p are justified since afterwards both arterial pressures correspond to each other in their mean pressures.

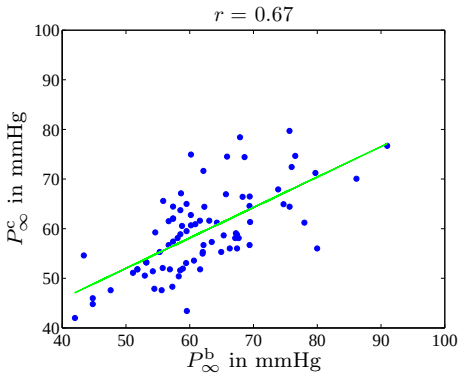

(a) Scatter plot: $\widetilde{P}^{b}_{\infty}$ vs. $\widetilde{P}^{c}_{\infty}$

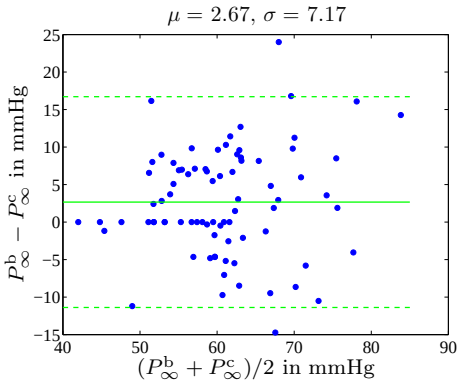

(b) Bland-Altman plot 1: $\widetilde{P}^{b}_{\infty}$ vs. $\widetilde{P}^{c}_{\infty}$

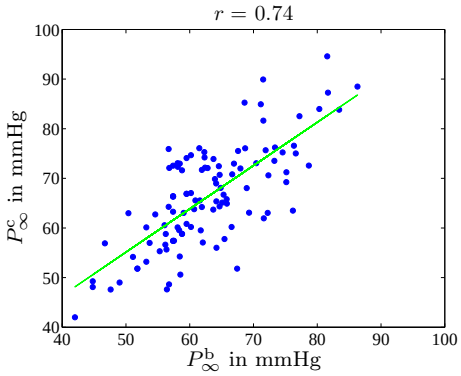

(c) Scatter plot: $\widehat{P}^{b}_{\infty}$ vs. $\widehat{P}^{c}_{\infty}$

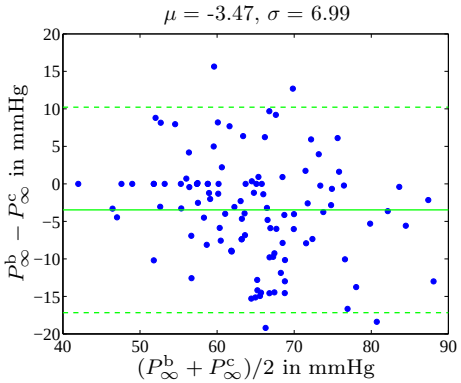

(d) Bland-Altman plot 1: $\widehat{P}^{b}_{\infty}$ vs. $\widehat{P}^{c}_{\infty}$

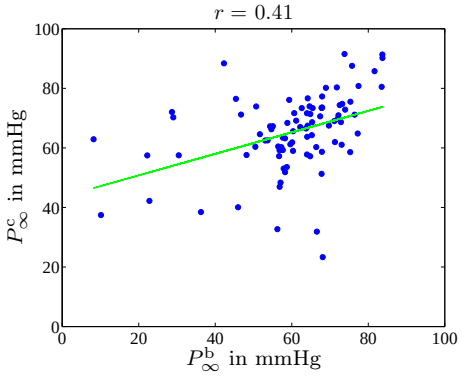

(e) Scatter plot: $\breve{P}^{b}_{\infty}$ vs. $\breve{P}^{c}_{\infty}$

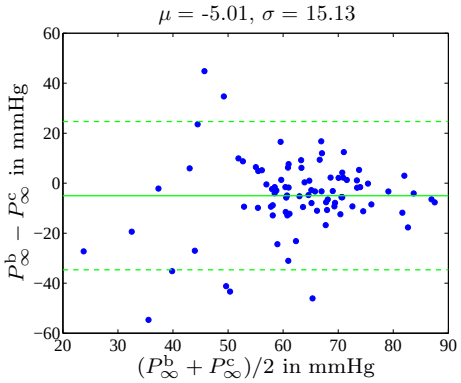

(f) Bland-Altman plot 1: $\breve{P}^{b}_{\infty}$ vs. $\breve{P}^{c}_{\infty}$

Figure 4.32: Brachial vs. Carotid Artery: Asymptotic pressures $\widehat{P}_{\infty}$ and $\breve{P}_{\infty}$ of the reservoir pressures $\widehat{p}_{\mathrm{res}}$ and $\breve{p}_{\mathrm{res}}$

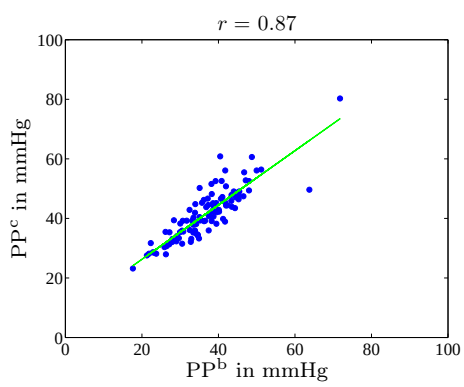

(a) Scatter plot: $\widehat{\mathrm{PP}}^{\mathrm{b}}$ vs. $\widehat{\mathrm{PP}}^{\mathrm{c}}$

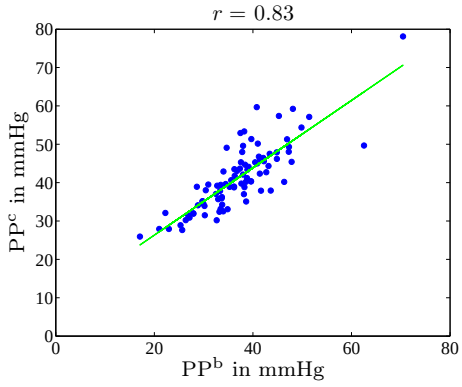

(b) Scatter plot: $\breve{\mathrm{PP}}^{\mathrm{b}}$ vs. $\breve{\mathrm{PP}}^{\mathrm{c}}$

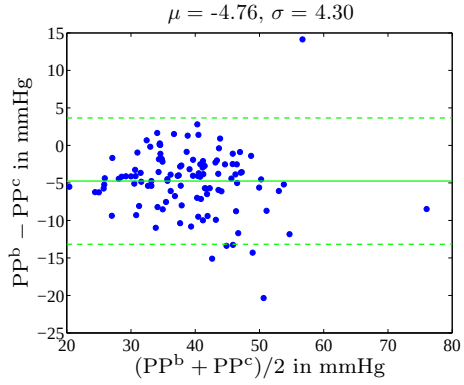

(c) Bland-Altman plot 1: $\widehat{\mathrm{PP}}^{\mathrm{b}}$ vs. $\widehat{\mathrm{PP}}^{\mathrm{c}}$

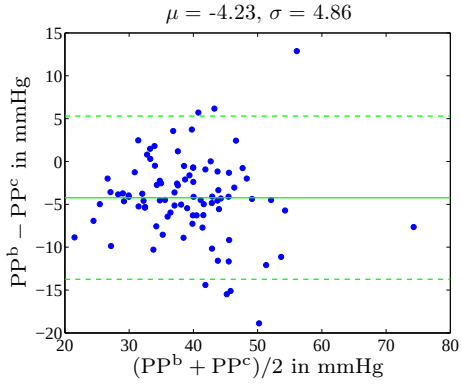

(d) Bland-Altman plot 1: $\breve{\mathrm{PP}}^{\mathrm{b}}$ vs. $\breve{\mathrm{PP}}^{\mathrm{c}}$

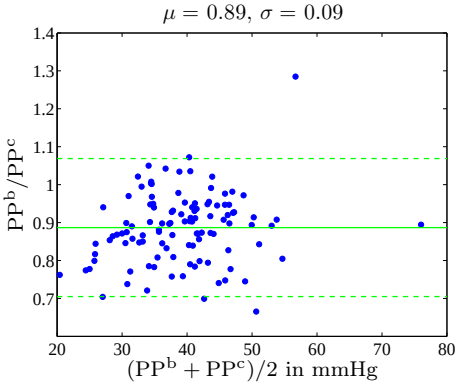

(e) Bland-Altman plot 2: $\widehat{\mathrm{PP}}^{\mathrm{b}}$ vs. $\widehat{\mathrm{PP}}^{\mathrm{c}}$

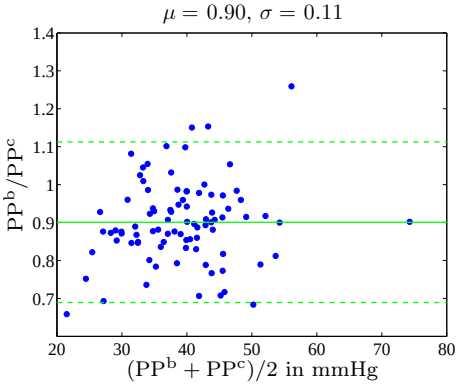

(f) Bland-Altman plot 2: $\breve{\mathrm{PP}}^{\mathrm{b}}$ vs. $\breve{\mathrm{PP}}^{\mathrm{c}}$

Figure 4.33: Brachial vs. Carotid Artery: Pulse pressure PP of the reservoir pressures $\widehat{p}_{\mathrm{res}}$ and $\breve{p}_{\mathrm{res}}$

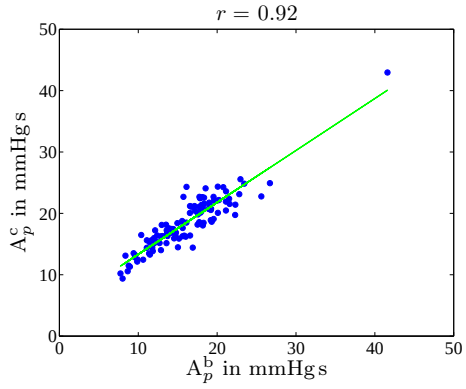

(a) Scatter plot: $\widehat{\mathrm{A}_p}^{\mathrm{b}}$ vs. $\widehat{\mathrm{A}_p}^{\mathrm{c}}$

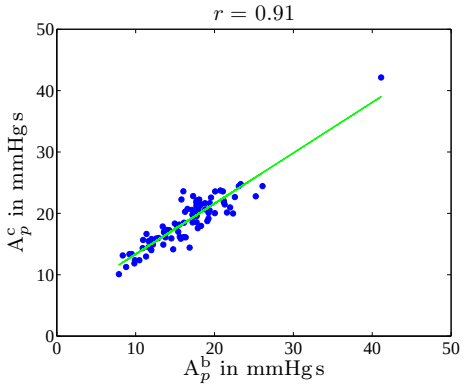

(b) Scatter plot: $\breve{\mathrm{A}}_p^{\mathrm{b}}$ vs. $\breve{\mathrm{A}}_p^{\mathrm{c}}$

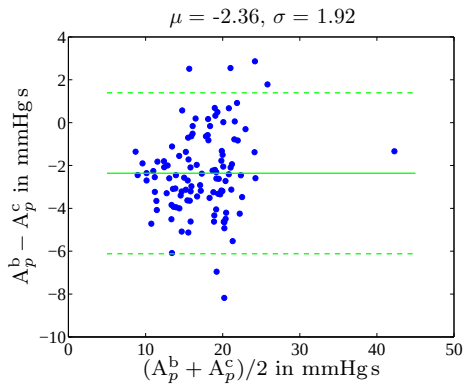

(c) Bland-Altman plot 1: $\widehat{\mathrm{A}_p}^{\mathrm{b}}$ vs. $\widehat{\mathrm{A}_p}^{\mathrm{c}}$

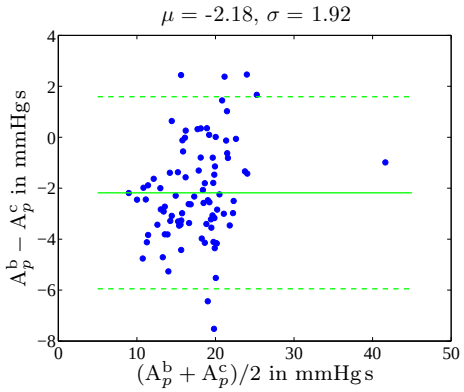

(d) Bland-Altman plot 1: $\breve{\mathrm{A}}_p^{\mathrm{b}}$ vs. $\breve{\mathrm{A}}_p^{\mathrm{c}}$

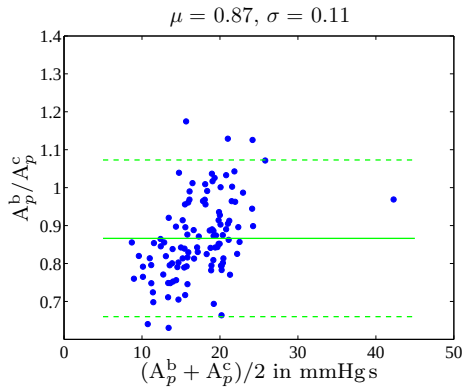

(e) Bland-Altman plot 2: $\widehat{\mathrm{A}_p}^{\mathrm{b}}$ vs. $\widehat{\mathrm{A}_p}^{\mathrm{c}}$

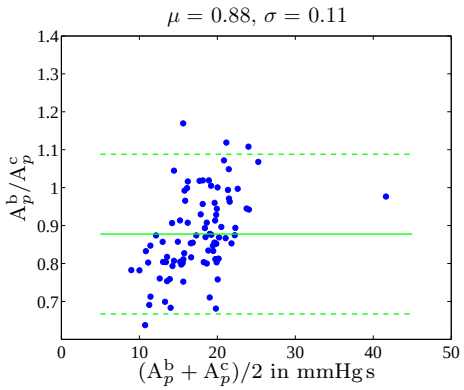

(f) Bland-Altman plot 2: $\breve{\mathrm{A}}_p^{\mathrm{b}}$ vs. $\breve{\mathrm{A}}_p^{\mathrm{c}}$

Figure 4.34: Brachial vs. Carotid Artery: Area A_p of the reservoir pressures $\widehat{p}_{\mathrm{res}}$ and $\breve{p}_{\mathrm{res}}$

4.5.4 Pressure Decay in Diastole

In this section the pressure decay in diastole is examined in order to investigate (A1) for the respective arteries which constitutes one of the the major assumptions for the extended Reservoir Theory. However, *due to* this assumption, the reservoir curves are presumed to have an exponential decay which is aligned to the measured waveform.

Since the majority of curves exhibit different beat durations and, hence, a different amount sampled time points, it is not possible to compare different curves by applying the (R)MSE. Therefore, one could use the respective time constants of the brachial and carotid reservoir pressure waveforms instead in order to quantify the pressure decay during diastole. The corresponding results of the time constants τ for both arteries are illustrated in fig. 4.35 computed by both the algorithms 3.2 and 3.3 whereby the samples for the respective algorithm consisted of 110 and 89 pressure curves at each arterial location.

Both illustrated comparison sets of $\widehat{\tau}$ and $\breve{\tau}$ between the arteries in fig. 4.35 show that the brachial time constant τ^{b} is systematically higher whereby the differences associated with $\widehat{\tau}$ are less substantial due to the lower standard deviation. In other words, the carotid pressure decay is indicated to be steeper for the majority of curves, which is also suggested by the figs. 4.12 and 4.13.

Nevertheless, in section 4.3.1 it was pointed out that the beat duration T_{b} of the carotid curve is generally longer within the provided sets of pressure curves. Therefore, this could have had an impact on the computation of the time constants. Since τ is obtained in order to match the pressure decay in diastole the respective diastolic durations $T_{\mathrm{d}} = T_{\mathrm{b}} - T_{\mathrm{s}}$ and their ratio to the the corresponding beat duration T_{b} are compared for both arteries in fig. 4.36. On the one hand it can be witnessed in figs. 4.36a, 4.36c and 4.36e that the estimated diastolic durations T_{d} are generally slightly longer for the carotid waveforms in absolute numbers. On the other, it is observable that the brachial and carotid diastolic durations are proportionally almost equal to their respective beat durations, cf. figs. 4.36b, 4.36d and 4.36f. In fact, the brachial ratios are marginally greater in comparison. Therefore, the apparent discrepancies in their respective diastolic durations seem to be a matter of scaling and, in further consequence, should not have affected the computation of the time constant largely.

Apart from the diastolic duration a closer look at the time duration it takes from the highest figure in the respective reservoir pressure to the

end of the beat might be of interest. Therefore the duration between

$$t_{\max} := \underset{t' \in \mathcal{T}_0^N}{\operatorname{argmax}} \left(p_{\mathrm{res}}(t') \right)$$

and the end of diastole is regarded. Since it holds $\mathrm{PP} = \max_{\mathcal{T}_0^N}(p_{\mathrm{res}}) - \mathrm{DBP}$ this time is associated with the reservoir pulse pressure. Hence, the time duration between $t_{\max}$ and the end of diastole shall be denoted by

$$T_{\mathrm{PP}} := T_{\mathrm{b}} - t_{\max}.$$

Provided that the results of $\widehat{p}_{\mathrm{res}}$ and $\breve{p}_{\mathrm{res}}$ are very similar, only the reservoir pressures $\breve{p}_{\mathrm{res}}$ are taken into further consideration. In fig. 4.37 the values of T_{PP} and their ratios to the respective diastolic durations T_{d} are illustrated for a direct comparison of the arteries. According to the figs. 4.37a, 4.37c and 4.37e it can be witnessed that the brachial T_{PP} is, in general, slightly lower in absolute numbers. However, for a relative comparison between the arteries the ratio $T_{\mathrm{PP}}/T_{\mathrm{d}}$ shall be regarded too. Firstly, and with respect to fig. 4.37b, it is observable that it always holds that $T_{\mathrm{PP}} > T_{\mathrm{d}}$ for both arteries. Hence, the maximum of $\breve{p}_{\mathrm{res}}$ is hit throughout within systole at both arteries and in particular, for the majority of curves, rather shortly prior to the estimated notch time. But more importantly with a view to further investigation, the comparison of the ratios $T_{\mathrm{PP}}/T_{\mathrm{d}}$ between the arteries in figs. 4.37d and 4.37f indicates that the relative time it takes from the highest point of the reservoir pressures to the pressure at the end of diastole is quite similar for both arteries.

Therefore, firstly, the reservoir pulse pressures at both arteries are considered as meaningful due to the carotid pressure scaling during data preprocessing. Secondly, the end-diastolic pressure values of both arterial reservoir curves are supposed to be close to the same DBP due to the diastolic fitting procedure. Hence, since the reservoir pulse pressures of the carotid arteries are systematically higher than those at the brachial artery but the relative time $T_{\mathrm{PP}}/T_{\mathrm{d}}$ it takes to drop for both pressures to the end-diastolic figure is quite comparable, a steeper pressure decay of the carotid pressure waveform is very likely regardless the acknowledged difficulties with respect to their direct comparison due to the different beat durations of the provided measured data sets.

Overall, these findings suggest that the brachial and carotid reservoir pressure decays differ during diastole. In consequence, in case of regarding the exponential curves as appropriate approximations, the same holds for the actual pressure waveforms.

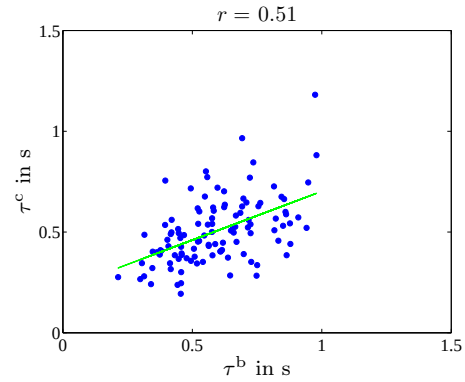

(a) Scatter plot: $\widehat{\tau}^b$ vs. $\widehat{\tau}^c$

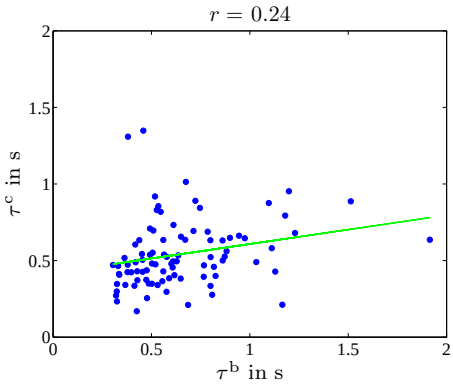

(b) Scatter plot: $\breve{\tau}^b$ vs. $\breve{\tau}^c$

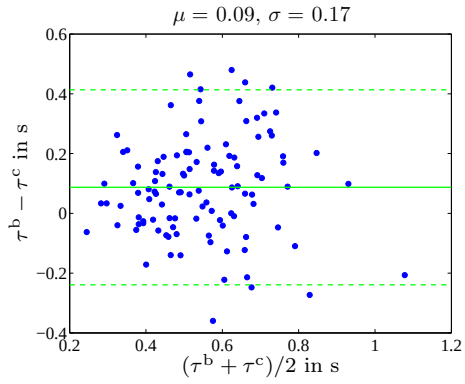

(c) Bland-Altman plot 1: $\widehat{\tau}^b$ vs. $\widehat{\tau}^c$

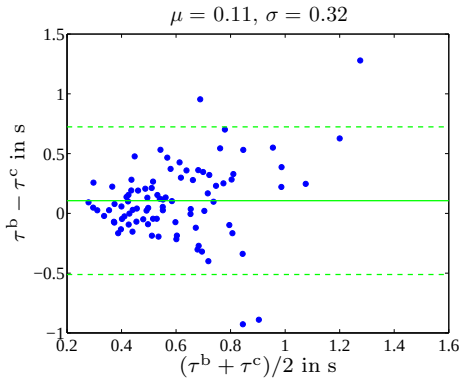

(d) Bland-Altman plot 1: $\breve{\tau}^b$ vs. $\breve{\tau}^c$

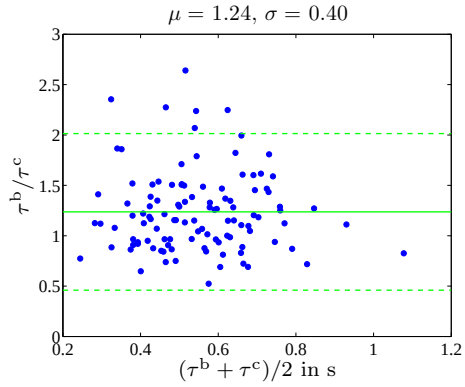

(e) Bland-Altman plot 2: $\widehat{\tau}^b$ vs. $\widehat{\tau}^c$

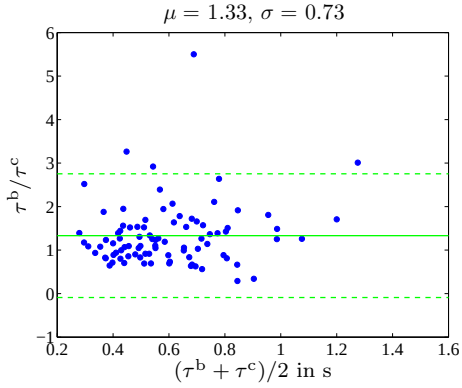

(f) Bland-Altman plot 2: $\breve{\tau}^b$ vs. $\breve{\tau}^c$

Figure 4.35: Brachial vs. Carotid Artery: Time constants $\widehat{\tau}$ and $\breve{\tau}$ of the reservoir pressures $\widehat{p}_{\text{res}}$ and $\breve{p}_{\text{res}}$

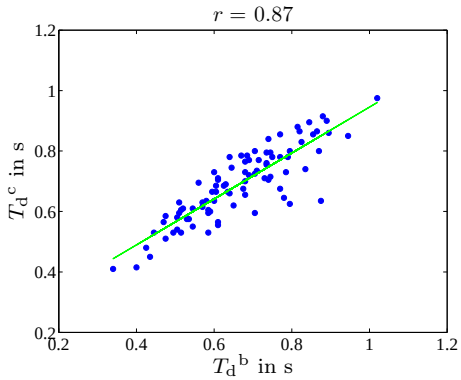

(a) Scatter plot: $T_d{}^b$ vs. $T_d{}^c$

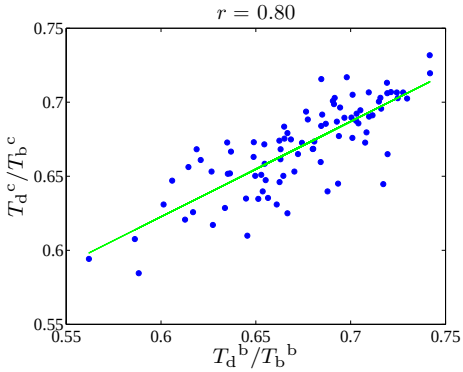

(b) Scatter plot: $T_d{}^b/T_b{}^b$ vs. $T_d{}^c/T_b{}^c$

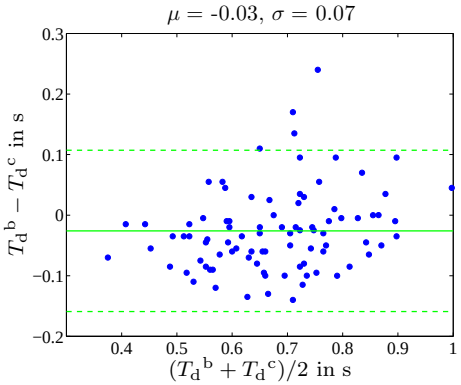

(c) Bland-Altman plot 1: $T_d{}^b$ vs. $T_d{}^c$

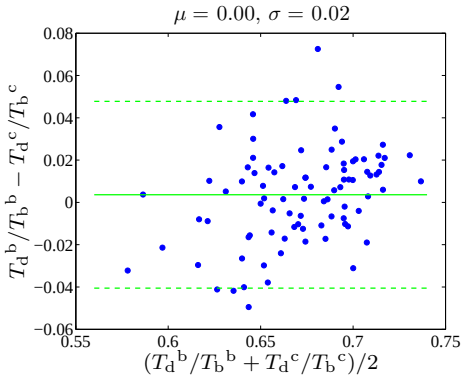

(d) Bland-Altman plot 1: $T_d{}^b/T_b{}^b$ vs. $T_d{}^c/T_b{}^c$

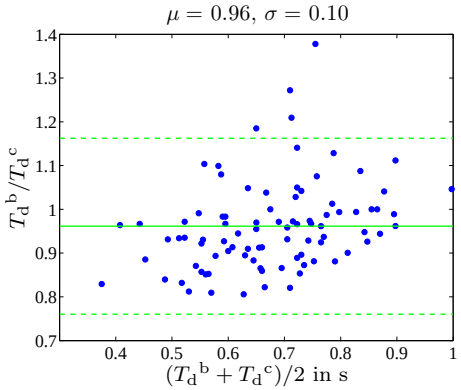

(e) Bland-Altman plot 2: $T_d{}^b$ vs. $T_d{}^c$

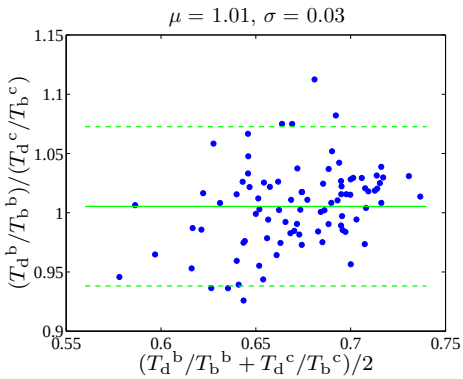

(f) Bland-Altman plot 2: $T_d{}^b/T_b{}^b$ vs. $T_d{}^c/T_b{}^c$

Figure 4.36: Brachial vs. Carotid Artery: Diastolic duration T_d

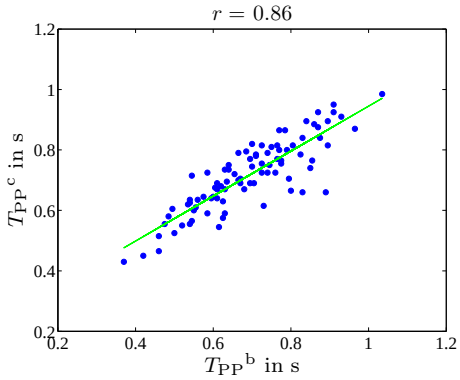

(a) Scatter plot: $T_{\mathrm{PP}}{}^{\mathrm{b}}$ vs. $T_{\mathrm{PP}}{}^{\mathrm{c}}$

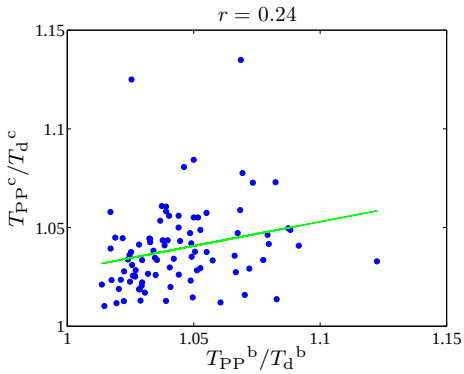

(b) Scatter plot: $T_{\mathrm{PP}}{}^{\mathrm{b}}/T_{\mathrm{d}}{}^{\mathrm{b}}$ vs. $T_{\mathrm{PP}}{}^{\mathrm{c}}/T_{\mathrm{d}}{}^{\mathrm{c}}$

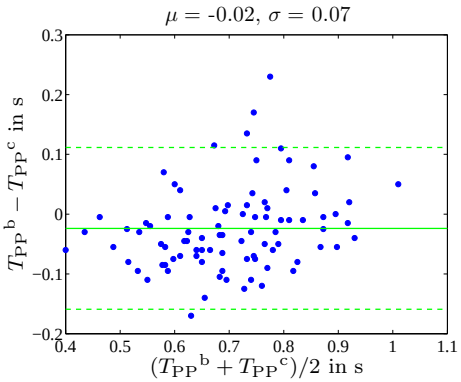

(c) Bland-Altman plot 1: $T_{\mathrm{PP}}{}^{\mathrm{b}}$ vs. $T_{\mathrm{PP}}{}^{\mathrm{c}}$

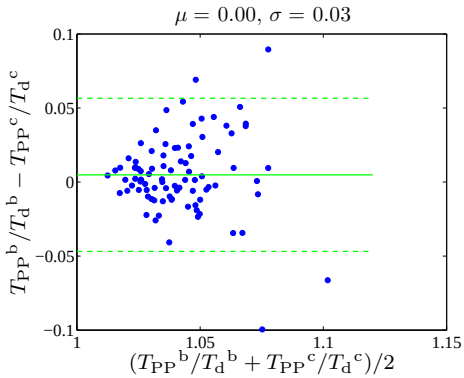

(d) Bland-Altman plot 1: $T_{\mathrm{PP}}{}^{\mathrm{b}}/T_{\mathrm{d}}{}^{\mathrm{b}}$ vs. $T_{\mathrm{PP}}{}^{\mathrm{c}}/T_{\mathrm{d}}{}^{\mathrm{c}}$

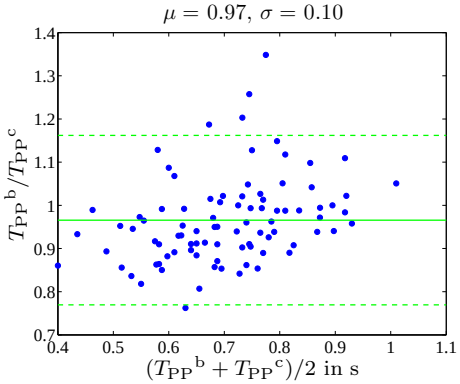

(e) Bland-Altman plot 2: $T_{\mathrm{PP}}{}^{\mathrm{b}}$ vs. $T_{\mathrm{PP}}{}^{\mathrm{c}}$

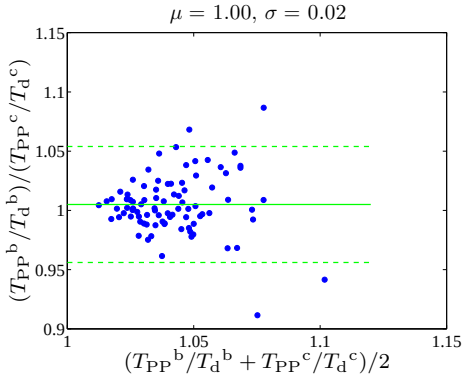

(f) Bland-Altman plot 2: $T_{\mathrm{PP}}{}^{\mathrm{b}}/T_{\mathrm{d}}{}^{\mathrm{b}}$ vs. $T_{\mathrm{PP}}{}^{\mathrm{c}}/T_{\mathrm{d}}{}^{\mathrm{c}}$

Figure 4.37: Brachial vs. Carotid Artery: Duration T_{PP} based on $\breve{p}_{\mathrm{res}}$ and its ratio to diastolic duration T_{d}

Chapter 5

Conclusions

Before presenting the major findings and conclusions some essential aspects shall be recalled:

Originally the Reservoir Theory was meant to resolve the differences of pressure and flow waveforms in the ascending aorta by regarding the actual pressure as an instantaneous sum of a time-dependent reservoir and a time- and location-dependent excess pressure. In order to acknowledge the propagation of the reservoir curve as well, it was modelled to be spatially uniform throughout the arterial tree but delayed in time. This was reasoned by the fact that the ascending aorta is the main driver of cushioning and recoiling within the systemic arteries. Therefore, it was assumed that

$$p(x,t) = p_{\text{res}}\big(t - \theta(x)\big) + p_{\text{ex}}(x,t) \tag{5.1}$$

with the time-delay $\theta(x) \geq 0$. In further consequence, by assuming $\theta(x)$ to be negligible, the pressure separation according to this approach became mathematically feasible[1]. Moreover, due to the observation that the excess pressure p_{ex} at the aortic root is proportional to the aortic flow the pressure separation could be performed by the mere knowledge of the pressure waveform.

Later, two observations were crucial so as to extend the concept on more distal locations within the arterial tree:

(A1) The pressure waveform decay measured at different locations in the arterial system is very similar during diastole.

(A2) The excess pressure at any aortic location is approximately proportional to the flow in the aortic root.

By *assuming* them for the respective arterial location one can perform the pressure separation without using the flow rate.

[1] From a different perspective, a two-element Windkessel model is applied in order to obtain p_{res} and then (5.1) is assumed for further considerations.

For the present thesis pressure and flow waveforms at the brachial and carotid artery were available in order to apply the Reservoir Theory on them. Two different approaches were considered:

Method 1: The pressure waveform at each artery was separated into reservoir and excess pressure by the use of both the pressure and flow velocity waveform.

Method 2: The pressure waveform at each artery was separated into reservoir and excess pressure by assuming (A1) and (A2).

Given that these two methods are based on different preconditions several interpretations are possible:

Method 1 – Interpretation: Since the flow velocity is used, two interpretations were associated with Method 1:

a) The measured data sets at the brachial and carotid artery are considered as an approximation to the aortic root waveforms and therefore the application of the (classic) Reservoir Theory using the flow is justified.

b) The pressure separation is applied to a different problem: A three-element lumped parameter model describes the respective arterial location where the pressure and flow into the system is given by the measured data.

Method 2 – Interpretation: It is taken for granted that both assumptions (A1) and (A2) are valid for both arteries and therefore the pressure separation according to the Reservoir Theory is applicable.

Prior to the application of the Reservoir Theory necessary data preprocessing was performed. In total, three different MATLAB-algorithms realized the two modelling approaches, whereby two distinct algorithms were used for Method 2[2]. In further consequence the Reservoir Theory was applied to 110 data sets by means of all algorithms and their corresponding results were compared to each other.

[2]One of these two algorithms was thankfully provided by Prof. Kim H. Parker and therefore constituted a different computational approach of Method 2.

5.1 Major Findings and Conclusions

In the course of the accomplishment of this thesis the major findings are:

- ***In general, it may not be expected that Method 1 and Method 2 generate similar results:*** This might have been anticipated since both are based on different preconditions. However, the obtained results testify this intuition. In general, systematic differences were observed in the regarded parameters. Particularly the pulse pressures and areas of pressure above diastolic blood pressure computed by Method 1 were systematically higher whereas the time constants were lower at both arteries in the majority of cases. Therefore it seems to be more reasonable to consider the respective pressure separation of Method 1 as one according to a local lumped parameter model such as illustrated in fig. 2.10b. But note, the same might be true for Method 2: Since it cannot be clarified with the available data whether the excess pressure waveform at the respective artery is "similar" to the flow in the aortic root the application of the extended Reservoir Theory could also be regarded as a local lumped parameter model. However, as opposed to Method 1 the input flow q of this model is assumed to equal $p_{\mathrm{ex}}/Z_{\mathrm{c}}$. Therefore, theoretically, Method 1 and Method 2 might still generate similar results in case that the input flows correspond to each other[3].

- ***The assumption (A2) can, in case of its validity, be refined:*** In the course of this thesis (A2) was extended in the following way:

  ($\widetilde{\mathbf{A2}}$) *The flow at the regarded arterial location is, up to a constant offset, approximately proportional to* the excess pressure at *the same site, which itself* is approximately proportional to the flow in the aortic root.

  In fact, ($\widetilde{\mathrm{A2}}$) helps to characterize the situation in which the assumption (A2) might hold at the regarded arterial location. Additionally, it is a real extension to (A2) since the flow at the "regarded arterial location" can be chosen to be the aortic root. However, it is still based on (A2) and its validity. Therefore, the computational procedure remains the same for Method 2. In further consequence, the stated points above can be refined such that Method 1

[3]The word "similar" is chosen since Method 2 assumes an exponential decay in diastole. However, in case of using the mathematical solution of p_{res} for the whole beat instead the respective reservoir results would correspond to each other.

and 2 are supposed to yield similar reservoir pressures in case of $q_0 + q \sim p_{\mathrm{ex}}/Z_{\mathrm{c}}$ with a constant offset q_0.

- ***The computed reservoir pressures are sensitive to the estimated notch time:*** Indeed, this is suggested by the numerical experiments. Since, in general, the notch time can only be an approximate estimation it would be highly desirable to dispose of algorithms which generate stable reservoir pressures. Therefore, this observation causes doubts in terms of a reliable prediction of clinically relevant parameters. However, it can be stated that the algorithm 3.3, provided by Prof. Kim H. Parker, seems to be the most stable among all regarded implementations.

- ***The brachial and carotid reservoir pressures obtained by the extended Reservoir Theory (Method 2) differ from each other:*** The computed pulse pressures and areas of pressure above diastolic blood pressure associated with the carotid reservoir waveforms were systematically higher compared to their brachial counterparts. Furthermore, the results suggest that the pressure decay of the respective reservoir pressures exhibits differences too. In combination with the discrepancies in their pulse pressure it is questionable whether (A1) is valid for those arteries. In further consequence, since a crucial assumption is that beside the "similar" pressure decay during diastole as well only time-delayed but spatially uniform reservoir curves are accepted by the inherent model theory, one might suspect that the extended Reservoir Theory is reasonably applicable at those arteries. However, additional data, such as flow waveforms at the aortic root, might be helpful in order to examine this more closely. Then, the respective excess pressure could as well be related to the aortic flow and (A2) could be discussed. Nonetheless, whereas the reservoir pressure waveform is regarded as spatially uniform the excess pressure is expected to reflect the local circumstances and shall help to explain the different pressure waveforms along the arterial tree. Hence, since the brachial and carotid reservoir pressures are indicated to be different, it is questionable if a comparison of the respective excess pressures is meaningful.

Limitations

In order to perform the Reservoir Theory on the peripheral waveforms some data preprocessing was necessary. Its procedure was carefully documented and its effects were examined. In general they were considered

as negligible and for many comparisons, like those of the pulse pressures and areas, even regarded as essential. For other comparisons, like for the time constant, the discrepancies of brachial and carotid data were taken into account in order to state the conclusions. Nevertheless, the provided data sets got altered.

Unfortunately, numerous results of the two algorithms 3.1 and 3.2 were affected by the chosen value domain of $0.7 \min_{t\in[0,\,T_\mathrm{b}]} p(t) \leq P_\infty \leq \min_{t\in[0,\,T_\mathrm{b}]} p(t)$ for the asymptotic pressure P_∞ since many computed values were found to be very close to the lower bound. This was discussed and taken into consideration during the comparison of the results and the formulation of the conclusion statements. However, the adaptation of the lower bound of the respective algorithms could be reasonable in order to perform a deeper analysis. This is especially true for algorithm 3.1 since, firstly, it was not possible to counter-check the results with another, unaffected algorithm[4] and secondly, its results differed notably depending on the initial values which was also observed at the algorithm 3.2. For the final parametrization of both algorithms "reasonable" initial values – based on the obtained results – were aimed to be chosen for the minimization routines.

5.2 Comparison with Literature

According to the current state of knowledge, the reservoir concept had never been applied to this high amount of brachial and carotid data sets in order to investigate the Reservoir Theory on a broader statistical base at these arteries. Nonetheless, many scientists have published their findings on the Reservoir Theory in the course of their research. Here, some of them shall be presented and – if possible – related to the results of this thesis.

In [7] the pressure separation according to Method 2 was discussed for a pair of brachial and carotid pressure waveform. Therein they say,

> "Despite the local arterial resistance and compliance being markedly different for each artery the reservoir pressure was almost identical, unlike the wave pressure [excess pressure] which differed markedly between the two arteries. This suggests that the reservoir pressure is a property of the central aorta, and is largely independent of differences in local compliance and resistance." [7, p. 43]

[4] The results of algorithm 3.2 were comparable with those of the unaffected algorithm 3.3.

The differences in the arterial resistance have been observed too since the brachial (area) resistances were, on average, approximately twice as high as their carotid counterparts. With respect to the compliance a clear statement by method 1 was not possible but method 2 indicated systematically higher carotid (area) compliances. The peripheral excess pressures have not been investigated but, as opposed to their observation, the findings in this thesis suggest that the reservoir pressures are generally different at the brachial and carotid artery. Moreover, some scientists say that the assumption of having location-independent reservoir pressures is not valid along the aorta either. In particular, in [18] it is stated that

> " ... contrary to a key assumption of the reservoir-wave approach, reservoir pressure was not spatially uniform [along the aorta] during systole." [18, p. 1]

Others conclude that

> " ... it is possible to demonstrate the effects of reflections on arterial pressure and flow clearly and directly only after appreciating that the measured aortic pressure is the instantaneous sum of a reservoir/windkessel pressure and a wave-related excess pressure." [32, p. 389.e8]

Especially this topic of wave propagation and reflection phenomena constitutes another big research field in this context and was not touched in the course of this thesis.

Overall, the Reservoir Theory remains controversial and still a lot of progress has to be made in order to illuminate this issue.

5.3 Outlook: Velocity Separation

In this thesis the focus was put on the *pressure* separation at both the brachial and carotid artery according to the Reservoir Theory. However, it is also possible to separate the *velocity* waveforms at arbitrary locations within the arterial tree [1]. With respect to the velocity separation it is assumed that the actual velocity waveform u can be regarded as an instantaneous sum of reservoir and excess velocities which now *both* depend on time and location. Thus, it is assumed that

$$u(x,t) = u_{\text{res}}(x,t) + u_{\text{ex}}(x,t),$$

whereby u_{res} is related to the reservoir pressure p_{res} and u_{ex} depends on local conditions. The procedure for the velocity separation now reads as

follows [1, §2.3]: The reservoir velocity is believed to be proportional to $(p_{\mathrm{res}} - P_\infty)$ at the end of diastole when the reservoir effect is believed to be dominant compared to the wave activity. Therefore, it holds that

$$u_{\mathrm{res}}(x,t) = \frac{p_{\mathrm{res}}(t) - P_\infty}{\overline{\mathcal{R}}(x)}$$

where $\overline{\mathcal{R}}$ describes the effective (area) resistance of all vessels downstream of the measurement site. The linear relationship between u and p is "difficult to identify, since waves may still be present" [1, p. 7]. However, for the computation and the presentation herein it is assumed that $\overline{\mathcal{R}}$ can be approximated by

$$\overline{\mathcal{R}} = \frac{\langle\!\langle p \rangle\!\rangle - P_\infty}{\langle\!\langle u \rangle\!\rangle}$$

where $\langle\!\langle p \rangle\!\rangle$ and $\langle\!\langle u \rangle\!\rangle$ denote the time-averaged pressure and velocity during diastole $T_{\mathrm{s}} \leq t \leq T_{\mathrm{d}}$. This particular choice is suggested in [1] but many other definitions are possible. For example the conversion formulas in (3.58), based on the pressure separation, could be used for this purpose too. Once u_{res} has been determined, the excess velocity then reads

$$u_{\mathrm{ex}}(x,t) = u(x,t) - u_{\mathrm{res}}(x,t).$$

In fig. 5.1 the separation of a brachial flow velocity is illustrated according to the computation procedure above. It can be witnessed that the excess velocity is prevalent during systole and diminishes during early diastole which models the intuitive approach that in early systole the wave-related phenomena are dominant whereas afterwards the reservoir effect drives the blood but with a considerably lower flow velocity. Another type of illustration is a so-called "PU-loop" which relates the pressure p with the flow velocity u. In fig. 5.2 the corresponding PU-loops are depicted for the respective pressure-velocity combinations whereby only the pressures above DBP have been considered. It is shown that in the early stage of systole the slope of the $p\,u$-loop is almost identical to the one of the $p_{\mathrm{ex}}\,u_{\mathrm{ex}}$-loop whereas in later diastole it is rather close to the one of $p_{\mathrm{res}}\,u_{\mathrm{res}}$. Thus, this type of representation of the simultaneous pressure and velocity separation as well suggests that both the reservoir- and wave-related phenomena constitute major drivers but one after another, depending on the stage within the cardiac cycle. Furthermore, the $p\,u$-loop at the beginning of systole states a linear relationship between p and u. In fact, this slope is proportional to the wave speed. This is a consequence of the *water hammer equation*

$$dP_\pm = \pm\,\varrho\,c\,dU_\pm$$

which relates the changes of unidirectional waves, i.e. forward and backward running waves, of pressure and velocity wavefronts[5] with the wave velocity c and the blood density ϱ [15].

Based on this short introduction it shall have been motivated that the local wave speed at both the brachial and carotid artery could also be compared and investigated by the approach of velocity separation. In this context the considerations in [2] and in [28] might also be of major interest. The former introduces a novel wave intensity analysis of arterial pulse wave propagation which takes account for peripheral reflections. The latter is dedicated to the impact of wave reflections on the estimation of the local wave speed by the PU- and QA-loop methods.

[5] A wavefront refers to an infinitesimal change in pressure dP and velocity dU. The forward wavefronts are denoted with a "+"- and the backward wavefronts with a "−"-subindex. A more detailed description can be found in [25] for example.

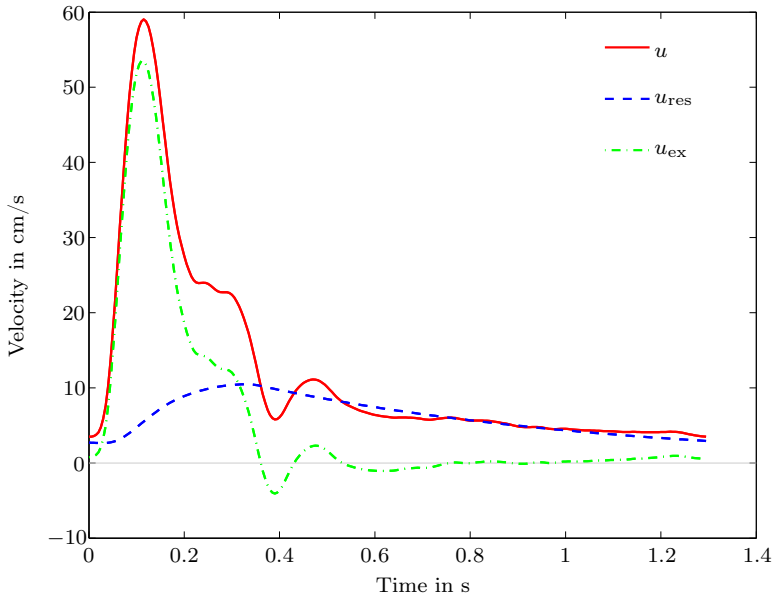

Figure 5.1: Brachial Artery: Separation of flow velocity

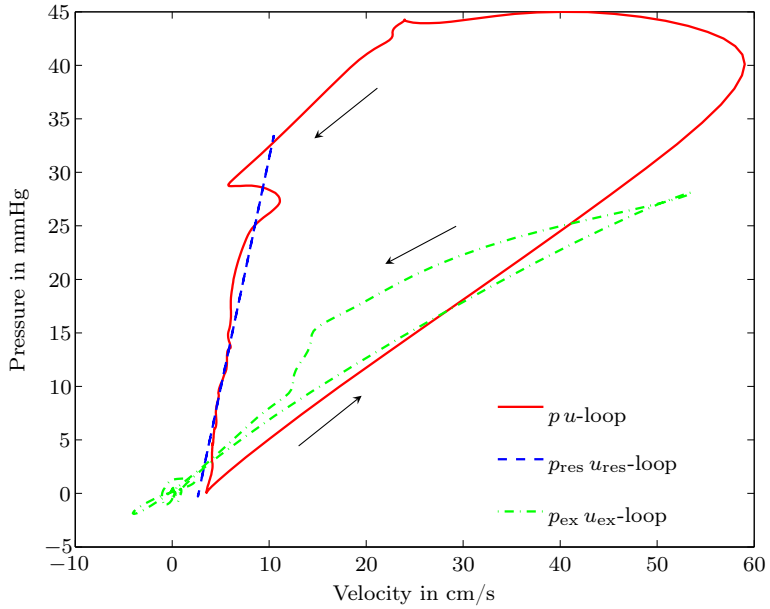

Figure 5.2: Brachial Artery: PU-Loop

Bibliography

[1] J. Aguado-Sierra, J. Alastruey, J.-J. Wang, N. Hadjiloizou, J. Davies, and K. H. Parker. Separation of the reservoir and wave pressure and velocity from measurements at an arbitrary location in arteries. *Proceedings of the Institution of Mechanical Engineers, Part H: Journal of Engineering in Medicine*, 222(4):403–416, 2007.

[2] J. Alastruey, A. A. E. Hunt, and P. D. Weinberg. Novel wave intensity analysis of arterial pulse wave propagation accounting for peripheral reflections. *International journal for numerical methods in biomedical engineering*, 30(2):249–79, Feb. 2014.

[3] J. Alastruey, K. H. Parker, J. Peiró, and S. J. Sherwin. Lumped parameter outflow models for 1-D blood flow simulations: Effect on pulse waves and parameter estimation. *Communications in Computational Physics*, 4(4):317–336, 2008.

[4] E. Baldaszti. *Jahrbuch der Gesundheitsstatistik 2012*. Statistik Austria, Vienna, 2013.

[5] A. Benetos, M. Safar, A. Rudnichi, H. Smulyan, J.-L. Richard, P. Ducimetiere, and L. Guize. Pulse Pressure: A Predictor of Long-term Cardiovascular Mortality in a French Male Population. *Hypertension*, 30(6):1410–1415, Dec. 1997.

[6] C. Caro, T. Pedley, R. Schroter, W. Seed, and K. Parker. *The mechanics of the circulation*, volume 41. Cambridge University Press, 2nd edition, 2012.

[7] J. E. Davies, N. Hadjiloizou, D. Leibovich, A. Malaweera, J. Alastruey-Arimon, Z. I. Whinnett, C. H. Manisty, D. P. Francis, J. Aguado-Sierra, R. A. Foale, I. S. Malik, K. H. Parker, J. Mayet, and A. D. Hughes. Importance of the aortic reservoir in determining the shape of the arterial pressure waveform – The forgotten lessons of Frank. *Artery Research*, 1(2):40–45, Sept. 2007.

[8] C. R. Ethier and C. A. Simmons. *Introductory Biomechanics: From Cells to Organisms*. Cambridge University Press, 2007.

[9] O. Frank. Die Grundform des Arteriellen Pulses: Erste Abhandlung. Mathematische Analyse. *Zeitschrift für Biologie*, 37:483–526, 1899.

[10] J. K. Hale and S. M. Verduyn Lunel. *Introduction to Functional Differential Equations*, volume 99. New York: Springer-Verlag, 1933.

[11] B. Hametner, S. Wassertheurer, A. D. Hughes, K. H. Parker, T. Weber, and B. Eber. Reservoir and excess pressures predict cardiovascular events in high-risk patients. *International Journal of Cardiology*, 171(1):31–36, 2014.

[12] W. F. Hamilton and P. Dow. *Handbook of physiology: A critical, comprehensive presentation of physiological knowledge and concepts*, volume 1. American Physiological Society, 1954.

[13] K. Hayashi, H. Handa, S. Nagasawa, A. Okumura, and K. Moritake. Stiffness and elastic behavior of human intracranial and extracranial arteries. *Journal of Biomechanics*, 13(2):175–184, 1980.

[14] M. Kawaguchi, I. Hay, B. Fetics, and D. A. Kass. Combined Ventricular Systolic and Arterial Stiffening in Patients With Heart Failure and Preserved Ejection Fraction: Implications for Systolic and Diastolic Reserve Limitations. *Circulation*, 107(5):714–720, Jan. 2003.

[15] A. Khir, A. O'Brien, J. Gibbs, and K. Parker. Determination of wave speed and wave separation in the arteries. *Journal of Biomechanics*, 34(9):1145–1155, Sept. 2001.

[16] R. C. Little and W. C. Little. *Physiology of the Heart and Circulation*. Year Book Medical Publishers, 1989.

[17] C. H. Manisty, A. Zambanini, K. H. Parker, J. E. Davies, D. P. Francis, J. Mayet, S. A. McG Thom, and A. D. Hughes. Differences in the magnitude of wave reflection account for differential effects of amlodipine- versus atenolol-based regimens on central blood pressure: an Anglo-Scandinavian Cardiac Outcome Trial substudy. *Hypertension*, 54(4):724–30, Oct. 2009.

[18] J. P. Mynard, D. J. Penny, M. R. Davidson, and J. J. Smolich. The reservoir-wave paradigm introduces error into arterial wave analysis: a computer modelling and in-vivo study. *Journal of Hypertension*, 30(4):734–743, Apr. 2012.

[19] J. P. Mynard and J. J. Smolich. Wave potential and the one-dimensional windkessel as a wave-based paradigm of diastolic arterial hemodynamics. *American journal of physiology. Heart and circulatory physiology*, May 2014.

[20] M. Nichols, N. Townsend, R. Luengo-Fernandez, J. Leal, A. Gray, P. Scarborough, and M. Rayner. *European Cardiovascular Disease Statistics 2012*. European Heart Network, Brussels, European Society of Cardiology, Sophia Antipolis, 2012.

[21] W. W. Nichols, M. F. O'Rourke, and C. Vlachopoulos. *McDonald's Blood Flow in Arteries: Theoretical, Experimental and Clinical Principles*. Hodder Arnold, 6th edition, 2011.

[22] A. Noordergraaf. *Circulatory System Dynamics*. Academic Press, 1978.

[23] R. M. Olson. Aortic blood pressure and velocity as a function of time and position. *J Appl Physiol*, 24(4):563–569, Apr. 1968.

[24] J. T. Ottesen, M. S. Olufsen, and J. K. Larsen. *Applied Mathematical Models in Human Physiology*. Society for Industrial and Applied Mathematics, 2004.

[25] K. H. Parker. An introduction to wave intensity analysis. *Med. Biol. Engineering and Computing*, 47(2):175–188, Feb. 2009.

[26] K. H. Parker, J. Alastruey, and G.-B. Stan. Arterial reservoir-excess pressure and ventricular work. *Medical & biological engineering & computing*, 50(4):419–24, Apr. 2012.

[27] J.-P. Richard. Time-delay systems: an overview of some recent advances and open problems. *Automatica*, 39(10):1667–1694, Oct. 2003.

[28] P. Segers, A. Swillens, L. Taelman, and J. Vierendeels. Wave reflection leads to over- and underestimation of local wave speed by the PU- and QA-loop methods: theoretical basis and solution to the problem. *Physiological measurement*, 35(5):847–61, May 2014.

[29] G. J. Tortora and B. H. Derrickson. *Principles of Anatomy and Physiology*. John Wiley & Sons, 2012.

[30] A. J. Vander, J. H. Sherman, and D. S. Luciano. *Human Physiology: The Mechanisms of Body Function*. McGraw-Hill, 1985.

[31] J.-J. Wang, A. B. O'Brien, N. G. Shrive, K. H. Parker, and J. V. Tyberg. Time-domain representation of ventricular-arterial coupling as a windkessel and wave system. *American journal of physiology. Heart and circulatory physiology*, 284(4):H1358–68, Apr. 2003.

[32] J.-J. Wang, N. G. Shrive, K. H. Parker, A. D. Hughes, and J. V. Tyberg. Wave propagation and reflection in the canine aorta: analysis using a reservoir-wave approach. *The Canadian journal of cardiology*, 27(3):389.e1–10, Jan. 2011.

[33] N. Westerhof, J.-W. Lankhaar, and B. E. Westerhof. The arterial Windkessel. *Medical & biological engineering & computing*, 47(2):131–41, Feb. 2009.

[34] N. Westerhof, N. Stergiopulos, and M. I. M. Noble. *Snapshots of Hemodynamics: An aid for clinical research and graduate education.* Springer, 2005.

[35] World Health Organization. The world health report 1998 – Life in the 21st century: A vision for all. Technical report, 1998.

[36] A. Zambanini, S. L. Cunningham, K. H. Parker, A. W. Khir, S. A. McG Thom, and A. D. Hughes. Wave-energy patterns in carotid, brachial, and radial arteries: a noninvasive approach using wave-intensity analysis. *American journal of physiology. Heart and circulatory physiology*, 289(1):H270–6, July 2005.